Investigation of *Oligo*-(*p*-phenyleneethynylene) (OPE) based Functional Organic and Inorganic-Organic Hybrid Assemblies

A Thesis Submitted for the Degree of

Doctor of Philosophy

By

Syamantak Roy

Chemistry & Physics of Materials Unit (CMPU)

Jawaharlal Nehru Centre for Advanced Scientific Research

(A Deemed University)

Bangalore-560064

April, 2018

Dedicated to my Mother

DECLARATION

I hereby declare that the matter embodied in the thesis entitled "**Investigation of *Oligo*-(*p*-phenyleneethynylene) (OPE) based Functional Organic and Inorganic-Organic Hybrid Assemblies**" is a result of the investigations carried out by me at the Molecular Materials Laboratory, Chemistry and Physics of Materials Unit, Jawaharlal Nehru Centre for Advanced Scientific Research (JNCASR), Bangalore, India under the supervision of **Prof. Tapas Kumar Maji** and that it has not been submitted elsewhere for the award of any degree or diploma.

In keeping with the general practice in reporting the scientific observations, due acknowledgement has been made whenever the work described is based on the findings of other investigators. Any omission that might have occurred due to oversight or error in judgement is regretted.

…….

Syamantak Roy

Date:

Place:

CERTIFICATE

I hereby certify that the work described in this thesis entitled **Investigation of *Oligo*-(*p*-phenyleneethynylene) (OPE) based Functional Organic and Inorganic-Organic Hybrid Assemblies**" has been carried out by **Mr. Syamantak Roy** under my supervision at the Molecular Materials Laboratory, Chemistry and Physics of Materials Unit, Jawaharlal Nehru Centre for Advanced Scientific Research (JNCASR), Bangalore, India and that it has not been submitted elsewhere for the award of any degree or diploma.

…….

Prof. Tapas Kumar Maji

(Research Supervisor)

Date:

Place:

ACKNOWLEDGEMENT

First and foremost, I want to express a heartfelt gratitude to my supervisor Prof. Tapas Kumar Maji for his constant guidance, mentoring and his encouragement to try new research ideas over the course of this investigation. He has helped me inculcate a strong sense of dedication and discipline within me for which I am ever grateful to him.

I thank Prof. C. N. R. Rao, FRS, who has been a constant source of inspiration.

I thank the past and present CPMU chairmen: Prof. Balasubramanian and Prof. Chandrabhas Narayan for allowing me to use the instrumental facility.

I am thankful to my course instructors: Prof. Rajaram, Prof. Maji, Prof. Sundaresan and NCU faculties, whose courses have been extremely helpful for carrying out the research work.

I also thank my collaborators: Prof. Pati (JNCASR), Prof. Ray (JU), Prof. Ramamurty (IISc), Prof. Prasad (CeNS), Dr. Arkamita Bandyopadhyay (JNCASR), Dr. Lakshmi Madhuri (CeNS), Dr. Devraj Raut (IISc) and Mr. Mrinmay Das (JU) who were always ready to discuss research problems and were always prompt in making quick communications of research work.

I want to thank the technical staff: Mrs. Usha, Mr. Vasu, Mr. Rao, Mr. Anil, Ms. Selvi, Mr. Mahesh and Mr. Shiva for their timely support in all kinds of measurements.

I am especially grateful to Prof. Rajaram and Dr. Ankit Jain for the technical discussions regarding organic synthesis and also Dr. Jay Ghatak and Swati for fruitful discussions, whenever I faced hurdles in my research venture.

I am thankful for the wonderful support I got from Hostel, Library, Complab, Academic and Admin to make my stay at JNCASR pleasant.

I thank Dr. Thirumalesh Reddy and Dr. Yogesh for getting my broken wrist back in place with proper movements. This allowed me to smoothly carry out research even after a bad injury.

Sharanappa also needs to be thanked for supplying a constant dose of caffeine during long hours of work. I enjoyed the fruitful conversations I had with Debu da over a cup of "strong Sharanappa coffee".

I am grateful to my undergrad professors: Dr. Sanjib Ganguly, Prof. Bhattacharyya and Prof. Mitra who have always helped me whenever required, without a show of discontent.

The lab family needs a special mention for providing the ideal atmosphere to carry out research: Sohini, Papri, Pramod, Subhajit, Dr. Debabrata Samanta, Dr. Ashish Singh, Dr. Sajad Ahmad Bhat, Dr. Darsi Rambabu, Dr. Subarna Dey, Dr. Chayanika Das, Parul, Mrinal, Sanchita, Tarandeep, Dr. Nivedita Sikdar, Dr. Anindita Chakraborty, Dr. Venakta Suresh Mothika, Dr. Arpan Hazra, Dr. Ritesh Haldar, Dr. Jayaramulu Kolleboyina, Dr. Sudip Mohapatra and Dr. Prakash Kanoo.

I thank my friends in JNCASR: Amrit Da, Ritesh da, Payel, Neha, Debu da, Arup da, Jia da, Arkamita, Suman, Arun, Praveen, Subhajit, Manjeet, Pradeep, Arjun, Anirban, Rajib, Dibya and Paramita for the good times spent together.

My friends from school, college and colony deserve a special mention: Babun, Riju, Debatama, Arup, Shombhu, Rohan, Joma, Anirban, Atreya, Shamayeeta, Arghya, Amrita and Vandana. They have always kept in touch and supported me.

I am thankful to my football gang in JNCASR, for keeping the dream alive of playing football throughout my life and also for being such nice company.

My Fantasy Premier League (FPL) gang made the weekends fun and enjoyable with discussions on team selection and analysis of matches: Arup, Arjun, Indrashish, Zubin, Davis and Abhijit.

I thank Supriti Madam for always being a lovely host and Neel-Sonai for the constant source of entertainment during the lab parties.

My aunt (mam), uncle (meshon) and sisters (Srijita and Shinjini) have always been a constant source of support and love even after living in a different city. They have always made sure that I am doing alright through regular visits and phone calls to let me know that they are there for me.

My family in JNCASR/IISc without whom, survival in JNCASR would have been impossible: Sohini, Broto, Ananya, CD, Arka, Sourav, Abhijit, Arpan da, Soma di and Bumba. They have always been there for me through the good and bad times. This is the reason I consider them as family over friends. I never imagined that I would have such a supportive group of individuals so close to me while doing Ph.D. They are genuine personalities and I am proud to have them as friends. Much love to them.

Some exceptional human beings have been there with my family over many years and have given their all for our well-being. I am lost for words every time I talk about their contribution in my life: Dr. Amitava Sarkar and Mrs. Sutanuka Sarkar, two extraordinary people whose unflinching support, love and care have always provided me with a sense of security. Mr. Arunava Ghosh and Dr. Sampa Chaudhuri, who treat me like their son and always shower a lot of love. Chhotomamidida and Anupama mashi, who I can always count on, to be there, when it matters most and Mr. Kartick Roy and Mrs. Neeta Roy who have always been supportive of my research endeavors.

I know my father, Mr. Sukanti Roy, would have been immensely proud to see me submit this thesis for the fulfillment of a doctoral degree and I wish he was here beside me in this moment of happiness. He was always the person who encouraged me to pursue my dreams and taught me to try out new things which helped me later on in life, particularly in doing research.

Last but not the least, my mother, Dr. Madhumita Bhattacharyya Roy and wife, Dr. Ritwika Ray were the constant pillar of support throughout the thesis work. They were always there for me through thick and thin. Without their constant motivation, this thesis would not have been possible. I must acknowledge their personal sacrifices which allowed me to carry out research in Bangalore with a peaceful mind. Their love and care is the best thing to happen to my life.

PREFACE

The thesis is organized into four chapters highlighting how diverse supramolecular assemblies with multi-functionalities can be constructed using chromophoric bola-amphiphilic π-systems. An *oligo*-(*p*-phenyleneethynylene) (OPE) rigid backbone has been taken as a model system on which side chains and terminal functional groups have been appended to give rise to organic supramolecular assemblies and metal-organic frameworks (MOFs) at the bulk and nanoscale. Polymorphism, liquid crystallinity, melt formation, gel formation, stimuli-responsive luminescence and photo-physical studies have been performed in the supramolecular π-assembled systems. The nanoscale MOFs (NMOFs) have been studied for their water repellence, dynamic morphology, semi-conduction and device based photo-conduction. Bulk MOFs constructed from the same OPE backbones have been structurally well characterized to reveal the organizational origin of superhydrophobicity and photo-physics in the inorganic-organic hybrid OPE systems.

Chapter 1 provides an introduction to non-covalent interactions, supramolecular synthons, crystal engineering and the outcome of these in the construction of polymorphism, liquid crystallinity, stimuli-responsive and water repellent supramolecular systems. It further introduces gels, amphiphiles, bola-amphiphiles, MOFs and NMOFs. Finally, it introduces OPE based π-chromophoric systems and highlights why such a system was chosen for investigation, culminating into the thesis work.

Chapter 2 consists of the synthesis of five new OPEs and generation of phase tunable multi-functional supramolecular systems from these. It is divided into three sub-chapters. **Chapter 2A** contains the design and synthesis of a new di-octadecyl functionalized OPE dicarboxylate (OPE-C_{18}-1) extended via non-covalent interactions. OPE-C_{18}-1 shows two single-crystal-to-single-crystal polymorphic phase transformations which have been well characterized. Further, due to interplay of strong and weak supramolecular forces, it shows stimuli-responsive emission properties and liquid crystallinity. Nanoindentation on single crystals reveals its mechanical strength and predicts molecular alignment of OPE chains along the single crystal. DFT calculations also support the experimental claims. **Chapter 2B** proposes that on changing the side chains to a more polar tetraethyleneglycol (TEG) and terminal groups from acid to ester guides the stimuli-responsive behavior of OPE systems. Further acid groups are essential for transforming these OPEs into the gel

state. Again two new OPEs, OPE-C_{gly}-E and OPEC_{gly}-A with TEG side chains and ester and acid groups respectively, have been synthesized and characterized. OPE-C_{gly}-E shows exclusive mechanochromism and chromic melt formation whereas OPE-C_{gly}-A shows exclusive polymorphism. The acid groups in OPE-C_{gly}-A further induce organogel and coordination polymer gel (CPG) formation, having nanorice and attoliter nanocontainer morphologies. **Chapter 2C** puts forward the synthesis and characterization of two novel bola-amphiphilic *oligo*-(*p*-phenyleneethynylene) (OPE) dicarboxylates having non-polar and mixed polar side chains (OPE-C_{12} and OPE-C_{mix}). This led to gelation in both with vesicular morphology. Upon in situ loading of a suitable dye and redox active molecule, pure white light emitting and charge transfer (CT)-gels, respectively, were realized in OPE-C_{mix}.

Chapter 3 is divided in two parts with the content having NMOF structures with water repellent and opto-electronic properties. **Chapter 3A** deals with a rational design approach to self-assemble OPE-C_{18}-1 with Zn^{II} in polar solvents and generate morphologically dynamic NMOF structures having extreme water repellence. The NMOF shows time dependent transformation of nanosheets to nanoscrolls. Water contact angles portray its superhydrophobicity. Periodicity and hierarchical surface structure generated upon framework structure formation also lead to self-cleaning, thus mimicking the lotus leaf effect. **Chapter 3B** uses the same concept of generating water repellent MOF nanostructures using self-assembly of OPE-C_{12}-1 with Zn^{II} in polar solvents. The MOF nanostructure showed semi-conducting property. Further, MOF nanosheets were cast on conducting electrodes to fabricate an opto-electrical device showing Schottky-diode like behavior. It further showed excellent photo-conductivity with potential applications in under-water devices.

Chapter 4 is partitioned into two parts, both containing the single crystal structures of superhydrophobic bulk MOFs and their applications. **Chapter 4A** contains the single crystal structure elucidation of a Cd^{II} based OPE-C_8 superhydrophobic and emissive MOF where permanent porosity is established by CO_2 adsorption at 195 K. Removal of coordinated DMF molecules leads to red shift in its emission. The original cyan emission can be brought back by re-exposure to DMF and acetonitrile while other solvents (THF, methanol and acetone) generate intermediate emission, thus showing the vapor sensing ability of the framework. **Chapter 4B** reveals the single crystal structure of a Mg^{II} and OPE-C_{18}-1 based MOF having surface projected alkyl chains leading to

superhydrophobicity. Single crystal face dependent and thin film electrical measurements have revealed the semi-conducting nature of the MOF and probable charge transport pathway through the extended network.

Chapter 5 contains the summary of the entire thesis work. It also contains a discussion about future work that can be done taking the concepts and methods given in the thesis.

TABLE OF CONTENTS

Chapter 1

Introduction

1.1. Supramolecular Interactions

Supramolecular chemistry is mainly concerned with non-covalent interactions, also termed as supramolecular interactions.[1] It encompasses both attractive and repulsive effects within molecules. Interestingly, an entire supramolecular system is held together by interplay of all possible supramolecular interactions present in the system. The interactions can be classified into (a) ion-ion, (b) ion-dipole, (c) dipole-dipole, (d) hydrogen bonding, (e) cation-π, (f) anion-π, (g) π-π, (h) van der Waals and (i) closed-shell interactions. These can arise due to both, host and guest as well as the surroundings such as crystal lattice arrangement, ion-pairing, solvation etc.[2]

1.1.1. Ion-ion Interactions

A classic example is the NaCl lattice where each Na^+ cation is surrounded by six Cl^- anions (Figure 1a).[3] The Na^+ ion organizes six donor Cl^- ion around itself leading to the overall lattice of NaCl. The interaction energies are comparable to the order of covalent bonds (Table 1).

1.1.2. Ion-dipole Interactions

The bonding of an ion with a polar molecule is an example of ion-dipole interactions. Na^+ when interacting with water molecules shows this kind of an interaction.[4] A more common example is the interaction of alkali metal cations with the polar oxygens of a crown ether. This makes them sit inside the cavity of the crown ethers (Figure 1b).

1.1.3. Dipole-dipole Interactions

When one dipole aligns with another and interacts through the matching of poles of the pair, it is termed as a dipole-dipole interaction (Figure 1c).[5] It can either be attractive (type I) or repulsive (type II). This interaction energy is slightly less than that of ion-dipole and ion-ion interactions. HCl, organic carbonyl compounds *etc.* show this type of interactive behavior.

1.1.4. Hydrogen Bonding Interactions

Hydrogen bonding can be regarded as a particular kind of dipole-dipole interaction in which a hydrogen atom attached to an electronegative atom (or electron withdrawing group) is attracted to a neighboring dipole on an adjacent molecule or functional group.[6]

The common representation of hydrogen bonds is D−H···A. D is usually an electronegative atom such as O or N and A is usually another electronegative atom. However, it must be noted that significant hydrogen bonding interactions have been reported in hydrogen donors of less electronegative atoms such as C. Hydrogen bonding is relatively strong and is directional in nature. This is the reason why it is often called as the "masterkey interaction in supramolecular chemistry". Based on their interacting length and bond angle, they can be classified into strong, moderate and weak (Table 2).[7]

1.1.5. Cation-π Interactions

Interactions of transition metal cations such as Fe^{2+} and Pt^{2+} forming complexes with olefinic and aromatic hydrocarbons fall under this category.[8] The interactions are quite strong and hover on the borderline of covalent and non-covalent interactions (Figure 1d).

1.1.6. Anion-π Interactions

At a first glance, it seems that this might be a repulsive interaction due to the excess charge on both the anion and the π-electron cloud. However, there lies a charge difference between the overall neutral aromatic ring and the anion and therefore, a possibility exists for an electrostatic attractive interaction (Figure 1e).[9] The overall energy is still low. Anion-aromatic complexes show examples of this interaction. It must be kept in mind that the aromatic molecule must be electron deficient in nature so as to generate a difference in charge between the interacting parts.

1.1.7. π-π Interactions

This interaction is also called a stacking interaction and occurs between aromatic rings. It may also be called a π-π stacking interaction and needs one interacting part to be slightly electron deficient than the other. It can occur in a face to face manner or in an edge to face manner.[10] Other geometries are also possible in this non-covalent interaction. The most widely known π-stacking interaction occurs between that of the aromatic sheets of graphite. This is mostly a face to face interaction. Edge to face interactions lead to a herringbone packing in systems. The calculated energy landscapes point to 1) 45-90^0 orientation angles with an offset of 2-6 Å between the pairs and 2) angles close to 180^0 with offset distances of 3-6 Å to be attractive interactions. All other combinations of orientation angles and offset distances are considered to be repulsive π-π stacking interactions (Figure 2).

1.1.8. Van der Waals Forces

A weak electrostatic interaction arising due to the polarization of an electron cloud by a neighboring cloud best defines van der Waals forces. These are non-directional in nature and have very weak interaction energies.[11] Inclusion compounds where small organic molecules are loosely trapped within a macrocycle gives an example of van der Waals forces occurring between the host and guest.

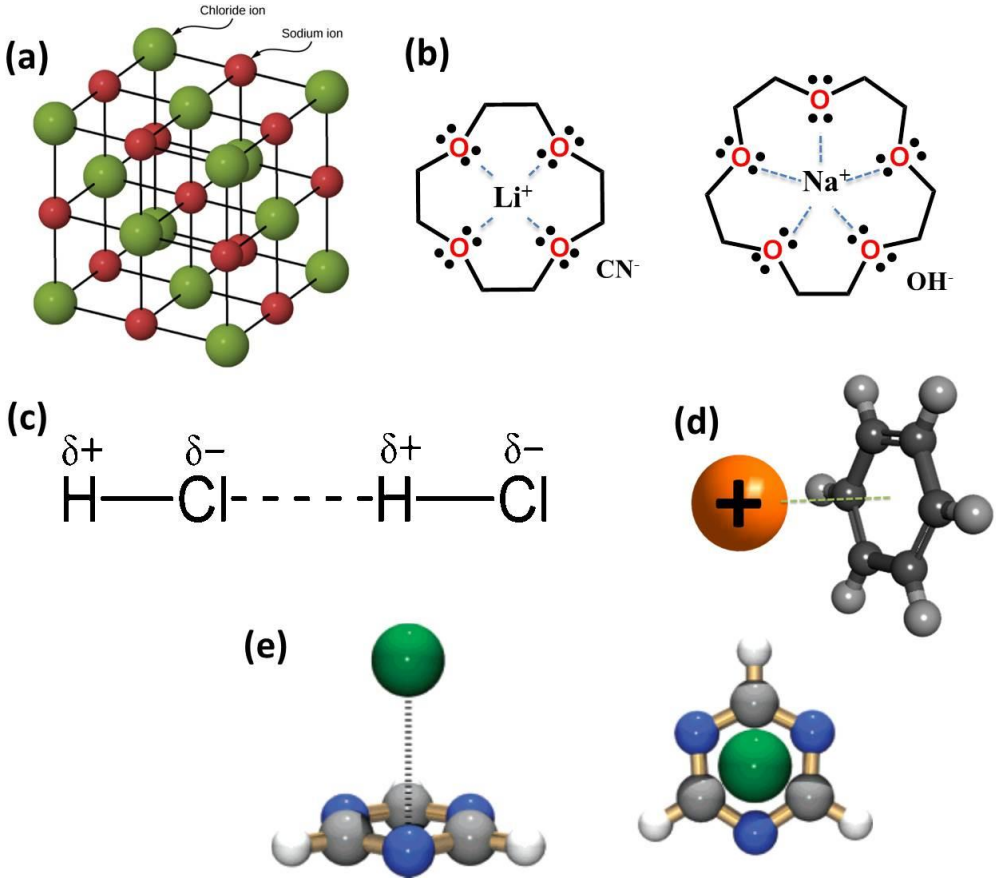

Figure 1. (a) Structure of the NaCl crystal lattice, an example of ion-ion interactions, (b) Structure of the crown ethers with alkali metal cations in their cavities, an example of ion-dipole interactions, (c) The HCl molecule, exhibiting dipole-dipole interactions, (d) Schematic of the cation-π interaction: (left) the basic interaction showing a generic cation positioned over benzene along the 6-fold axis and (e) Initial theoretical observation of anion-π complexes occurred in a study of the interaction between Cl^- and triazine.

1.1.9. Other Weak Hydrogen Bonds

Apart from the strong O−H···O and N−H···O hydrogen bonds, weak hydrogen bonds occur, which play a significant role in supramolecular packing interactions.[12] The two

most significant ones are the C−H···π and the C−H···O hydrogen bonds.[13] When the interaction strength is discussed, one has to keep in mind, both the bonding angles and the distances that play a key role in determining the interaction energy. Figure 3a shows the required nomenclature used to calculate the interaction strengths of C−H···O bonds. D values span the range 3.00-4.00 Å. Generally θ = 130-180°, a wide range of angles which vary based on the functional groups. Acceptable *d* values for strong interactions are in the region of 2-2.5 Å, but maybe considered upto 3.7 to 3.8 Å for very weak interactions.[7,12,13] The upper interaction limit of strong C-H···π interactions is usually considered to be 2.9 Å. However, there have been reports of very weak C−H···π interactions can go upto 4.0 Å (Figure 3b).[13c]

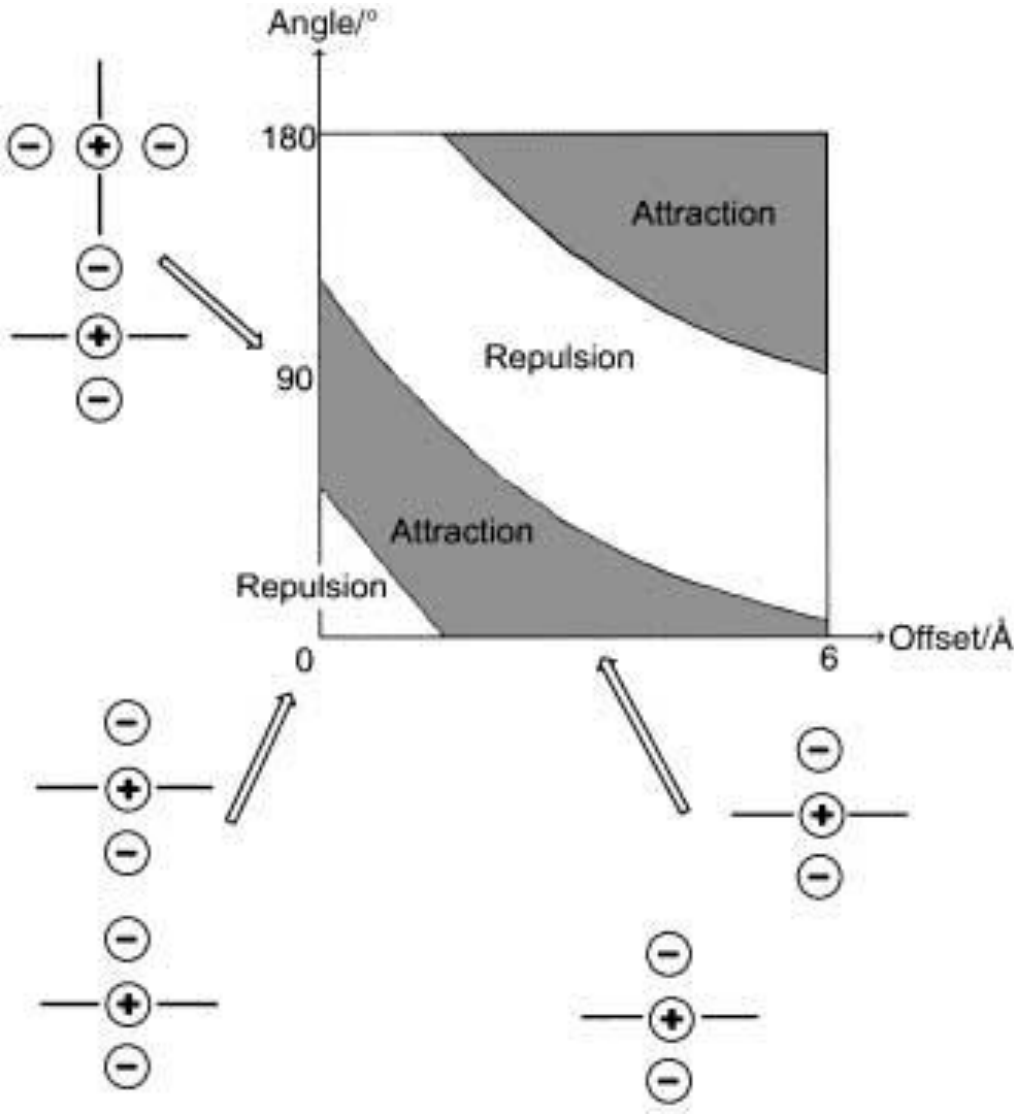

Figure 2. Electrostatic interactions between π-charge distributions as a function of orientation. This figure has been reproduced with permission from reference no. 10a.

1.2. Host Guest Systems

The simplest way in which host-guest systems can be visualized is that a molecular host binds another molecule, often called a guest to produce a 'host-guest' complex or supermolecule.[14] The host is said to have convergent binding sites (Lewis basic donor atoms, hydrogen donor atoms etc) whereas the guest is said to have divergent binding sites (Lewis acidic metal cation, hydrogen bond acceptor halide anion. Numerous examples of host-guest systems can be given such as crown ethers,[1,4] cylodextrins,[1,4] calixarenes,[1,4] metal-organic frameworks (MOFs)[15] and covalent organic frameworks (COFs),[16] incorporating guest dye molecules via non-covalent interactions, porous carbons incorporating metal nanoparticles into its pores etc.[17] Interestingly, host-guest chemistry can also occur via molecule-surface interactions. Surface assembled host networks can show specificity to guest binding, similar to other porous materials such as zeolites, MOFs and COFs.[18] The advantage of these surface hosts is that, the nanoscale architecture allows easy integration into membranes etc.

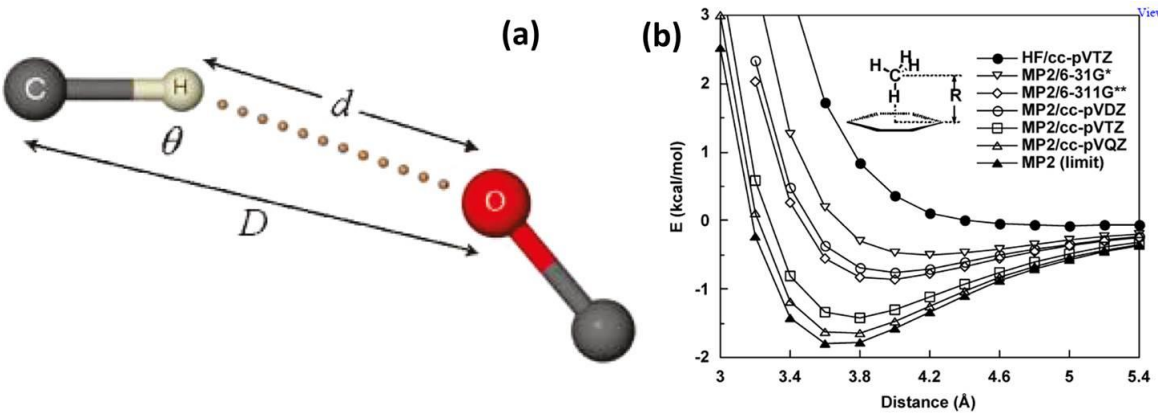

Figure 3. (a) Schematic showing the bonding distances and angular parameters used to calculate a C–H···O hydrogen bonding strength and (b) Basis set effects on the interaction energies of C–H···π interactions calculated for the benzene-methane cluster by the MP2 method. This figure has been reproduced with permission from reference no. 13b and 13e.

This leads to real-life applications in separation technology,[19] molecular sensing[20] and catalysis.[21] Calixarene functionalized 3D surface nanomaterials have been utilized extensively for selective recognition of ions, amino acids, proteins, and other biological molecules. Kinjo *et al.* recently showed that an amphiphilic *p*-sulfonatocalix[4]arene assembled water-soluble CdSe/ZnS QDs could recognize neurotransmitter acetylcholine (ACh) (Figure 4).[22] The calix[4]arene was holding on to the CdSe/ZnS QDs surface and

formed a bilayer structure with trioctylphosphine oxide (TOPO) molecules by virtue of hydrophobic interactions. This created an electron rich cavity, and the *p*-sulfonatocalix[4]arene could selectively bind ammonium based cationic compounds by host–guest interactions. Hence it was specific towards Ach binding.

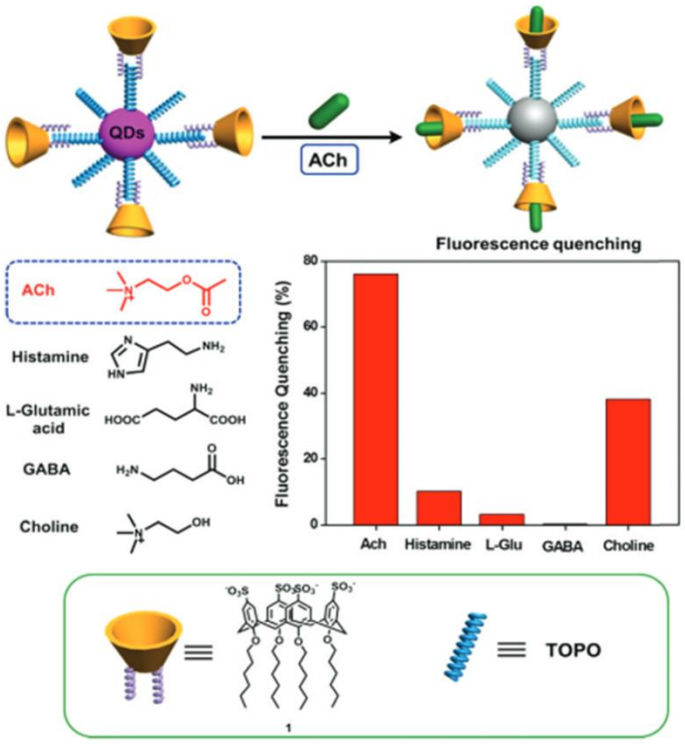

Figure 4. Schematic representation of *p*-sulfonatocalix[4]arene modified CdSe/ZnS QDs for selective recognition of acetylcholine (ACh). This figure has been reproduced with permission from reference no. 22.

1.3. Crystal Engineering

Crystal engineering is a direct outcome of supramolecular chemistry.[24] It is defined as the understanding of intermolecular interactions in the context of crystal packing and the utilization of such understanding, in design of new solids with desired physical and chemical properties. It integrates two fields: crystallography and synthesis.[25] The question that this approach tries to answer is: given a molecular structure of a compound, what is its crystal structure? Via this approach, one tries to interpret a crystal structure in terms of inter/intramolecular interactions. The final outcome is the definition of a reliable design strategy using these interactions. Through this, one finally attempts to direct crystal design for a property that may be needed.

Table 1. Properties of non-covalent interactions[23]

Interaction	Interacting distance (Å)	Interaction angle (^{0})	Interaction energy (kJ/mol)
Ion-ion	Depends on the geometry and interacting ions	Depends on the geometry and interacting ions	100-350
Ion-dipole	Depends on the geometry and interacting moieties	Depends on the geometry and interacting moieties	50-200
Dipole-Dipole	-	-	5-50
Cation-π	-	-	6-80
Anion-π	2.9-3.7	-	5-50
π-π	3.3-4.6	-	-
Van der Waals	3-10	-	-

Discussing about crystal engineering, several terms such as surpramoelcular synthons, supramolecular interactions, polymorph, co-crystal, coordination polymer, metal–organic framework etc come up. To predict the associated crystal growth of these compounds, one needs to simplify the entire structure into a representative unit called a supramolcular synthon.[26] They are defined as structural units of supramolecules formed and/or assembled by known or conceivable synthon operations involving intermolecular interactions.[23] As the synthon is considered the smallest interacting unit in a supramolecule, it can be envisioned that the overall structure is built up by a collection of robust synthons. A robust synthon is that which is made up of strong and directional supramolecular interactions.

Table 2. Properties of different types of hydrogen bonding interactions[23]

Type	Strong	Moderate	Weak
A–H···B interaction	Mainly covalent	Mainly electrostatic	Electrostatic
Bond energy (kJ/mol)	60-120	16-60	Less than 12
Bond Lengths (Å)			
H···B	1.2-1.5	1.5-2.2	2.2-3.2
A···B	2.2-2.5	2.5-3.2	3.2-4.0
Bond angles (^{0})	175-180	130-180	90-150
Examples	Gas phase dimers with strong acids/bases, proton sponge, HF complexes	Acids, alcohols, biological molecules	C-H hydrogen bonds, O-H···π hydrogen bonds

Hence, the more robust the synthon, the more robust is the supramolecule. Supramoelcular synthons can range from a simple O–H···O hydrogen bond in acids to complex halogen···halogen interactions as illustrated in Figure 5. Generally, directional O–H···O bonding is considered as a strong synthon which can build structurally rigid supramolecules, whereas van der Waal interaction mediated synthons are usually considered weak, thereby generating supramolecules, whose properties can be easily tuned by the breakage of these interactions.[1,4,11,23] It can therefore be assumed in supramolecular chemistry, that design of strong and weak synthons can provide a toolbox to generate desired functionalities in surpamolecular materials. However, it should also be noted that discontinuities in the building up process of supramolecules lead to a

difference in prediction of what property, a synthon might generate to the actual property of the supramolecule.

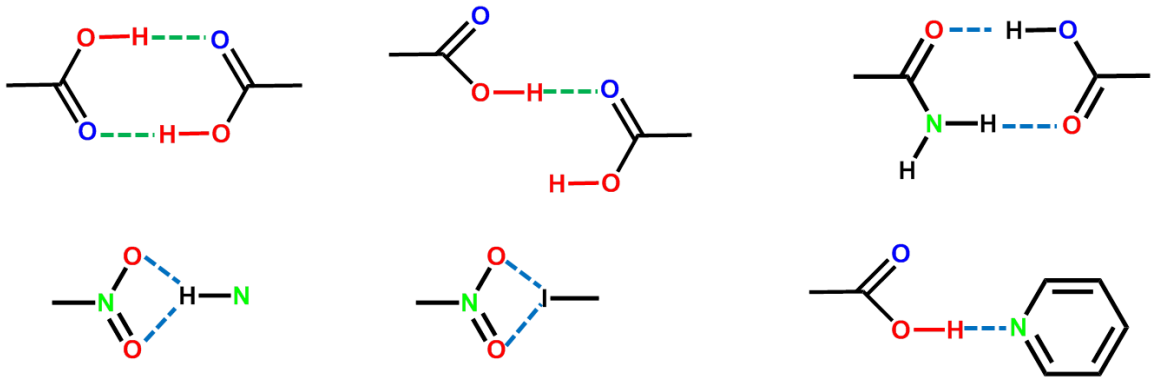

Figure 5. Representative supramolecular synthons. Dimer and catemer forms illustrate crystal packing in acids. The nitro···amino and nitro···iodo synthons show the similarity between hydrogen bonding and halogen bonding. Amide···acid and acid···pyridine heterosynthons are of relevance in the formation of pharmaceutical cocrystals.

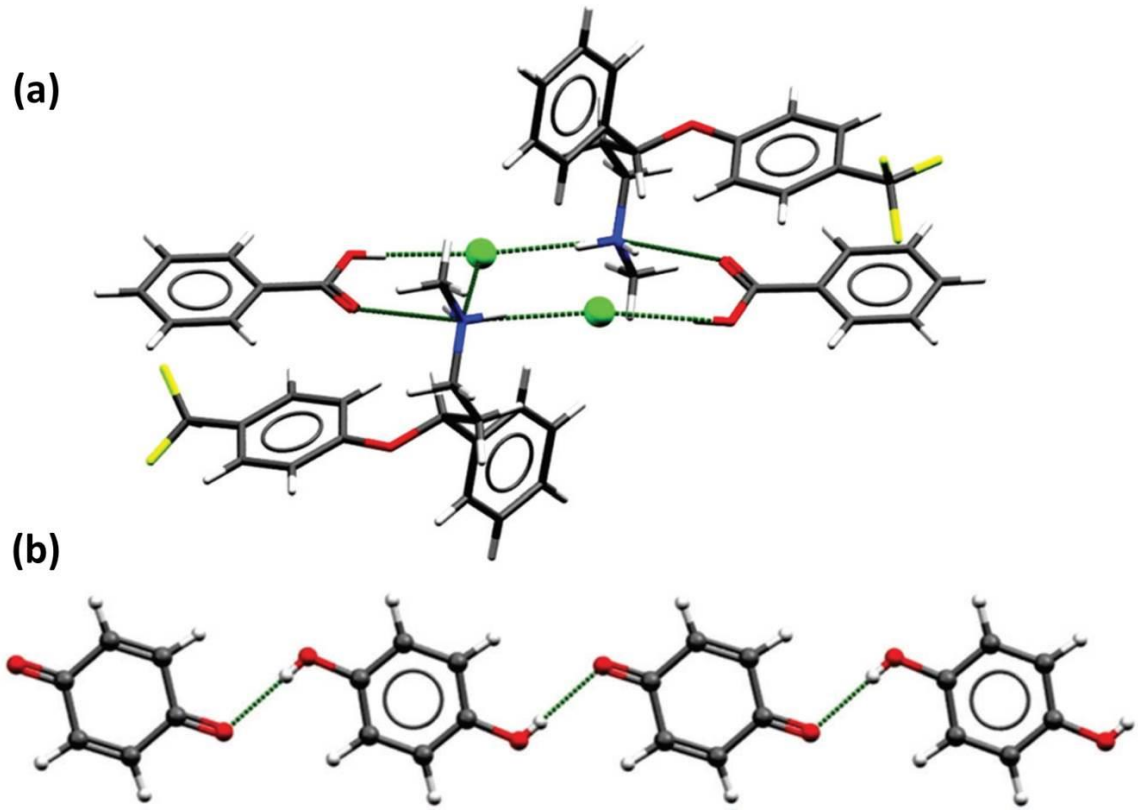

Figure 6. (a) The discrete assembly that is sustained by charge assisted hydrogen bond interactions in fluoxetine hydrochloride–benzoic acid and (b) Illustration of the 1D chain sustained by O–H···O hydrogen bonds in hydroquinone–quinone, quinhydrone. This figure has been reproduced with permission from reference no. 27a.

1.4. Co-crystals

The United States Food and Drug Administration (FDA), has put forward the definition of a co-crystal: Solids that are crystalline materials composed of two or more molecules in the same crystal lattice.[27] These have come into recent focus and are an integral part of pre-formulation stage of drug development. Co-crystals can be classified into classes, namely "molecular" and "ionic". Molecular cocrystals (MCCs) contain two or more different neutral conformers in a stoichiometric ratio and are typically, but not always exclusively, sustained by hydrogen bonds or halogen bonds. Most reported pharmaceutical co-crystals fall into this category. Ionic co-crystals (ICCs) are typically built-up by charge assisted hydrogen bonds and/or coordination bonds. Thus, some ICCs could also be classified as coordination polymers. Large families of ICCs include acid salts (carboxylate salt and carboxylic acid) and conjugate acid–base co-crystals (an ion and its neutral counterpart). An example of ICC is the fluoxetine hydrochloride with benzoic acid which is sustained by charge assisted hydrogen bonding (Figure 6a).[27c] Similarly, a classic example of MCC is quinone and hydroquinone (quinhydrone) which is sustained by an interacting carbonyl-hydroxyl heterosynthon (Figure 6b). [27d,e]

1.5. Metal-Organic Frameworks (MOFs)

Metal–organic frameworks (MOFs), also known as porous coordination polymers, are hybrid solids with infinite network structures built from organic bridging ligands and inorganic connecting points. MOFs can be constructed from pre-designed building blocks to impart unique properties for a wide range of potential applications including gas storage and separation, sensing, non-linear optics, drug delivery, opto-electronics, catalysis, magnetism and drug delivery.[28] They possess unprecedented high porosity. Depending on the size of ligands and inorganic connecting points and network connectivity, the porosity of MOFs can be readily tuned to afford open channels and pores with dimensions of several angstroms to several nanometers. The reason why MOFs are called inorganic-organic hybrid materials is because they sit in-between porous organic materials such as porous carbons, organic porous polymers, like covalent organic frameworks, conjugated microporous polymers and purely inorganic porous materials such as silica and zeolites (Figure 7a,b). MOFs can be further classified into 1st generation, where the structure disintegrates upon guest solvent removal; 2nd generation, where the rigid structure is stable (permanent porosity) after guest solvent removal; 3rd

generation, where the structure is not only stable after solvent removal, but is also flexible based on external stimulus; 4th generation, where the structure is modifiable by positions of metal nodes and organic linkers (Figure 7c).[28e]

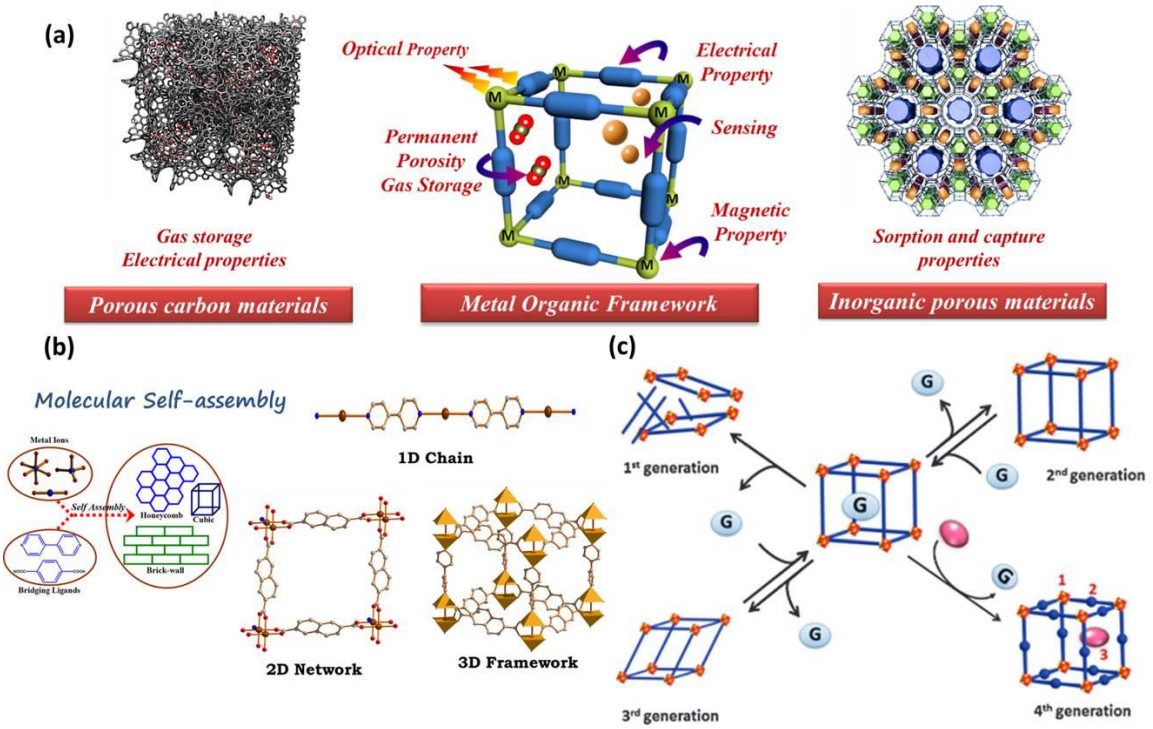

Figure 7. (a) Classes of porous materials and their applications, (b) Schematic showing the formation of MOFs via molecular self-assembly and (c) Classification of MOFs. This figure has been reproduced with permission from reference no. 28e and 28f.

The reason for the massive number of reported MOF structures is due to the vast choice of organic linkers and metal ions which can linked together via many permutations and combinations (Figure 7b). MOFs can also be prepared by using more than one linker to self-assemble with metal ions in solution to form mixed-linker MOFs. Isoreticular series of metal organic frameworks (MOFs) were first prepared with octahedral-shaped metal-containing ("inorganic") SBUs joined with a variety of linear ditopic carboxylate linkers to form 16 distinct compounds based on the same topology (MOF-5).[28g] Other reported and well known MOFs are the a) zeolitic imdiazolate frameworks (ZIFs) fabricated from tetrahedral metal ions (Fe^{2+}, Co^{2+}, Cu^{2+}, Zn^{2+}) and imdiazolate organic linkers.[29] ZIF-8 and ZIF-11 consists of Zn^{2+}, methylimidazolate and benzimidazolate and are one of the most stable and permanently porous MOFs. Chromium(III) dicarboxylate MOFs, MIL-53, 101 (MIL: Materials Institute Lavoisier)[30] show high surface areas upto 4100 m^2/g. Apart from these, there are several MOFs exhibiting very high surface areas e.g. NU-110

(NU- Northwestern University)[31] exhibits surface area of 7140 m^2/g, while MOF-177: 5640 m^2/g, MIL-101: 5900 m^2/g, UMCM-2: 6000 m^2/g and MOF-210: 6240 m^2/g.[31] However, apart from all the above discussed applications and high surface areas exhibited by MOFs, they suffer from the drawback of solution processability which negates any device based applications of MOFs.

1.6. Nanoscale Metal-Organic Frameworks (NMOFs)

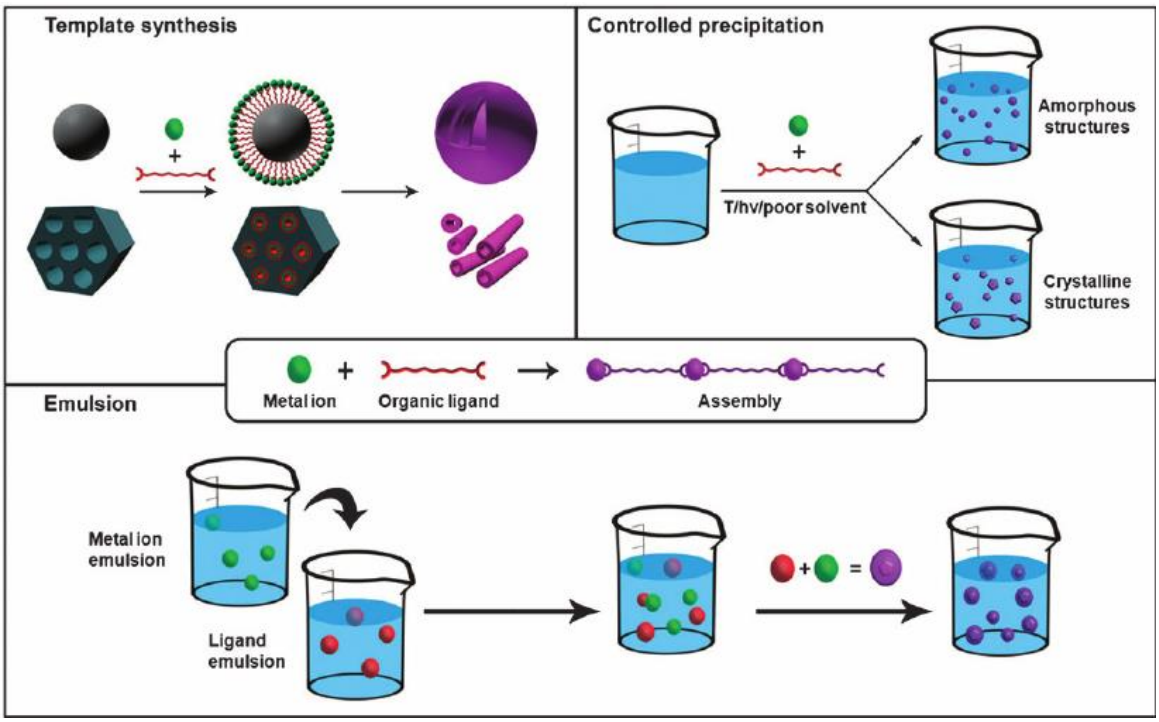

Figure 8. Schematic representation of the principal synthetic strategies used for synthesizing 0- and 1-D metal–organic nanostructures using conventional coordination chemistry, including the LbL growth on templates, the controlled precipitation of metal–organic nanostructures and the microemulsion techniques. This figure has been reproduced with permission from reference no. 32d

As discussed in the previous section, MOFs do not always do not always meet the intended applications due to lack of processability and cannot be immobilized at specific locations on surfaces. This demands a miniaturization of MOF structures at the nanoscale to get enhanced properties. Nanoscopic dimensions of MOFs would allow it to be internalized into cells, and this would trump bulk MOFs as delivery vehicles, diagnostics, etc.[32] The small dimension of NMOFs also allows them to be dispersed in aqueous media or other solvents, and to efficiently coat them for improving their biocompatibility or

recognition capabilities. Nanomaterials, in general, have higher surface areas than their macroscopic counterparts.[32d] This property can improve the catalytic, ion exchange, separation, sensing and sorption properties of MOFs. NMOFs also show enhanced

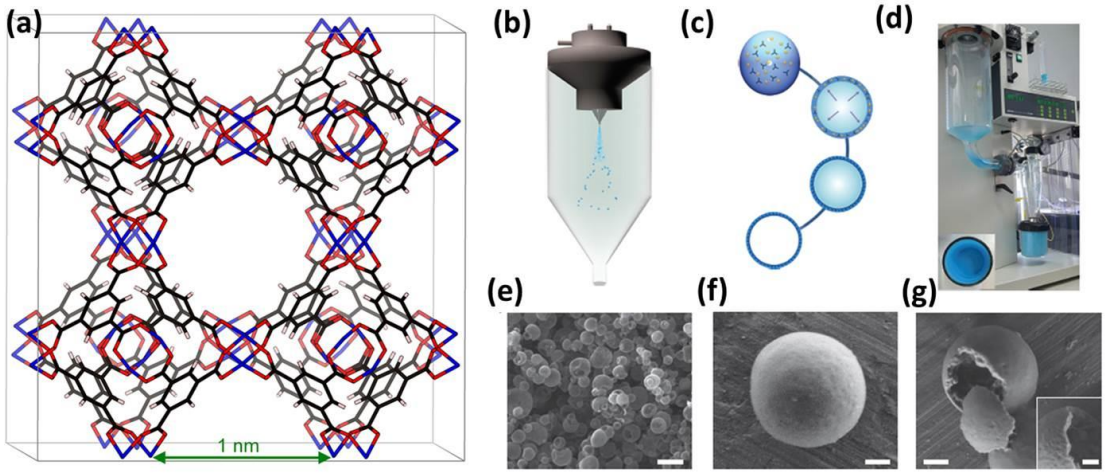

Figure 9. Spray-drying synthesis of spherical hollow HKUST-1 superstructures: (a) Structure of HKUST-1, (b) Schematic showing the spray-drying process used to synthesize HKUST-1 superstructures. Blue dots, sprayed solution; blue spheres, formed spherical superstructures, (c) Proposed spherical superstructure formation process (emphasized by purple arrows), which implies the crystallization of nanoMOF crystals. Within a droplet, the MOF precursors (metal ions, orange; spheres and ligands, tri-rods) concentrate and crystallize at the surface into spherical superstructures, (d) Photograph of the spray-dryer after its use in synthesizing large amounts of blue HKUST-1 superstructures, (e–g) Representative FESEM images showing a general view of the spherical HKUST-1 superstructures (e), the wall of a single HKUST-1 superstructure showing the assembly of nanoHKUST-1 crystals (g), and a mechanically broken hollow superstructure showing the internal cavity and the thickness of its wall (f and inset). Scale bars: 5 mm (e), 500 nm (f,g), 200 nm (f, inset). This figure has been reproduced with permission from reference no. 33.

physical properties. It is well known that unique physical properties emerge when at least one dimension of a material is reduced to the nanometre scale. Thus, NMOFs are also expected to hold highly desirable size-dependent optical, electrical and magnetic properties. The miniaturization of MOFs down to the nanometre length scale is therefore a unique opportunity to develop a new class of highly tailorable nanoscale materials that combine the rich diversity of compositions, structures and properties of classical metal–

organic materials with the obvious advantages of nanomaterials. Synthesis of NMOFs can be carried out using a variety of techniques such as template synthesis, controlled precipitation, emulsion method or a coordination directed self-assembly approach (Figure 8). All these arrest the growth of framework structures in one dimension leading to formation of various nanostructures depending on reaction condition and environment. Maspoch and co-workers described an entirely new and highly effective methodology to synthesize either nanoMOFs or hollow MOF superstructures using a spray drying technique.[33] This strategy was applicable to a broad range of MOFs, drastically reduced their production times and costs, and enabled continuous and scalable nanoMOF synthesis as well as solvent recovery (Figure 9). HKUST-1 was the MOF whose hollow super-structures were preliminarily synthesized using this unique technique.

1.7. Polymorphism

Polymorphism is best defined as the occurrence of two or more crystalline forms of the same compound in the solid state.[34] Difference in intermolecular interactions plays a subtle role in guiding different arrangements of molecular building units in the structure leading to the existence of polymorphs (Figure 10A). These are not only of fundamental importance, but are also of interest to the industry. This is because different polymorphs have different physicochemical properties such as melting point, solubility, bioavailability and hygroscopicity. Polymorphs can be classified into two types, monotropes and enantiotropes, This is done with their stability with respect to temperatures and pressures. If one of the polymorphs is stable over a certain temperature range and pressure, while the other polymorph is stable over a different temperature range and pressure, then the two polymorphs are said to be enantiotropes. On the other hand, if only one polymorph is stable at all temperatures below the melting point, then these polymorphs are called monotropes. The stability relationships between polymorphs are usually done via thermal analysis such as thermogravimetric analysis (TGA) and differential scanning calorimetry (DSC). However, unambiguous characterization of thermally related polymorphs is best done via studying single crystal to single crystal transformations (SCSCT) at a range of temperatures.[35] It is a direct outcome of the crystal engineering approach. Although, it is the best method, SCSCT analysis is somewhat rare in organic systems, as single crystallinity is often lost due to cooperative movement of atoms in the solid state. This is the reason why analysis of polymorphic structures using

SCSCT becomes challenging and calls for more exploration. It is also interesting to point out that variance in surpamolecular interactions can also lead to the existence of multiple polymorphs in non-covalently bonded systems. This interplay of non-covalent interactions can again be visualized via single crystal x-ray diffraction analysis to throw light upon the structural picture.

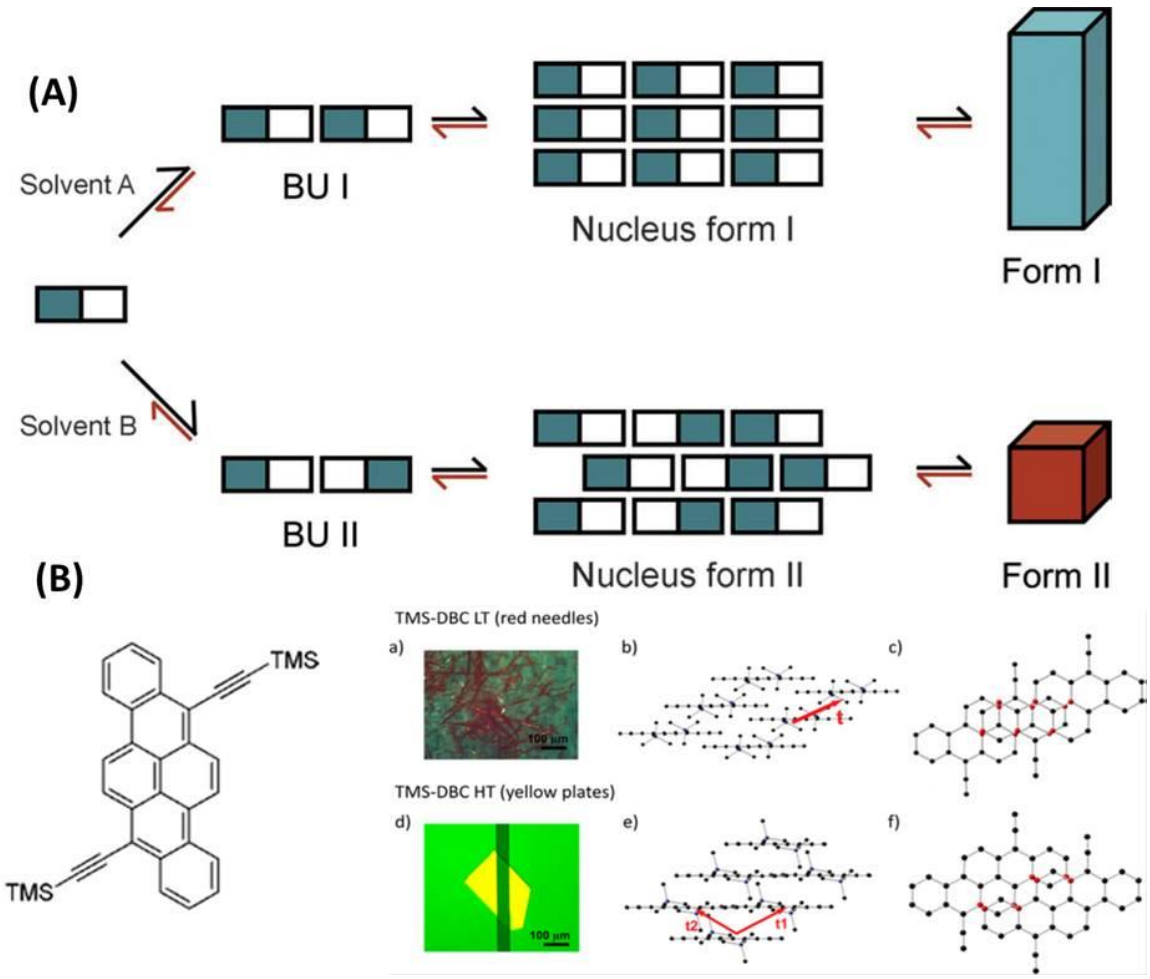

Figure 10. (A) Self-association in different solvents might lead to the formation of different building units (BU I in solvent A, BU II in solvent leading to polymorphic structures. These building units form the differently packed nuclei and thus the crystalline phases form I and form II, (B) (a) and (d) Crystal color, size, and shape of the LT red and HT yellow polymorphs of TMS-DBC, (b) and (c) Side and top views of the crystal packing in the red LT polymorph, (e) and (f) Side and top views of the crystal packing in the yellow HT polymorph. The directions corresponding to the largest calculated electronic couplings are indicated with arrows. This figure has been reproduced with permission from reference no. 34e and 34f.

Collis and co-workers showed that temperature can also play an important role in the existence of polymorphism in molecular systems.[34e] The 7,14-bis((trimethylsilyl)ethynyl)dibenzo[b,def]-chrysene (TMS-DBC) (Figure 10B) synthesized by them formed two polymorphic structures (one at low temperature and the other at higher temperature) with distinctly different structural packing and physical properties. The polymorph formation was guided by the temperature of the substrate during crystal growth. The uniqueness in the finding was that both polymorphs were extremely stable and did not convert to the other structure even upon applying external stimuli. The yellow plate like form of one polymorph had a much higher mobility (2.1 $cm^2\ V^{-1}\ s^{-1}$) compared to the red needle like polymorph (0.028 $cm^2\ V^{-1}\ s^{-1}$). This was a direct result of the different packing arrangement of the two polymoprhs. This work therefore showed that the same molecule can exist in polymorphic structures tuned by surrounding temperatures and having different physical properties and further highlights the importance of polymorphism in molecular systems.

1.8. Stimuli-Responsive Behavior

Nature is the best teacher and we find stimuli-responsive behavior all around us. The best example is the human body. It can selectively tailor molecular assemblies and interfaces that provide a specific chemical function and structure, which change in their environment. This is the basis of sustenance of life forms in the universe. Scientists have always taken a cue from nature and this has inspired studies on stimuli-responsive synthetic materials that mimic nature in changing its physical form or properties based on external perturbance. Macromolecular nanostructures have therefore been extensively studied and found great promise in practical applications from drug delivery, diagnostics, tissue engineering, 'smart' optical systems, to as biosensors, microelectromechanical systems, coatings and textiles.[36a] These polymers undergo conformational and chemical changes upon receiving an external signal. The stimuli can vary from temperature and pressure to change in its surrounding chemical environment such as pH. Researchers have constructed a galaxy of nanostructured stimuli-responsive polymer materials. These materials rely on the phase behavior of macromolecular assemblies in thin films (polymer brushes, multilayered films made of different polymers, hybrid systems that combine polymers and particles, thin films of polymer networks, and membranes that are thin films with channels/pores), and nanoparticles (micelles, nanogels, capsules and vesicles,

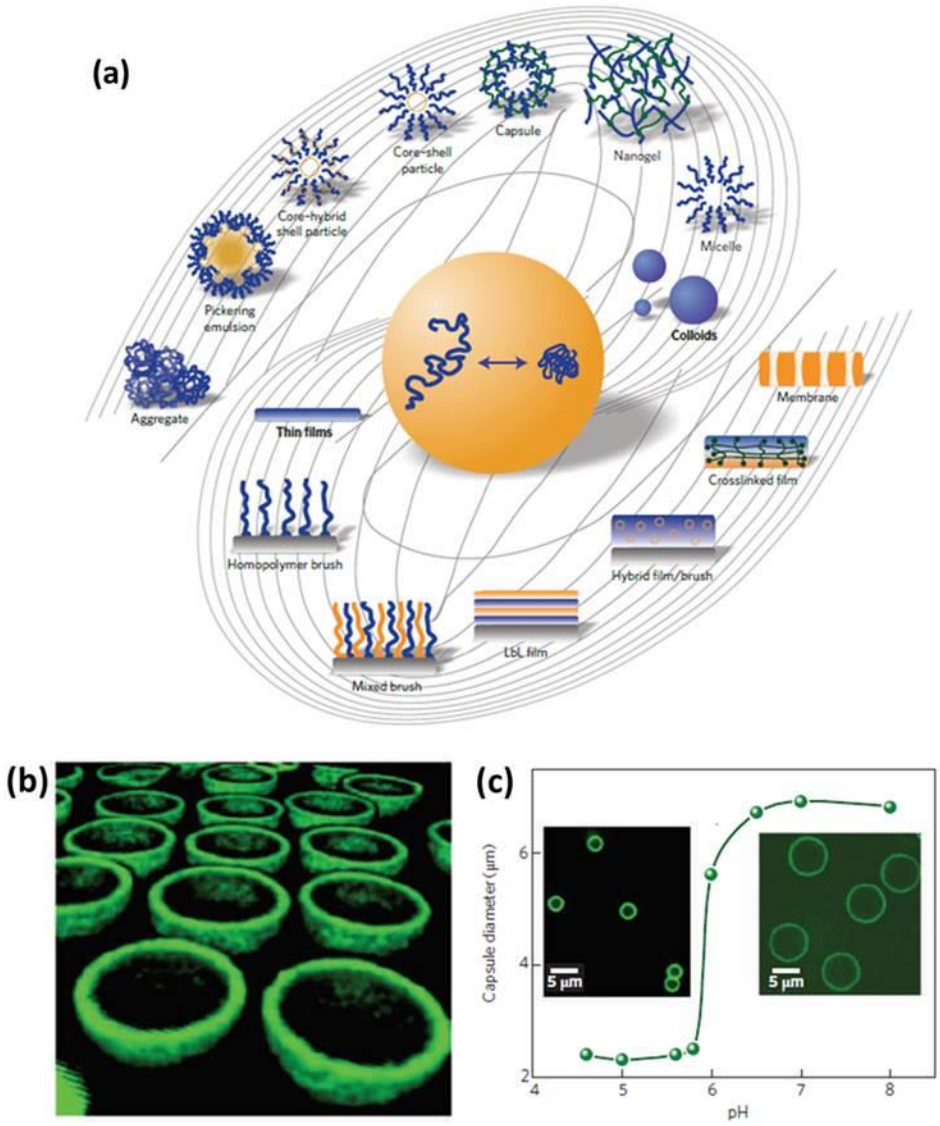

Figure 11. (a) Schematic showing a collection of stimuli-responsive synthetic polymeric nanostructures and their macromolecular assemblies that have been formed by applying external stimuli, (b) 3D reconstruction of the confocal images of the 3-μm LbL PMAA microcapsules and (c) pH-dependence of the diameter of the crosslinked PMAA microcapsules. This figure has been reproduced with permission from reference no. 36a.

core–shell particles, hybrid particle-in-particle structures, and their assemblies in solutions and at interfaces in emulsions and foams) (Figure 11a).[36a] However, there still remains issues with the long term stability and durability. The ultimate goal to realize practical applications in this field is to design robust and stable materials that can intelligently respond to external stimuli for bio-computing facilities encoded nanostructures that can target specific applications.[36b] For example, stimuli-responsive colloidal particles could find applications in catalysis, sensors and drug-delivery capsules

(Fig. 11b,c). For applications of these materials, electrostatic layer-by-layer (LbL) assembly has been introduced as a universal method for the facile fabrication of nanostructured, organized, multilayered, organic and hybrid thin films.[36c] In the fabrication of LbL interfacial assemblies, supramolecular interactions such as ion-ion interactions, hydrogen bonding, and polar and hydrophobic interactions are exploited to facilitate alternative deposition of complementary species which form functionalized conformal nanostructured interfaces. In an interesting work, researchers have created Poly(methyl methacrylate) (PMMA) microcapsules using the LbL method which change their diameter upon change in pH (Figure 11b,c). These could have implications as drug-delivery vehicles.[36a] Stimuli-responsive chromic materials also have wide-spread applications as sensor cores to detect pressure changes in the environment.[36a]

1.9. Liquid Crystallinity

Liquid crystals (LC) are a special class of supramolecular systems where an ordering is present along with a high degree of mobility within the same system. They are considered an intermediate class between a crystalline solid and a mobile liquid, retaining the properties of both to some extent.[37] This combination leads to the self-healing, adaptive, and stimuli-responsive behavior of these systems.[38] A condensed matter state can be considered as LC, if there is orientational or positional long range order in at least one direction and no fixed position for individual molecules. Long-range order could be orientational and positional. When molecules adopt a parallel alignment to minimize the excluded volume and to maximize the attractive intermolecular interactions, it is called an orientational ordering. Figure 12a shows the simplest types of LC phases. LC phases which have exclusive orientational order are assigned as nematic (N) phases. Along with the orientational order, the LCs can adopt a long-range of their preferred positions along one direction (1D), leading to layers (smectic phases = Sm) or along two different directions (2D phases); in the latter case columns are formed and these LC phase are assigned as columnar phases (Col). LCs with periodicity in all three dimensions (3D phases), often have cubic symmetry (Cub).

The presence of birefringence in liquid crystals leads to the typical textures observed under a polarization microscope. With the exception of cubic phases, all LCs show characteristic textures (Figure 12b). This is because cubic mesogens are isotropic and hence appear dark under a polarization microscope. But polarization microscope is not

enough to provide a structural picture for LC materials. Dynamic scanning calorimetry (DSC) and x-ray diffraction (XRD) are essential tools to characterize the thermal parameters and also the ordering and positioning of constituent molecules within a mesogenic or LC phase. Scientists have taken the use of self-assembly to synthesize a vast variety of LCs showing practical applications. Apart from LCDs, LCs find applications in organic photoconductors, field-effect transistors (FETs) and also photovoltaics (PVs).[39] Fundamentally, the ability of LC phases, to select the lowest energy state, can even be used to get best solutions for basic mathematical problems under complex boundary conditions (complex 2D tiling patterns and 3D cellular structures).

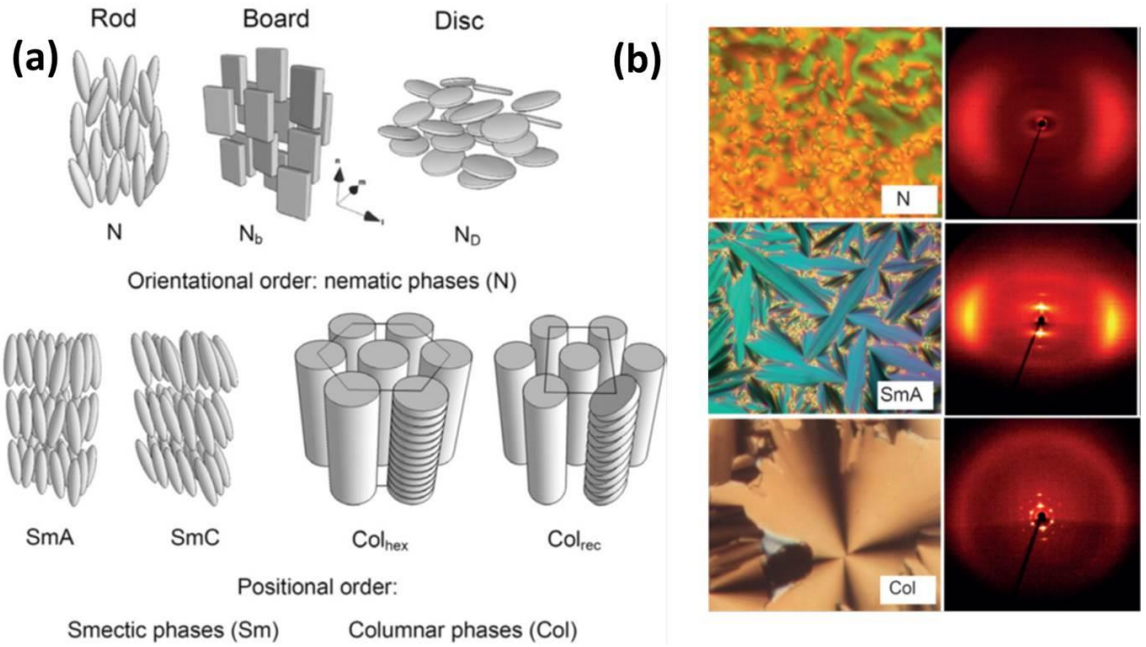

Figure 12. (a) LC phases of rod-like, board-like (sanidic), and disc-like molecules and (b) Typical textures (left) and representative 2D XRD patterns (right) of nematic (N), smectic (SmA), and columnar (Colhex) LC phases (aligned samples). This figure has been reproduced with permission from reference no. 37a.

1.10. Superhydrophobicity

Young's equation ($\cos\theta = (\gamma_{sv}-\gamma_{sl})/\gamma_{lv}$ where θ is the contact angle between the solid-liquid interface, $\gamma_{sv,sl \text{ and } lv}$ are the corresponding surface tensions between the solid, liquid and air interfaces) is used to describe the wettability on a smooth surface. On a rough surface, the same is explained by two models: Wenzel and Cassie Baxter (Figure 10).[40] (According to the Wenzel model, the water droplet on a rough surface is spherical in

shape and wets the surface. As a consequence it will not roll off the surface under the slightest disturbance. A transition from the Wenzel to the Cassie-Baxter model occurs when we consider that rough textures on a surface trap air-pockets in between. Therefore the water droplet cannot assume a spherical shape and rests on the rough texture with air-pockets trapped in between. This results in a low adhesion of the droplet to the surface and hence on the smallest perturbance, water rolls off the surface. It is theorized and verified experimentally that low surface energy along with a hierarchical surface roughness is essential to generate such superhydrophobic structures. A hierarchical structure implies the presence of roughness at two regimes: micro and nano. (**Figure 13**). This leads to water contact angles >150° giving rise to superhydrophobicity and self-cleaning applications.

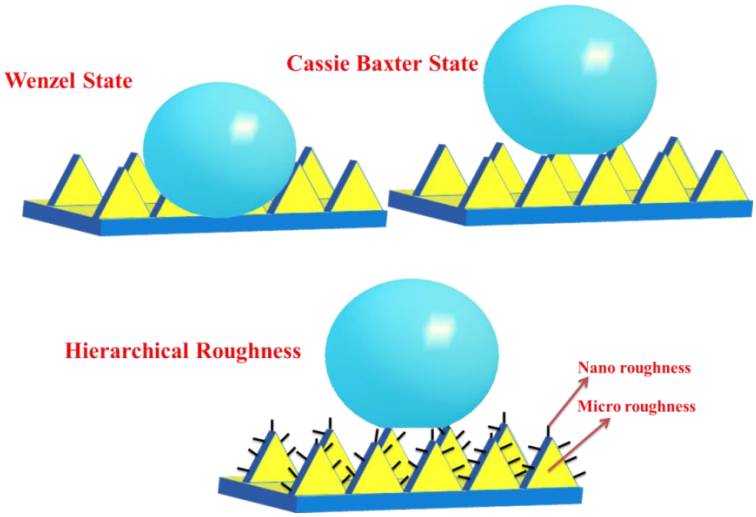

Figure 13. Schematic depicting two different theoretical models to explain water repellency of a liquid on a rough surface (Wenzel model and Cassie-Baxter model) and also the requirement of a hierarchical surface structure for the generation of superhydrophobicity and self-cleaning.

1.11. Supramolecular Gels

Gels are soft materials in which an organic or metal-organic scaffold mobilizes and traps solvent. A simple method to check for gelation is to invert the pot containing the gel and see whether it can hold its own weight, without submitting to gravitational force.[41] Based on the solvent phase in the gel, it can be classified into a) hydrogel (contains more than 50% by volume of water) and b) organogel (major percentage of solvent is organic in nature). Supramolecular gels are a special type of gel network where the molecular

scaffolds are associated with non-covalent interactions (Figure 14).[42] These supramolecular gels are composed of low molecular weight gelators (LMWGs). As the name suggests, LMWGs are small in size and contain few functional groups. This allows easy design principles for LMWGs and their derived gels. Conventionally gels form a fibrous network. However, gelator molecules can undergo further self-assembly to form interesting nanostructures with practical applications. This field is therefore vast and several gel materials with innumerable functionalities have been reported.

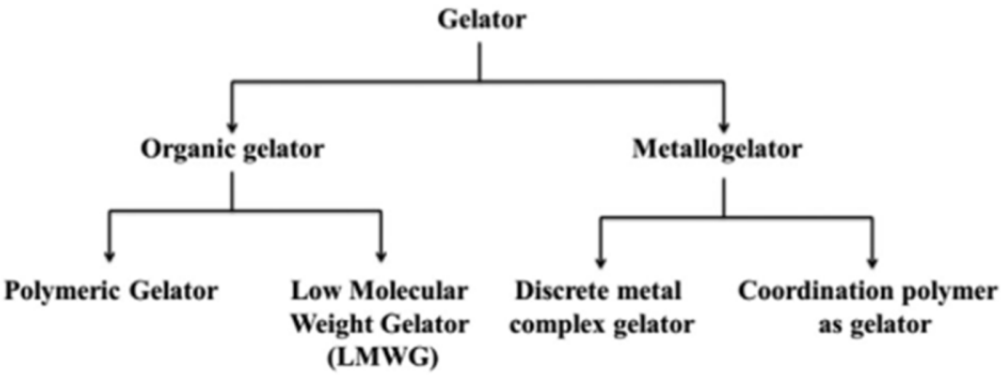

Figure 14. Classification of different type of gelators. This figure has been reproduced with permission from reference no. 48a.

1.11.1. Organogels

Organogelation has been discovered to be an excellent approach to synthesize supramolecular assemblies with tunable properties. Numerous reports of organogels show fibrous network type morphology.[43] Use of π-conjugated molecules for the synthesis of these fibrous networks would obviously lead to electronic applications of these organogels.[44] Not only this, the organogels scaffolds have the ability to accommodate different components that can induce host-guest charge transfer properties. This can lead to tunable electrical properties in organogels. However, one major drawback for electronic organogels is its lack of device applications till date. No breakthrough in this regard has been made so far. However there have been a few path-breaking studies so far to address this issue. A self-sorting approach can be used to synthesize organogels of donor-acceptor systems. This can then be designed as heterojunction organic semiconductors. Such a two-component gel of thiophene (6) and perylenebisimide (7) (Figure 15a),[44,45]composed of entangled fibrous aggregates was useful in fabricating photovoltaic devices. The fiber crossing points could be considered equivalent to p-n

heterojunctions (Figure 15b). Upon visible-light irradiation, anodic photocurrent was also generated from the cast films (Figure 15c).

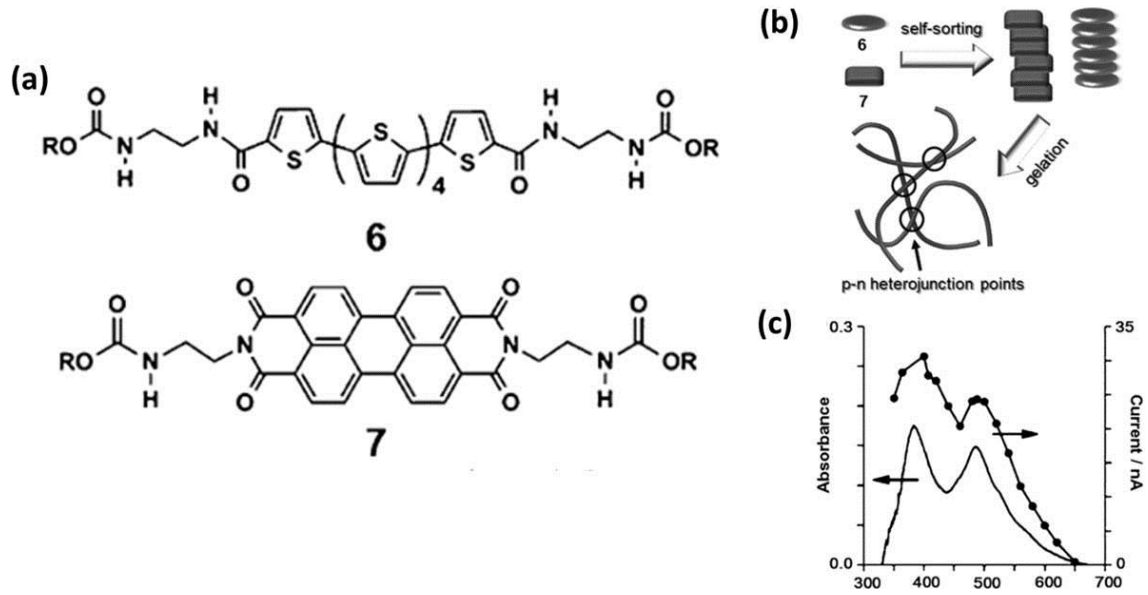

Figure 15. (a) Chemical structure of compounds (6) and (7), (b) Schematic representation of the self-sorting organogel formation of (6) and (7) yielding p-n heterojunction points and (c) Absorption spectrum and photocurrent action spectrum of the cast film prepared from 6/7 self-sorting gel on an indium tin oxide (ITO) electrode: applied potential = 0.2 V vs. Ag/AgCl. This figure has been reproduced with permission from reference no. 44.

Organogels have also been used for other applications such as OFETs, photovoltaics, sensing, moisture resistance, magneto-optical switches, tissue engineering, drug delivery and different miniaturized applications.

1.11.2. Coordination Polymer Gels

Coordination polymer gels (CPGs) can be constructed by metal-ligand coordination in an organic or aqueous medium. For the construction of CPGs, it is imperative that the LMWG contain at least two metal binding sites.[46] When a metal ion binds to the binding sites of LMWGs, spontaneous self-assembly occurs in solution to lead to interesting nanostructuring in the resulting metal-organic soft material. The structure of the resulting coordination polymer network is strongly dependent on the geometry of metal ions, the conformation and binding sites of LMWGs. This is indicative of the fact that, by a suitable choice of metal ions and LMWGs, interesting structural forms of CPGs can be generated, thus suiting specific applicative demands.

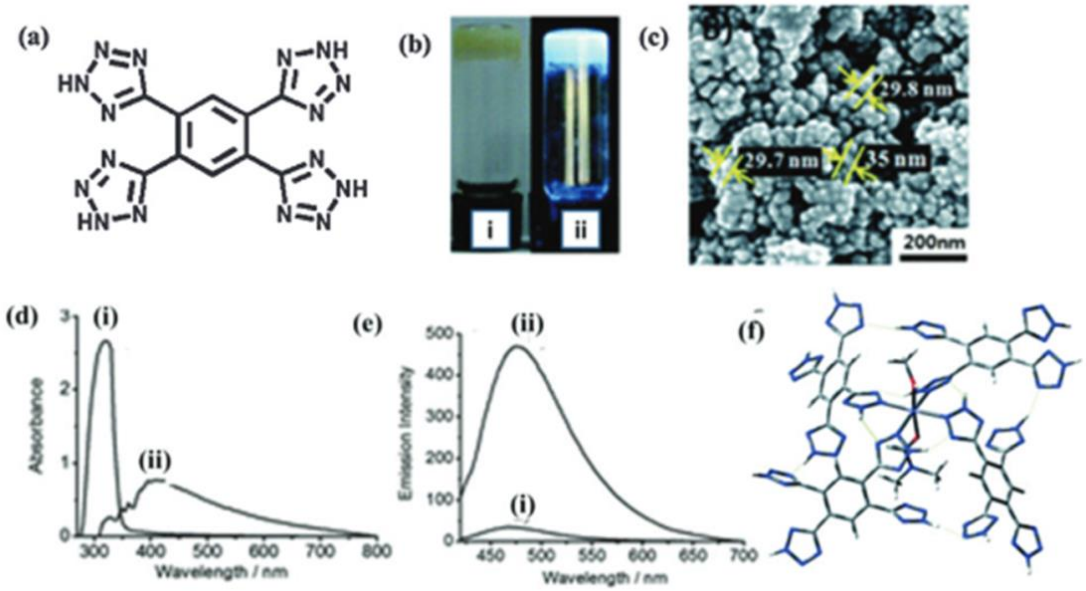

Figure 16. (a) Molecular structure of L3, (b) Photographs of the ZnL3 CPG under (i) daylight and (ii) under UV-light, (c) SEM image of the ZnL3 CPG, (d) UV-Vis spectra of (i) solution of L3 in DMF/MeOH and (ii) ZnL3 CPG, (e) Emission spectra (λ^{ex} = 320 nm) of (i) solution of L3 in DMF/MeOH and (ii) ZnL3 CPG and (f) Optimized molecular structure of ZnL3 obtained from DFT calculations. This figure has been reproduced with permission from reference no. 48a.

Several luminescent CPGs have been reported to date and the origin of emission have been found to be either LMWG based or metal ion based.[46d,e] Use of chromophoric LMWG for CPG synthesis leads to a LMWG based emission property while use of luminescent metal ions such as lanthanides lead to metal centred emission in CPGs. Jung *et al.* reported the preparation of a luminescent CPG from a tetrazole-based LMWG (L3) and Zn^{2+} in DMF, DMA and DMF/MeOH (Figure 16a).[47] L3 exhibited a typical π–π* band at 300 nm in the UV-Vis absorption spectrum. Interestingly, the same π–π* transition band of ZnL3 CPG appeared at 410 nm, indicating J-type aggregation in gel state (Figure 16b,c). The ZnL3 CPG exhibited strong blue emission with a maximum at λ_{max} = 475 nm (λ_{ex}= 300 nm) (Figure 16d). The fluorescence intensity of ZnL3 CPG was enhanced markedly as compared to the solution of L3 in DMF/MeOH (Figure 16e). The strong emission of ZnL3 CPG originated due to coordination- driven self-assembly of L3 which ultimately favoured J-aggregation and restricted the formation of excimers (Figure 16f). This work is a classic example of a LMWG centred emission in CPGs.

Maji and co-worker reported a white light emitting CPG whose emission was tuned via the control of different molar ratios of Eu^{3+} and Tb^{3+} metal ions. They synthesized a new low molecular weight gelator (LMWG) having 9,10-diphenylanthracene core and terminal terpyridine (Figure 17).[48] Tb^{III} and Eu^{III} ion coordination to the LMWG resulted in green and pink emissive coordination polymer gels. Further, control over stoichiometry of LMWG:Tb^{III}:Eu^{III} led to yellow and white light emitting bimetallic gels. This unique piece of work showed that metal based emissions can be utilized to tune the emission color of gels and a combination of LMWG emission and metal centred emission can be exploited to realize white light emission in CPGs.

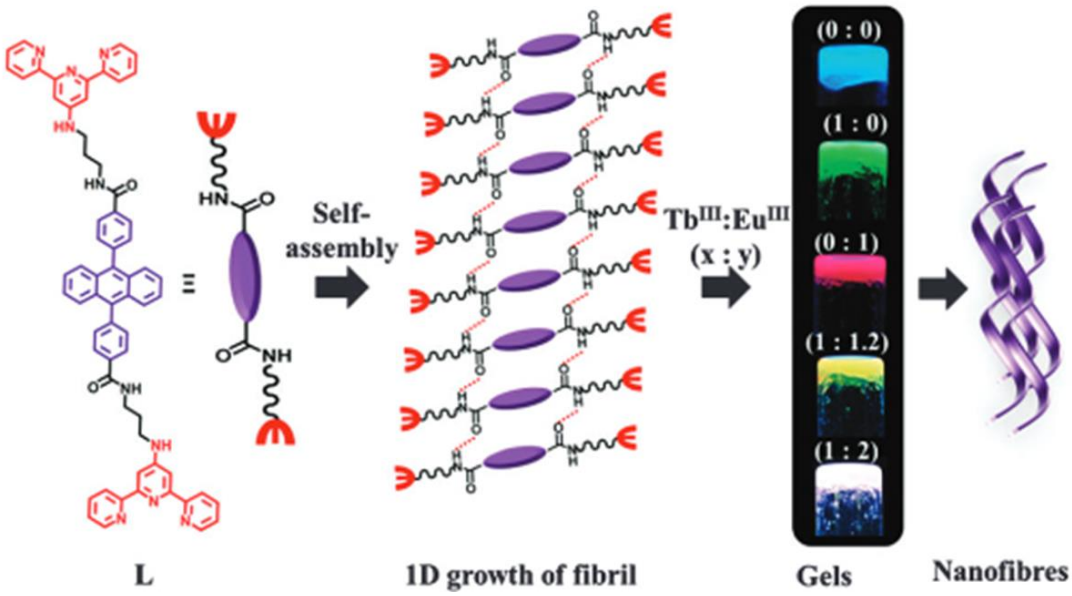

Figure 17. Schematic showing the self-assembly of L though H-bonding and π–π stacking interactions and its coordination to Ln^{III} forming luminescent CPGs. This figure has been reproduced with permission from reference no. 48b.

1.12. Amphiphiles and Bola-amphiphiles

An amphiphile is a covalently bonded molecule having both hydrophilic and hydrophobic parts.[49] Amphiphiles self-assemble in aqueous solution to form well defined nanostructures, such as micelles, nanotubes, nanorods, nanosheets, and vesicles, which can be applied in many fields ranging from nanodevices, drug/gene delivery, template synthesis, and cell imaging.[50] The structures and the properties of the self-assemblies formed by amphiphiles are determined by their nanoscale architectures (interplay between the hydrophilic−hydrophobic balance and geometric packing constraints) and

experimental conditions, such as concentration, temperature, pH, and ionic strength. Polymeric amphiphiles are also known in literature.[51] Due to its polymeric extension, polymeric amphiphiles have more structural diversity and stability. Self-assemblies of monomeric amphiphiles are more dynamic in solution owing to their solubilization in the

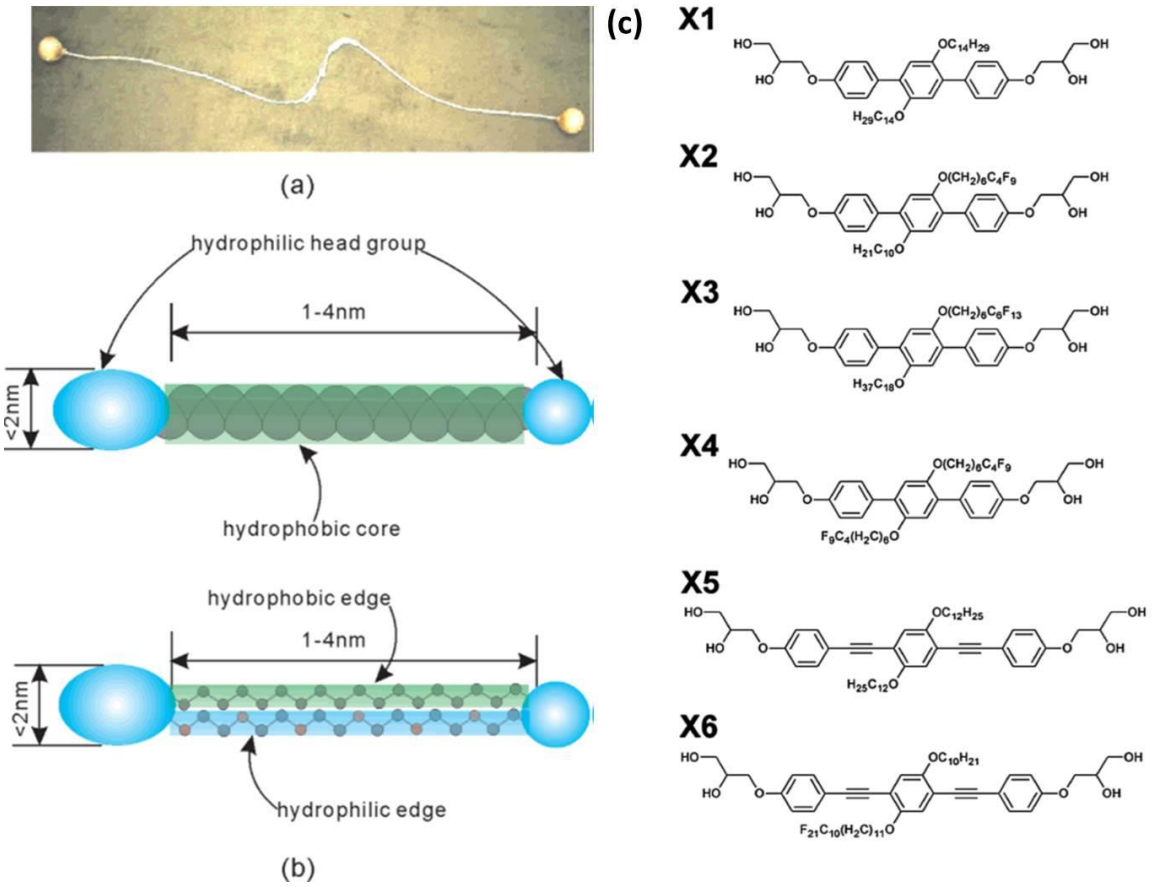

Figure 18. (a) Photograph of an argentine bola with leather balls, (b) Schematic drawings of a bolaamphiphile (abbreviation, bola). Green coloring indicates hydrophobic parts; blue means hydrophilic and (c) Molecular structures of X-shaped bolaamphiphiles. This figure has been reproduced with permission from reference no. 53a.

solvent and breakage of aggregates. Polymeric amphiphiles on the other hand, show much more stability in solution owing to entanglement of polymeric side chains and hence are protected from molecular exchange interactions. Supramolecular amphiphiles are a result of combination of supramolecular chemistry and amphiphile chemistry leading to amphiphiles constructed from non-covalent interactions.[52] The advantage these have over conventional covalent polymeric amphiphiles is that by placing functional groups at strategic positions of building blocks of amphiphiles, supramolecular amphiphiles can be built. This avoids the necessity of tedious covalent bond synthesis.

Bola-amphiphiles are a special class of amphiphiles where a central hydrophobic core or skeleton is end-capped by two water soluble groups (Figure 18).[53] An example of a natural bola-amphiphile is the compound present in cell membrane of archaebacteria. Their lipid membrane contains a bola-amphiphilic part which allows them to survive in volcanic environments such as hot sulfuric acid. Synthetic bola-amphiphiles initially aimed to mimic the lipid bilayer like arrangement but recent research has pushed their applications towards the study of self-assembly in polar to non-polar solutions. Mostly, these bola-amphiphilic self-assemblies forms ordered layered structures owing to their structural periodicity of polar and non-polar groups. Bola-amphiphiles have also been used to construct extended framework materials in solution where the property of the bola-amphiphile is translated into the framework functionality.[54]

1.13. *Oligo*-(*p*-phenyleneethynylene) (OPE) Based Functional Assemblies

Conjugated systems find applications in electronic and photonic devices such as light emitting diodes (LEDs) and photovoltaic devices (PDs).[55] A vast number of conjugated molecular systems are available, which show excellent opto-electronic output. However, one such class of oligomers that stand out from the rest are called *oligo*-phenyleneethynylenes (OPEs).[56] OPEs are known to show excellent conducting profile, quantum efficiency and solution processability when compared to other conjugated species. Quantum yield, emissive wavelength, and absorption profile are sensitively dependent upon the specific environment that the OPE-chains are in. The structure of OPEs is constituted of aryl units linked to each other via triple bonds. There exists a certain degree of rotational freedom around the single bonds connecting the triple bonds. This leads to twisting of some aryl units out of plane of the long axis. However, the overall structure remains linear. The twisting can be induced in individual OPEs via several factors such as temperature, pressure, light, molecular environment and also intermolecular interactions. This twisting does not affect the conjugation length and the electrical properties remain intact. However, the optical property depends on the degree of twisting (Figure 19).[57] A subclass of OPEs is the *para* substituted OPEs whose *para* extension leads to the formation of a linear chain. Owing to the rigidity and linearity of the alkyne connectivity, the *para* substituted OPEs behave as rigid rods.

So why does this particular system warrant so much attention in opto-electronics? This is because they have a collection of the following excellent properties that make them highly useful:

1) Synthesis of OPE is easy, and a lot of established reaction methods are available in the literature.

2) Biologically active ligands can be introduced into the monomer and then coupled via Sonogashira reaction to obtain biologically active OPEs.

3) Functionalization is easy. Monomers carrying sulfonate, carboxylate, amine, hydroxy, etc. functionalities can be introduced using the Sonogashira-coupling.

4) The OPEs display high quantum output of emission combined with significantly enhanced photo-stability when compared to related materials.

5) The fluorescence and the absorption of most OPEs are dependent upon their surroundings, due to their torsion and planarization-induced shifts that are brought about by their torsion-dependent modulation of electronic properties.

6) OPEs with specific side chains and end groups can be used as supramolecular building units to form interesting nanostructures with practical applications.

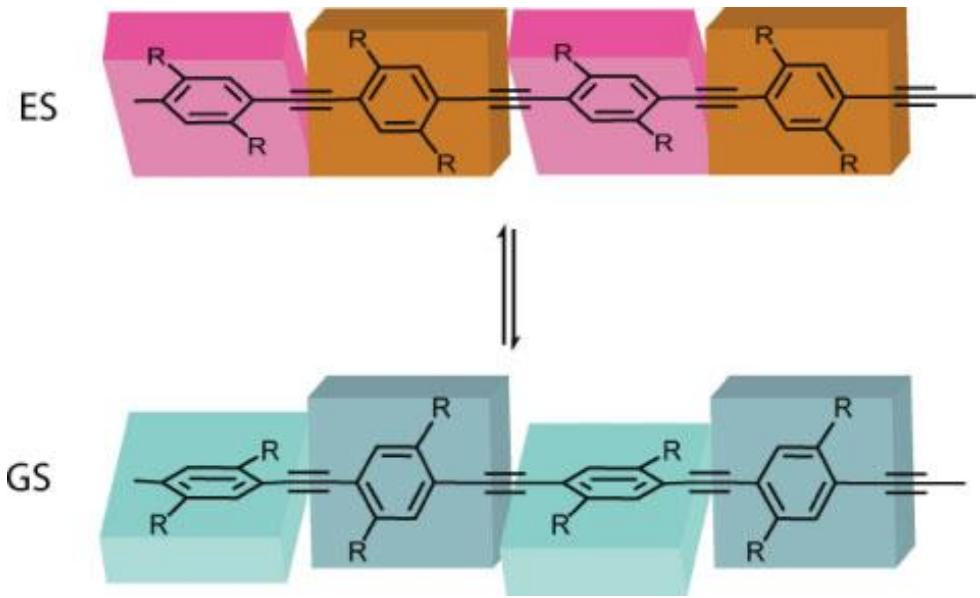

Figure 19. Pictorial representation of how optical properties of OPEs are influenced by the twisting of the phenyl rings connected by the triple bonds. This figure has been reproduced with permission from reference no. 56b.

There are two main synthetic methods for the synthesis of OPEs: 1) Pd catalyzed coupling of diethynylarenes to substituted dihaloarenes and 2) molybdenum hexacarbonyl/phenol induced or metal carbyne catalyzed alkyne metathesis of propynylated dialkylarenes (Figure 20). The in situ alkyne metathesis reaction can be carried out with non-dried dichlorobenzene also. The reaction is performed under slight purging with nitrogen or argon at temperatures from 120 ^{0}C–150 ^{0}C, giving quantitative reaction yields.[58] The compound is isolated after precipitation in methanol and washing with acid and base to remove unreacted molybdenum catalyst and phenol co-catalyst. Pd catalyzed synthesis of OPEs work best with dibromoarenes and diiodoarenes.[59] However, the reactivity of the iodoarenes are better than the bromo counterparts. Generally, bromo-coupled OPEs show a brownish or purplish colour indicating defects in the structure. Then, further purification becomes necessary. However, iodo-coupled OPEs usually show bright green to yellowish-orange color depending on the functional groups present in them. Depending on the chain length of the oligomers desired, reaction conditions can be easily tuned. Usually a fixed molar ratio of the haloarenes and diethynylarenes lead to controlled oligomerization. Variation of reaction times also has an effect on the oligomer chain length.

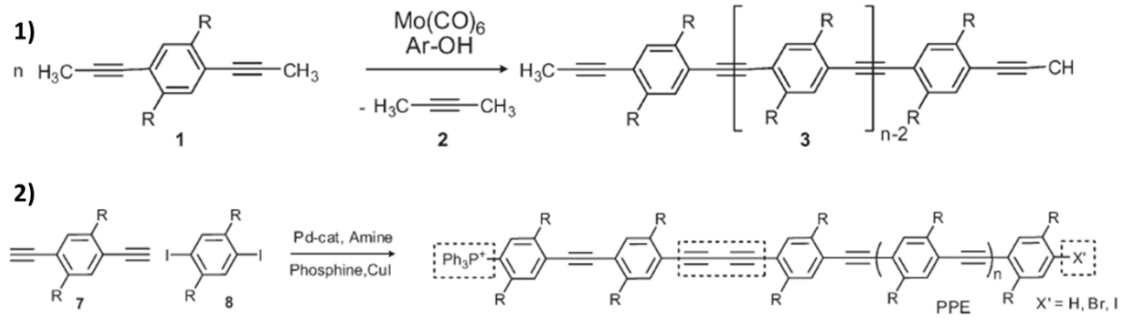

Figure 20. 1) Synthesis of OPEs by alkyne metathesis and 2) Synthesis of OPEs by the Pd-catalyzed reaction of aryldihalides with dialkynylarenes. This figure has been reproduced with permission from reference no. 56b.

OPEs have shown high potential in opto-electronic applications. As discussed before, synthesis of OPEs is not really a cumbersome process and vast varieties of OPEs can be synthesized to meet application demands. Structural picture of OPE chains having practical applications are important for the pre-design of OPEs meeting specific demands. Surprisingly, reports of crystal structures of OPEs are still few.[60] A particular reason cannot be inferred, that has led to this lacunae. One reason might be that growing single

crystals of these oligomers is not easy and takes careful examination of solubility of them in different solvents.

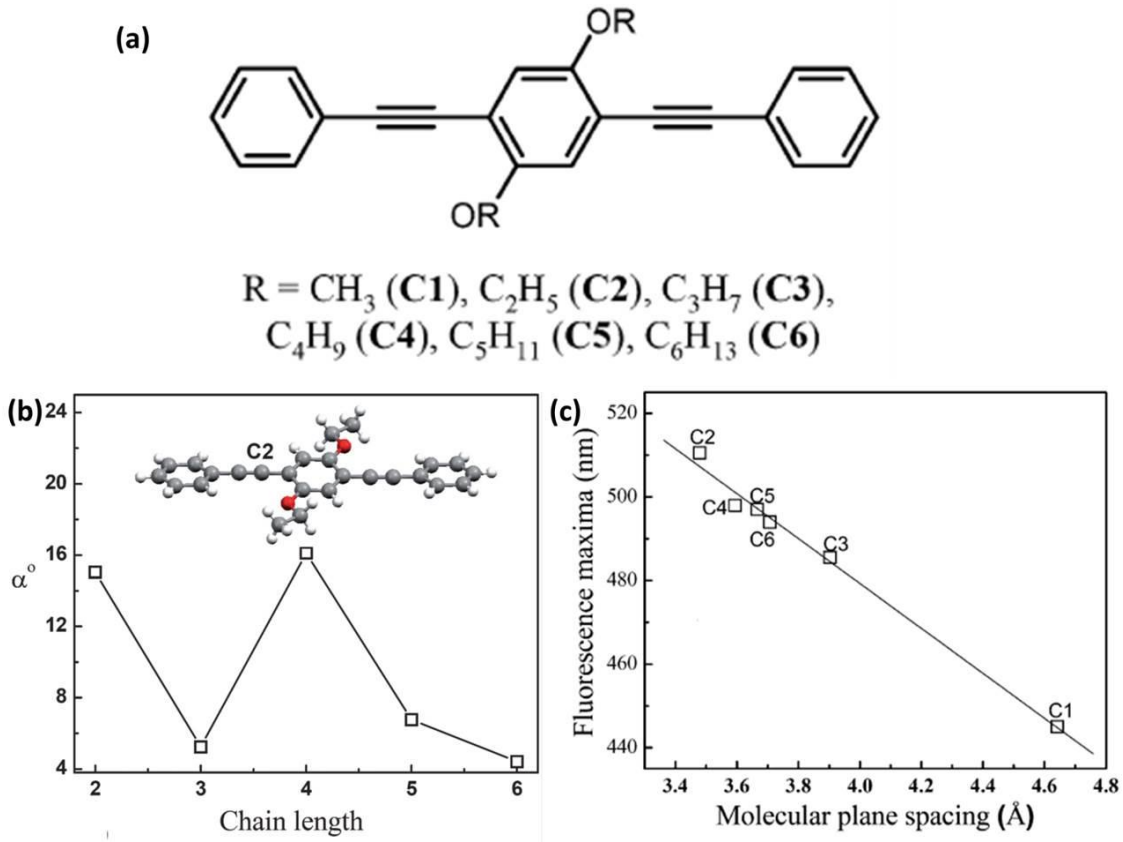

Figure 21. (a) Molecular structures of OPEs used for structural study, (b) Deviation of the phenyl ring from planarity with respect to the alkyl chain length and (c) Variation of the emission maximum with the spacing between the interacting molecules in crystals of C1 to C6 (excitation 360 nm). This figure has been reproduced with permission from reference no. 60c.

However, there have been important reports in the literature, that help in understanding, how the packing of these oligomers influence their optical and electrical properties. The Thomas group synthesized and crystallized several oxyhexyl side chain functionalized OPE backbones with different end capping functional groups to investigate their structure and their self-organization on conducting surfaces. They revealed a host of supramolecular interactions which lead to a herringbone and criss-cross packing. Kulkarni and co-workers also synthesized OPEs with side chains varying from methyl to hexyl and studied the effect of packing on fluorescence spectra.[60 b,c] Interestingly, they found that all the OPEs exhibited similar fluorescence maxima in solution, however, their solid state spectra varied. There was no direct correlation between increase in alkyl chain

length to the shift in fluorescence maxima (Figure 21). This negated the possibility of alkyl chain influence in emission properties and pointed to the fact that packing of OPE backbones direct fluorescence behavior in OPEs. It was ultimately found that spacing between the interacting pair of molecules in the J-aggregates influenced the emission spectrum: the lower the spacing, the greater the red shift. In solution phase this interaction between J aggregates was lost and hence emission maxima appeared at the same position.

In another work, Sharber et al functionalized side chains of OPEs with neutral and electron withdrawing groups, keeping the end capping groups same, to study the electronic effect of the backbone on their emission properties.[57a] Interestingly, they observed that electron withdrawing side chain also had an influence on crystal packing. Therefore, combination of steric and electronic effects had a profound effect on the emission properties of OPEs (Figure 22). It was found that more the electron density difference between the end capping groups and the side chains, the more red shifted the emission. However, twisting of OPE aryl rings induced by interacting side chains had the opposite effect. So a combination of both led to tuning of emission of the synthesized OPEs.

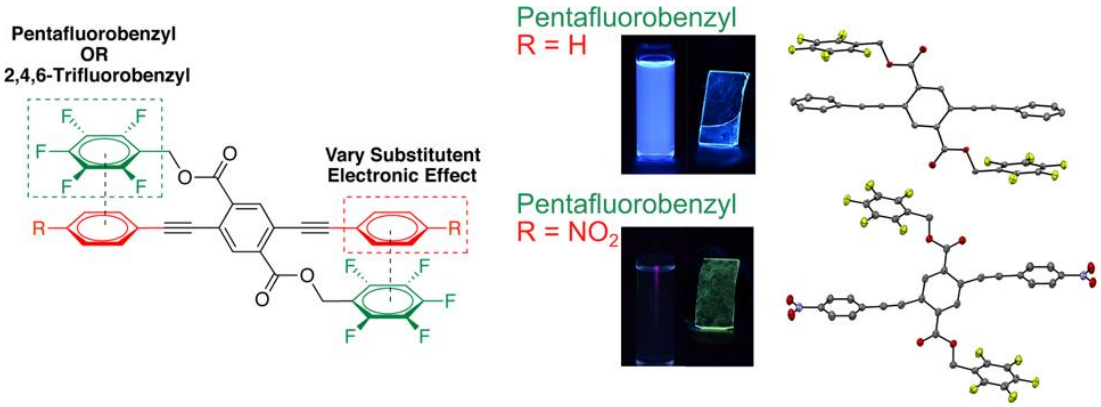

Figure 22. Substituent effects that control conjugated OPE oligomer conformation through non-covalent interactions. This figure has been reproduced with permission from reference no. 57a.

The properties of OPEs can be mainly divided into two parts: opto-electronic and supramolecular. The π backbone directs the optical and electronic applications whereas the side chains increase solubility and help in self-assembly of OPEs in solution.[61] Interestingly, when all three applications are coupled, solution processable opto-electronic devices from OPEs can also be realized. Wandowlski and co-workers created highly conducting single molecular junctions of OPE derivatives by selective cleaving of

trimethylsilyl groups.[62] By doing this, they created covalent anchoring sites of Au-C which were mechanically stable and had high conductance values around one order of magnitude higher as compared to those of traditional anchoring groups (Figure 23). This approach and the in depth study provided a basis for fundamental charge transporting behavior investigation of OPE based semi-conductors. There have been several other OPE based electronic materials reported which compete with the best in the field.

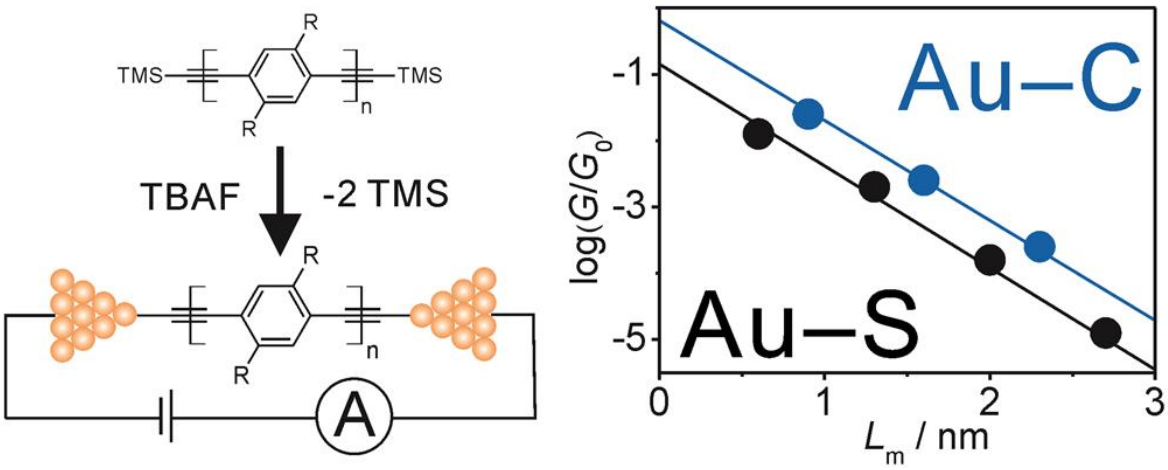

Figure 23. Cleavage of trimethylsilyl groups to create covalent Au−C anchoring in an OPE system which was developed for single-molecule junction conductance measurements. This figure has been reproduced with permission from reference no. 62.

The fluorescence properties of OPEs have also been used for sensing studies and OPEs have shown great promise as sensor materials. As in the case of other sensing studies, OPE sensors also follow the quenching mechanism to detect or sense an analyte. Swager and co-workers designed a side chain cyclophane appended PPE to detect the molecule paraquat.[63] They observed that upon coordination of one paraquat molecule, the fluorescence of the 12-meric model PPE were completely quenched. Other OPE and derived materials have also been used to sense vast variety of analytes (Figure 24).

As discussed before, the functional groups appended to the π-conjugated OPE backbone directs self-assembly in solution. Ajayaghosh and co-workers, synthesized a new dioxydodecyl functionalized OPE backbone and its chiral analogue and found a sergeant-soldier effect occurring during the self-assembly process of both.[61a] Co-assembly of OPE1 with the chiral analogue OPE2 retarded the formation of vesicular assemblies and facilitated the evolution of helical structures (Figure 25). Though OPE2 alone was unable

to self-assemble, when mixed with OPE1, it participated in co-assembly and transferred chiral information to the latter. This was the first report of the sergeant-and-soldiers

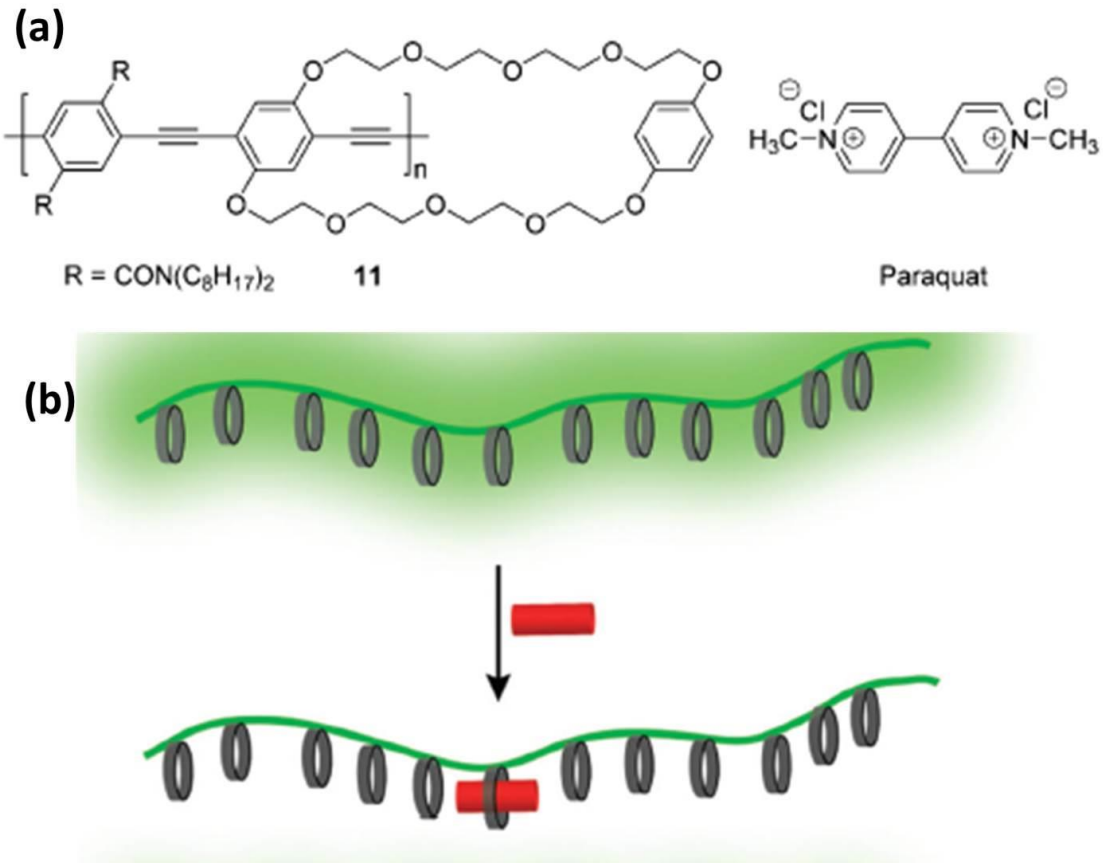

Figure 24. (a) Structure of cyclophane-appended PPE 11 and the employed analyte paraquat and (b) Schematic of how one paraquat molecule (red cylinder) quenches in this picture a PPE with 12 appended receptors. This figure has been reproduced with permission from reference no. 63a.

approach to chirality-induced transformation from vesicles to helical tubules. Marshall and co-workers studied another approach in self-assembly of OPEs. They functionalized the end groups of the OPE backbone by carboxylic acid groups. This allowed them to self-assemble the OPEs with Zr metal to form a series of MOF structures. The work reported the crystal structures of all the OPE based MOFs. The emission properties of the MOFs were also studied. The structural understanding allowed the authors to correlate the degree of twisting of OPE linkers to the shift in emission spectra. They concluded that the higher degree of twisting of OPE chains, the more red shifted was the emission spectrum of the MOF(Figure 26). Other such self-assembly studies of OPE systems have projected

this system as ideal candidates for generation of shape controlled fluorescent nanostructures in solution.

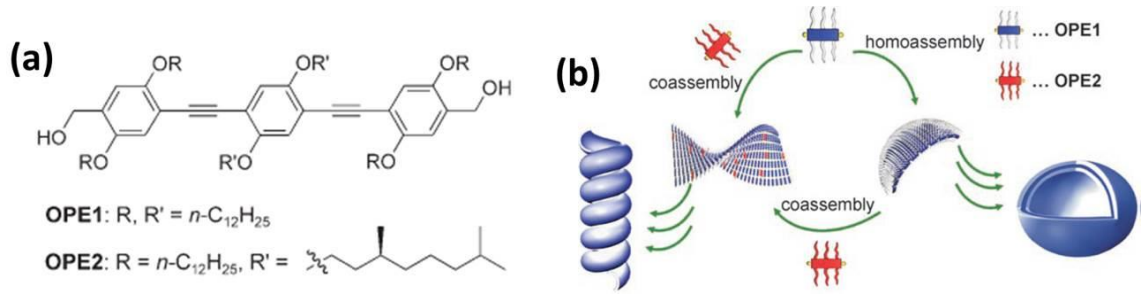

Figure 25. (a) Structure of the synthesized OPEs and (b) Self-assembly of vesicles and subsequent transformation into helical tubes in decane. This figure has been reproduced with permission from reference no. 61a.

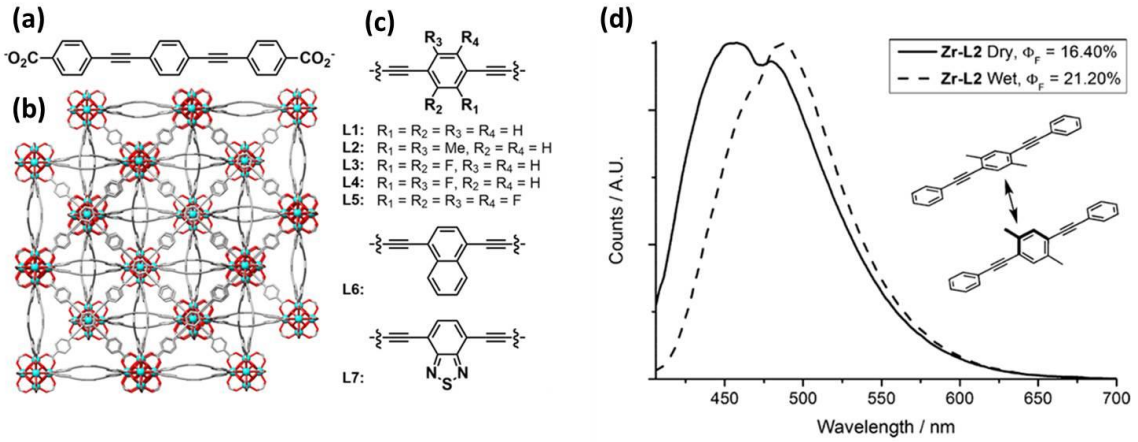

Figure 26. (a) Chemical structure of OPE based ligand used for the study, (b) The solid-state packing structure of the interpenetrated MOF it forms with Zr, (c) Structural description and naming scheme of the functionalized OPE ligands used throughout the study. (d) Normalized solid-state photoluminescence emission of Zr based MOFs under dry and wet conditions alongside a schematic representation of the observed twisting of the ligands (λex = 396 nm). This figure has been reproduced with permission from reference no. 57b.

1.14. Scope Of The Work

Supramolecular chemistry has opened up new possibilities in research which was unimaginable before. The power to control structures of mega molecules via non-covalent interactions has given chemists and material scientists a tool box to venture into

unchartered territories of practical properties and utilities of different systems. Therefore molecular tectonics and crystal engineering techniques have come to the forefront for researchers to 'play around with' chemical structures of materials. Now, on the other hand, several applications of supramolecular π-systems, oragno/metallogels, bulk and nanoscale MOFs have been discussed previously and their utilities have been put forward. But like any material, they are covered with drawbacks. The following discussion summarizes the individual lacunae existing in each field:

Supramolecular π-systems have been mainly utilized for studying the optoelectronic properties of self-assembled amphiphiles/ bola-amphiphiles and soft hybrids. As discussed before, they show amazing applicative output. However, there still remains a large void in a structural understanding of their functions. Several explanations of their properties have been speculative and hence desire more effort in getting a structural basis for their multi-functionalities. Similarly, for gels, it is still a challenge to maintain the same quantum output from the low molecular weight gelator to the gel state. This is because; there occurs a lot of solvent mediated quenching mechanisms leading to decreased device performance. MOFs on the other hand suffer from a lot of drawbacks such as solution processability, water instability and poor electrical conductivity and device applications. There has been a breakthrough in MOF devices by downsizing MOFs to the nanoscale. MOFs have also shown adaptability towards moisture resistance. However, a lot remains unexplored in this regard and demands and extensive exploration to further this field.

It is to be noted that in all the applicative drawbacks discussed above, one point remains that we need to build a supramolecular synthon or a molecular system that could be used to generate π-supramolecular systems, gels and framework structures at the nanoscale. It is also imperative that single crystals of these systems must be grown, so that a proper structural picture can be generated. We therefore, focused on developing a conjugated molecular backbone that would have excellent charge transport and light emitting properties. We aimed to functionalize the ends of the conjugated system with metal coordinating and hydrogen bonding groups so that framework materials and hydrogen bonding assisted gels can be synthesized using the same building block. Furthermore, we decided to introduce property desired side chains to suit a particular application. For example, long alkyl chains which are known to decrease the surface energy of a material and thereby increase contact angles could be used to induce superhydrophobicity. As

discussed before, OPEs satisfy all these requirements and hence we decided to use the OPE backbone to meet all the criteria required for the development of moisture resistant opto-electrical properties of gels, MOFs, NMOFs and also the stimuli-responsive properties of π-supramolecular systems (Figure 27). The lack of having a structure-property relationship was another issue we aimed to address in the design. Extensive

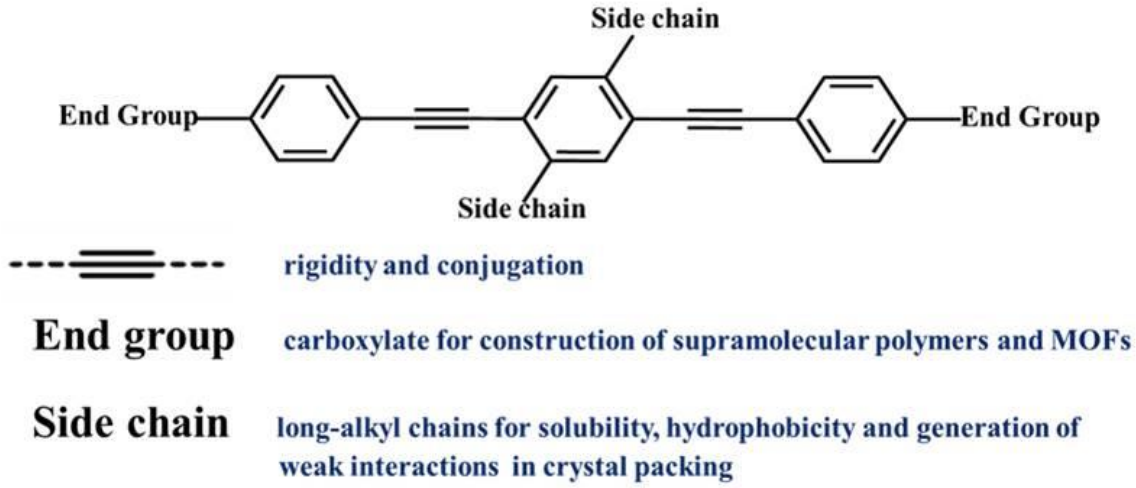

Figure 27. Design strategy followed to construct moisture resistant, opto-electrically active, liquid crystalline and polymorphic π-supramolecular systems, gels, MOFs and NMOFs.

literature search yielded that only a handful of OPE based MOFs and supramolecular π-systems crystal structures are reported till date.[57,60] This egged us to delve deeper into this field to provide a progressive route towards a better understanding of this interesting material that can give rise to a galaxy of interesting properties. This, we believed would aid future researchers in devising more planned strategies for molecular design of OPE based novel materials and increase human knowledge on supramolecular properties of related materials.

The overall thesis is therefore based on synthesis of five novel OPE dicarboxylates, out of which three have dioxyalkyl chains (H_2OPE-C_8, H_2OPE-C_{12} and H_2OPE-C_{18}); one has bis-triethyeleneglycoltmonomethylether side chain (H_2OPE-C_{gly}); and another has a mixed approach of one side functionalized with oxyalkyl and another side functionalized with triethyeleneglycoltmonomethylether side chain (H_2OPE-C_{mix}) (Figure 28, 29). The purpose of synthesizing these specific OPE dicarboxylates was to satisfy precise needs of the properties we want to introduce in the materials discussed above. For example, H_2OPE-C_8, H_2OPE-C_{12} and H_2OPE-C_{18} served the purpose of constructing NMOF and

bulk MOF structures having opto-electronic properties and also were used in structure elucidation. H_2OPE-C_{18}, H_2OPE-C_{gly} and H_2OPE-C_{mix} were exploited to synthesize π-

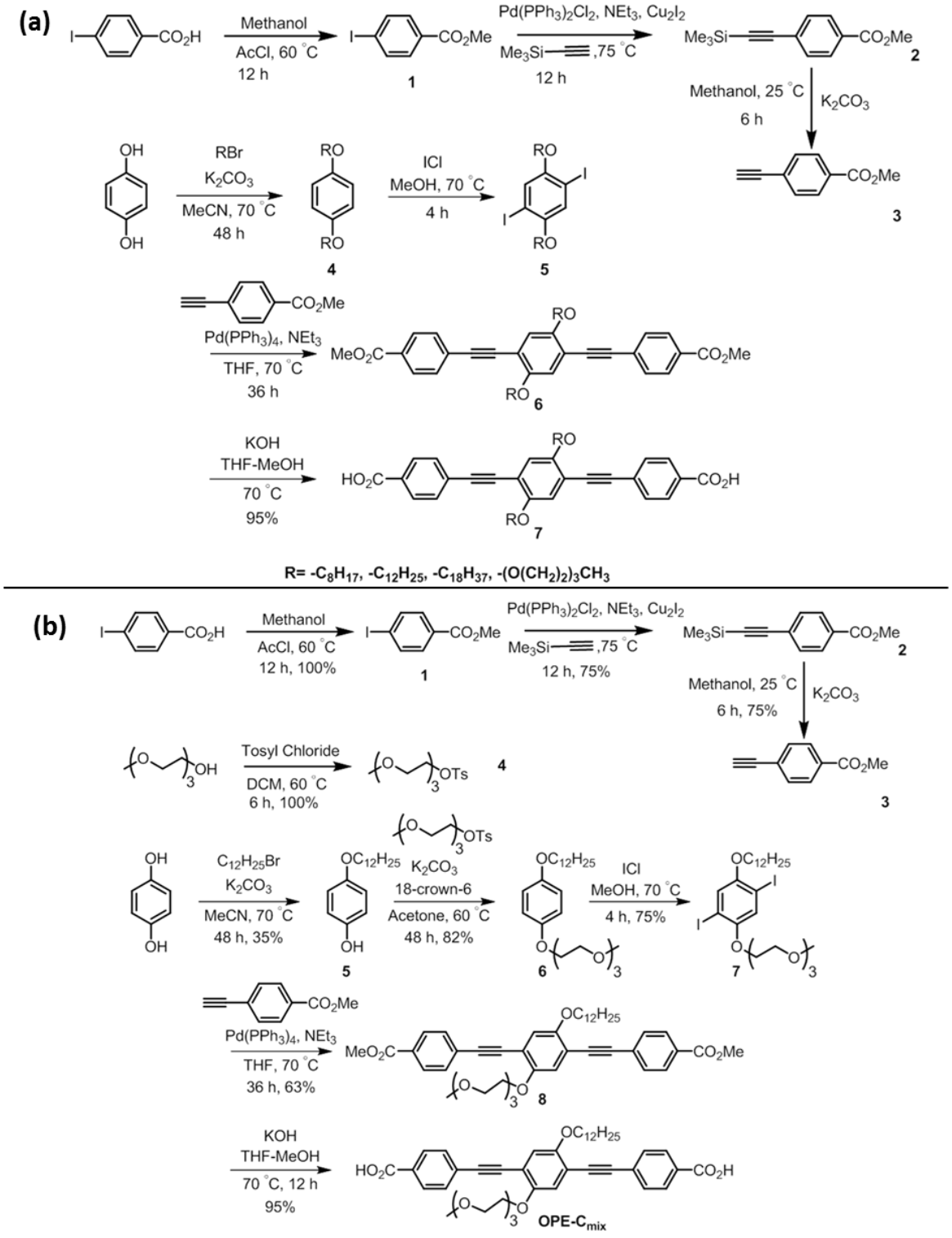

Figure 28. General synthetic scheme for (a) Symmetrically substituted and (b) Unsymmetrically substituted OPEs synthesized in the thesis work.

supramolecular polymers, organo/ metallogels having liquid crystalline, polymorphic, stimuli-responsive, light-harvesting and electronic properties.

To summarize the findings, the thesis first discusses the design of π-conjugated supramolecular systems and their reversibly polymorphic, liquid crystalline and stimuli-responsive behavior. The crystal structures of these systems are also discussed to throw light on the properties. Further, it discourses the formation of luminescent gels and metallogels and their nanoscale morphologies. The light-harvesting and charge transfer behavior of the gels have also been highlighted. Secondly, the thesis throws light on the coordination directed self-assembly of two OPEs to form nanoscale architectures of MOFs and discusses methods on how to induce superhydrophobicity and realize the lotus-effect based on the NMOFs. Device fabrication and opto-electronic behavior NMOFs have also been shown. Finally it brings forward a structural understanding of the water resistant, opto-electronic properties of the frameworks via the synthesis of MOFs having such properties and elucidation of their single crystal structures.

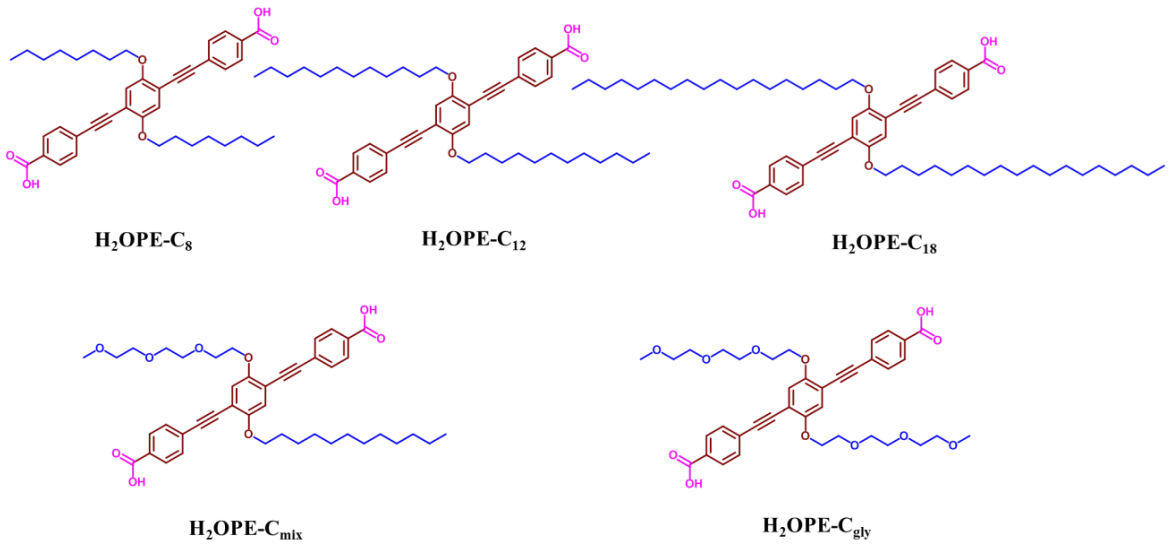

Figure 29. Structure of five novel OPE dicarboxylates used for the synthesis of moisture resistant, opto-electrically active, liquid crystalline and polymorphic π-supramolecular systems, gels, MOFs and NMOFs.

1.15. References

1 (a) J-M. Lehn, *Chem. Soc. Rev.*, 2007, **36**, 151; (b) J-M. Lehn, *Angew. Chem. Int. Ed.*, 1988, **27**, 89; (c) J-M. Lehn, *Angew. Chem. Int. Ed.*, 1990, **30**, 1304.

2 E. V. Anslyn and D. A. Dougherty. *Modern Physical Organic Chemistry*, University Science Books, Sausalito, CA, USA, 2006, 162.

3 (a) P. J. Garratt, A. J. Ibbett, J. E. Ledbury, J. E. O'Brien, M. B. Hursthouse and K. M. A. Malik, *Tetrahedron*., 1998, **54**, 949; (b) N. A. Mazer, G. B. Benedek and M. C. Carey, *J. Phys. Chem.*, 1976 , **80**, 1075.

4 (a) T. M. Krygowski and W. R. Fawcett, *J. Am. Chem. Soc*., 1975, **8**, 2143; (b) H. S. Park and W-Y. Wen, *Discuss. Faraday Soc*., 1957, **24**, 133.

5 (a) J. Stuhler, A. Griesmaier, T. Koch, M. Fattori, T. Pfau, S. Giovanazzi, P. Pedri and L. Santos, *Phys. Rev. Lett*., 2005, **95**, 150406; (b) B. T. Thole, *Chem. Phys*., 1981, **59**, 341.

6 G. A. Jeffrey, *Introduction to Hydrogen Bonding*, Oxford University Press: Oxford, 1997.

7 (a) J. Bernstein., R. E. Davis, L. Shimoni and N-L. Chang, *Angew. Chem. Int. Ed*., 1995, **34**, 1555; (b) G. R. Desiraju, *Acc. Chem. Res*., 2002, **35**, 565; (c) D. Braga, F. Grepioni and G. R. Desiraju, *J. Organomet. Chem*., 1997, **548**, 33; (d) M. C. Etter, *Acc. Chem. Res*., 1990, **23**, 120.

8 (a) J. C. Ma and D. Dougherty, *Chem. Rev*., 1997, **97**, 1303; (b) D. A. Dougherty, *Science*, 1996, **271**, 5246; (c) R. A. Kumpf and D. A. Dougherty, *Science*, 1993, **261**, 1708.

9 (a) O. B. Berryman, V. S. Bryantsev, D. P. Stay, D. W. Johnson and B. P. Hay, *J. Am. Chem. Soc*., 2007, **129**, 48; (b) D. Quinonero, C. Garau, C. Rotger, A. Frontera, P. Ballester, A. Costa and P. M. Deya, *Angew. Chem. Int. Ed*., 2002, **114**, 3539.

10 (a) C. A. Hunter, K. R. Lawson, J. Perkins and C. J. Urch, *J. Chem. Soc., Perkin Trans*., 2001, **2**, 651; (b) C. A. Hunter and J. K. M. Sanders, *J. Am. Chem. Soc*., 1990, **112**, 5525.

11 (a) A. I., Kitaigorodskii, *Organic Chemical Crystallography*, Consultants Bureau, New York, 1961; (b) A. Dalgarno and A. E. Kingston, *Proc. Phys. Soc*., 1959, **73**, 2251.

12 (a) S. Scheiner, *Phys. Chem. Chem. Phys*., 2011, **13**, 13860; (b) S. Scheiner, *J. Phys. Chem. B*, 2005, **109**, 16132; (c) S. Sarkhel and G. R. Desiraju, *Proteins*, 2004, **54**, 247.

13 (a) G. R. Desiraju, *Acc. Chem. Res*., 1996, **29**, 441; (b) G. R. Desiraju, *Chem. Commun*., 2005, 2995; (c) M. J. Plevin, D. L. Bryce and J. Boisbouvier, *Nat. Chem*.,

2010, **2**, 466; (d) M. Nishio, *CrystEngComm.*, 2004, **6**, 130; (e) S. Tsuzuki, *Annu. Rep. Prog. Chem., Sect. C: Phys. Chem*., 2012, **108**, 69.

14 (a) E. P. Kyba, R. C. Helgeson, K. Madan, G. W. Gokel, T. L. Tarnowski, S. S. Moore and D. J. Cram, *J. Am. Chem. Soc*., 1977, **99**, 2564; (b) D. J. Cram and J. M. Cram, *Science*, 1974, **183**, 803; (c) H. Yang, B. Yuan and X. Zhang, *Acc. Chem. Res.*, 2014, **47**, 2106.

15 H-C. Zhou and S. Kitagawa, *Chem. Soc. Rev*., 2014, **43**, 5415.

16 X. Feng, X. Ding and D. Jiang, *Chem. Soc. Rev.*, 2012, **41**, 6010.

17 (a) S. Zhu, H. Zhou, M. Hibino, I. Honma and M. Ichihara, *Adv. Funct. Mater.*, 2005, **15**, 381; (b) S. H. Joo, S. J. Choi, I. Oh, J. Kwak, Z. Liu, O. Terasaki and R. Ryoo, *Nature*, 2001, **412**, 169.

18 (a) T. Kudernac, S. Lei, J. A. A. W. Elemans and S. De Feyter, *Chem. Soc. Rev*., 2009, **38**, 402; (b) R. Madueno, M. T. Räisänen, C. Silien and M. Buck, *Nature*, 2008, **454**, 618; (c) S. Stepanow, M. Lingenfelder, A. Dmitriev, H. Spillmann, E. Delvigne, N. Lin, X. Deng, C. Cai, J. V. Barth and K. Kern, *Nat. Mater.* 2004, **3**, 229; (d) J. A. A. W. Elemans, S. Lei and S. De Feyter, *Angew. Chem. Int. Ed*., 2009, **48**, 7298.

19 V. A. Russell, C. C. Evans, W. Li and M. D. Ward, *Science*, 1997, **276**, 575.

20 H. Liang, Y. He, Y. Ye, X. Xu, F. Cheng, W. Sun, X. Shao, Y. Wang, J. Li and K. Wu, *Coord. Chem. Rev*., 2009, **253**, 2959.

21 M. C. Daniel and D. Astruc, *Chem. Rev*., 2004, **104**, 293.

22 T. Jin, F. Fujii, H. Sakata, T. Mamoru and M. Kinjo, *Chem. Commun*., 2005, 4300.

23 J. W. Steed and J. L. Atwood, *Supramolecular Chemistry*, John Wiley and Sons, Ltd Publication, Second Edition, UK, 2009.

24 (a) G. R. Desiraju, *Angew. Chem. Int. Ed*., 2007, **46**, 8342; (b) G. R. Desiraju, *J. Chem. Sci*., 2010, **122**, 667; (c) G. R. Desiraju, *J. Am. Chem. Soc*., 2013, **135**, 9952; (d) G. M. Whitesides, E. E. Simanek, J. P. Mathias, C. T. Seto, D. N. Chin, M. Mammen and D. M. Gordon, *Acc. Chem. Res*., 1995, **28**, 37.

25 (a) G. R. Desiraju, *Angew. Chem. Int. Ed*., 1995, **34**, 2311; (b) G. R. Desiraju, *Curr. Opin. Solid State Mater. Sci*., 1997, **2**, 451; (c) T. K. Adalder, D. P. Kumar and P. Dastidar, *Cryst. Growth Des*., 2014, **14**, 11; (d) M. B. J. Atkinson, S. V. S. Mariappan, D-K. Bucar, J. Baltrusaitis, T. Frisic, N. G. Sinada and L. R. Macgillivray, *Proc. Natd. Acad. Sci.*, 2011, **108**, 10974.

26 (a) D. S. Reddy, D. C. Craig and G. R. Desiraju, *J. Am. Chem. Soc*., 1996, **118**, 4090; (b) V. R. Thalladi, B. S. Goud, V. J. Hoy, F. H. Allen, J. A. K. Howard and G. R. Desiraju., *Chem. Commun*., 1996, 401; (c) G. R. Desiraju, *J. Mol. Str.*, 2003, **656**, 5; (d) K. Biradha, *CrystEngComm*., 2003, **5**, 374.

27 (a) S. Aitipamula, R. Banerjee, A. K. Bansal, K. Biradha, M. L. Cheney, A. Roy Choudhury, G. R. Desiraju, A. G. Dikundwar, R. Dubey, N. Duggirala, P. P. Ghogale, S. Ghosh, P. K. Goswami, N. R. Goud, R. R. K. R. Jetti, P. Karpinski, P. Kaushik, D. Kumar, V. Kumar, B. Moulton, A. Mukherjee, G. Mukherjee, A. S. Myerson, V. Puri, A. Ramanan, T. Rajamannar, C. M. Reddy, N. Rodriguez-Hornedo, R. D. Rogers, T. N. Guru Row, P. Sanphui, N. Shan, G. Shete, A. Singh, C. C. Sun, J. A. Swift, R. Thaimattam, T. S. Thakur, R. K. Thaper, S. P. Thomas, S. Tothadi, V. R. Vangala, N. Variankaval, P. Vishweshwar, D. R. Weyna, and M. J. Zaworotko, *Cryst. Growth Des*., 2012, **12**, 2147; (b) N. K. Duggirala, M. L. Perry, O. Almarsson and M. J. Zaworotko, *Chem. Commun*., 2016, **52**, 640; (c) S. L. Childs, L. J. Chyall, J. T. Dunlap, V. N. Smolenskaya, B. C. Stahly and G. P. Stahly, *J. Am. Chem. Soc*., 2004, **126**, 13335; (d) T. Sakurai, *Acta Crystallogr*., 1965, **19**, 320; (e) T. Sakurai, *Acta Crystallogr., Sect. B: Struct. Sci*., 1968, **24**, 403.

28 (a) S. Kitagawa, R. Kitaura and S.-I. Noro, *Angew. Chem. Int. Ed*., 2004, **43**, 2334; (b) T. K. Maji, R. Matsuda and S. Kitagawa, *Nat. Mater*., 2007, **6**, 142; (c) H. Li, M. Eddaoudi, M. O'Keeffe and O. M. Yaghi, Nature, 1999, **402**, 276; (c) Z. R. Herm, B. M. Wiers, J. A. Mason, J. M. van Baten, M. R. Hudson, P. Zajdel, C. M. Brown, N. Masciocchi, R. Krishna and J. R. Long, *Science*, 2013, **340**, 960; (d) S. M. Cohen, *Chem. Sci*., 2010, **1**, 32; (e) J. Liu, L. Chen, H. Cui, J. Zhang, L. Zhang and C-Y. Su, Chem. Soc. Rev., 2014, **43**, 6011; (f) S. Roy, A. Chakraborty and T. K. Maji, *Coord. Chem. Rev*., 2014, **273–274**, 139; (g) M. Eddaoudi, J. Kim, N. Rosi, D. Vodak, J. Wachter, M. O' Keefe and O. M. Yaghi, *Science*, 2002, **295**, 469.

29 K. S. Park, Z. Ni, A. P. Côté, J. Y. Choi, R. Huang, F. J. Uribe-Romo, H. K. Chae, M. O'Keeffe and O. M. Yaghi, *Proc. Natl. Acad. Sci. U. S. A*., 2006, **103**, 10186.

30 (a) G. Ferey, C. Mellot-Draznieks, C. Serre, F. Millange, J. Dutour, S. Surble and I. Margiolaki, *Science*, 2005, **309**, 2040; (b) G. Ferey, *Chem. Soc. Rev*., 2008, **37**, 191; (c) F. Millange, C. Serre and G. Ferey, *Chem. Commun*., 2002, 822; (d) C. Serre, F. Millange, C. Thouvenot, M. Noguès, G. Marsolier, D. Louër and G. Férey, *J. Am. Chem. Soc*., 2002, **124**, 13519.

31 (a) O. K. Farha, I. Eryazici, N. C. Jeong, B. G. Hauser, C. E. Wilmer, A. A. Sarjeant, R. Q. Snurr, S. T. Nguyen, A. O. Yazaydın and J. T. Hupp, *J. Am. Chem. Soc*., 2012, **134**, 15016; (b) H. K. Chae, D. Y. Siberio-Perez, J. Kim, Y. Go, M. Eddaoudi, A. J. Matzger, M. O'Keeffe and O. M. Yaghi, *Nature*, 2004, **427**, 523; (c) G. Férey, C. Mellot-Draznieks, C. Serre, F. Millange, J. Dutour, S. Surble and I. Margiolaki, *Science*, 2005, **309**, 2040; (d) K. Koh, A. G. Wong-Foy and A. J. Matzger, *J. Am. Chem. Soc*., 2009, **131**, 4184; (e) H. Furukawa, N. Ko, Y. B. Go, N. Aratani, S. B. Choi, E. Choi, A. O. Yazaydin, R. Q. Snurr, M. O'Keeffe, J. Kim and O. M. Yaghi, *Science*, 2010, **329**, 424.

32 (a) A. Umemura, S. Diring, S. Furukawa, H. Uehara, T. Tsuruoka and S. Kitagawa, *J. Am. Chem. Soc*., 2011, **133**, 15506; (b) H. Xu, F. Liu, Y. Cui, B. Chen and G. Qian, *Chem. Commun*., 2011, **47**, 3153; (c) J. Della Rocca, D. Liu and W. Lin, *Acc. Chem. Res*., 2011, **44**, 957; (d) A. Carne, C. Carbonell, I. Imaz and D. Maspoch, *Chem. Soc. Rev*., 2011, **40**, 291; (e) I. Imaz, J. Hernando, D. Ruiz-Molina and D. Maspoch, *Angew. Chem. Int. Ed*., 2009, **48**, 2325.

33 A. Carné-Sánchez, I. Imaz, M. Cano-Sarabia and D. Maspoch, *Nat. Chem*., 2013, **5**, 203.

34 (a) S. L. Price, *Acc. Chem. Res*., 2009, **42**, 117; (b) J. Bernstein, R. J. Davey and J-O. Henck, *Angew. Chem. Int. Ed*., 1999, **38**, 3440; (c) Y. Zhang, Q. Song, K. Wang, W. Mao, F. Cao, J. Sun, L. Zhan, Y. Lv, Y. Ma, B. Zou and C. Zhang, *J. Mater. Chem. C*, 2015, **3**, 3049; (d) G. Zhang, J. Lu, M. Sabat and C. L. Fraser, *J. Am. Chem. Soc*., 2010, **132**, 2160; (e) L. A. Stevens, K. P. Goetz, A. Fonari, Y. Shu, R. M. Williamson, J-L. Brédas, V. Coropceanu, O. D. Jurchescu and G. E. Collis, *Chem. Mater*., 2015, **27**, 112; (f) R. J. Davey, S. L. M. Schroeder, and J. H. ter Horst, *Angew. Chem. Int. Ed*., 2013, **52**, 2166.

35 D. Das, E. Engel and L. J. Barbour, *Chem. Commun*., 2010, **46**, 1676.

36 (a) M. A. C. Stuart, W. T. S. Huck, J. Genzer, M. Müller, C. Ober, M. Stamm, G. B. Sukhorukov, I. Szleifer, V. V. Tsukruk, M. Urban, F. Winnik, S. Zauscher, I. Luzinov and S. Minko, *Nat. Mater*., 2010, **9**, 101; (b) M. Motornov, J. Zhou, M. Pita, V. Gopishetty, I. Tokarev, E. Katz and S. Minko, *Nano Lett*., 2008, **8**, 2993; (c) Y. Lvov, K. Ariga, I. Ichinose and T. Kunitake, *J. Am. Chem. Soc*., 1995, **117**, 6117.

37 (a) C. Tschierske, *Angew. Chem. Int. Ed*., 2013, **52**, 8828; (b) E. E. Burnell and C. A. de Lange, *Chem. Rev*., 1998, **98**, 2359; (c) S. K. Prasad, *Angew. Chem. Int. Ed*.,

2012, **51**, 10708; (d) E-W. Lee, K. Takimoto, M. Tokita, J. Watanabe and S. Kang, *Angew. Chem. Int. Ed.*, 2014, **53**, 8216.

38 (a) M. Krikorian, S. Liu and T. M. Swager, *J. Am. Chem. Soc*., 2014, **136**, 2952; (b) M. P. Bhatt, J. Du, E. A. Rainbolt, T. M. S. K. Pathiranage, P. Huang, J. F. Reuther, B. M. Novak, M. C. Biewer and M. C. Stefan, *J. Mater. Chem. A*, 2014, **2**, 16148; (c) N. Hu, R. Shao, Y. Shen , D. Chen, N.l A. Clark and D. M. Walba, *Adv. Mater*., 2013, **26**, 2066; (d) M. Yan, J. Tang, H-L. Xie, B. Ni, H-L. Zhang and E-Q. Chen, *J. Mater. Chem. C*, 2015, **3**, 8526.

39 (a) H. Lino, T. Usui and J-i. Hanna, *Nat. Commun.*, 2015, **6**, 1; (b) H. Harada, M. Gomyo, Y. Okano, T. Gan, C. Urano, Y. Yamaguchi, T. Uesaka and H. Arisawa, *J. Soc. Inf. Disp*., 2008, **16**, 1243; (c) M. Kumar and S. Kumar, *Polym. J*., 2017, **49**, 85.

40 (a) A. B. D. Cassie and S. Baxter, *Trans. Faraday Soc*., 1944, **40**, 546; (b) R. N. Wenzel, *Ind. Eng. Chem*., 1936, **28**, 988.

41 (a) P. Terech and R. G. Weiss, *Chem. Rev*., 1997, **97**, 3133; (b) L. A. Estroff and A. D. Hamilton, *Chem. Rev*., 2004, **104**, 1201; (c) D. J. Abdallah and R. G. Weiss, *Adv. Mater*., 2000, **12**, 1237.

42 (a) N. M. Sangeetha and U. Maitra, *Chem. Soc. Rev*., 2005, **34**, 821; (b) M-O. M. Piepenbrock, G. O. Lloyd, N. Clarke and J. W. Steed, *Chem. Rev*., 2010, **110**, 1960; (c) L. E. Buerkle and S. J. Rowan, *Chem. Soc. Rev*., 2012, **41**, 6089.

43 (a) S. Banerjee, R. K. Das and U. Maitra, *J. Mater. Chem*., 2009, **19**, 6649; (b) O. J. Dautel, M. Robitzer, J-P. Lère-Porte, F. Serein-Spirau, and J. J. E. Moreau, *J . Am. Chem. Soc.*, 2006, **128**, 16213; (c) X. Y. Liu and P. D. Sawant, *Appl. Phys. Lett*., 2001, **79**, 3518.

44 S. S. Babu, S. Prasanthkumar and A. Ajayaghosh, *Angew. Chem. Int. Ed*., 2012, **51**, 1766.

45 (a) K. Sugiyasu, S.-i. Kawano, N. Fujita and S. Shinkai, *Chem. Mater*., 2008, **20**, 2863; (b) P. Xue, R. Lu, L. Zhao,D. Xu, X. Zhang, K. Li, Z. Song, X. Yang, M. Takafuji and H. Ihara, *Langmuir*, 2010, **26**, 6669.

46 (a) N. N. Adarsh, P. Sahoo, and P. Dastidar, *Cryst. Growth & Des*., 2010, **10**, 4976; (b) M-O. M. Piepenbrock, N. Clarke and J. W. Steed, Langmuir, **2009**, *25*, 8451; (c) X. Yan, T. R. Cook, J. B. Pollock, P. Wei, Y. Zhang, Y. Yu, F. Huang and P. J. Stang, *J. Am. Chem. Soc*., 2014, **136**, 4460; (d) V. K-M. Au, N. Zhu and V. W-W. Yam, *Inorg. Chem*., 2013, **52**, 558; (e) A. V. Y. Tam and V. W-W. Yam, *Chem. Soc. Rev*., 2013, **42**, 1540.

47 H. Lee, S. Kang, J. Y. Lee and J. H. Jung, *Soft Matter*, 2012, **8**, 2950.

48 (a) P. Sutar and T. K. Maji, *Chem. Commun*., 2016, **52**, 8055; (b) P. Sutar, V. M. Suresh and T. K. Maji, *Chem. Commun*., 2015, **51**, 9876.

49 (a) G. Yu, K. Jie and F. Huang, *Chem. Rev*., 2015, **115**, 7240; (b) K. Jie, Y. Zhou, Y. Yao and F. Huang, *Chem. Soc. Rev*., 2015, **44**, 3568.

50 (a) X. Zhao, F. Pan, H. Xu, M. Yaseen, H. Shan, C.A. E. Hauser, S. Zhang and J. R. Lu, *Chem. Soc. Rev*., 2010, **39**, 3480; (b) P. Alexandridis, *Curr. Opin. Colloid Interface Sci*., 1996, **1**, 490.

51 (a) D. E. Discher and A. Eisenberg, *Science*, 2002, **297**, 967; (b) C. Wang, Z. Wang and X. Zhang, *Acc. Chem. Res*., 2012, **45**, 608.

52 (a) X. Zhang and C. Wang, *Chem. Soc. Rev*., 2011, **40**, 94; (b) T. Shimizu, M. Masuda and M. Minamikawa, *Chem. Rev*., 2005, **105**, 1401.

53 (a) J-H. Fuhrhop and T. Wang, *Chem. Rev*., 2004, **104**, 2901; (b) J-H. Fuhrhop and D. Fritsch, *Acc. Chem. Res*., 1986, **19**, 130.

54 S. Roy, V. M. Suresh and T. K. Maji, *Chem. Sci*., 2016, **7**, 2251.

55 (a) J. Huang, N. Sun, Y. Dong, R. Tang, P. Lu, P. Cai, Q. Li, D. Ma, J. Qin and Z. Li, *Adv. Funct. Mater*., 2013, **23**, 2329; (b) A. C. Arango, L. R. Johnson,V. N. Bliznyuk, Z. Schlesinger, S. A. Carter and H-H. Horhold, *Adv. Mater*., 2000, **12**, 1689.

56 (a) U. H. F. Bunz, *Chem. Rev*., 2000, **100**, 1605; (b) U. H. F. Bunz, *Macromol. Rapid Commun*., 2009, **30**, 772.

57 (a) S. A. Sharber, R. N. Baral, F. Frausto, T. E. Haas, P. Müller and S. W. Thomas III, *J. Am. Chem. Soc*., 2017, **139**, 5164; (b) R. J. Marshall, Y. Kalinovskyy, S. L. Griffin, C. Wilson, B. A. Blight and R. S. Forgan, *J. Am. Chem. Soc*., 2017, **139**, 6253.

58 G. Brizius, N. G. Pschirer, W. Steffen, K. Stitzer, H. C. zur Loye and U. H. F. Bunz, *J. Am. Chem. Soc*., 2000, **122**, 12435.

59 E. Negishi and L. Anastasia, *Chem. Rev*., 2003 **103**, 1979.

60 (a) K. Yoosaf, A. R. Ramesh, Jino George, C. H. Suresh, and K. G. Thomas, Chem. Commun., *J. Phys. Chem. C*, 2009, **113**, 11836; (b) A. R. Ramesh and K. G. Thomas, *Chem. Commun*., 2010, **46**, 3457; (c) R. Thomas, S. Varghese and G. U. Kulkarni, *J. Mater. Chem*., 2009, **19**, 4401; (d) R. Gupta, R. Thomas and G. U. Kulkarni, *J. Mater. Chem*., 2012, **22**, 19139; (e) S. Roy, A. Hazra, A. Bandyopadhyay, D. Raut, P. L. Madhuri, D. S. S. Rao, U. Ramamurty, S. K. Pati, S. K. Prasad and T. K. Maji, *J. Phys. Chem. Lett*., 2016, **7**, 4086.

61 (a) A. Ajayaghosh, R. Varghese, S. Mahesh and V. K. Praveen, *Angew. Chem. Int. Ed*., 2006, **118**, 7893; (b) S. Roy, D. Samanta, P. Kumar and T. K. Maji, *Chem. Commun*., 2018, **54**, 275.

62 W. Hong, H. Li, S-X. Liu, Y. Fu, J. Li, V. Kaliginedi, S. Decurtins and T. Wandlowski, *J. Am. Chem. Soc*., 2012, **134**, 19425.

63 (a) U. H. F. Bunz, K. Seehafer, M. Bender and M. Porz, *Chem. Soc. Rev*., 2015, **44**, 4322; (b) Q. Zhou and T. M. Swager, *J. Am. Chem. Soc*., 1995, **117**, 12593.

Chapter 2A

Reversible Polymorphism, Liquid Crystallinity, and Stimuli- Responsive Luminescence in a Bola-amphiphilic π-System: Structure–Property Correlations Through Nanoindentation and DFT Calculations

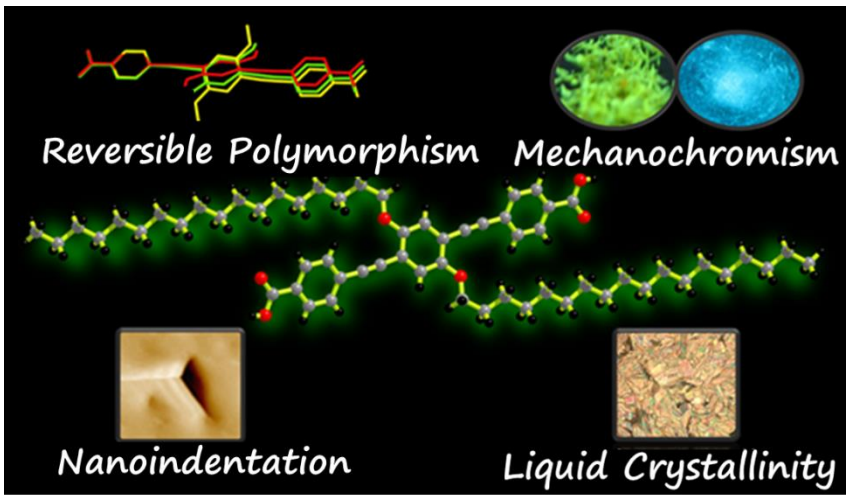

Summary

This chapter discusses the design, synthesis, detailed characterization, and analysis of a new multifunctional π-conjugated bola-amphiphilic chromophore: *oligo*-(*p*-phenyleneethynylene)-dicarboxylic acid with dialkoxyoctadecyl side chains (**OPE-C_{18}-1**). **OPE-C_{18}-1** shows two polymorphs at 123 K (**OPE-C_{18}-1′**) and 373 K (**OPE-C_{18}-1″**), whose crystal structures were characterized via single crystal X-ray diffraction. **OPE-C_{18}-1** also exhibits thermotropic liquid crystalline property revealing a columnar phase. The inherent π-conjugation of **OPE-C_{18}-1** imparts luminescence to the system. Photoluminescence measurements on the mesophase also reveal similar luminescence as in the crystalline state. Additionally, **OPE-C_{18}-1** shows mechano-hypsochromic luminescence behavior. Density functional theory (DFT) based calculations unravel the origins behind the simultaneous existence of all these properties. Nanoindentation experiments on the single crystal reveal its mechanical strength and accurately correlate the molecular arrangement with the liquid crystalline and mechanochromic luminescence behavior.

The work based on this chapter is published:

S. Roy, A. Hazra, A. Bandyopadhyay, D. Raut, P. L. Madhuri, D. S. Shankar Rao, S. K. Pati, S. K. Prasad and T. K. Maji, *J. Phys. Chem. Lett.*, 2016, **7**, 4086−4092.

2A.1. Introduction

In the context of the development of stimuli-responsive organic supramolecular assemblies,[1] molecular tectonics is useful for the specific design of functional materials with tailorable properties.[2] It also allows for comprehension and control of desired properties at the molecular level. Polymorphism is one such property that can be controlled via molecular tectonics.[3] Specifically, the design of stimuli responsive polymorphic materials showing liquid-crystalline[4] and mechanochromic luminescence (ML)[5] properties can lead to promising applications. Coupled with ML behavior, liquid crystalline (LC) materials[6] can find cutting-edge applications such as pressure sensors and security ink.[7] The collective approach toward the design of LC materials is the introduction of complementary weak and strong interactions.[8] Crystal engineering, via a molecular tectonics approach can assist in balancing the interplay between these strong and weak supramolecular interactions.[9] This maintains the rigid crystalline as well as mobile liquid nature within the same structure. Columnar liquid crystalline structures are a major class of LC materials having a huge potential for applications in molecular electronics.[10] A general design strategy to realize columnar thermotropic liquid crystalline phases requires strategic positioning of the flexible chains such that in the mesophase, they occupy the peripheral region around the central rigid core.[11] In this respect, long alkyl chains would fit well for such a packing scheme. Additionally, luminescent LC materials have been a cornerstone for the latest device-based technologies and for the development of such materials, π-conjugation in the system would promote luminescence.[12] In this regard, *oligo*-(*p*-phenyleneethynylenes) (OPEs) possessing a conjugated triple bond backbone and having flexibility in altering its side chains with long alkyl groups would prove to be excellent candidates for the synthesis of such materials.[13] Therefore, the control of non-covalent interactions in different crystallographic directions via molecular tectonics and inherent luminescence induced by conjugation can lead to luminescent liquid crystalline materials. The π-conjugation due to the triple bonds would not only lead to luminescence but also a conformational change or polymorphism via their rotational degree of freedom. The disruption of such weak packing forces could also yield mechanochromism in the same material leading to useful applications.[14] In the recent past, nanoindentation technique was successfully applied to develop such an understanding for molecular materials.[15] The technique involves quantitative measurement of mechanical properties of materials that are available only in

small quantities, such as small single crystals. The existence of strong and weak interactions on particular planes can be inferred well from the experimental measurements of elastic modulus, E, and hardness, H, of different faces of a crystal.[16] Stimuli-responsive behavior can thus be measured and rationalized by nanoindentation.

In this chapter, the design and synthesis of a chromophoric organic bola-amphiphilie; *oligo*-(*p*-phenynyleneehtylene) dicarboxylic acid (**OPE-C_{18}-1**) is described, which exhibits multifunctional properties such as polymorphism, liquid crystallinity, and mechanochromic luminescence. Carboxylic acid groups and octadecyl chains were strategically placed to satisfy antagonistic requirements of strong and weak supramolecular interactions to realize such a material. Nanoindentation on different faces of the single crystals of **OPE-C_{18}-1** reveals their E and H, which correlate well with the functional properties of it. The experimental results are also well supported by DFT calculations.

2A.2. Experimental Section

2A.2.1. Materials

$Pd(PPh_3)_4$ was obtained from Sigma-Aldrich Chemical Co and cuprous iodide was obtained from Loba Chemie Pvt. Ltd. Acetone, N,N-dimethyl formamide (DMF) and tetrahydrofuran (THF) were obtained from Spectrochem Pvt. Ltd (Mumbai, India). THF was pre-dried using standard procedure and all other reagents, solvents were of reagent grade and used without further purification.

2A.2.2. Physical Measurements

The elemental analysis was carried out using a Thermo Scientific Flash 2000 CHN analyzer. Infrared spectral study was performed by making samples with KBr pellets using Bruker FT-IR spectrometer. ^1H and ^{13}C spectrum were recorded on a Bruker AV-400 spectrometer with chemical shifts recorded as ppm and all spectra were calibrated against TMS. Powder X-ray diffraction studies were recorded on a Bruker D8 discover instrument using Cu-Kα radiation. Thermal stability of the **OPE-C_{18}-1** was analyzed using Mettler Toledo TGA 850 instrument under N_2 atmosphere in the temperature range of 25-500 °C at a heating rate of 3 °C /min. UV–Vis spectra were recorded on a Perkin Elmer Model Lambda 900 spectrophotometer. Fluorescence studies were accomplished using Perkin Elmer Ls 55 Luminescence spectrometer. The mesogenic compound was

investigated for their liquid crystalline behavior (birefringence and fluidity) by employing a polarizing optical microscope (Nikon Eclipse LV100POL) equipped with a programmable hot stage (Mettler Toledo FP90). Clean glass slides and coverslips were employed for polarizing optical microscopic observations. X-ray diffraction measurements of the mesogenic phase were carried out using image plate (IP) and a solid state detector. In this apparatus Cu Kα (λ =0. 15418 nm) radiation from a source (GeniX3D, Xenocs) operating at 50 kV and 0.6 mA in conjunction with a multilayer mirror was used to illuminate the sample, which was contained in a glass capillary tube (Capillary Tube Supplies Ltd). The temperature of the sample was varied using a Mettler hot stage/programmer (FP82HT/FP90). The diffraction patterns were collected on a 2D IP detector of 345 mm diameter and 0.1 mm pixel size (Mar345, Mar Research). The nanoindenter used for the experiment was Triboindenter of Hysitron, Minneapolis, USA. A three-sided pyramidal Berkovich diamond indenter (tip radius ≈ 100 nm) was used for the experiments. The selected crystal faces were firmly mounted on a stud using a thin layer of cyanoacrylate glue prior to nanoindentation. Indentation experiments were possible on (001) and (043) faces. The loading/unloading rate was 100 μN/ s and peak load was 500 μN. A minimum of 10 indentations were performed on each crystallographic face to ensure reproducibility.

2A.2.3. Computational Details

Gaussian 09 software[17] was used for all the electronic property calculations, considering wB97-XD functional[18] and 6-31+G(d,p) basis set. This functional can take care of the long range dispersion interactions, which was very much important for this study. Due to the larger size of the systems, optical properties of the systems have been calculated using the density functional theory (DFT) method as implemented in the SIESTA package.[19] Generalized gradient approximation (GGA) in the Perdew–Burke–Ernzerhof (PBE) form[20] were used to consider the exchange–correlation function. Double-z-polarized numerical atomic-orbital basis sets were used for all the atoms. Norm-conserving pseudo-potentials were used [21] in the fully nonlocal Kleinman–Bylander form for all the atoms.[22] A mesh cut-off value of 400 Ry was also used. As systems were considered to be zero-dimensional (molecular system), all the calculations were performed only at the gamma (**Γ**) point of the Brillouin zone. A vacuum of 20 Å was used in all the three directions to avoid any unwanted interactions.

2A.2.4. Single crystal X-ray Diffraction (SCXRD)

Suitable single crystals of compound **OPE-C_{18}-1**, **OPE-C_{18}-1′** and **OPE-C_{18}-1″** were mounted on a thin glass fiber with commercially available super glue. X-ray single crystal structural data were collected on a Bruker D8 VENTURE with Mo-Kα radiation (λ = 0.71073 Å) operating at 50 kV and 1 mA. The program SAINT[23] was used for the integration of diffraction profiles and absorption correction was made with SADABS[24] program. All the structures were solved by SIR 92[25] and refined by full matrix least square method using SHELXL.[26] All the hydrogen atoms were fixed by HFIX and placed in ideal positions. All crystallographic and structure refinement data of **OPE-C_{18}-1**, **OPE-C_{18}-1′** and **OPE-C_{18}-1″** are summarized in Table 1. All calculations were carried out using SHELXL 97,[26] SHELXS 97[26] and WinGX system, Ver 1.80.05.[27]

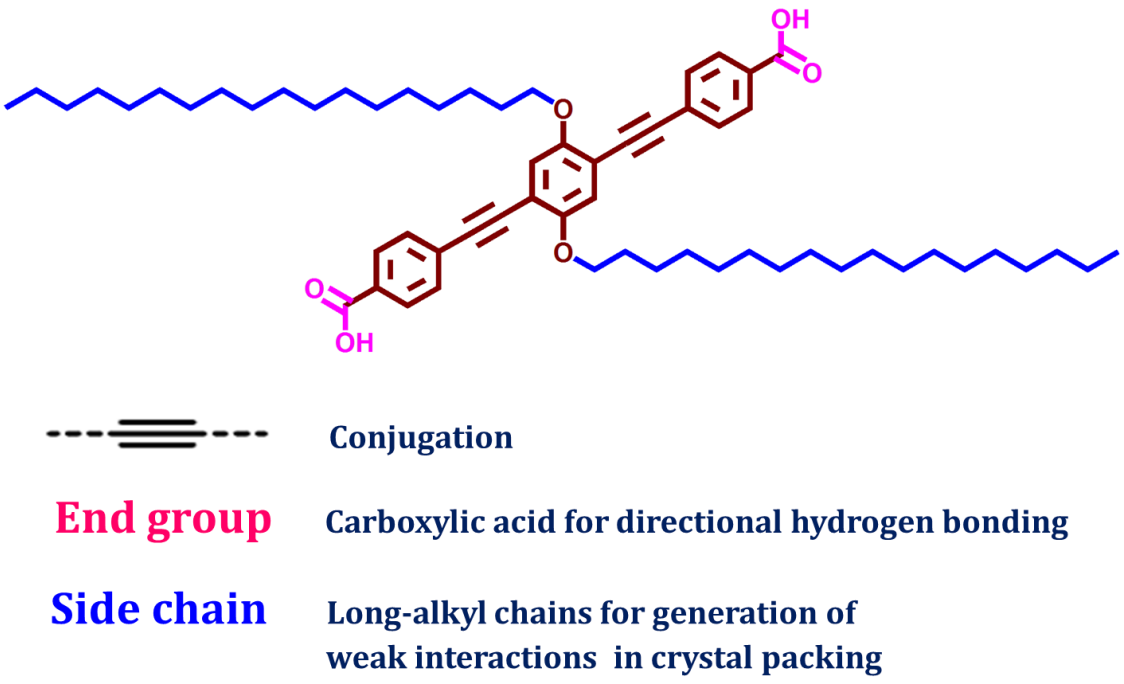

Scheme 1. Design principle for the construction of a bola-amphiphilic chromophore having polymorphic, liquid crystalline and mechanochromic luminescence property.

2A.2.5. Synthesis of 4,4'-(2,5-bis(octadecyloxy)-1,4-phenylene)bis(ethyne-2,1-diyl)dibenzoic acid (OPE-C_{18}-1) and Crystallization

General procedure and characterization

Chemical shifts (δ) are indicated in ppm. The following abbreviations were used to illustrate NMR signals: s = singlet, d = doublet, t = triplet, td = triplet of doublets, dd =

doublet of doublets, ddd = doublet of doublets of doublets, m = multiplet. Compounds 1-5 were synthesized according to reported procedures.[28,29]

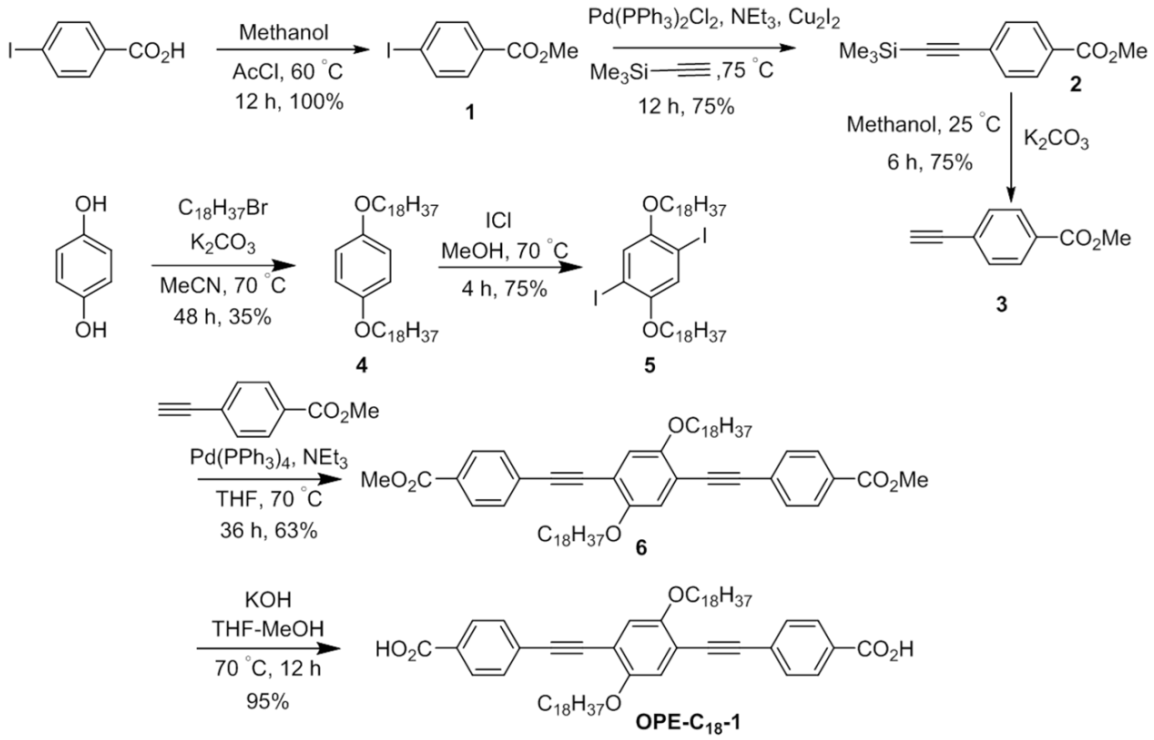

Scheme 2. Synthetic scheme for **OPE-C_{18}-1**.

Synthesis of dimethyl 4,4'-(2,5-bis(octadecyloxy)-1,4-phenylene)bis(ethyne-2,1-diyl)dibenzoate (6). A 250 mL three-neck round-bottomed flask, charged with 1,4-diiodo-2,5-bis(octadecyloxy)benzene (**5**) (1.00 g, 1.15 mmol), methyl 4-ethynylbenzoate (**3**) (0. 37 g, 2.30 mmol), 25 mL tetrahydrofuran and 10 mL triethylamine, was degassed by freeze-pump-thaw procedure (three times). The $Pd(PPh_3)_4$ (310 mg, 270 µmol) was added to it. The resulting reaction mixture was refluxed at 70 °C for 48 h under inert atmosphere for completion of the coupling reaction. The resulting solution was concentrated and purified by column chromatography (silica gel, hexane/ethyl acetate = 98: 3) to obtain dimethyl 4,4'-(2,5-bis(octadecyloxy)-1,4-phenylene)bis(ethyne-2,1-diyl)dibenzoate (6) (0. 510 g, 564 µmol, 49 % yield) as a bright green solid compound. ^{1}H NMR (400 MHz, $CDCl_3$) δ = 0.87 (t, *J* = 6.8 Hz, 6H), 1.26-1.43 (m, 60H), 1.65-1.75 (m, 4H), 3.91 (s, *J* = 6.4 Hz, 6H), 4.04 (t, *J* = 5.2 Hz, 4H), 7.51 (s, *J* = 7.7 Hz, 2H), 7.78 (d, *J* = 7.8 Hz, 4H), 8.03 (d, *J* = 8.4 Hz, 4H), ppm. ^{13}C NMR (100 MHz, $CDCl_3$) δ = 14.2, 22.8, 26.0, 29.5, 29.5, 29.5, 29.5, 29.5, 29.5, 29.5, 29.5, 29.5, 29.5, 29.6, 32.2, 51.6,

68.2, 84.3, 96.0, 112.4, 127.1, 128.2, 129.6, 129.9, 129.8, 132.3, 166.0 ppm. HRMS-EI (*m/z*) for $C_{62}H_{90}O_6$ [M^+] Calcd. 930.672, found 930.663. Anal. Calcd. for $C_{62}H_{90}O_6$: C, 79.95; H, 9.74. Found: C, 79.04; H, 8.9.

Synthesis of 4,4'-(2,5-bis(octadecyloxy)-1,4-phenylene)bis(ethyne-2,1-diyl)dibenzoic acid (OPE-C_{18}-1). K_2CO_3 flakes (1.00 g, 7.25 mmol) was added to a solution of dimethyl 4,4'-(2,5-bis(octadecyloxy)-1,4-phenylene)bis(ethyne-2,1-diyl)dibenzoate (**6**) 500 mg, 537 µmol) in 40 mL methanol. The resulting solution was refluxed for 12 h at 70 °C to complete ester hydrolysis. The clear solution was added dropwise over 4 N aq. HCl solution (250 mL) and bright green precipitate of 4,4'-(2,5-bis(octadecyloxy)-1,4-phenylene)bis(ethyne-2,1-diyl)dibenzoic acid (**OPE-C_{18}-1**) was formed which was filtered off and washed with water (100 mL) and methanol (25 mL, caution: slightly soluble) to get pure compound (420 mg, 465 µmol, 87% yield). ^{1}H NMR (400 MHz, DMSO-d^6) δ = 0.88 (t, *J* = 6.8 Hz, 6H), 1.26-1.43 (m, 60H), 1.65-1.75 (m, 4H), 4.11 (t, *J* = 5.2 Hz, 4H), 7.51 (s, *J* = 7.7 Hz, 2H), 7.71 (d, *J* = 7.7 Hz, 4H), 7.91 (d, *J* = 8.4 Hz, 4H), 11.93 (brs, 2H) ppm. ^{13}C NMR (100 MHz, $CDCl_3$, DMSO-d^6) δ = 14.2, 22.8, 26.0, 29.5, 29.5, 29.5, 29.5, 29.5, 29.5, 29.5, 29.5, 29.5, 29.5, 29.6, 32.2, 68.2, 84.3, 96.0, 112.4, 118.4, 128.0, 130.0, 130.0, 132.3, 169.4 ppm. HRMS-EI (*m/z*) for $C_{60}H_{86}O_6$ [M^+] Calcd. 902.641, found 902.640. Anal. Calcd. for $C_{60}H_{86}O_6$: C, 79.78; H, 9.60. Found: C, 79.14; H, 9.24.

THF solution of pure **OPE-C_{18}-1** powder was taken into a 3 mL glass vial. The vial was kept in a 10 mL glass vial containing acetone and the entire system was sealed so that no solvent vapor could escape. Long needle shaped crystals appeared on the sides of the 3mL glass vial after a few days.

2A.3. Results and Discussion

The Sonogashira−Hagihara coupling scheme was employed for the synthesis of **OPE-C_{18}-1**.[28,29] The design scheme suggests that an interplay of strong and weak interactions within the supramolecular system is desired (Scheme 1, 2). Directional linear hydrogen bonding is reported widely in the literature as a supramolecular structure directing interaction.[30] Coupling with weak van der Waals interaction between long alkyl chains can result in a supramolecular organization with interesting physical properties. Motivated with the synthesis of such a compound, we targeted to delineate its exact structure. The powder form of the product was crystallized by vapor diffusion of acetone

into a THF solution of **OPE-C_{18}-1** to afford long needle-shaped green colored crystals. The crystals were about 1 mm long and suitable for single crystal X-ray diffraction (SC-XRD).

2A.3.1. Single Crystal Structure of OPE-C_{18}-1

Single crystal structure determination at 298 K revealed that **OPE-C_{18}-1** crystallizes in the triclinic crystal system with space group $P\bar{1}$ (Table 1). The single molecule of **OPE-C_{18}-1** is linear where phenyl ring containing octadecyl side chains in the center is sandwiched by benzoic acid groups on either side through ethynyl units (Figure 1a). The asymmetric unit comprises half of the **OPE-C_{18}-1** molecule. The dihedral angle between the plane containing the central phenyl ring with octadecyl side chains and the plane containing the terminal benzoic acids is 28.2°. Terminal benzoic acid groups of adjacent molecules of **OPE-C_{18}-1** take part in hydrogen bonding resulting in a 1D chain like arrangement (hydrogen bonding D−A distance; 1.83 Å, ∠D−H···A; 179.8°) (Figure 1b).[31] The adjacent 1D chains further take part in C−H···π and C−H···O interactions to generate a 2D layer as shown in Figure 1c,d. The methylene hydrogen of octadecyl chains of one 1D chain interacts with the phenyl π core of adjacent 1D chain resulting in a C−H···π interaction with a distance of 3.325 Å.[32] C−H···O interactions exist between carboxylate oxygen of one 1D chain and aromatic hydrogen of adjacent chain (D−A distance; 2.68 Å, ∠D−H···A; 130.1°).[33] These non-covalent interactions offset to the *ac* plane leads to an ABAB type packing in 2D (Figure 1d). Thus, the 2D layer is generated by a combination of C−H···π and C−H···O interactions. The resulting 2D arrangement reinforces the close packing of octadecyl chains of adjacent 1D chains. These 2D layers are in turn stacked such that the octadecyl alkyl chains of neighboring layers are separated by a distance of 6.07 Å (Figure 1e). There exists a weak van der Waals interaction between the octadecyl side chains of the 2D layers, which extends the layers oblique to the *bc* plane. Therefore, a combination of strong and weak interaction coexists along different planes of **OPE-C_{18}-1**.

Thermogravimetric analysis revealed that **OPE-C_{18}-1** is stable up to almost 530 K without any observable weight loss (Figure 2a). However, the existence of hierarchical strong and weak supramolecular interactions in **OPE-C_{18}-1**, prompted us to carry out differential scanning calorimetry (DSC) experiments to find possible phase changes over a wide temperature range 90 to 523 K (Figure 2b). The DSC thermogram revealed

reversible exo- and endo-thermic peaks at 123, 373, 469, and 500 K with the enthalpy values of 6.5, 5.4, 8.0, and 6.4 kJ/ mol, respectively (Table 2).

Table 1. Crystallographic data and structure refinement parameters for **OPE-C_{18}-1**, **OPE-C_{18}-1′** and **OPE-C_{18}-1″**.

	OPE-C_{18}-1	**OPE-C_{18}-1′**	**OPE-C_{18}-1″**
empirical formula	$C_{60}H_{86}O_6$	$C_{60}H_{86}O_6$	$C_{60}H_{86}O_6$
M	903.29	903.29	903.29
crystal system	triclinic	triclinic	triclinic
space group	$P\bar{1}$ (No. 2)	$P\bar{1}$ (No. 2)	$P\bar{1}$ (No. 2)
a (Å)	7.1245(3)	5.6873(4)	6.6764(10)
b (Å)	12.6264(6)	11.0563(9)	13.184(3)
c (Å)	16.7681(10)	21.3282(17)	17.361(3)
α (deg)	101.132(2)	76.848(2)	73.665(9)
β (deg)	101.941(3)	83.218(2)	83.571(10)
γ (deg)	103.882(2)	89.785(3)	83.54(1)
V (Å^3)	1385.09(12)	1296.44(17)	1452.0(5)
Z	1	1	1
T (K)	298	110	383
λ (Mo K_α)	0.71073	0.71073	0.71073
D_c (g/cm^3)	1.083	1.157	1.033
μ (mm^{-1})	0.068	0.072	0.065
$\theta_{min}/\theta_{max}$	2.6/ 25.0	1.0/25.0	2.5/25.0
total data	19273	7568	21718
unique reflection	4809	4407	5082
R_{int}	0.041	0.029	0.327
data [I>2σ(I)]	2124	2839	1227
R^a	0.0668	0.0542	0.1370
$R_w{}^b$	0.2436	0.2084	0.3438
GOF	1.02	1.07	1.02
Δρ min/max [e Å^{-3}]	-0.18, 0.24	-0.47, 0.37	-0.11, 0.13

$^aR=\sum||F_o|-|F_c||/\sum|F_o|$. $^bR_w=[\sum\{w(F_o^2-F_c^2)^2\}/\sum\{w(F_o^2)^2\}]^{1/2}$

2A.3.2. Polymorphism in OPE-C_{18}-1

The possibility that these phase change signatures could be due to existence of either polymorphic or liquid crystalline transformations, necessitated further detailed investigations. To investigate the phase transformation at 123 K, SC-XRD data was

collected at 110 K, which revealed a new polymorphic structure that is labeled as **OPE-C_{18}-1′.**

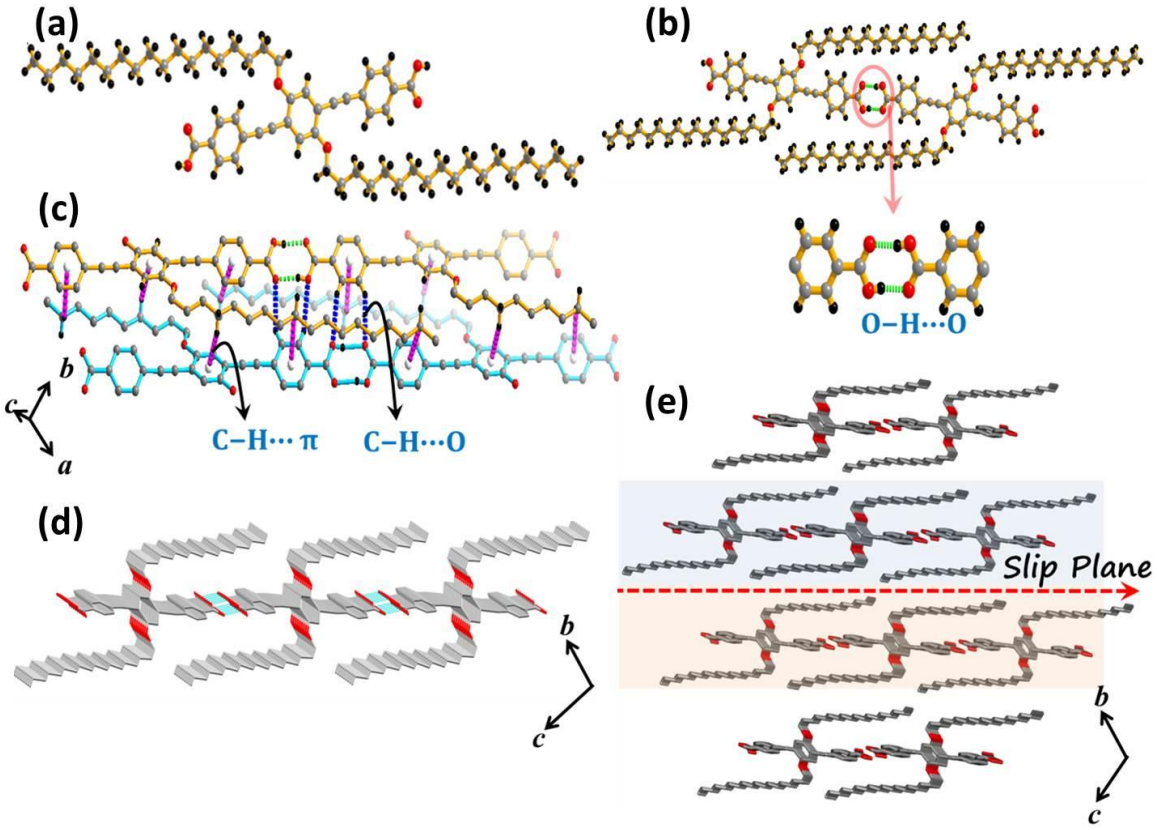

Figure 1. Structural representation of **OPE-C_{18}-1**: (a) View of the single molecule, (b) View of the 1D coordination chain extended via strong O–H···O hydrogen bonding (represented by green dashed circle), (c) View of different types of non-covalent interactions between adjacent 1D chains (blue and pink dashed lines represent the C–H···O and C–H···π interactions respectively), (d) View of the 2D supramolecular packing and (e) Extension of 2D structure via van der Waals interactions of octadecyl chains. Red line indicates potential slip plane.

It also exists in the same crystal system (triclinic) and space group ($P\bar{1}$) as **OPE-C_{18}-1** but presents significant changes in the cell parameters as seen in Table 1. The difference from **OPE-C_{18}-1** structure lies in the arrangement of the central phenyl ring containing the alkoxyoctadecyl of an individual molecule. Here, the dihedral angle, θ, between the planes containing the central phenyl ring and that containing the terminal benzoic acid groups is 6.1°. This is a large shift in θ as compared to a θ of 28.2° in **OPE-C_{18}-1** (Figure 3a). **OPE-C_{18}-1′** molecule is also extended by a hydrogen bonding interaction (D–A

distance; 1.87 Å, ∠D−H···A; 179.8°) to give rise to a 1D chain like structure (Figure 4a). These 1D chains are further extended into 2D by C−H···π interactions (D−A distance; 3.876 Å)

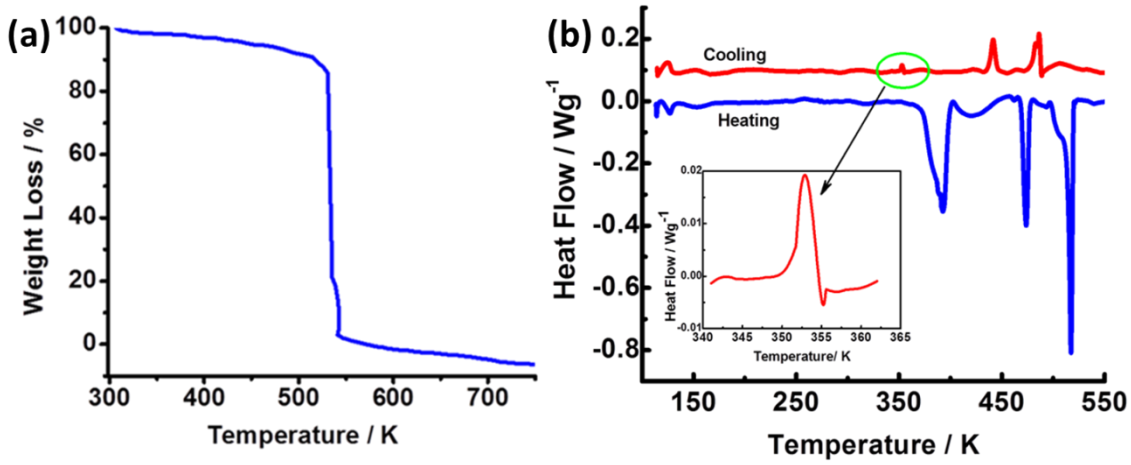

Figure 2. (a) TGA thermogram of **OPE-C_{18}-1** carried out in the temperature range 298-775 K and (b) DSC thermogram of **OPE-C_{18}-1** under N_2 atmosphere showing different phase transformations. Blue curve indicates the heating cycle and red curve indicates the cooling cycle. Inset: Magnified area showing the phase transitions at 350 K.

leading to the similar 2D supramolecular architecture of as in **OPE-C_{18}-1** (Figure 3b, 4b). Interestingly, the C−H···O interaction, which is present along with C−H···π interactions in **OPE-C_{18}-1**, is non-existent in **OPE-C_{18}-1′**. We predict that, due to the attainment of planarity, the proximity of carboxylate and aromatic hydrogens of the neighboring 1D chains are lost, negating the possibility of such interactions. This also forces the octadecyl chains to pack closely as in **OPE-C_{18}-1** with the shortest spacing of 3.069 Å. Similar to **OPE-C_{18}-1**, adjacent 2D layers are further packed via weak van der Waals interaction (Figure 4c).

The SC-XRD data at 383 K reveal yet another polymorphic structure, **OPE-C_{18}-1″**, which has the same crystal system and space group as **OPE-C_{18}-1** and **OPE-C_{18}-1′** (Table 1), but with the following two structural differences (Figure 3c): (i) The acetylenic linkages between the phenyl rings are bent and (ii) The θ between planes containing the central ring with octadecyl side chains and the plane containing the terminal benzoic acid groups is 22.1° as opposed to 28.2° for **OPE-C_{18}-1** and 6.1° for **OPE-C_{18}-1′** (Figures 1a, 3a, c, and 6). This generates a highly strained structure of **OPE-C_{18}-1″**. However, following the previous trends of the polymorphs, strong hydrogen bonding interactions

(D−A distance; 1.821 Å, ∠D−H···A; 172.9°) extends the structure into 1D, whereas weak C−H···π (D−A distance; 3.796 Å) interactions between 1D chains extend the structure into 2D (Figure 5a,b). As in the case of **OPE-C_{18}-1′**, decrease in the dihedral angle negates the possibility of C−H···O interaction between successive 1D chains (Figure 3d).

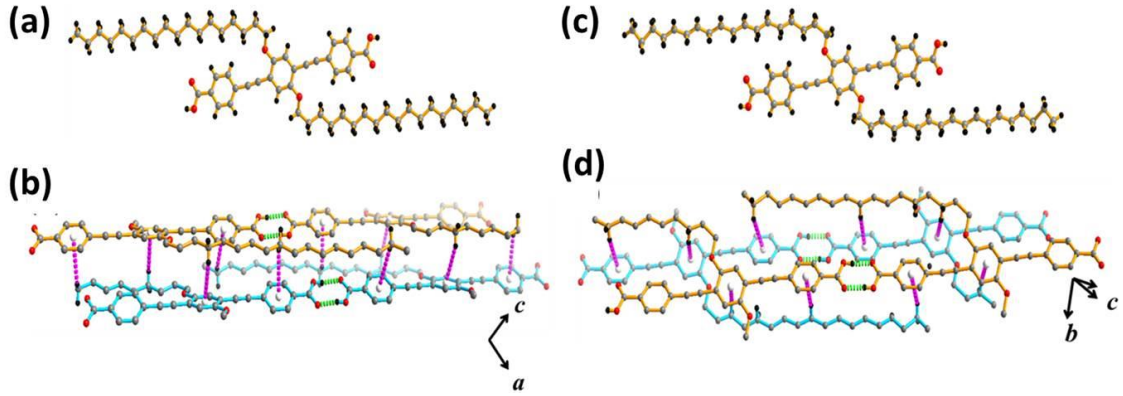

Figure 3. Structural representation of polymorphic structures of **OPE-C_{18}-1**: (a) and (c) View of the single molecule of **OPE-C_{18}-1′** and **OPE-C_{18}-1"**, View of the non-covalent interactions leading to the generation of 2D layers of (b) **OPE-C_{18}-1′** and (d) **OPE-C_{18}-1"**. Pink and green dashed lines are representing C−H···π and O−H···O interactions respectively.

Analogous to the two other polymorphs, the 2D layers (Figure 5b) of **OPE-C_{18}-1″** interact via the weak van der Waals interactions between octadecyl chains to extend the packing (Figure 5c).

Ab initio density functional theory (DFT) calculations were performed to understand the temperature-dependent polymorphic phase transitions in **OPE-C_{18}-1**. The low temperature, room temperature, and high temperature crystal structures were optimized by keeping the cell parameters the same (to avoid getting **OPE-C_{18}-1′** in every case). Here, the energy differences between the unit cells of **OPE-C_{18}-1**, **OPE-C_{18}-1′**, and **OPE-C_{18}-1″** were calculated. We found that **OPE-C_{18}-1′** is stable by an energy content of 0.03 eV compared to **OPE-C_{18}-1**. This suggests that the formation of **OPE-C_{18}-1** is only possible at higher (room) temperatures. The same calculation was also done for **OPE-C_{18}-1″** to find the possibility of its occurrence at a higher temperature. **OPE-C_{18}-1″** is found to be higher in energy by 0.58 eV when compared to **OPE-C_{18}-1**. We believe that this polymorphic behavior of **OPE-C_{18}-1** is arising due to the rotational degree of freedom of the single bonds connecting the phenyl rings and the triple bonds. The change in temperature induces varying rotational degrees in the phenyl rings, thereby guiding the

formation of the different polymorphic structures. At low temperature (T = 110 K), there is negligible rotation of phenyl rings around the triple bonds. This gives rise to the stable structure of **OPE-C_{18}-1′**, where the single molecular entity is nearly linear and the central phenyl ring makes a θ of 6.1° with the terminal ones. Availability of higher energy (T = 298 K) forces a significant rotation of phenyl rings around the triple bond (θ = 28.1°) giving rise to the room temperature structure **OPE-C_{18}-1**. At even higher temperatures (T = 373 K), there is sufficient energy to bend the acetylenic linkages to reveal a strained structure of **OPE-C_{18}-1″**. The lower degree of rotation of phenyl rings compared to **OPE-C_{18}-1** is compensated by the energy required to distort the acetylenic linkages of **OPE-C_{18}-1″**.

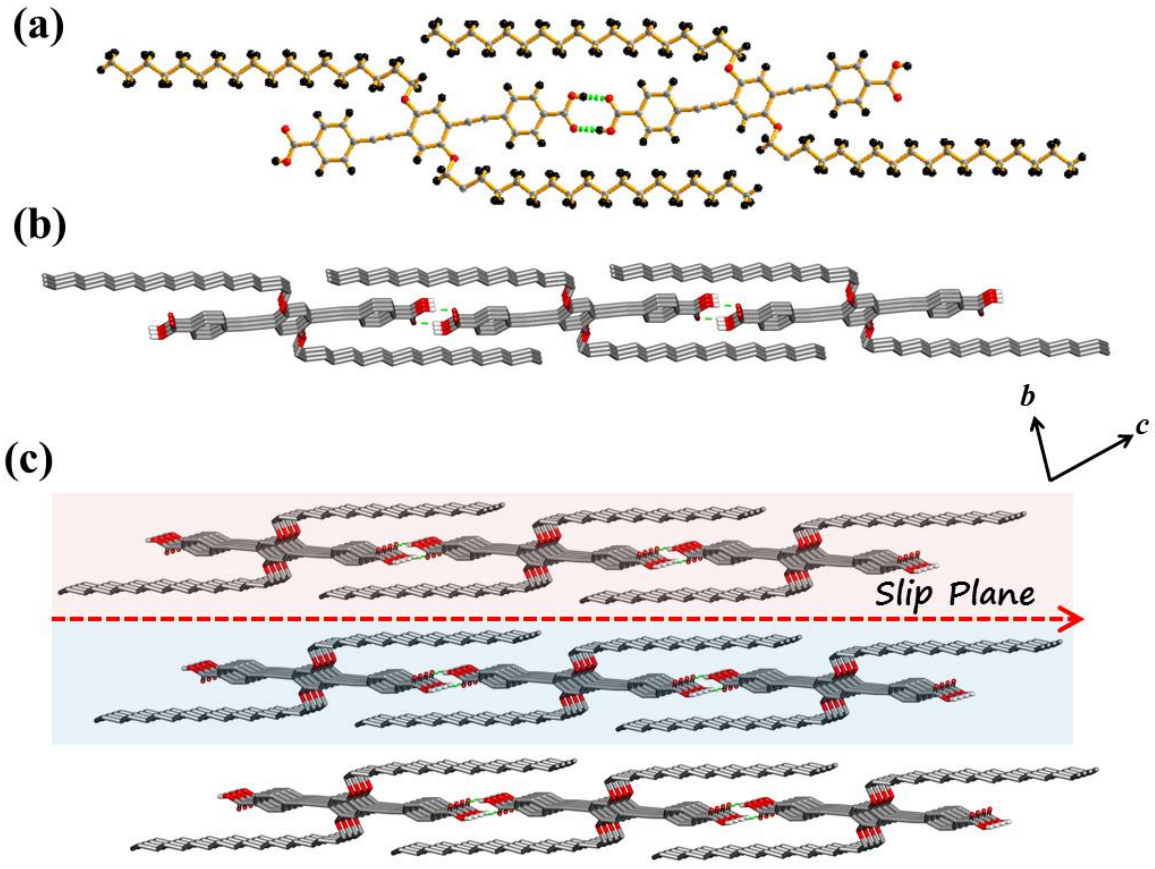

Figure 4. Structural representation of **OPEC_{18}-1′** showing the generation of (a) 1D coordination chain of **OPE-C_{18}-1′** extended via strong hydrogen bonding, (b) View of the 2D supramolecular packing of **OPE-C_{18}-1** extended via C−H···π interactions and (c) Extension of structure into 3D via van der Waals interaction of octadecyl chains of adjacent 2D layers.

Therefore, availability of varying amounts of energy is forcing the phenyl ring rotations around the triple bonds. This is guiding the formation of the different polymorphic structures of **OPE-C_{18}-1**, with different supramolecular interactions. Next, we calculated the amount of energy required to distort **OPE-C_{18}-1** from its original stacking position. Various interactions, namely, the H-bonding, C–H···π, C–H···O, and van der Waals interactions, exist.

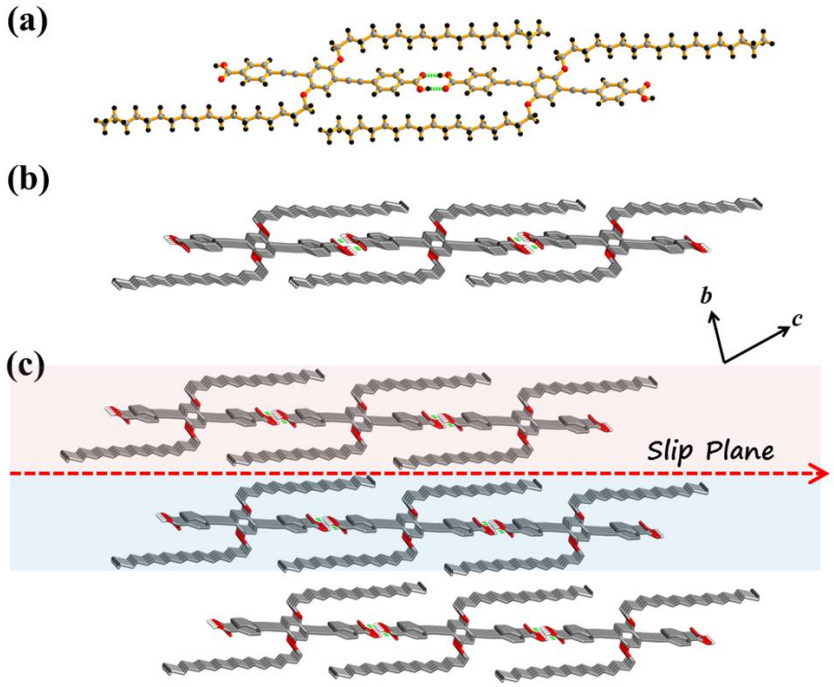

Figure 5. Structural representation of **OPEC_{18}-1″** showing the generation of (a) 1D coordination chain of **OPE-C_{18}-1″**extended via strong hydrogen bonding, (b) View of the 2D supramolecular packing of **OPE-C_{18}-1″** extended via C–H···π interactions and (c) extension of structure into 3D via van der Waals interaction of octadecyl chains of adjacent 2D layers.

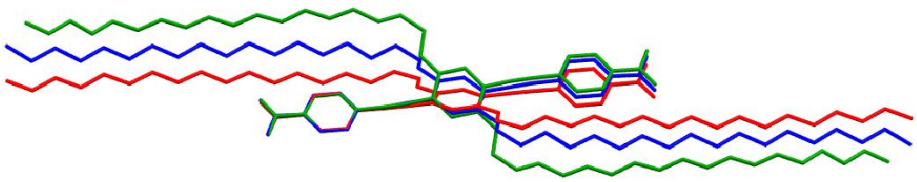

Figure 6. Overlay image of **OPE-C_{18}-1** (red), **OPE-C_{18}-1′** (green) and **OPE-C_{18}-1″** (blue) showing the change in dihedral angle (28.2° (red), 6.1° (green) and 22.1° (blue)) with variance in temperature (One terminal phenyl ring is fixed within the same coordinates to visualize the change in position of the other part of the molecule).

Table 2. Phase sequence transition temperatures (in K) and the associated transition enthalpy ΔH (in kJ/mol), shown in parentheses, for **OPE-C_{18}-1**.

Phase	T (K) (ΔH (kJ/mol)) ⟶ ⟵ T (K) (ΔH (kJ/mol))	Phase
OPE-C_{18}-1′	**123 (6.5)** ⟶ ⟵ 126 (6.0)	OPE-C_{18}-1
OPE-C_{18}-1	373 (5.4) ⟶ ⟵ 353 (2.1)	OPE-C_{18}-1″
OPE-C_{18}-1″	469 (8.0) ⟶ ⟵ 441 (5.0)	OPE-C_{18}-1_{LC}
OPE-C_{18}-1_{LC}	500 (6.4) ⟶ ⟵ 485 (6.1)	OPE-C_{18}-1″

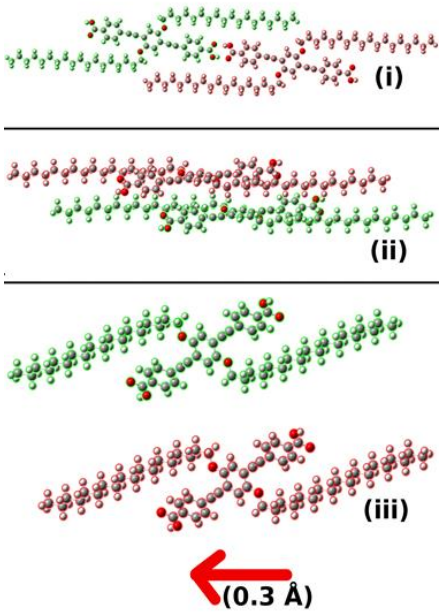

Figure 7. Molecular pairs in (i) H-bonding direction (ii) C–H···π and C–H···O interaction direction and (iii) weak van der Waals interaction direction. The green molecules are fixed and the red molecules are moved by 0.3 Å along the red arrow direction.

To understand contributions from each of these interactions, we considered a molecular dimer pair for the ease of theoretical studies and calculated their interaction energies. Subsequently, we moved one dimer with respect to another by a distance of 0.3 Å along the direction of the respective planes and calculated the energy required for this distortion (Figure 7). From this calculation, it was very clear that, although the number of interacting atoms are more in the molecular dimer pairs along C−H···π and C−H···O direction, the energy required to distort the pairs is maximum along the O−H···O H-bonding direction. In fact, we gain 0.24 eV in energy by moving the molecular pair along C−H···π and C− H···O direction (Table 3). This observation suggests that the H-bonding direction is the most rigid and directional plane present in the crystal, which compares well with the experimental observations. Also, there is negligible interaction between alkyl chains of adjacent 2D sheets showing that van der Waals interaction strength is minimal in **OPE-C_{18}-1**.

Table 3. Energy required to distort an individual non-covalent interaction of the pair of molecules along different directions.

Interactions between molecular pairs along the plane	**Relative energy (eV)**	**Energy required to distort the pairs (eV)**
O–H···O bonding	1.23	0.41
C–H···π, C–H···O	0	-0.24
Weak van der Waals interaction	2.48	0.00

2A.3.3. Liquid Crystallinity in OPE-C_{18}-1

As discussed previously, **OPE-C_{18}-1** is thermally stable up to 530 K. After the polymorphic phase at 373 K, the DSC profile of **OPE-C_{18}-1** shows additional exothermic peaks at 469 and 500 K (Figure 2b). The enthalpy values suggested the possibility of the existence of a liquid crystalline phase. POM textural analysis within this temperature range revealed the existence of textures characteristic to columnar liquid crystalline (LC) phases of **OPE-C_{18}-1** (**OPE-C_{18}-1_{LC}**) (Figure 8). It is clearly seen that the LC texture appears at 469 K and starts to disappear at 498 K, transforming into the isotropic liquid phase. The combination of the optical textural pattern, shear test while observing under the polarizing microscope, DSC enthalpy, and diffuse peak seen in the wide angle region of the X-ray diffraction (XRD) scan (vide infra) confirmed this phase to be liquid crystal-

like. A number of sharp peaks are seen in the XRD scan (Figure 9) obtained at 473 and 497 K. These can be indexed to a columnar phase with a 2D rectangular lattice (Table 4). The reflections, highlighted as 9 and 11 in the plot, are resolved to a sharp peak plus a diffuse peak. The sharp peak is associated with the diffuse peak. This diffuse peak arises due to a packing of the molecular cores within the column. Upon correlating the XRD with the structural information, the nature of the molecular arrangement in the LC phase can be extracted. The (01) peak with the d-spacing of 2.74 nm (Figure 9) is associated with the repeat distance of carboxylates of the two adjacent OPE 1D chains; this spacing corresponds to length of the discs.

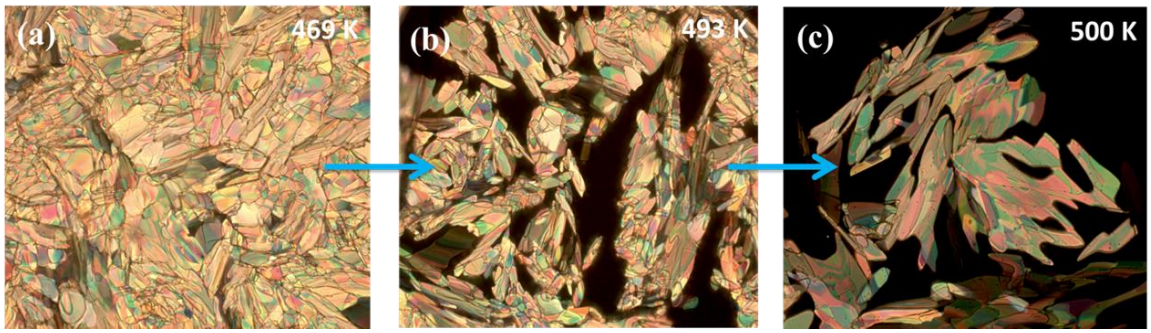

Figure 8. POM textures of **OPE-C_{18}-1** at different temperatures: (a) At 469 K, (b) At 493 K showing pattern characteristic of columnar phase and (c) At 500 K in the region of transition from the birefringent columnar to the isotropic liquid phase.

Four adjacent 1D chains are found to make up the breadth (16.13 Å) of the discs as evidenced by the (10) peak. This is a multiple of 4 times the diffuse peak (40), which makes up the plane containing the weakened C−H···π and C−H···O interactions. The discs are further stacked in a rectangular arrangement, interacting via oxyoctadecyl side chains in the (05) plane to generate a columnar structure (Scheme 3). Upon increase in temperature, the alkyl chains melt and form a disordered region around the OPE cores. This induces mobility in the system while the hydrogen bonded 1D chain and weakened C−H···π, C−H···O interactions maintain rigidity of the entire system.

It is also interesting to note that in addition to the broad diffuse peak centered around 0.5 nm, there is another, sharper, peak with a spacing of 0.4 nm that does not have its origin from the lattice structure. We associate this to be arising from the packing of the molecular cores within the column, a feature commonly observed with columnar structure from disc-like molecules. These features impart the LC character to the phase.

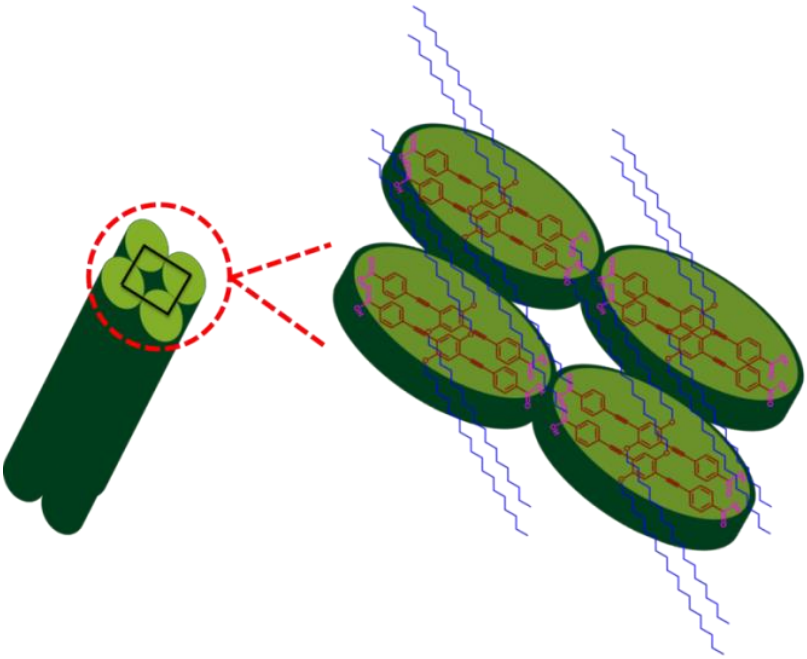

Scheme 3. Schematic showing the generation of columnar rectangular LC phase (**OPE-C_{18}-1_{LC}**) of **OPE-C_{18}-1**.

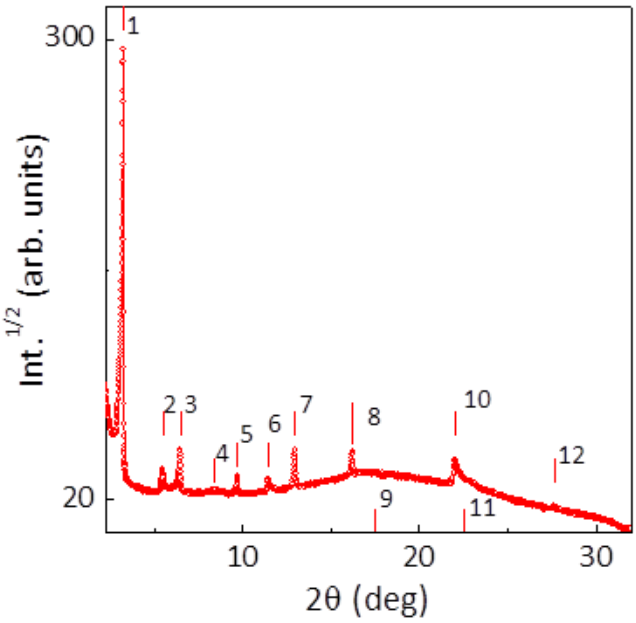

Figure 9. XRD profile of **OPE-C_{18}-1** at 224 ^{o}C. Peaks numbered as 9 and 11 are diffuse peaks arising because of liquid like ordering of alkyl chain, central core-core packing. The spacing of the other sharp peaks get indexed to a two dimensional rectangular lattice.

Table 4. The results of (hk) indexation of XRD profile at a given temperature (T) of mesophases.

T (°C) / Phase		d_{meas} (Å)	d_{calc} (Å)	(hk)	Lattice parameters (Å), lattice area S (Å^2), Lattice volume V (Å^3), Number of molecules in a unit cell Z
T=224°C /Colr	1	27.39	27.37	01	a_R =16.14 Å; b_R = 27.39 Å; S=442.1 Å^2; V = 1748.7; Z = 1.2
	2	16.14	16.17	10	
	3	13.70	13.70	02	
	4	10.50	10.44	12	
	5	9.12	9.13	03	
	6	7.73	7.74	21	
	7	6.84	6.85	04	
	8	5.47	5.48	05	
diffuse	9	4.92			
	10	4.03	4.03	40	
diffuse	11	3.96			
	12	3.23	3.23	50	
		d_{meas} (Å)	d_{calc} (Å)	(hk)	
T=200°C / Colr	1	27.06	27.06	01	a_R =16.02 Å; b_R = 27.06 Å; S=433.4 Å^2; V = 1704.0; Z = 1.1
	2	16.02	16.02	10	
	3	13.55	13.53	02	
	4	10.47	10.34	12	
	5	9.02	9.02	03	
	6	7.73	7.68	21	
	7	6.77	6.76	04	
	8	5.41	5.41	05	
diffuse	9	4.90			
	10	4.00	4.00	40	
diffuse	11	3.93			
	12	3.21	3.20	50	

2A.3.4. Photoluminescence and Mechanochromism in OPE-C_{18}-1

The π-conjugation present in **OPE-C_{18}-1** led us to explore its photoluminescence property. In THF solution, it absorbs at 320 and 380 nm and fluoresces at 450 nm (Figure 10). This solution state photoluminescence behavior points to the involvement of monomers of **OPE-C_{18}-1**. DFT calculations reveal the existence of both HOMO and LUMO states on the single molecule of **OPE-C_{18}-1** (Figure 11c), with respective energies of −4.32 and −2.10 eV, leading to a band gap of 2.22 eV. In the solid state, **OPE-C_{18}-1** absorbs at 440 nm and emits at 485 nm upon excitation at 430 nm (Figures 11a,b). In the solid state, the bands are red-shifted. This can be attributed to solid-state aggregation behavior of **OPE-C_{18}-1**.[34] This behavior remains intact in the mesophase **OPE-C_{18}-1_{LC}**. When **OPE-C_{18}-1_{LC}** was excited at 430 nm at both 473 and 493 K, it revealed an emission maximum at 485 nm at both the temperatures (Figure 12).

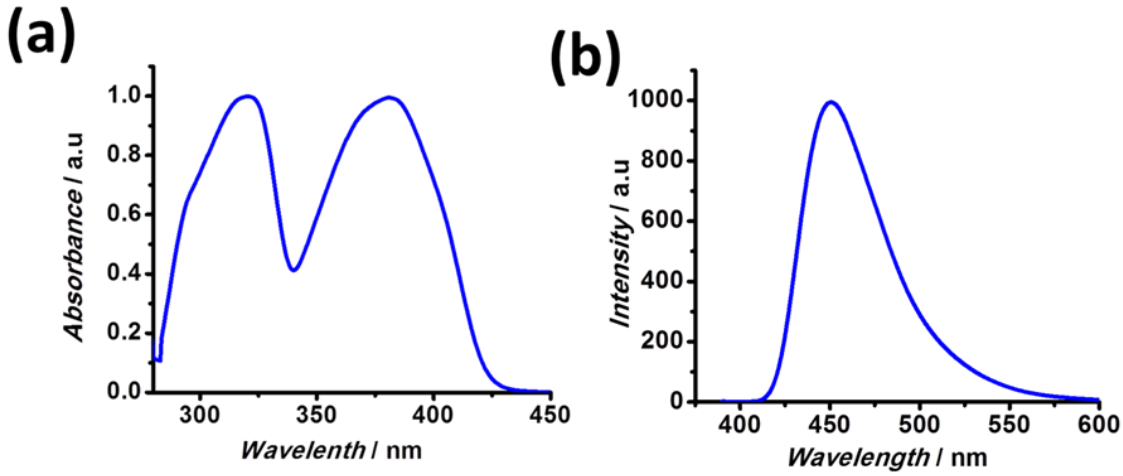

Figure 10. (a) UV and (b) PL of **OPE-C_{18}-1** in THF solution upon excitation at 380 nm.

The spectra were similar to the one collected at room temperature (**OPE-C_{18}-1**). The existence of complementary strong and weak interactions in **OPE-C_{18}-1** prompted us to check further for any change in luminescence upon application of external stimulus (Figure 13). When single crystals of **OPE-C_{18}-1** were ground for 60 s in a mortar, an instant change in color from green to cyan was observed (Figure 13a). Both UV and PL profiles confirmed mechanochromic luminescence (ML) (Figure 13b, 14). UV profile of the ground crystals are more broadened. The absorption maximum also appears blue-shifted by 7 nm, indicating change in the absorption behavior upon grinding. The PL profile further confirmed the ML change (Figure 13b). Here also, the emission profile of the ground film offered a broadened profile encompassing the blue and cyan region of spectrum along with a hypsochromic shift of 5 nm. We believe that upon grinding, the supramolecular organization of **OPEC_{18}-1** fragments to give rise to monomeric and oligomeric states. The contributions from these new states give rise to the shift and broadening of the spectrum.

This behavior was checked for reversibility by allowing it to stand for 1 h (a) at room temperature (~25 °C) and (b) at 60 °C. In neither case, a reversal to the original emission color was observed, establishing the nonreversibility of the ML. We then investigated the ML of the system theoretically. For this purpose, we performed the DFT calculation using SIESTA, where the imaginary part of the dielectric function was calculated. Using this parameter, the optical absorption spectra of the system was determined.

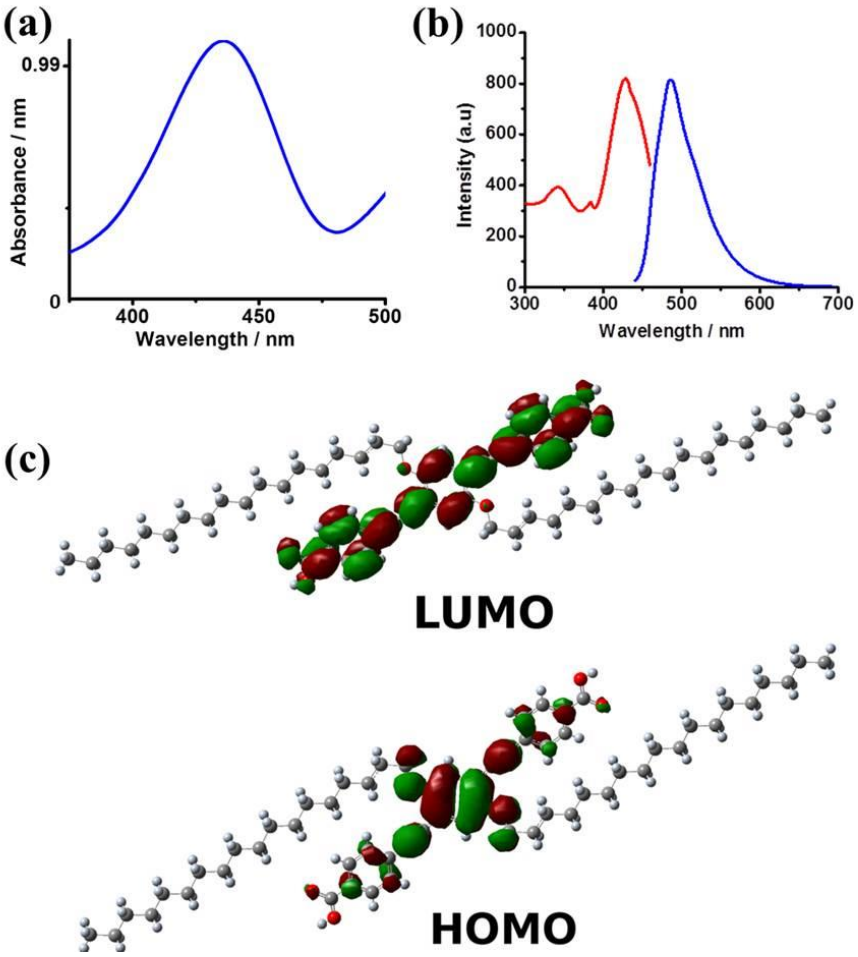

Figure 11. **OPE-C_{18}-1** solid state (a) UV and (b) Emission spectrum (blue) and excitation spectrum (red), (c) Figure showing HOMO and LUMO energy states of **OPE-C_{18}-1**.

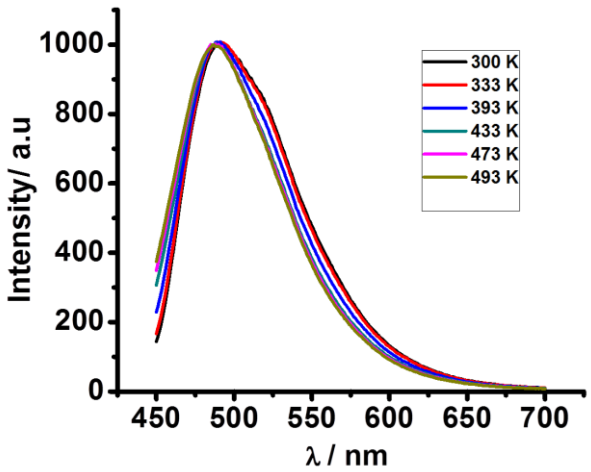

Figure 12. Temperature dependent PL spectra of **OPE-C_{18}-1** spanning the range 300-493 K.

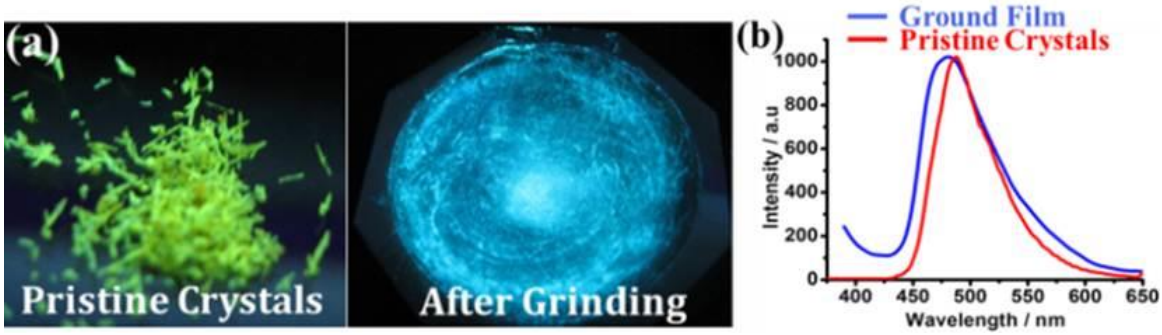

Figure 13. (a) Images of the associated color change on grinding **OPE-C_{18}-1** and (b) PL profile of **OPE-C_{18}-1** single crystal and ground film indicating broadness and hypsochromic peak shift after grinding.

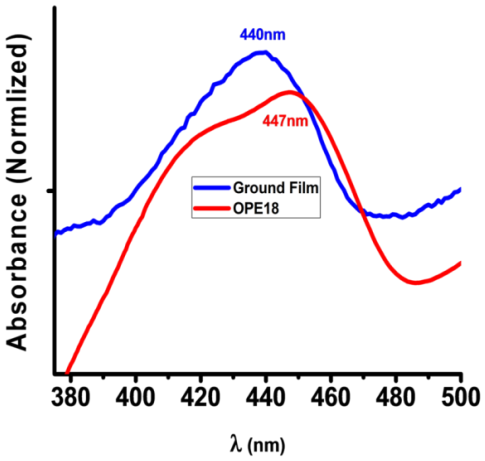

Figure 14. UV profiles of **OPE-C_{18}-1** single crystal and ground film.

As described in the previous paragraphs, experiments show that, with grinding, a broadening of absorption spectra occurs along with the absorption maxima shift to a lower wavelength (blue shift) by ~7 nm. It was predicted that the movement of one C−H···π plane over another leads to this shift. Theoretically, we took into account the C−H···π and C−H···O interactions among varying pairs of molecules, from dimer to tetramer. For all the systems, the C−H···π and C−H···O interactions between various pairs were disrupted and the optical absorption spectra for all the systems were obtained (Figures 15a,b). We found that λ_{max} of the regular tetramer shows a shift of 12 nm, and a similar shift of 5 nm for the dimer is in good agreement with experiments. In fact, upon plotting the wave functions, we found that the disruption in the C−H···π and C−H···O interaction leads to the blue shift of the absorption spectra, but the change is not much. It was also found that the transition always is of the π to π* type and occurs within a single

molecular unit. Consequently, disruption in the C–H···π and C–H···O interactions does not change the origin of the transition.

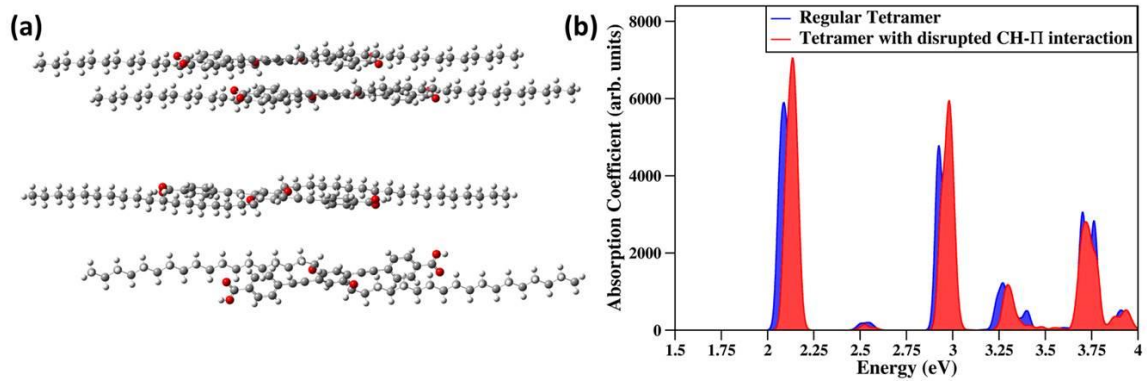

Figure 15. (a) Figure showing the breakage performed of C–H···π and C–H···O interactions between two pairs of dimers of **OPE-C_{18}-1** for theoretical calculations and (b) Theoretically calculated absorption spectra of the molecular pair with perfect C–H···π and C–H···O interactions (blue) and with disrupted C-H···π interaction (red).

2A.3.5. Nanoindentation of OPE-C_{18}-1 Single Crystal Faces

Face indexing of the **OPE-C_{18}-1** single crystals revealed three main faces of the needle shaped crystal: the broad face (001), side narrow face (043), and the top face (341) (Figures 16 and 17a, b).

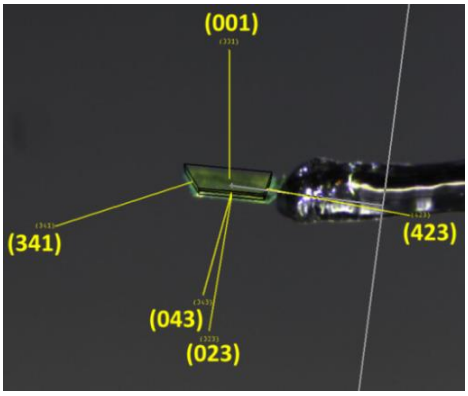

Figure 16. Face index analysis of **OPE-C_{18}-1** based on single crystal x-ray crystallography.

The dimensions of two faces [(001) and (043)] were found sufficient in size for the nanoindentation experiments, which were performed on firmly mounted crystals using a Berkovitch tip with loading/ unloading rate of 100 μN/ s and peak load of 500 μN. Representative load, P, versus depth of penetration, h, responses on the two faces of the

crystal are displayed in Figure 17c. The P−h response obtained on (001) face is serrated, with discrete displacement bursts of the size of ~5 nm occurring at regular intervals; the P−h response of (043) face is smooth. The serrations in the P−h curves observed on (001) imply intermittent plastic flow and the magnitude of the displacement jump can be related to the integral multiples of the inter-planar spacing of the (001) plane.[35] In contrast, the P−h response obtained on (043) are smooth, indicating homogeneous plasticity. The P−h curves were utilized to extract E and H for the respective orientations by using the standard Oliver−Pharr method for extracting those properties. They are 5.63 ± 0.21 GPa and 400 ± 23 MPa, respectively, for (001) and 4.74 ± 0.26 GPa and 171 ± 18 MPa for (043). These data indicate that the mechanical response of the crystal, when measured on (001), is considerably stiffer (~19%) and harder (~134%) than that of (043). The soft and smooth plastic deformation behavior of (043) indicates the presence of favorably oriented slip planes for indentation on this plane, which allow for relatively easy shear sliding of the molecular planes past each other due to the applied force. The AFM images of the indentation area in both the faces also comply with the above results (Figure 17 d,e). The AFM images of the indenter impression on the crystal surface does not show any pile up in the radial or oblique direction, indicating plasticity of the indented faces. Structural origins for the observed anisotropy in plasticity were sought through the examination of the crystal structure of **OPE-C_{18}-1**. We saw that the (001) plane contains the hydrogen bonding interactions between two successive molecular units (Figure 18), which resist easy sliding of the planes. This is possibly the reason for the observed serrations, which are a result of the intermittent shear sliding of the hydrogen bonded planes. By contrast, the (043) plane passes through octadecyl alkyl chains, which makes an angle of approximately 90° with the slip planes (Figure 18). So any indentation along this face would result in smooth and easy slippage of these planes, which leads to the observed low H. From these observations, we propose that strong interaction (O−H···O H-bonding) showing pop-in signatures in the P−h curve exist along the broad face of the crystal (001), whereas a weak interaction with possible slip planes exists along the perpendicular (043), i.e., the side face of the crystal. Thus, from nanoindentation, we were able to identify two possible interactions of different energy leading to the existence of complementary slip planes and planes containing stronger interactions (Figure 18). The liquid crystalline property also arises due to the interplay of strong and weak interactions. The weak interactions break readily, leading to a loss in positional order while the strong interactions hold the orientational order of the entire system. The existence of slip planes

indicated by the nanoindentation results shows that higher temperatures provide sufficient energy to break the interaction contained in the (043) plane. Upon further increase in temperature, a melting of alkyl chains occurs around the molecular packing, and the slip planes glide to show liquid crystalline property. Nanoindentation experiments also helped us to explain the ML. It was seen earlier that the existence of the slip planes within the crystal structure could potentially give rise to ML (Figure 1e).[35]

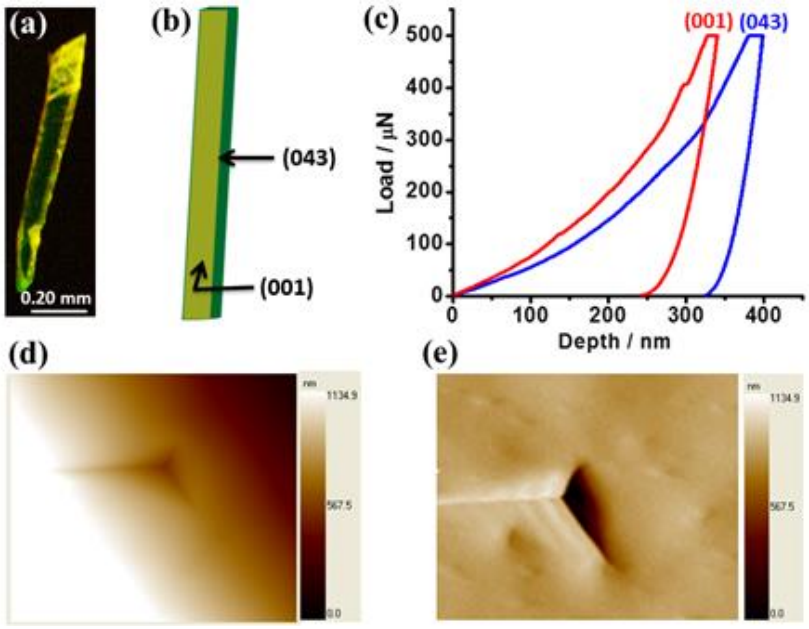

Figure 17. Optical micrographs showing (a) **OPE-C_{18}-1** single crystal, (b) Schematic showing the habit planes with the face indices, (c) Representative load vs. penetration depth curves obtained during the nanoindentation on (001) face (red) and (043) face (blue) of the single crystals, (d,e) Phase AFM images, representation of the indentation area of (001) and (043) faces, respectively.

We envisage that the movements of slip planes containing the weaker C–H···π, C–H···O, and van der Waals interactions are responsible for this phenomenon. Upon application of mechanical pressure, the energy is sufficient to break these weak interactions and, as a result, this plane can glide, giving rise to ML. It is possible that the hypsochromic shift arises due to monomeric and oligomeric contributions. This creates a new crystal phase having a high density of defects. The elastic energy at this point is not sufficient enough to bring the crystal back to its original state, causing an irreversible change in the luminescent property. The non-reversibility is further supported by the large residual penetration depth of 250 nm upon unloading (Figure 17c). This means that upon the

withdrawal of mechanical force, the planes are reluctant to resume the original position and will stay in its new more preferred stable state. Thus, with the aid of nanoindentation, we can offer a quantitative explanation for both liquid crystallinity as well as irreversible ML.

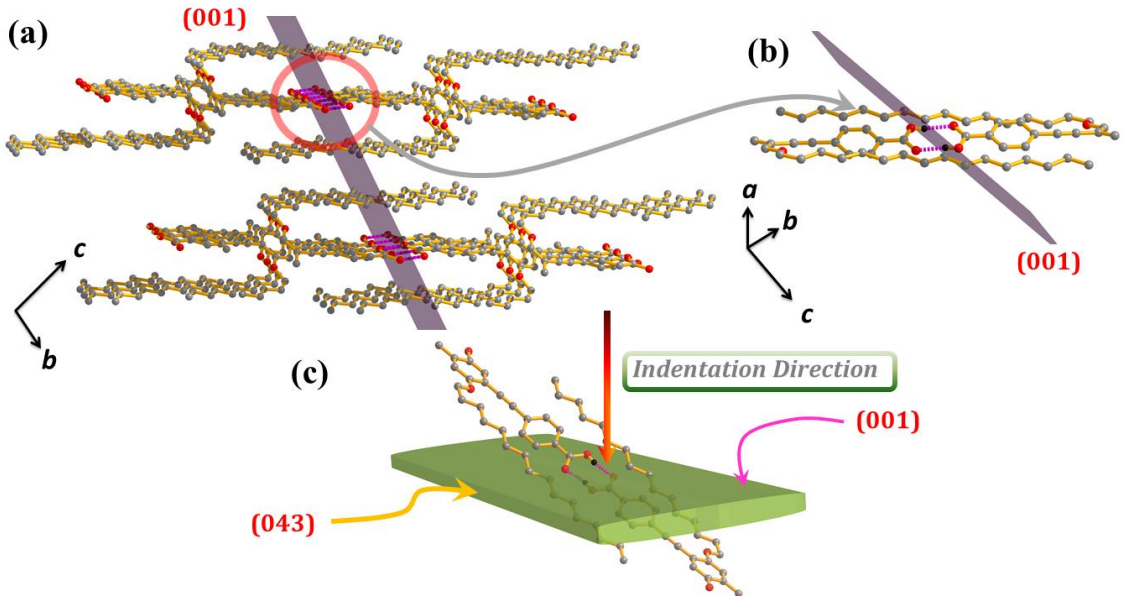

Figure 18. Structure property correlation of **OPE-C_{18}-1** broad face (001) and the side face (043): (a) Image showing the position of the (001) plane in the crystal packing, (b) Magnified image of (a) Showing that the (001) and parallel planes contain the O–H···O H-bonding interaction and (c) Image showing the direction of indentation and the plane lying perpendicular to it.

2A.4. Conclusion

In conclusion, this chapter demonstrated the design, synthesis and characterization of an organic bola-amphiphilic chromophoric π system **OPE-C_{18}-1**, which showed reversible temperature-dependent polymorphism, thermotropic liquid crystallinity, and mechanochromic luminescence. To the best of our knowledge, this is the first study of the simultaneous existence of all the three properties in the same system. The targeted molecular design allowed the concurrent existence of strong and weak non-covalent interactions in **OPE-C_{18}-1**, which led to the occurrence of such properties. The structures of all three polymorphs were explained in detail via SCXRD and backed up with DFT calculations. The LC property was also thoroughly characterized via XRD, POM, and DSC experiments. The stimuli-responsive luminescence behavior was then studied and

elucidated via nanoindentation. Theoretical insights into the interactions present in the system also shed light on the manifestation of such a property. The work reported in this chapter will guide the design of multifunctional materials of practical importance based on a molecular tectonics approach.

2A.5. References

1 X. Yan, F. Wang, B. Zheng and Huang, F. *Chem. Soc. Rev.,* 2012, **41**, 6042.

2 (a) M. W. Hosseini, *Acc. Chem. Res.,* 2005, **38**, 313; (b) J. D. Wuest, *Chem. Commun.,* 2005, 5830.

3 (a) P. Dechambenoit, S. Ferlay, M. W. Hosseini and N. Kyritsakas, *Chem. Commun.* **2007**, 4626; (b) B. Moulton and M. J. Zaworotko, *Chem. Rev,*. 2001, **101**, 1629; (c) D. Das, E. Engel and L. J. Barbour, *Chem. Commun.,* 2010, **46,** 1676.

4 (a) N. Saito, K. Kanie, M. Matsubara, A. Muramatsu and M. Yamaguchi, *J. Am. Chem. Soc.,* 2015, **137**, 6594; (b) T. Ube and T. Ikeda, *Angew. Chem. Int. Ed.,* 2014, **53**, 10290; (c) J. R. Cox, J. H. Simpson and T. M. Swager *J. Am. Chem. Soc.,* 2013, **135**, 640.

5 Z. He, L. Zhang, J. Mei, T. Zhang, J. W. Y. Lam, Z. Shuai, Y. Q. Dong and B. Z. Tang, *Chem. Mater.,* 2015, **27**, 6601.

6 (a) Y. Sagara and T. Kato, *Angew. Chem. Int. Ed.,* 2011, **50**, 9128; (b) B. R. Kaafarani, *Chem. Mater.,* 2011, **23**, 378; (c) C. Weder, C. Sarwa, A. Montali, C. Bastiaansen and P. Smith, *Science,* 1998, **279**, 835; (d) R. H. Chen, *Liquid Crystal Displays: Fundamental Physics and Technology*; Wiley-VCH: Hoboken, NJ, 2011.

7 (a) M. Kinami, B. R. Crenshaw and C. Weder, *Chem. Mater.,* 2006, **18**, 946; (b) J. N. Palasagaram and R. Ramadoss, *IEEE Sens. J.,* 2006, **6**, 1374.

8 (a) C. Tschierske, *Angew. Chem. Int. Ed.,* 2013, **52**, 8828; (b) C. Tschierske, *Chem. Soc. Rev.,* 2007, **36**, 1930; (c) P. Vemula, U. Aslam, A. Mallia and G. John, *Chem Mater.,* 2007, **19**, 5203.

9 (a) G. R. Desiraju, *Angew. Chem. Int. Ed.,* 2007, **46**, 8342; (b) G. R. Desiraju, *J. Am. Chem. Soc.,* 2013, **135**, 9952.

10 M. Yoshio, T. Kagata, K. Hoshino, T. Mukai, H. Ohno and T. Kato, *J. Am. Chem. Soc.,* 2006, **128**, 5570.

11 M. Krikorian, S. Liu and T. M. Swager, *J. Am. Chem. Soc.,* 2014, **136**, 2952.

12 M. J. Hollamby, M. Karny, P. H. H. Bomans, N. A. J. M. Sommerdjik, A. Saeki, S. Seki, H. Minamikawa, I. Grillo, B. R. Pauw and P. Brown, *Nat. Chem.,* 2014, **6**, 690.

13 U. H. F. Bunz, *Macromol. Rapid Commun.,* 2009, **30**, 772.

14 (a) Y. Gong, Y. Zhang, W. Z. Yuan, J. Z. Sun and Y. Zhang, *J. Phys. Chem. C,* 2014, **118**, 10998; (b) Y. Q. Dong, J. W. Y. Lam and B. Z. Tang, *J. Phys. Chem. Lett.,* 2015, **6**, 3429.

15 U. Ramamurty and J.-i. Jang, *CrystEngComm.,* 2014, **16**, 12.

16 S. Varughese, M. S. R. N. Kiran, U. Ramamurty and G. R. Desiraju, *Angew. Chem. Int. Ed.,* 2013, **52**, 2701.

17 Gaussian 09, Revision D.01, M. J. Frisch, G. W. Trucks, H. B. Schlegel, G. E. Scuseria, M. A. Robb, J. R. Cheeseman, G. Scalmani, V. Barone, B. Mennucci, G. A. Petersson, H. Nakatsuji, M. Caricato, X. Li, H. P. Hratchian, A. F. Izmaylov, J. Bloino, G. Zheng, J. L. Sonnenberg, M. Hada, M. Ehara, K. Toyota, R. Fukuda, J. Hasegawa, M. Ishida, T. Nakajima, Y. Honda, O. Kitao, H. Nakai, T. Vreven, J. A. Montgomery, Jr., J. E. Peralta, F. Ogliaro, M. Bearpark, J. J. Heyd, E. Brothers, K. N. Kudin, V. N. Staroverov, J. Kobayashi, K. Normand, A. Raghavachari, J. C. Rendell, S. S. Burant, J. Iyengar, M. Tomasi, R. Cossi, N. Rega, J. M. Millam, M. Klene, J. E. Knox, J. B. Cross, V. Bakken, C. Adamo, J. Jaramillo, R. Gomperts, R. E. Stratmann, O. Yazyev, A. J. Austin, R. Cammi, C. Pomelli, J. W. Ochterski, R. L. Martin, K. Morokuma, V. G. Zakrzewski, G. A. Voth, P. Salvador, J. J. Dannenberg, S. Dapprich, A. D. Daniels, Ö. Farkas, J. B. Foresman, J. V. Ortiz, J. Cioslowski and D. J. Fox, Gaussian, Inc., Wallingford CT, 2009.

18 (a) J.-D. Chai and M. Head-Gordon, *Phys. Chem. Chem. Phys.,* 2008, **10**, 6615; (b) J.-D Chai and M. J. Head-Gordon, *Chem. Phys.*, 2008, **8**, 84106.

19 J. M. Soler, E. Artacho, J.D. Gale, A. García, J. Junquera, P. Ordejón and D. Sánchez-Portal, *J. Phys.: Condens. Matter.*, 2002, **14**, 2745.

20 K. Burke, J. P. Perdew and M. Ernzerhof, *Int. J. Quantum Chem.,* 1997, **61**, 287.

21 N. Troullier and J. L. Martins, *Phys. Rev. B: Condens. Mater. Mater. Phys.,* 1991, **43**, 1993.

22 L. Kleinman and D. Bylander, *Phys. Rev. Lett.,* 1982, **48**, 1425.

23 S. V. a. SMART (V 5.628), XPREP, SHELXTL; Bruker AXS Inc. Madison, Wisconsin, USA, 2004.

24 G. M. Sheldrick, SADABS, Empirical Absorption Correction Program. University of Göttingen, Göttingen, 1997.

25 A. Altomare, G. Cascarano, C. Giacovazzo and A. Guagliardi, *J. Appl. Crystallogr.*, 1993, **26**, 343.

26 G. M. Sheldrick, SHELXL 97, Program for the Solution of Crystal Structure, University of Göttingen, Germany, 1997.

27 L. Farrugia, *J. Appl. Crystallogr.*, 1999, **32**, 837.

28 (a) S. Roy, V. M. Suresh and T. K. Maji, *Chem. Sci.,* 2016, **7**, 2251; (b) V. M. Suresh, S. J. George and T. K. Maji, *Adv. Funct. Mater.*, 2013, **23**, 5585.

29 (a) N. V. Harris, S. Christopher and B. Keith, Synlett, 1990, 577; (b) S. Chakraborty, S. G. Ramkumar, S. Ramakrishnan, *Macromolecules*, 2017, **50**, 5004; (c) P. K. Lo and H. F. Sleiman, *J. Am. Chem. Soc*., 2009, **131**, 4182; (d) M. Sankarapillai, T. Rajasekaran, Y. Shiki, K. Akihide and A. Ayyappanpillai, *Chem. Commun*., 2009, **40**, 5984.

30 G. R. Desiraju, *Cryst. Growth Des.,* 2011, **11**, 896.

31 G. R. Desiraju, *Acc. Chem. Res.,* 2002, **35**, 565.

32 (a) M. J. Plevin, D. L. Bryce and J. Boisbouvier, *Nat. Chem.,* 2010, **2**, 466; (b) M. Nishio, *CrystEngComm,* 2004, **6**, 130.

33 (a) G. R. Desiraju, *Acc. Chem. Res.,* 1996, **29**, 441; (b) G. R. Desiraju, *Chem. Commun.,* 2005, 2995.

34 (a) L. T. Liu, D. Yaron, M. I. Sluch and M. A. Berg, *J. Phys. Chem. B,* 2006, **110**, 18844; (b) Y. Wang, A. J. Zappas II, J. N. Wilson, I-B. Kim, K. M. Solntsev, L. M. Tolbert and U. H. F. Bunz, *Macromolecules*, 2008, **41**, 1112.

35 (a) G. R. Krishna, M. S. R. N. Kiran, C. L. Fraser, U. Ramamurty and C. M. Reddy, *Adv. Funct. Mater.,* 2013, **23**, 1422; (b) M. K. Mishra, G. R. Desiraju, U. Ramamurty and A. D. Bond, *Angew. Chem. Int. Ed.,* 2014, **53**, 13102.

Chapter 2B

Tunable Physical States of a Bola-amphiphilic π-system Assisted by Functional Group Design

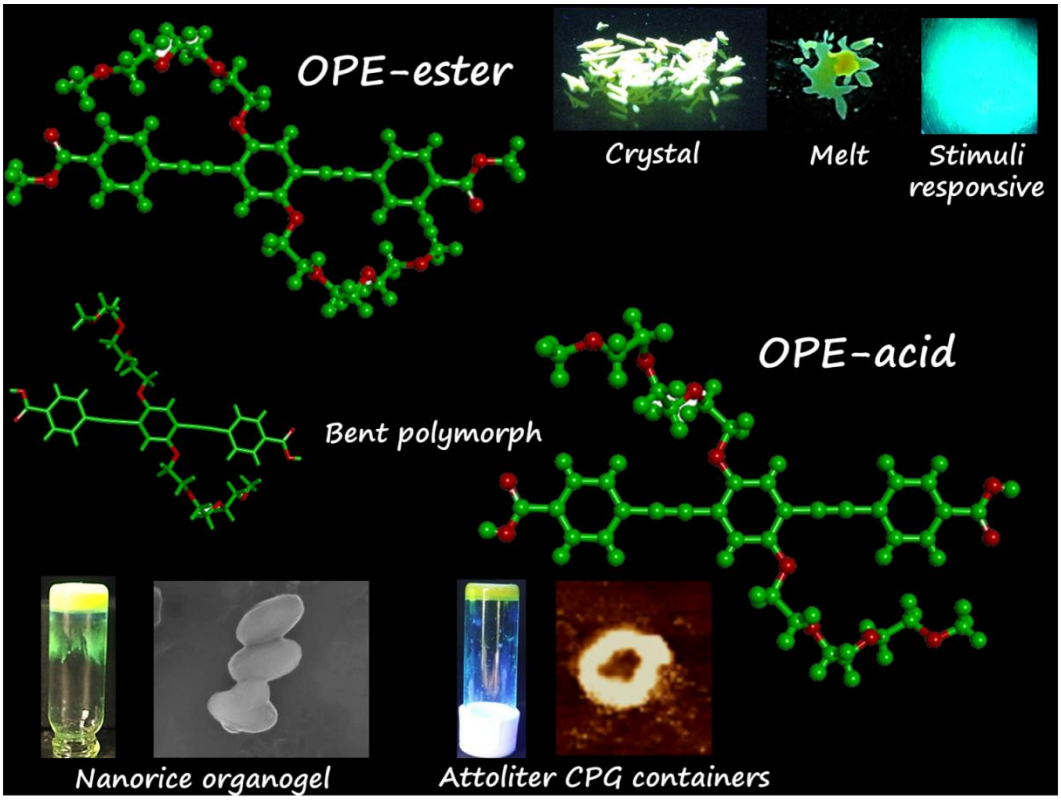

Summary

Structural understanding and correlation of physical properties of π-systems can lead to improved design strategies for opto-electronic materials. In this chapter, we demonstrate via single crystal x-ray diffraction analysis, how end groups (ester and acid) of bola-amphiphilic *oligo*-(*p*-phenyleneethynylenes) (OPEs) lead to selective polymorphism and mechanochromic luminescence in **OPE-C_{gly}-E** and **OPE-C_{gly}-A**. **OPE-C_{gly}-E** and **OPE-C_{gly}-A** have the same π-conjugated backbones with bis-triethyleneglycol side chains, only differing in having end capped ester and acid groups respectively. **OPE-C_{gly}-E** has a less densely packed structure than **OPE-C_{gly}-A** due to the absence of 1D extension of OPE molecules via O−H···O hydrogen bonding. This leads to exclusive mechanochromic behavior in **OPE-C_{gly}-E** whereas **OPE-C_{gly}-A** generates polymorphic structures which are not present in **OPE-C_{gly}-E**. Unlike **OPE-C_{gly}-E**, terminal carboxylic acid groups in **OPE-C_{gly}-A** also assist in luminescent organogel formation with nanorice like morphology. Ditopic **OPE-C_{gly}-A** was also utilized to coordinate to Cu^{II} to form a coordination polymer gel (CPG) with nano-container like morphology. The nanocontainers possess attoliter volumes in the cavities and hence could be used for miniaturized applications. This work hence delineates the importance of end capped groups in guiding different physical properties in opto-electronically important π-systems.

The work based on this chapter is communicated:

S. Roy, D. Samanta, S. Bhattacharyya, P. Kumar, A. Hazra and T. K. Maji, *Manuscript submitted.*

2B.1. Introduction

Oligo-(*p*-phenyleneethynylenes) (OPEs) are a class of rigid rod like oligomers where phenyl rings are bridged by alkyne groups.[1] Owing to their excellent opto-electrical activity, several OPE based materials such as supramolecular π-systems,[2] organogels,[3] metal-organic frameworks (MOFs)[4] and covalent-organic frameworks (COFs)[5] with varied properties have been reported. Interestingly, the OPE backbone can be further functionalized with several functional groups such as hydrophobic, hydrophilic and metal binding moieties.[6] Such amphiphilic or bola-amphiphilic molecules can also show properties such as liquid crystallinity, mechanochromism, polymorphism, stimuli responsive behavior with applications in security inks, pressure sensors and actuators.[2a,7]Furthermore, self-assembly of such systems in polar or non-polar medium result in versatile nanostructures.[8] OPEs with strategically placed carboxylic acid groups can also act as low molecular weight gelators (LMWGs).[3] Such LMWGs could also act as a linker toward the self-assembly with metal ions to form coordination polymer gels (CPGs).[9] Interestingly, in such hybrid 'soft' materials, metal ion based optical, redox and magnetic properties can be introduced. Furthermore, rigidity and stability of the system can also be enhanced by metal coordination and subsequent nanoscale morphologies of such systems can be further tuned and novel applications can be realized.[4]

In spite of the vast potential of OPEs, only a tiny progress has been made in the structural understanding behind the occurrence of such properties.[10] Recently, it has been revealed that conformational twisting of the OPE backbone leads to variance in emission properties of OPEs in a work by Sharber et al.[11a] The authors derived a correlation between the aggregative packing of fluorinated side chain containing OPEs and how their electronic effects modulate the photoluminescence of a family of such OPEs. Marshall and co-workers have further shown how OPE based linkers translate tunable emissive properties in MOFs based on twisting of the OPE backbone.[11b] However, there still remains little understanding of what type of interactions in OPEs lead to the occurrence of different properties of supramolecular polymers gels and MOFs. Recently, it was reported by our group that introducing complementary strong and weak interactions in OPEs could lead to simultaneous existence of polymorphism, mechanochromism and liquid crystallinity.[2a] It was also seen that tuning the polarity of side chains could result in gelation ability of these OPEs.[3a] Taking inspiration from these studies, we decided to

introduce strong interactions between side chains and vary the end capping groups with and without hydrogen bonding capability and also introduce polarity in the side chains. We conjectured that this would lead to control of physical states and also induce stimuli-responsive properties in the system.

The design strategy therefore involved tinkering with the end groups of π-chromophoric OPEs keeping the side chains uniform to synthesize two new OPEs. Both had triethyleneglycol (TEG) chains on both sides of the backbone but end capping group in one was an ester group (**OPE-C_{gly}-E**), whereas it was an acid group in the other (**OPE-C_{gly}-A**). Directional O-H···O hydrogen bonds between carboxylic acid groups and interdigitation between TEG side chains in **OPE-C_{gly}-A** led to a more rigid structure while **OPE-C_{gly}-E**, devoid of strong hydrogen bonds, showed the existence of slip planes in its structure. This difference in strengths of hydrogen bonds, guided variable physical properties of the two systems. Mechanochromic luminescence (ML) was observed in **OPE-C_{gly}-E**, but not in **OPE-C_{gly}-A**. **OPE-C_{gly}-E** also had a lower melting temperature than **OPE-C_{gly}-A**. DFT calculations also provided insights into the breakage of weak interactions in **OPE-C_{gly}-E** leading to such behavior. Linear hydrogen bonded 1D chains of **OPE-C_{gly}-A** allowed the existence of polymorphic phase transformations while **OPE-C_{gly}-E**, devoid of such interactions showed no polymorphic behavior. **OPE-C_{gly}-A** also showed carboxylic acid assisted luminescent organogel formation with nanorice like morphology. Upon coordination with Cu^{II} metal ion, nanocontainers of OPE based CPGs were obtained, where the morphology could be changed from that of the organogel. These nanocontainers possessed attolitre volumes and this space could be used for miniaturized applications. This chapter therefore shows how differential hydrogen bond strengths, guide the formation of several physical states in supramolecular π-systems.

2B.2. Experimental Section

2B.2.1. Materials

$Pd(PPh_3)_4$, $CuCl_2 \cdot 2H_2O$ and triethyleneglycol monomethyl ether were obtained from Sigma-Aldrich Chemical Co and cuprous iodide was obtained from Loba Chemie Pvt. Ltd. Tetrahydrofuran (THF) were obtained from Spectrochem Pvt. Ltd (Mumbai, India). Tetrahydrofuran was pre-dried using standard procedure and all other reagents, solvents were of reagent grade and used without further purification.

2B.2.2. Physical Measurements

Thermal stability of the **OPE-C_{gly}-E** and **OPE-C_{gly}-A** is analyzed using Mettler Toledo TGA 850 instrument under N_2 atmosphere in the temperature range of 25-500 °C at a heating rate of 3 °C /min. UV–vis spectra were recorded on a Perkin Elmer Model Lambda 900 spectrophotometer. Fluorescence studies were accomplished using Perkin Elmer Ls 55 Luminescence spectrometer. The elemental analyses were carried out using a Thermo Scientific Flash 2000 CHN analyzer. Powder X-ray diffraction studies were recorded on a Bruker D8 discover instrument using Cu-Kα radiation. Morphological studies have been carried out using Lica-S440I Field Emission Scanning Electron Microscope (FESEM) by placing samples on a silicon wafer under high vacuum with an accelerating voltage of 10 kV. Transmission Electron Microscopy (TEM) analysis has been performed using JEOL JEM-3010 with an accelerating voltage at 300 kV. For this analysis the samples were dispersed in ethanol by sonication before drop casting on a carbon-coated copper grid. Energy dispersive spectroscopy (EDS) analysis was performed with an EDAX genesis instrument attached to the FESEM column.

2B.2.3. Computational Details

All the optical and electronic properties have been calculated using Gaussian 09 software.[12] B3LYP exchange correlation functional in combination with 6-31G(d) basis set was utilized for gas-phase geometry optimization in the S_0 electronic state.[13] Time dependant DFT (TD-DFT) computations were used for the excited electronic state calculations.

2B.2.4. Single crystal X-ray Diffraction (SCXRD)

Suitable single crystals of compounds **OPE-C_{gly}-E** and **OPE-C_{gly}-A** were mounted on a thin glass fiber with commercially available super glue. X-ray single crystal structural data were collected on a Bruker D8 VENTURE with Mo-Kα radiation (λ = 0.71073 Å) operating at 50 kV and 1 mA. The data collection was performed at 298 K for **OPE-C_{gly}-E** and **OPE-C_{gly}-A** and 110 K for **OPE-C_{gly}-A′**. The program SAINT[14] was used for the integration of diffraction profiles and absorption correction was made with SADABS[15] program. All the structures were solved by SIR 92[16] and refined by full matrix least square method using SHELXL.[17] All the hydrogen atoms were fixed by HFIX and placed in ideal positions. All crystallographic and structure refinement data of **OPE-C_{gly}-E** and

OPE-C_{gly}-A are summarized in Table 1. All calculations were carried out using SHELXL 97,[17] SHELXS 97[17]and WinGX system, Ver 1.80.05.[18]

2B.2.5. Synthesis of dimethyl 4,4'-(2,5-bis(2-(2-(2-methoxyethoxy)ethoxy)ethoxy)-1,4-phenylene)bis(ethyne-2,1-diyl)dibenzoate (OPE-C_{gly}-E) and 4,4'-(2,5-bis(2-(2-(2-methoxyethoxy)ethoxy)ethoxy)-1,4-phenylene)bis(ethyne-2,1-diyl)dibenzoic acid (OPE-C_{gly}-A).

Step-wise synthetic details for **OPE-C_{gly}-E** and **OPE-C_{gly}-A** are given in Scheme 1. **OPE-C_{gly}-E** was prepared in good yields via the Sonogashira-Hagihara coupling procedure using methyl 4-ethynylbenzoate (**5**) and 1-butoxy-2,5-diiodo-4-(2-methoxyethoxy)benzene (**8**).[3a] Yellow powders of **OPE-C_{gly}-E** were further subjected to a base catalyzed hydrolysis reaction to yield quantitative amounts of yellowish-green powders of **OPE-C_{gly}-A**.

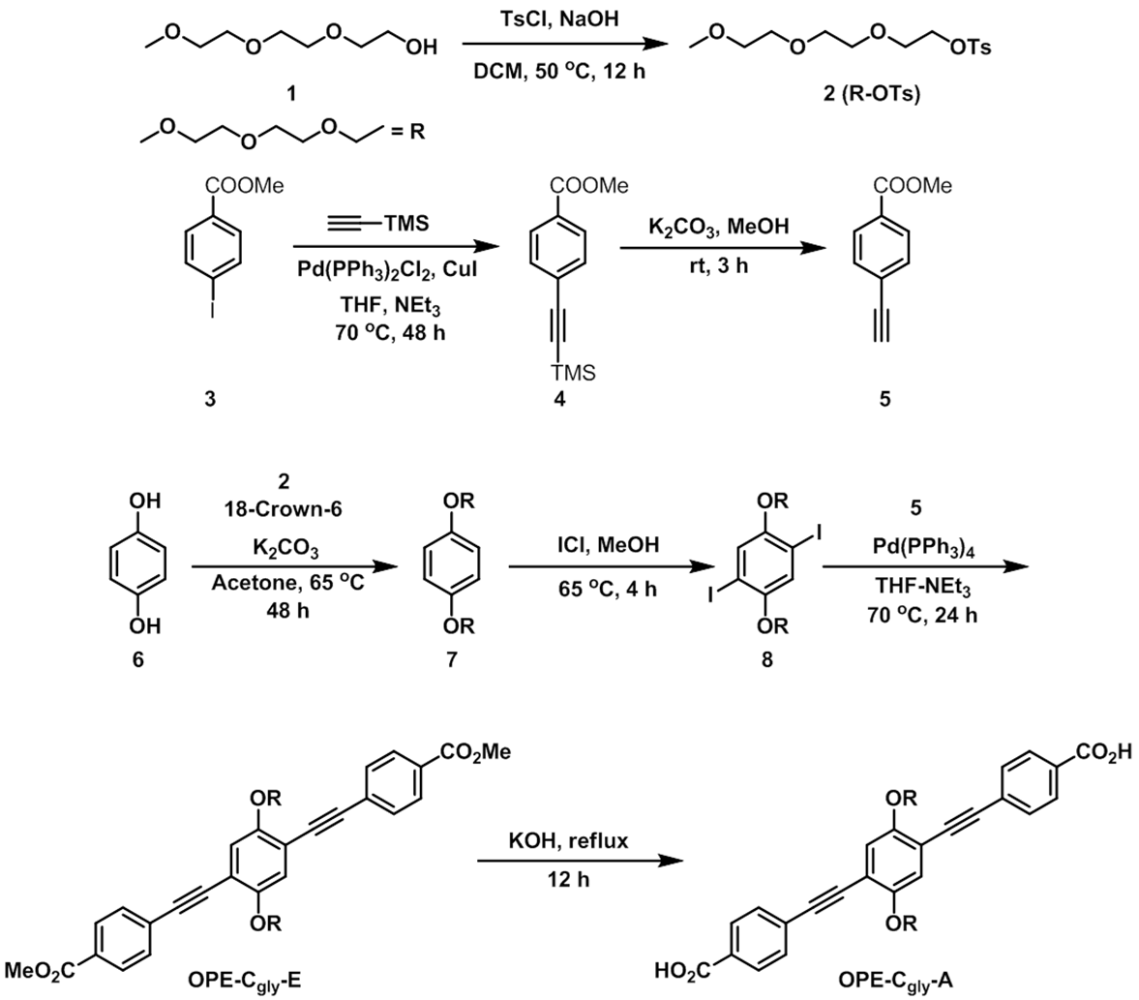

Scheme 1. Synthetic scheme for **OPE-C_{gly}-E** and **OPE-C_{gly}-A**.

General procedure and characterization. Chemical shifts (δ) are indicated in ppm. The following abbreviations were used to illustrate NMR signals: s = singlet, d = doublet, t = triplet, td = triplet of doublets, dd = doublet of doublets, ddd = doublet of doublets of doublets, m = multiplet. Compounds **2-8** were synthesized according to reported procedures.[3,4]

Synthesis of dimethyl 4,4'-(2,5-bis(2-(2-(2-methoxyethoxy)ethoxy)ethoxy)-1,4-phenylene)bis(ethyne-2,1-diyl)dibenzoate (OPE-C_{gly}-E). A sealed tube was loaded with compound **8** (968 mg, 1.48 mmol), **5** (593 mg, 3.70 mmol), $Pd(PPh_3)_4$ (340 mg, 296 μmol), degassed NEt_3 (20 mL) and tetrahydrofuran (60 mL). The resulting solution was kept at 70 °C for 12 h for completion of coupling reaction. Then the reaction mixture was evaporated to dryness and the crude product was subjected for column chromatography (silica gel) using ethyl acetate as eluent to afford **OPE-C_{gly}-E** (660 mg, 918 μmol) as light green solid compound. Yield 62%; ^{1}H NMR (400 MHz, DMSO-d_6) δ = 3.32 (s, 3H), 3.56-3.81 (m, 8H), 4.33 (t, J = 6.5 Hz, 2H), 7.43 (s, 1H), 7.82 (d, J = 7.1 Hz, 2H), 8.26 (d, J = 7.1 Hz, 2H) ppm. ^{13}C NMR (100 MHz, $CDCl_3$, DMSO-d^6) δ = 51.6, 59.4, 68.8, 70.1, 70.2, 70.5, 70.5, 71.7, 84.3, 96.0, 112.4, 118.4, 127.2, 129.6, 129.9, 132.3, 151.4, 166.0 ppm; HRMS-EI (m/z) for $C_{40}H_{46}O_{12}$ [M^+] calcd 718.299, found 718.300; Anal. Calcd. for $C_{40}H_{46}O_{12}$: C, 66.84; H, 6.45. Found: C, 67.03; H, 6.31.

Synthesis of 4,4'-(2,5-bis(2-(2-(2-methoxyethoxy)ethoxy)ethoxy)-1,4-phenylene)bis(ethyne-2,1-diyl)dibenzoic acid (OPE-C_{gly}-A). 20 mL methanolic solution **OPE-C_{gly}-E** (600 mg, 835 μmol) and KOH (819 mg, 14.6 mmol) was taken in a round-bottomed flask equipped with a water condenser and refluxed for 24 h. The resulting solution was added dropwise to an aqueous HCl solution (100 mL, 4 N). The greenish-yellow precipitate was filtered, washed with water and dried under vacuum oven at 60 °C to afford **OPE-C_{gly}-A** (531 mg, 768 μmol) as greenish-yellow solid. Yield 92%; ^{1}H NMR (400 MHz, DMSO-d_6) δ = 3.32 (s, 3H), 3.56-3.81 (m, 8H), 4.33 (t, J = 6.5 Hz, 2H), 7.43 (s, 1H), 7.72 (d, J = 7.1 Hz, 2H), 8.19 (d, J = 7.1 Hz, 2H), 11.81 (s, 1H) ppm. ^{13}C NMR (100 MHz, $CDCl_3$, DMSO-d^6) δ = 59.4, 68.8, 70.1, 70.2, 70.5, 70.5, 71.7, 84.3, 95.6, 112.4, 118.4, 128.0, 130.0, 130.0, 132.3, 151.4, 169.4 ppm; HRMS-EI (m/z) for $C_{38}H_{42}O_{12}$ [M^+] calcd 690.268, found 690.267; Anal. Calcd. for $C_{38}H_{42}O_{12}$: C, 66.08; H, 6.13. Found: C, 66.32; H, 6.49.

The pure compounds were then subjected to crystallization for further studies.

2B.3. Results and Discussion

2B.3.1. Single Crystal Structure of OPE-C_{gly}-E

Orange colored needle like crystals of **OPE-C_{gly}-E** were isolated based on solvent evaporation method by dissolving it in a DCM/methanol mixture. The needle shaped crystals (~1 mm length and 0.5 mm width) allowed determination of single crystal structure. **OPE-C_{gly}-E** crystallized in a triclinic crystal system with a space group of $P\bar{1}$ as determined from SCXRD. The single molecule of **OPE-C_{gly}-E** contains a central rigid core of three phenyl rings connected by alkyne modules (Figure 1a). It is capped by ester groups at the termini. The central phenyl ring in the OPE core is decorated with TEG side chains on both sides resulting in a bola-amphiphilic structure of **OPE-C_{gly}-E**. The dihedral angle between the central phenyl ring and terminal rings containing the ester group was found to be 32°. Due to the inability of terminal ester groups to take part in O−H···O hydrogen bonding interactions, adjacent OPEs are stacked offset to each other assisted by π-π and C−H···O interactions (Figure 1b).[19,20] (C−H···O D−A distance; 2.6 ± 0.1 Å, ∠D−H···A; 145.0 ±1°). Weak C−H···π interactions also exist between the aromatic C−H and π-core of terminal phenyl rings of adjacent OPE molecules (*d*=4.1 Å).[21] The culmination of all these supramolecular interactions lead to the 1D extension of **OPE-C_{gly}-E** with the OPE cores packed in a slightly offset manner along the diagonal of the *ab* plane to maximize these non-covalent interactions (Figure 1c). This arrangement reinforces the proximity of TEG chains in adjacent 1D chains to lead to a 2D extension via interdigitated C−H···O hydrogen bonding interactions between the TEG side chains of 1D chains (D−A distance; 3.1 Å, ∠D−H···A; 143.3°) (Figure 1d). When viewed along the *a*-axis, it is seen that there are minimal non-covalent interactions between adjacent 2D sheets leading to the formation of zipper like slip planes (Figure 1e). Therefore there exists a combination of strong and weak interactions of the bola-amphiphilic cores to lead to an overall 2D packing of **OPE-C_{gly}-E**.

2B.3.2. Single Crystal Structure of OPE-C_{gly}-A

Green needle shaped crystals of **OPE-C_{gly}-A** were isolated upon solvent diffusion of pentane into a THF solution of **OPE-C_{gly}-A**. The needle shaped crystals (~1 mm length and 0.3 mm width) allowed determination of single crystal structure. SCXRD revealed that **OPE-C_{gly}-A** also crystallized in the triclinic crystal system having a space group of $P\bar{1}$. Although the crystal

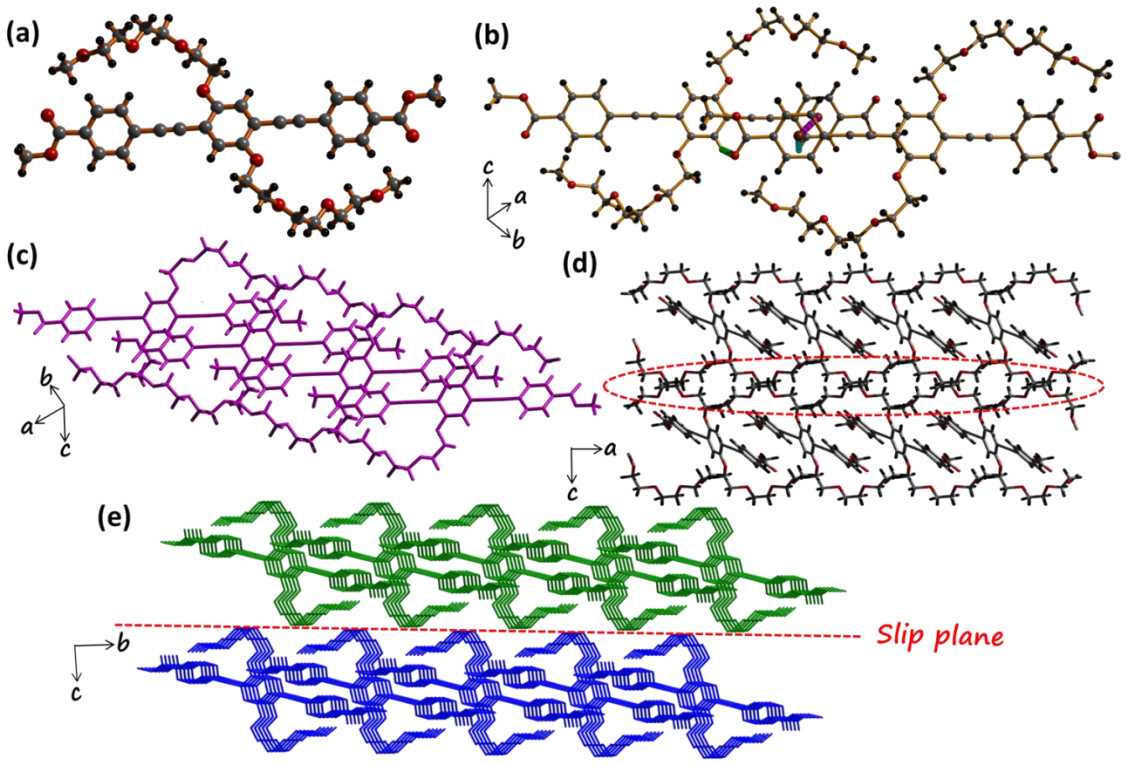

Figure 1. Structural representation of **OPE-C$_{gly}$-E**: (a) View of the single molecule, (b) View of different types of non-covalent interactions between adjacent single molecules (green and pink dashed lines represent the C−H···O and π-π interactions, respectively), (c) View of the 1D coordination chain extended via the above mentioned supramolecular interactions, (d) View of the 2D supramolecular packing along the *ac* plane assisted by C−H···O interactions between TEG side chains of individual 1D chains and (e) Presence of slip planes contained in the *bc* plane (hydrogens have been omitted for clarity).

symmetry remained similar to **OPE-C$_{gly}$-E**, there was a vast difference in the crystal packing. Again, the central core of **OPE-C$_{gly}$-A** contains three aryl units connected via triple bonds having TEG side chains flanking both sides of the core (Figure 2a). It was calculated that the dihedral angle between the central phenyl ring and the terminal ones was 8.8^0. This linearity is attained due to end-capping carboxylic acid groups which take part in O−H···O hydrogen bonding interactions (D−A distance; 1.82 Å, ∠D−H···A; 167.9°) between the –COOH groups resulting in a rigid and linear 1D chain extension (Figure 2b).[22] π-π stacking and C−H···π interactions between the 1D chains are further involved to generate the 2D extension of **OPE-C$_{gly}$-A** (Figure 3a,b). An edge to face distance between the central phenyl ring of one OPE core and the terminal phenyl ring of the adjacent OPE core was found to be 3.85 Å. The same set of phenyl rings also takes part in

C−H···π interactions to proliferate the supramolecular interactions between two 1D chains. This 2D arrangement leaves slight void spaces in the 2D plane where TEG side chains of adjacent 2D sheets are further interdigitated to lead to a condensed 3D structure of **OPE-C$_{gly}$-A** (Figure 3c).

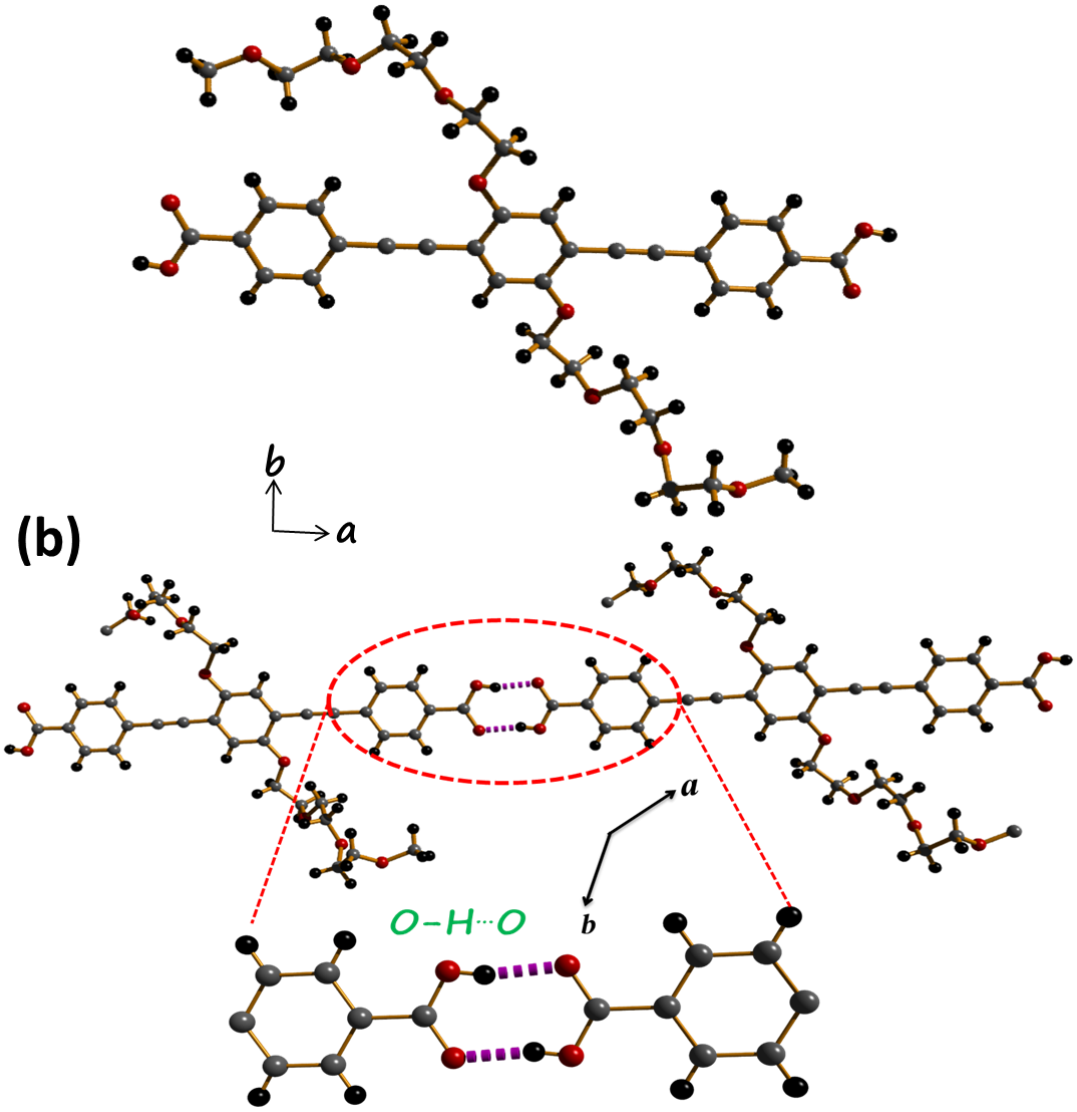

Figure 2. Structural representation of **OPE-C$_{gly}$-A**: (a) View of the single molecule and (b) View of 1D chain generated via linear O−H···O hydrogen bonding (pink dashed lines).

2B.3.3. TG Analysis and DSC of OPE-C$_{gly}$-E and OPE-C$_{gly}$-A

Thermogravimetric analysis (TGA) revealed that **OPE-C$_{gly}$-E** and **OPE-C$_{gly}$-A** are stable upto 310 °C and 320 °C respectively (Figure 4a,b). The higher thermal stability of **OPE-C$_{gly}$-A** over **OPE-C$_{gly}$-E** is due to the presence of carboxylic acid group driven 1D chain extension.

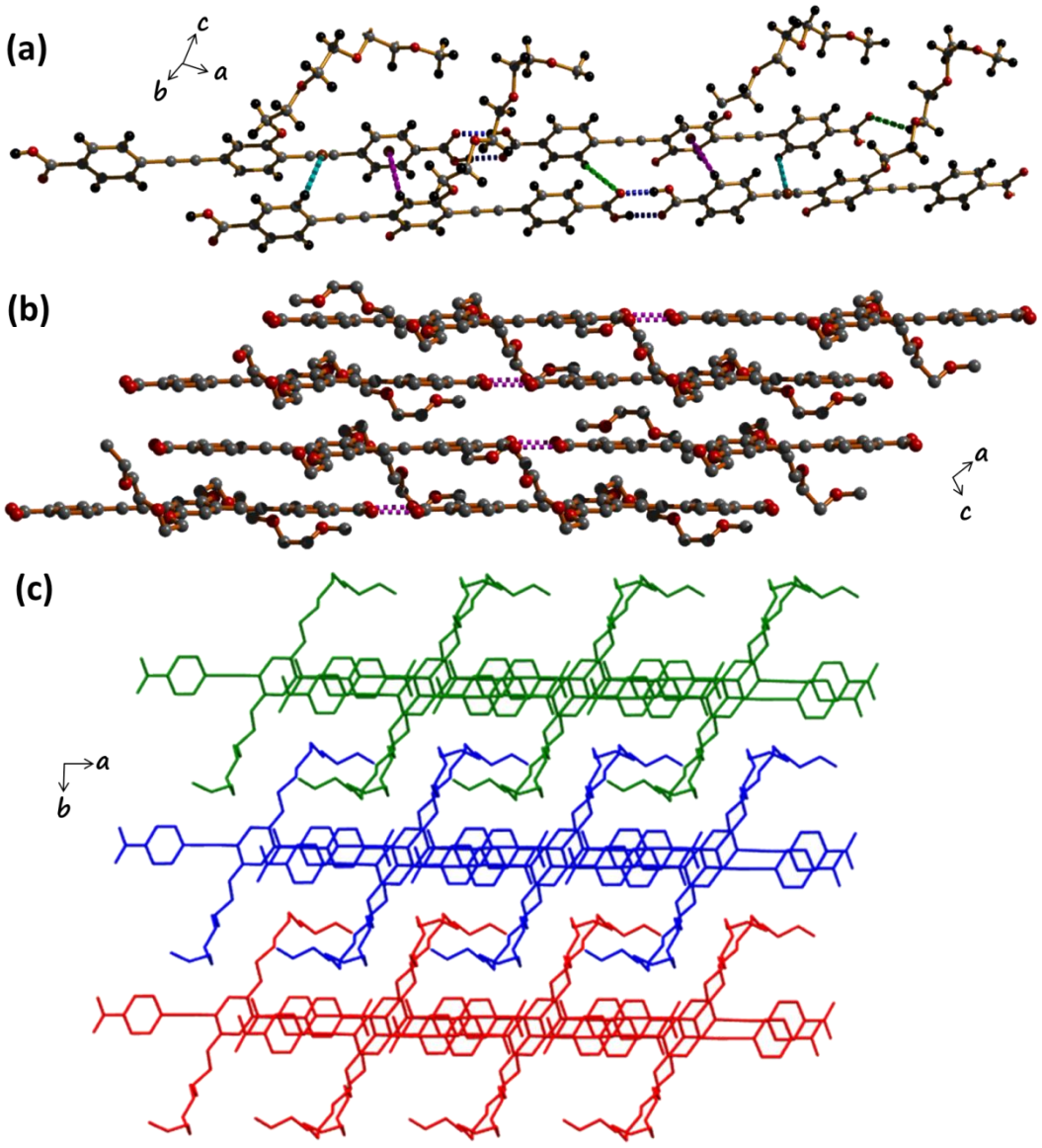

Figure 3. Structural representation of **OPE-C$_{gly}$-A**: (a) View of supramolecular interactions between successive 1D chains (cyan, pink and green dashed lines represent different types of C−H···π and C−H···O interactions, respectively, (b) View of the overall 2D supramolecular packing and (c) View of the condensed 3D packing assisted by interdigitation of TEG side chains.

Due to the presence of variable supramolecular interactions in both the structures, we decided to perform differential scanning calorimetry (DSC) experiments. This would throw light upon any thermally induced phase changes due to the breakage of the non-covalent interactions of different strengths. Scanning was carried out over a wide temperature range of -190 °C to 275 °C (Figure 5a,b). DSC thermogram of **OPE-C$_{gly}$-E** indicated a single irreversible exothermic peak at 90 °C (Figure 5a). The enthalpy value

of this peak was 45 kJ/ mol. Interestingly, there were three reversible exothermic peaks for **OPE-C$_{gly}$-A** at -150 °C, 150 °C and 180 °C (Figure 5b). The enthalpy values of these peaks were 4.0 kJ/ mol, 27.0 kJ/ mol and 15 kJ/ mol, respectively. This observation indicated that interplay of different degrees of non-covalent interactions was generating phase changes in both the compounds.

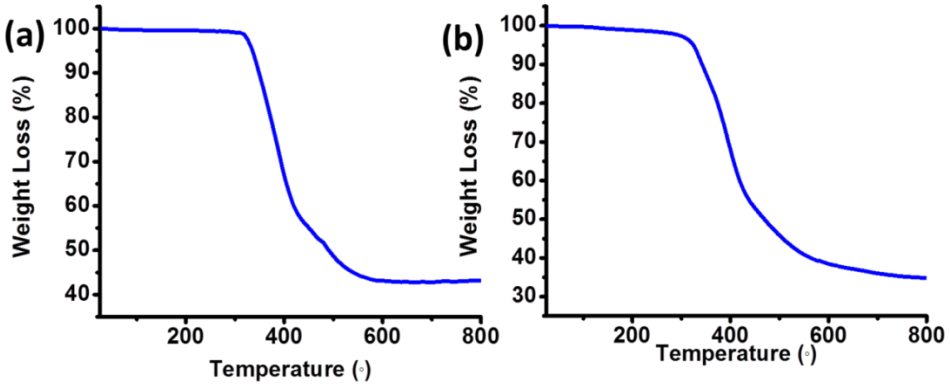

Figure 4. Thermogravimetric analysis for (a) **OPE-C$_{gly}$-E** and (b) **OPE-C$_{gly}$-A**.

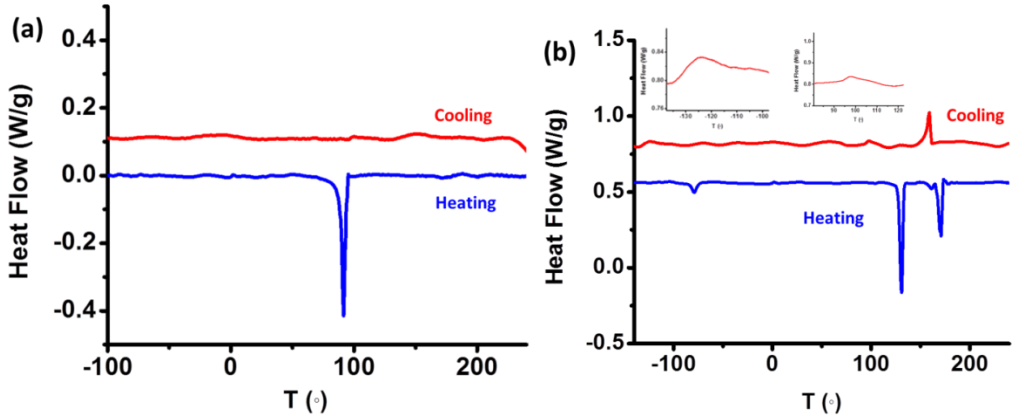

Figure 5. Differential scanning calorimetry (DSC) plots for (a) **OPE-C$_{gly}$-E** and (b) **OPE-C$_{gly}$-A**.

Heating of **OPE-C$_{gly}$-E** at 95 °C on a hot plate resulted in melt formation (Figure 6a,b). However, the melt recrystallizes upon solidification for over 30 minutes, with a different packing arrangement to **OPE-C$_{gly}$-E**, as evidenced by the PXRD pattern (Figure 7). This phase transition from solid to a melting phase transformation is also reflected in the high value of enthalpy. However heating of **OPE-C$_{gly}$-A** single crystals on a hot plate at 160 °C did not result in any melt formation but the crystals melted upon raising the

temperature upto 180 °C. The transformation back to crystalline phase was immediate and hence investigations on the melt were not possible (Figure 8). When single crystals of **OPE-C$_{gly}$-A** were frozen at -150 °C, they remained intact. This pointed to the fact that there might be single crystalline polymorphs of **OPE-C$_{gly}$-A** existing at -150 °C and at 150 °C. Buoyed by this observation, we collected SCXRD data at -150 °C and at 160 °C.

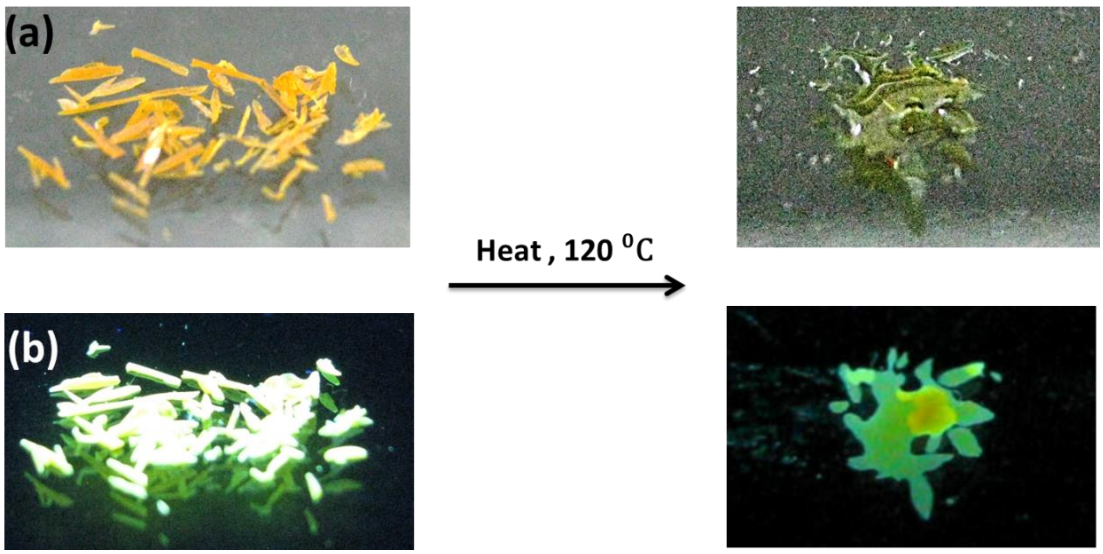

Figure 6. Images of **OPE-C$_{gly}$-E** before and after heating at 120 °C leading to melt formation under (a) Visible and (b) UV light.

2B.3.4. Polymorphic Structure of OPE-C$_{gly}$-A

The excellent single crystallinity maintained at -150 °C allowed us to elucidate the structure. It revealed a new polymorphic structure of **OPE-C$_{gly}$-A** (**OPE-C$_{gly}$-A′**). Similar to **OPE-C$_{gly}$-A**, the central core of **OPE-C$_{gly}$-A′** contains a sequence of three phenyl rings connected via triple bonds and having TEG side chains on both sides of the OPE core (Figure 9a). The end carboxylic acid groups also take part in intermolecular hydrogen bonding interactions. However, the single molecule of **OPE-C$_{gly}$-A′** is slightly more twisted than **OPE-C$_{gly}$-A**. The dihedral angle between the central phenyl ring and the terminal ones was calculated to be 11.9° as opposed to 8.8° in **OPE-C$_{gly}$-A**. Expectedly, the 1D chain in this structure is propagated via strong O−H···O hydrogen bonding interactions (hydrogen bonding D−A distance; 1.79 Å, ∠D−H···A; 171.3°) (Figure 9b). The strength of this supramolecular interaction is comparable to that present in **OPE-C$_{gly}$-A**. A combination of π-π stacking, C−H···π and C−H···O interactions and interdigitation of TEG side chains leads to the 2D extension of **OPE-C$_{gly}$-A′** similar to

OPE-C_{gly}-A (Figure 9c). Nearly co-facial distance between the phenyl rings of adjacent OPE cores was found to be 4.25 Å. Again, as in **OPE-C_{gly}-A**, the same set of phenyl rings take part in C−H···π interactions to compound the supramolecular interactions between two 1D chains (D-A distance; 3.85 Å) (Figure 9c). Interestingly, additional C−H···O interactions exist between the side chains of adjacent OPE cores (D−A distance; 2.7 Å, ∠D−H···A; 138.9°) (Figure 9c). The overall 3D extension was found similar to that of **OPE-C_{gly}-A**.

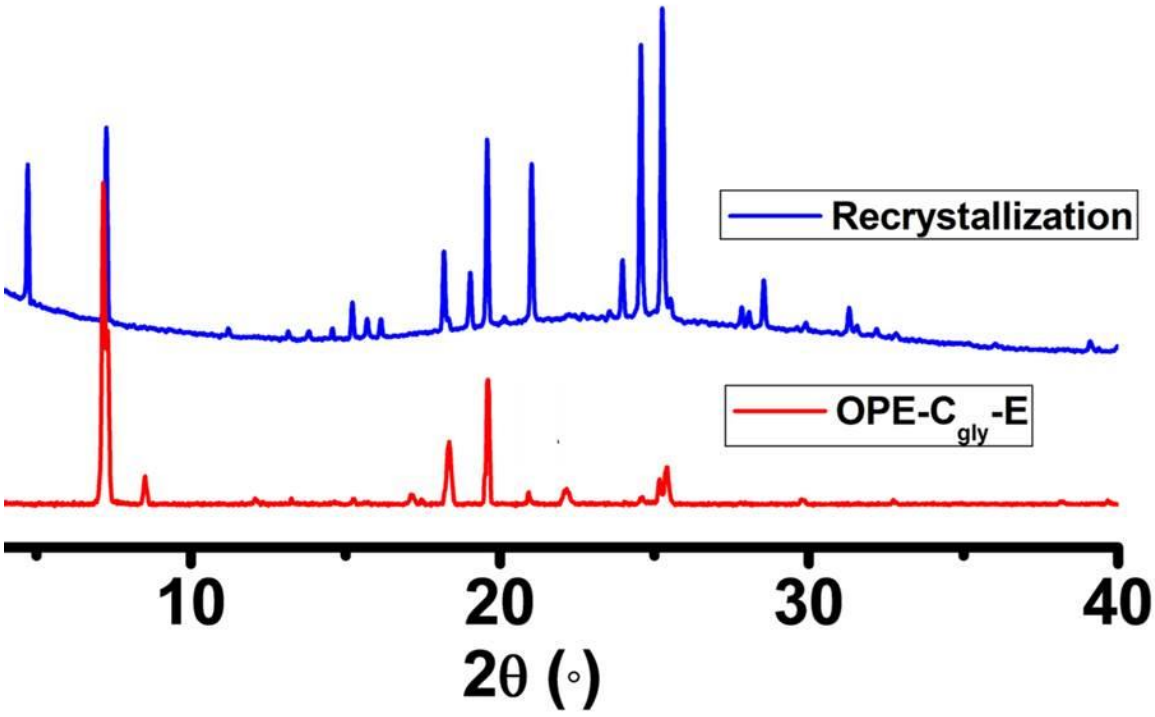

Figure 7. PXRD pattern for **OPE-C_{gly}-E** (red) and recrystallized **OPE-C_{gly}-E** after melt formation (blue).

Figure 8. Images of **OPE-C_{gly}-A** showing melt formation upon heating and instant recrystallization upon cooling.

We were unable to collect data in SCXRD for the polymorph at 160 °C because of loss of single crystalline quality at high temperatures leading to weak diffraction spots. But by

visual observation, we can safely conclude that at 160 °C, there occurs a crystal to crystal phase transformation in **OPE-C$_{gly}$-A**.

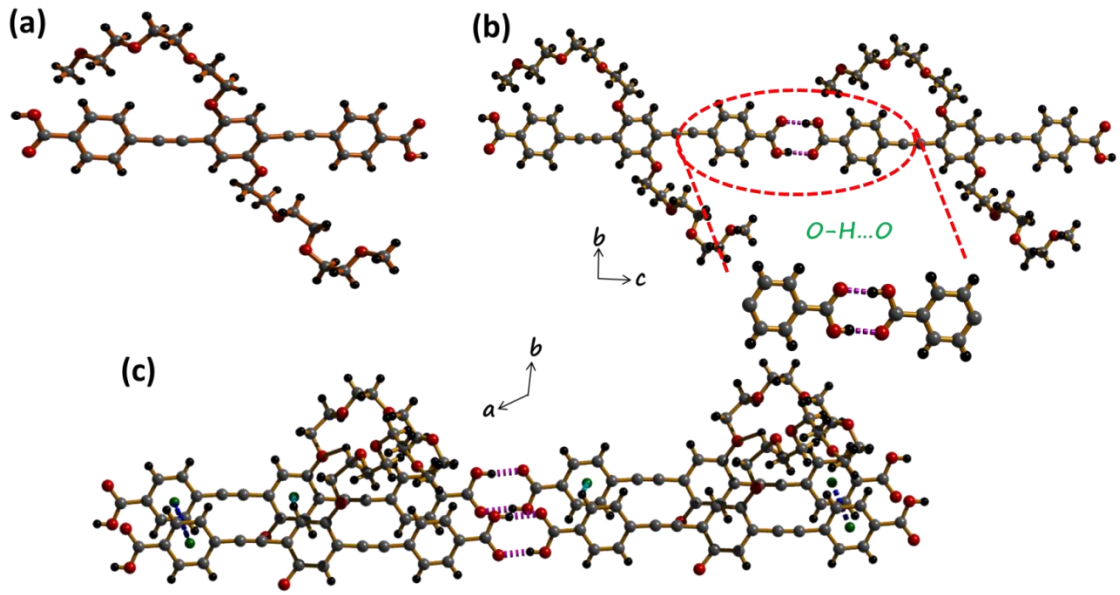

Figure 9. Structural representation of **OPE-C$_{gly}$-A′**: (a) View of the single molecule, (b) View of 1D chain generated via linear O−H···O hydrogen bonding (pink dashed lines) and (c) View of supramolecular interactions between successive 1D chains (cyan, pink and green dashed lines represent different types of C−H···π and C−H···O interactions respectively.

The variance in phase transformation properties in **OPE-C$_{gly}$-E** and **OPE-C$_{gly}$-A** can be attributed to the change in structural packing induced by end-capped carboxylic acid groups in **OPE-C$_{gly}$-A** which is not present in **OPE-C$_{gly}$-E**. **OPE-C$_{gly}$-A** has a 3D supramolecular packing whereas **OPE-C$_{gly}$-E** extends only in 2D. The 1D chain is extended via directional hydrogen bonding in **OPE-C$_{gly}$-A** and the 2D plane is extended via C−H···O and C−H···π, interactions. C−H···O interactions between 2D sheets propagates the structure into 3D. In contrast, due to the absence of O−H···O hydrogen bonds, 1D chain in **OPE-C$_{gly}$-E** is extended C−H···O, C−H···π, and π-π interactions. 2D sheets are generated via C−H···O interactions between the glycol chains of 1D chains. It can be therefore be visualized that **OPE-C$_{gly}$-A** has a more condensed structure than **OPE-C$_{gly}$-E**. **OPE-C$_{gly}$-A** also has a directional 1D linear chain extended via intramolecular hydrogen bonding. It was reported by us that OPE polymorphs arise via

the twisting of phenyl rings around single bonds connecting the triple bonds and phenyl rings.[2a] For this, a 1D intermolecular hydrogen bonding extension is required to provide support required for the twisting. It is absent in **OPE-C$_{gly}$-E**. However, due to the existence of such O–H···O hydrogen bond assisted 1D chain extension, there exists rotational degree of freedom of single bonds leading to the polymorphism observed in **OPE-C$_{gly}$-A**. Therefore ester and acid groups, via their ability to take part in 1D O–H···O hydrogen bonding, led to the existence and absence of polymorphism in **OPE-C$_{gly}$-A** and **OPE-C$_{gly}$-E** respectively.

2B.3.5. Photoluminescence of OPE-C$_{gly}$-E and OPE-C$_{gly}$-A

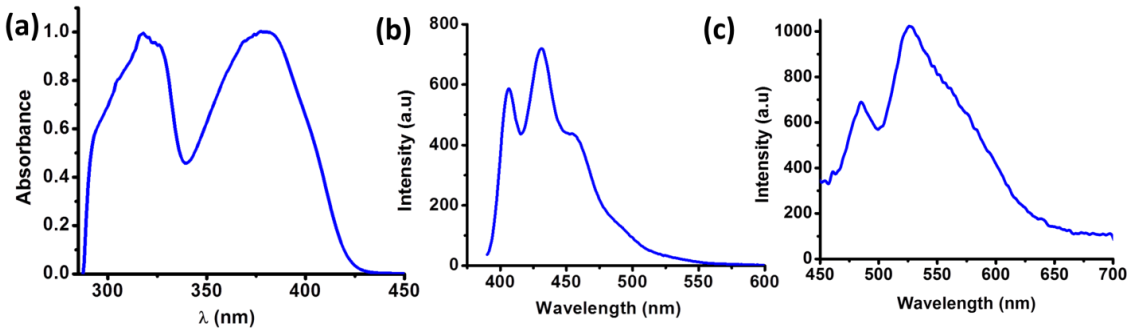

Figure 10. (a) UV and (b) PL plots in THF solution and (c) Solid state PL plot for **OPE-C$_{gly}$-E**.

The inherent conjugation present in both **OPE-C$_{gly}$-E** and **OPE-C$_{gly}$-A** motivated us to study their photoluminescence properties. A THF solution of **OPE-C$_{gly}$-E** shows absorption maxima at 320 and 380 nm while it emits at 430 nm with shoulder bands at 405 and 460 nm upon excitation at 380 nm (Figure 10a,b). This arises due to twisting of OPE around the single bonds connecting the triple bonds. Here, the high dihedral angle (32°) leads to the appearance of multiple bands in the monomeric state of **OPE-C$_{gly}$-E**. In the solid state, it absorbs at 420 nm and emits at a 525 nm maximum with another peak at 485 nm (Figure 10c). We further checked the emission properties of the melt phase of **OPE-C$_{gly}$-E**. We hypothesized based on the image of the melt under UV that there might be changes in the PL spectrum. Our conjecture was corroborated by the fact that the melt showed a broad emission feature. The peak centred around 505 nm (Figure 11a). This again backs up why the melt portrayed a cyan emission under UV light. This blue shift of the emission peak maybe due to monomeric OPE states with a wide variety of twisted dihedral angles in the central phenyl core. Interestingly, the melt upon cooling over time,

gives back the original emission peaks centred at 525 nm and 485 nm (Figure 11b). This maybe due to the re-occurrence of similar packing arrangement as in the original crystalline phase, over a large time scale. **OPE-C_{gly}-A** absorbs at 320 nm and 380 nm in THF solution (Figure 12a). Upon excitation at 380 nm, it shows an emission maximum at

Table 1. Crystallographic data and structure refinement parameters for compounds **OPE-C_{gly}-E**, **OPE-C_{gly}-A** and **OPE-C_{gly}-A′**.

	OPE-C_{18}-E	**OPE-C_{18}-A**	**OPE-C_{18}-A′**
empirical formula	$C_{40}H_{46}O_{12}$	$C_{38}H_{42}O_{12}$	$C_{38}H_{42}O_{12}$
M	718.77	690.72	690.72
crystal system	triclinic	triclinic	triclinic
space group	$P\bar{1}$ (No. 2)	$P\bar{1}$ (No. 2)	$P\bar{1}$ (No. 2)
a (Å)	7.7785(4)	9.9274(4)	10.504(2)
b (Å)	10.3936(7)	10.7198(4)	10.613(2)
c (Å)	12.0891(8)	17.6445(7)	15.799(3)
α (deg)	99.643(2)	90.429(2)	92.215(9)
β (deg)	91.771(2)	103.642(2)	103.356(10)
γ (deg)	91.880(2)	96.616(2)	98.434.54(11)
V (Å^3)	962.38(10)	1811.43(12)	1690.3(6)
Z	1	2	2
T (K)	296	293	110
λ (Mo K_α)	0.71073	0.71073	0.71073
D_c (g/cm^3)	1.240	1.157	1.357
μ (mm^{-1})	0.091	0.094	0.101
$\theta_{min}/\theta_{max}$	2.4/ 25.7	2.2/25.7	2.4/28.3
total data	17596	37456	40142
unique reflection	3479	6884	7445
R_{int}	0.080	0.050	0.113
data [I>2σ(I)]	2090	4718	4564
R[a]	0.0788	0.0829	0.0904
R_w[b]	0.2456	0.3283	0.2848
GOF	1.02	1.07	1.02
Δρ min/max [e Å^{-3}]	-0.40, 0.43	-0.47, 0.70	-0.74, 0.65

[a]$R=\sum||F_o|-|F_c||/\sum|F_o|$. [b]$R_w=[\sum\{w(F_o^2-F_c^2)^2\}/\sum\{w(F_o^2)^2\}]^{1/2}$

450 nm (Figure 12b).This is because of the planarity attained (low dihedral angle of 8.8°) in the monomer of **OPE-C_{gly}-A** which negates any red shift in emission of OPEs. In the solid state, **OPE-C_{gly}-A** absorption maximum appears at 420 nm whereas it emits at 520 nm (Figure 12c,d).

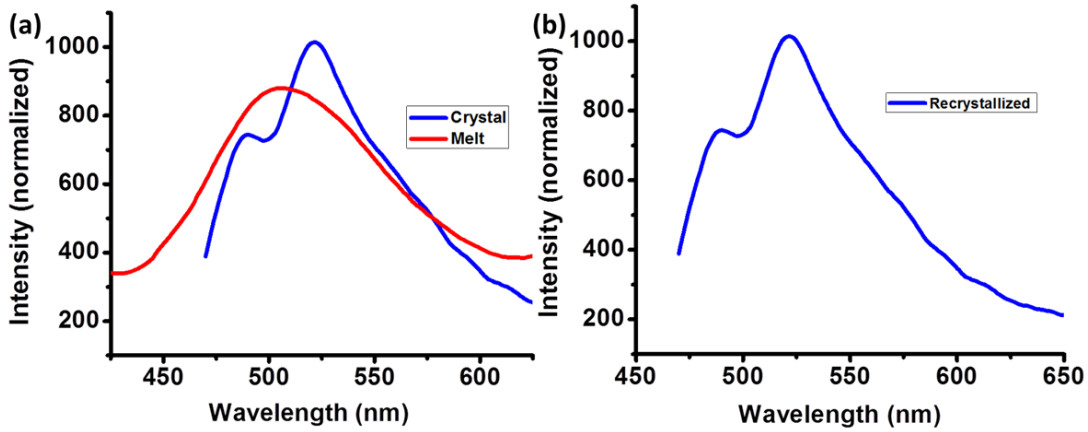

Figure 11. PL plots of (a) **OPE-C_{gly}-E** (blue) and melt of **OPE-C_{gly}-E** (red) and (b) **OPE-C_{gly}-E** after recrystallization.

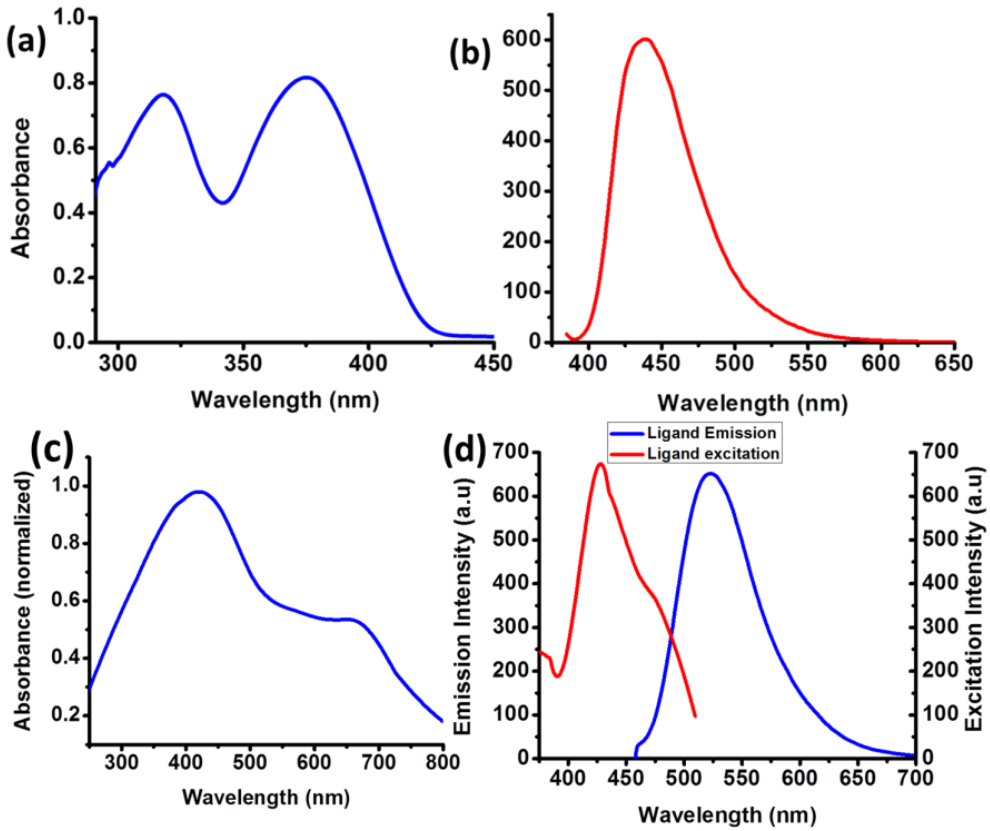

Figure 12. OPE-C_{gly}-A: (a) UV and (b) PL in THF solution, (c) UV and (d) PL in the solid state.

2B.3.6. Mechanochromism in OPE-C_{gly}-E

The existence of strong and weak supramolecular interactions present in both the molecules led us check for their stimuli-responsive luminescent properties. Single crystals of **OPE-C_{gly}-E** were ground in a mortar for 1 minute. Instant change of color under UV light was observed from yellow to green (Figures 13b-d). PL profiles before and after grinding corroborated the ML present in **OPE-C_{gly}-E** (Figure 13a). It was quite evident that the broad nature of the emission profile of the pristine crystals got constricted upon grinding. Hence, after grinding, it did not cover a wide range of wavelength. This leads to the shift in emission color from yellow to green.

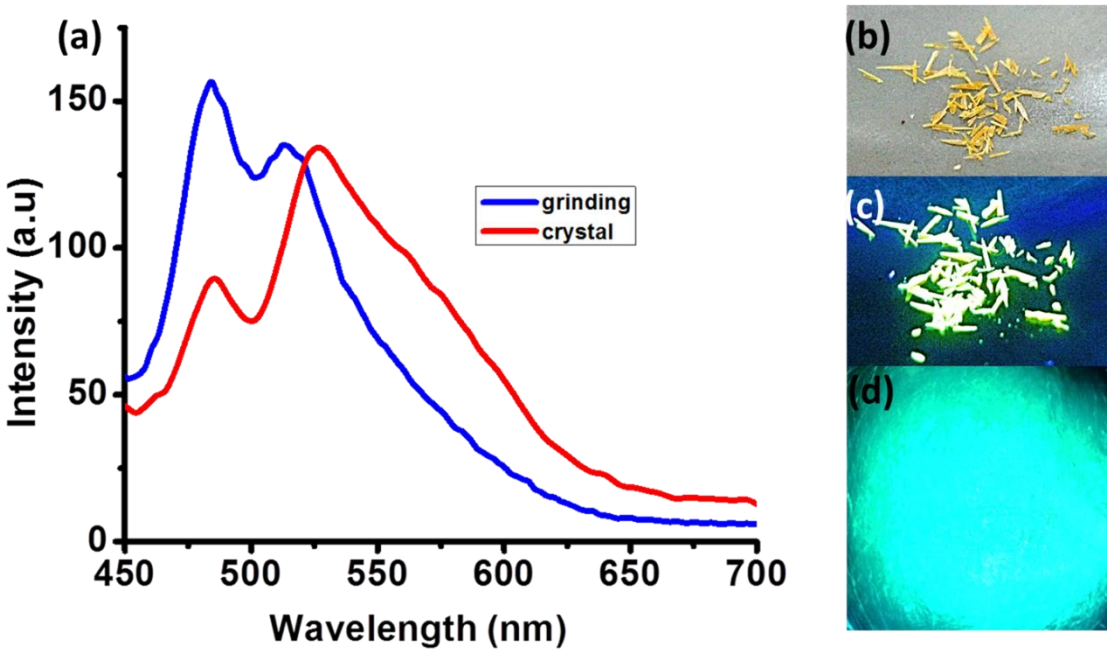

Figure 13. (a) PL profile of **OPE-C_{gly}-E** single crystal (red) and ground film (blue) indicating broadness and hypsochromic peak shift after grinding and (b) Images of the associated color change on grinding **OPE-C_{gly}-E**.

It was also observed that there was a variance in intensity and shift in the emission peaks at 485 nm and 525 nm. The 485 nm peak increased in intensity after grinding when compared to the crystals of **OPE-C_{gly}-E**. Interestingly, the 525 nm band remained equal in intensity even after grinding but underwent a hypsochromic shift of 15 nm to 510 nm. Therefore, the increase in intensity of the 485 nm peak and the blue shift of the 525 nm also contributes to the shift in emission color from yellow to green. However, upon keeping the ground crystals overnight and also exposing them to solvent vapors and heat

did not reverse back the color to the original yellow emission. The PXRD pattern of the pristine **OPE-C_{gly}-E** crystals reveals its high crystalline ordering (Figure 14). Upon grinding, the PXRD pattern showed the loss of numerous peaks along with broadening of the existing ones. This points to a transition to a disordered state of **OPE-C_{gly}-E**. It can also be estimated from the PXRD data that breakage of supramolecular interactions leads to loss in 2D packing resulting in the phase transformation.

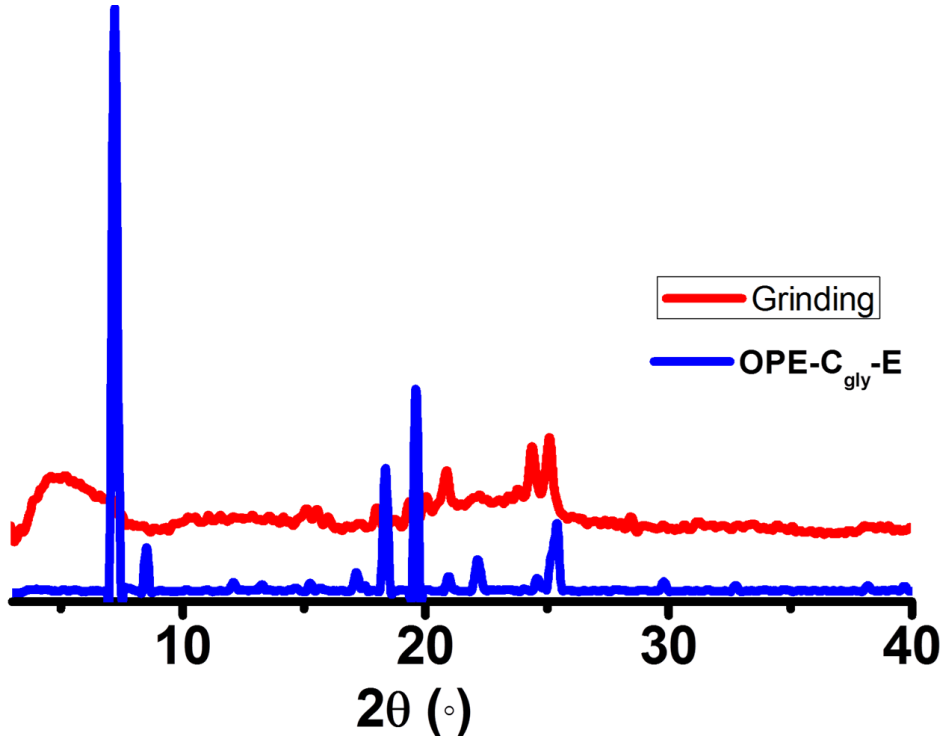

Figure 14. PXRD of **OPE-C_{gly}-E** (blue) and **OPE-C_{gly}-E** after grinding (red).

From a structural point of view we can ascertain that upon grinding, variance in rotational freedom of the phenyl rings of the OPE chain occurs around the single bonds. This because of slippage of the slip planes having a zipper like arrangement. The slip planes glide over one another breaking the supramolecular interactions leading to the blue shift in emission colour. As was discussed previously, the red shifted emission band at higher wavelengths appears due to the twisting of the central phenyl rings in OPE. There is a significant dihedral angle of 32.1° in **OPE-C_{gly}-E**. At this conformation, the supramolecular interactions are maximized which hold the dihedral angle at this particular value. This leads to the appearance of the band at 525 nm. Now, upon grinding, the supramolecular interactions break, leading to the release of the strain and subsequent decrease of the dihedral angle. This is automatically reflected in the blue shift of the

emission band to 510 nm. Furthermore, the conjugation of the OPE backbone which gains more contributory importance due to the relaxation predominates the emission profile. Hence, the band at 485 nm increases in intensity. Non-reversibility of the ML of **OPE-C_{gly}-E** can be best explained from PXRD. The huge loss of peaks upon grinding and broadening indicate that there occurs a significant shift in the packing mode. As multiple interactions break, this may account for a huge energy loss. Methods of resuscitation of the original supramolecular interactions do not provide the energy required to bring it back. Hence, a non-reversible ML is seen in **OPE-C_{gly}-E**.

2B.3.7. Theoretical Calculation for OPE-C_{gly}-E Mechanochromic Behavior

In order to get insight of the observed mechanochromic shift, we performed density functional theoretical (DFT) computations on a fragmented **OPE-C_{gly}-E** unit, using Gaussian09 program package. We envisaged that the mechanical grinding could rupture weak interactions (mainly hydrogen bonds and weak π-π stacking) in the crystal packing. For this reason, we have computed and compared the emission wavelength of a single molecule (no intermolecular interaction) and a dimer (with intermolecular interaction) of **OPE-C_{gly}-E** as found in the crystal structure. In details, the monomer of **OPE-C_{gly}-E** exhibited the lowest energy electronic transition from at 419 nm (HOMO → LUMO, f = 1.37) and corresponding emission appeared at 465 nm (Figure 15). Similarly, electronic excitation search on the dimer showed the lowest energy transition at 421 nm (HOMO-1 → LUMO, f = 0.59; HOMO → LUMO + 1, f = 0.37) and corresponding emission appeared at 541 nm. Therefore, computational outcomes predict that the rupture of all the intermolecular interaction could lead to 76 nm hypsochromic shift of the luminescent spectrum. The experimentally observed shift of 15 nm in PL spectrum could be a result of rupturing only few interactions. **OPE-C_{gly}-A** however, did not show any change in emission color upon grinding for over half an hour. The color remained static at green. The PL profile also revealed the overlap of spectra before and after grinding. PXRD pattern revealed minor changes indicating that major structural changes do not occur upon applying mechanical stimulus. Structural picture of **OPE-C_{gly}-A** suggests a more condensed 3D structure of it when compared to **OPE-C_{gly}-E**. The additional directional O−H···O hydrogen bonding interactions present in **OPE-C_{gly}-A** holds the structure firmly compensates for the bond breakage induced by mechanical stimuli energy. Therefore, there are no structural rearrangements in **OPE-C_{gly}-A** and hence no ML.

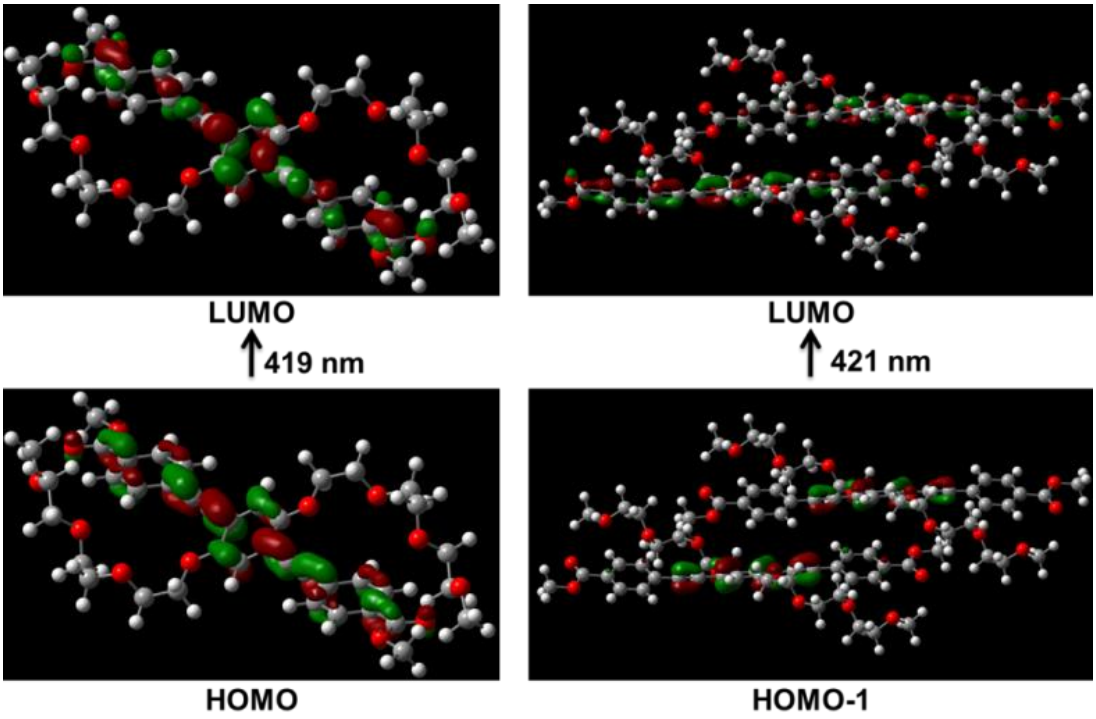

Figure 15. HOMO-LUMO plots for **OPE-C_{gly}-E** (left) and **OPE-C_{gly}-E** (dimer, right).

2B.3.8. Gelation of OPE-C_{gly}-A

We have recently reported the gelation ability of symmetrical and unsymmetrical OPE based bola-amphiphiles. These showed pure white emission and CT gel formation upon doping with chromophoric dyes and redox-active molecules respectively. As **OPE-C_{gly}-E** and **OPE-C_{gly}-A** are bola-amphiphilic with the same structural backbone, we decided to check for their gelation abilities in different solvents. Several combinations of organic solvent mixtures failed to induce gelation in **OPE-C_{gly}-E**. In stark contrast, **OPE-C_{gly}-A** showed gelation in a 3:1 toluene/ methanol mixture (**OPE-C_{gly}-A-G**). The gel formation occurred after 5 minutes of allowing the solvent mixture of **OPE-C_{gly}-A** to stand (Figure 16a,b). The sol-gel transformation occurred every-time it was subjected to heating and then standing at room temperature. This portrayed the thermo-reversibility of **OPE-C_{gly}-A-G** (Figure 16c). Inversion test further confirmed the gel state of **OPE-C_{gly}-A**. Field emission scanning electron microscopy provided insights into the nanomorphology of **OPE-C_{gly}-A-G**. It was observed that **OPE-C_{gly}-A-G** formed nanorice like morphology. The nanorice were having an average length of 500 nm with blunt ends (Figure 17). The distribution found under the scanning range was uniform. PXRD peaks showed that **OPE-C_{gly}-A-G** had excellent crystallinity (Figure 18).

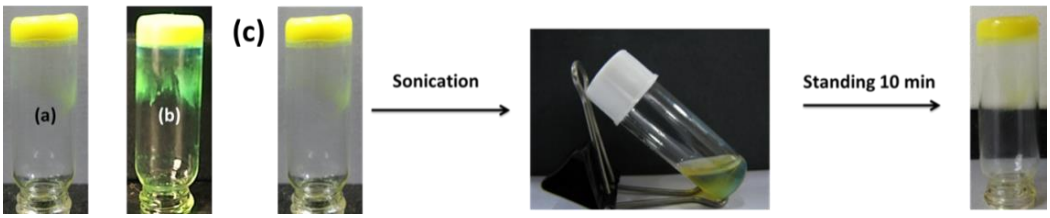

Figure 16. Images of the **OPE-C_{gly}-A-G** under (a) Normal light and (b) UV light, (c) Images of the thermoreversibility test performed on **OPE-C_{gly}-A-G**.

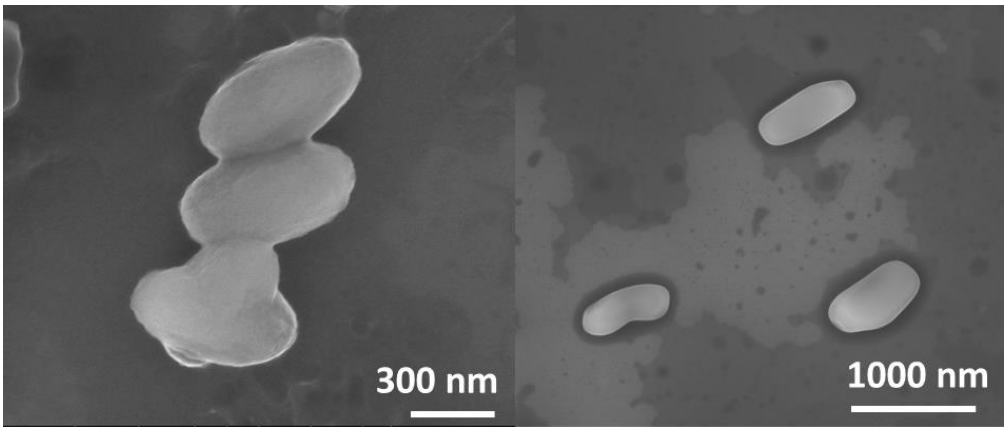

Figure 17. FESEM images of **OPE-C_{gly}-A-G**.

2B.3.9. Photoluminescence studies of OPE-C_{gly}-A-G

We then proceeded to study the photoluminescence property of **OPE-C_{gly}-A-G**. Similar to **OPE-C_{gly}-A**, a solution of **OPE-C_{gly}-A-G** in toluene/ methanol mixture showed two absorption maxima at 320 nm and 380 nm (Figure 19a). Upon excitation at 380 nm, it displayed an emission maximum at 440 nm (Figure 19b). Solid state absorbance of **OPE-C_{gly}-A-G** was observed at 420 nm (Figure 19c). Upon excitation at this wavelength, an emission maximum was observed at 520 nm. It was interesting to note that there was no shift in the emission peak of **OPE-C_{gly}-A-G** to that of **OPE-C_{gly}-A** (Figure 19d). This indicated that the packing in **OPE-C_{gly}-A** was not perturbed upon solvent trapping in its scaffold. Images under UV light portray a greenish yellow emissive gel state of **OPE-C_{gly}-A** (Figure 16b).

2B.3.10. Metallogel formation using OPE-C_{gly}-A

The solubility of **OPE-C_{gly}-A** in methanol led us to try metallogel formation using it owing to the excellent solubility of most metal salts in it. Heating a (1:1) molar mixture of **OPE-C_{gly}-A** and $CuCl_2 \cdot 2H_2O$ in a (1:4) methanol and toluene mixture at 60^0C and then

cooling resulted in stable gel formation after 5 minutes of standing (**OPE-C_{gly}-A-G_M**) (Figure 20, inset,b). The resulting coordination polymer gel showed a change in color from bright green to dull green (Figure 20, inset, b). This also indicated the coordination of copper to the acid groups of **OPE-C_{gly}-A**. The presence of copper was further proved by the energy dispersive x-ray spectroscopy (EDS) spectroscopy (Figure 20). Elemental and ICP analysis of the xerogel afforded a molecular formula of Cu(OPE-C_{gly}-A) ·2MeOH.

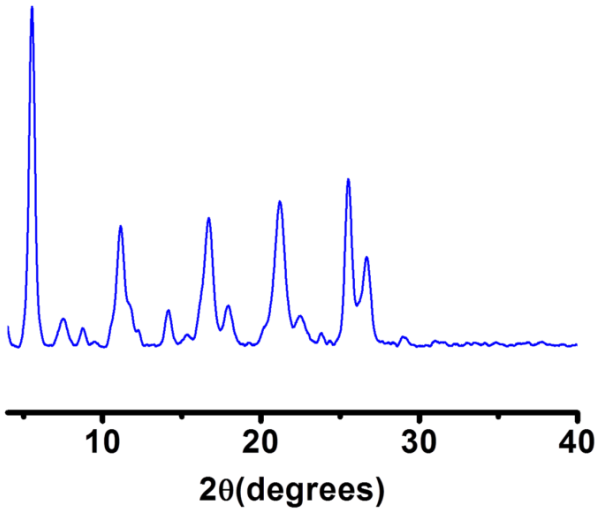

Figure 18. PXRD pattern of **OPE-C_{gly}-A-G** xerogel.

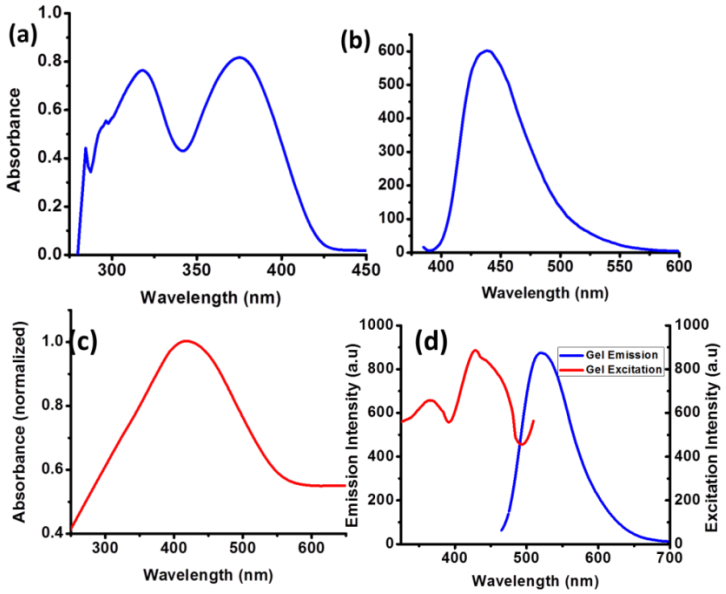

Figure 19. (a) UV and (b) PL plots in a methanol/toluene mixture, (c) UV and (d) PL plots for **OPE-C_{gly}-A-G** xerogel in the solid state.

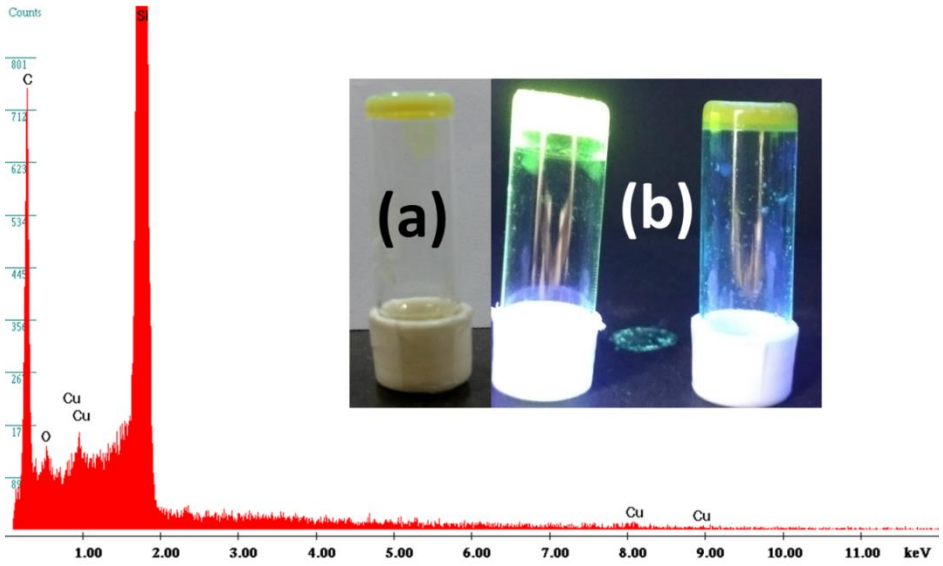

Figure 20. EDS spectum for **OPE-C_{gly}-A-G_M**, Inset: Images of the **OPE-C_{gly}-A-G_M** under (a) Normal light and (b) UV light (left: **OPE-C_{gly}-A-G**, right: **OPE-C_{gly}-A-G_M**).

TG analysis of the metallogel provided more insights into the molecular formula (Figure 21). Trapped solvent molecules showed a steady weight loss of 15% upto 180 °C. The metallogel was further stable upto 310 °C.

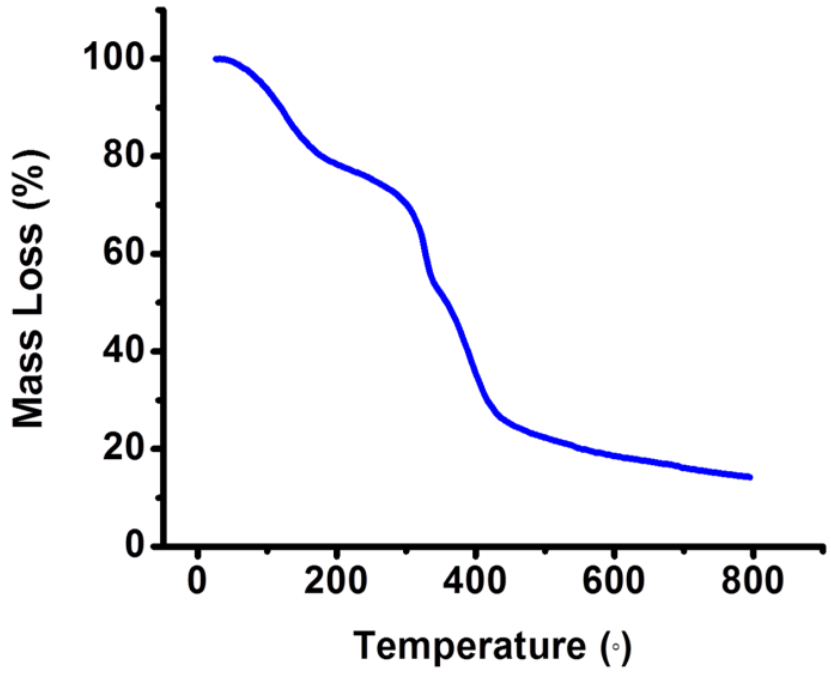

Figure 21. Thermogravimetric plot for **OPE-C_{gly}-A-G_M**.

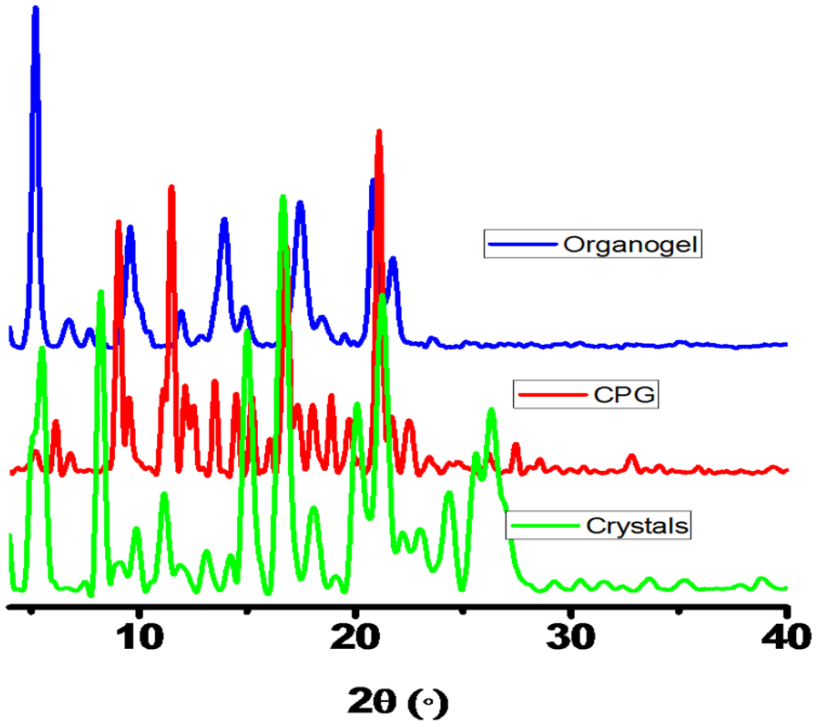

Figure 22. Overlapped PXRD plots for **OPE-C_{gly}-A** crystals (green), **OPE-C_{gly}-A-G_M** (red) and **OPE-C_{gly}-A-G** (blue).

PXRD indicated a high degree of crystalline ordering and presence of π-π stacking in **OPE-C_{gly}-A-G_M** (Figure 22). A highly intense peak at 2θ = 20.2° with a *d*-spacing of 4.3 Å indicated a moderate degree of π stacking interactions between coordination chains of **OPE-C_{gly}-A-G_M**. Interestingly the PXRD pattern matched very closely with the pattern of single crystals of **OPE-C_{gly}-A**. FESEM and TEM analysis were carried out to study the nanomorphology of **OPE-C_{gly}-A-G_M**. Interestingly; it was observed from FESEM that **OPE-C_{gly}-A-G_M** formed a nano-container like morphology (Figure 23a-d). The size of the containers was 400-700 nm with a hollow centre and bright edges. TEM analysis further confirmed the formation of nano-containers of **OPE-C_{gly}-A-G_M** (Figure 23e,f). The size of the containers was again in the range of 400-800 nm with good contrast between the periphery and centre of the nanostructures. The hollow central part was lighter compared to the outer dark region. To further investigate the 3D supramolecular organization of the nano-containers, atomic force microscopic (AFM) analysis was carried out. Nanocontainers of thickness 300-400 nm were observed. From the 3D topographical image, the exterior height was observed to be 4-10 nm while the interior cup height was found to be 1-6 nm. This gives a total volume of the container space to be

1-1.8 attoliters (10^{-18} L) (Figure 24, Scheme 2). Such sub nanometer scale free volumes can further be used or miniaturization applications. Through visual observation, it was noticed that the emission of **OPE-C_{gly}-A-G** was quenched upon metallogel formation. This prompted us to investigate its photoluminescence properties. When compared to the UV spectrum **OPE-C_{gly}-A-G**, **OPE-C_{gly}-A-G_M** showed an additional band at 670 nm along with the original band at 420 nm due to OPE absorption (Figure 25a). This extra peak is due to the absorption emanating from the *d-d* transition of the Cu^{II} centre present in the metallogel. Interestingly, the OPE based emission peak maxima at 520 nm almost quenched completely when compared to the emission peak intensity of **OPE-C_{gly}-A-G** (Figure 25b). This intense emission quenching can be attributed to self-absorption of Cu^{II}.

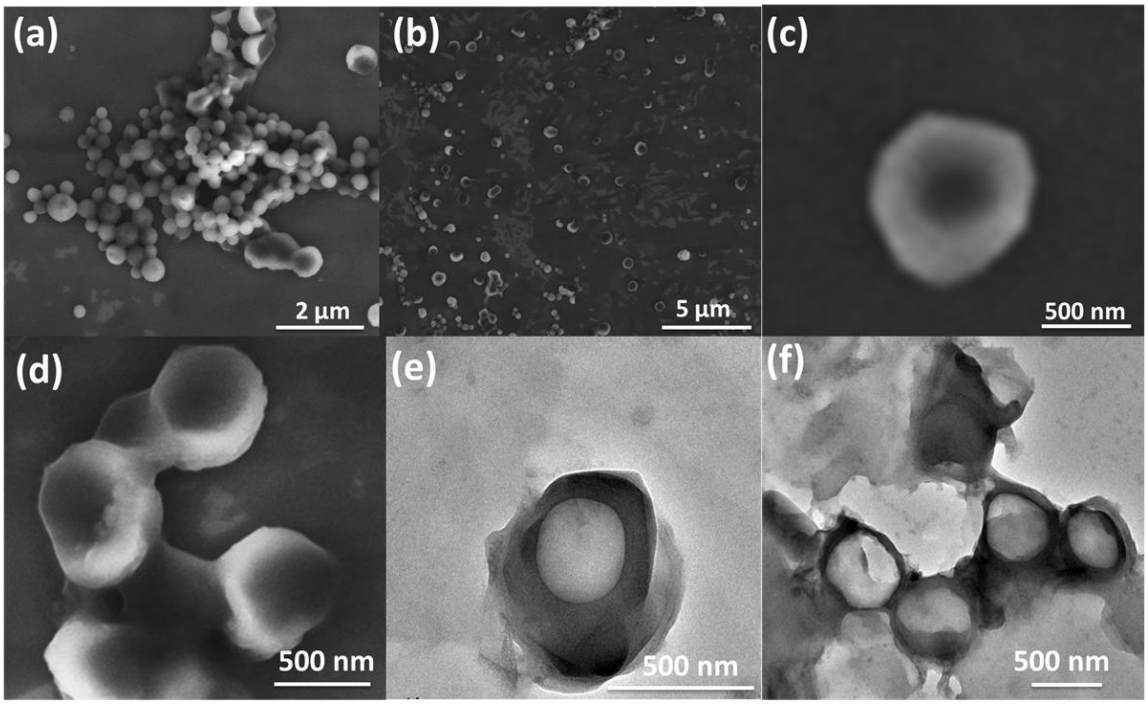

Figure 23. (a-d) FESEM images and (e,f) TEM images of **OPE-C_{gly}-A-G_M**.

It is therefore evident that end capping groups play a major role in tuning the physical states of OPE bola-amphiphiles. **OPE-C_{gly}-E** is not able to pack via directional O−H···O hydrogen bonding interaction and hence does not give rise to a linear rigid 1D chain like **OPE-C_{gly}-A**. This forces consecutive OPEs to come one over the other to generate a weakly interacting 1D chain in **OPE-C_{gly}-E**. Whereas **OPE-C_{gly}-A** has an overall strongly hydrogen bonded 3D structure, **OPE-C_{gly}-E** has a 2D structure with slip planes between the 2D sheets. This directly reflects in its mechanochromic property where external

physical perturbance makes the slip planes glide, to give rise to stimuli-responsive behavior.

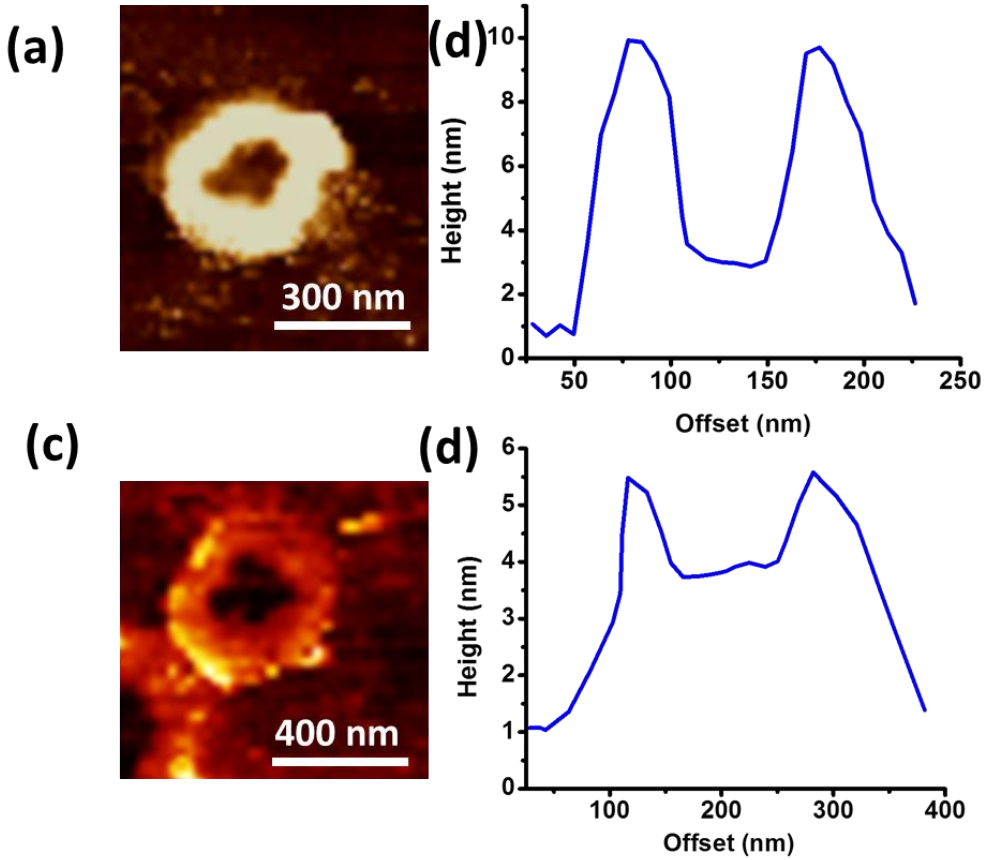

Figure 24. AFM images for **OPE-C_{gly}-A-G_M** (a,c) nanocontainers and (b,d) corresponding height profile plots for the nanocontainers.

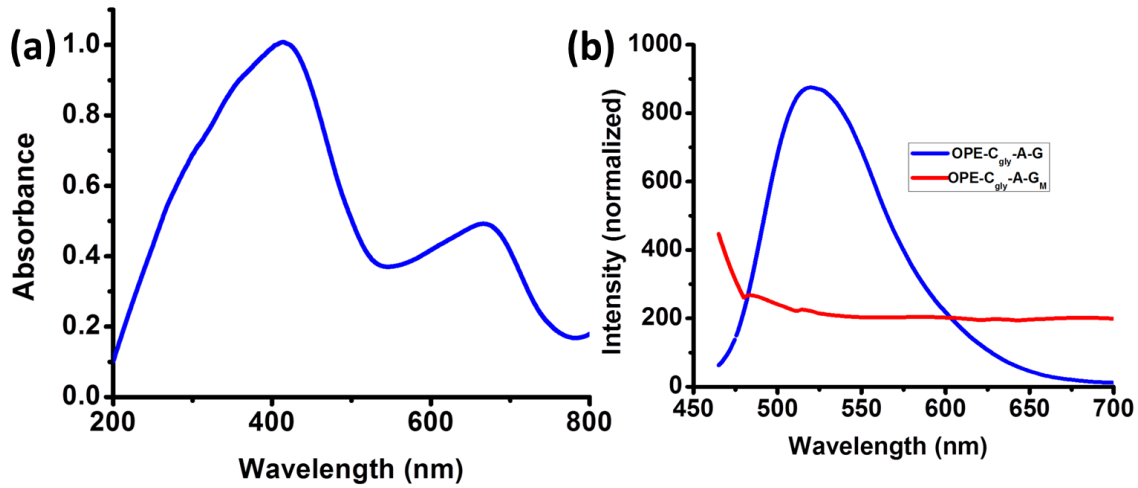

Figure 25. (a) UV spectrum for **OPE-C_{gly}-A-G_M** and (b) PL spectra for **OPE-C_{gly}-A-G_M** (red) and **OPE-C_{gly}-A-G** (blue).

The structural difference between the two also explains the lower melting temperature of **OPE-C_{gly}-E** over **OPE-C_{gly}-A**. **OPE-C_{gly}-A** expectedly does not show mechanochromic behavior due to its condensed structure. However, its end capping acid groups assist in organogel as well as metallogel formation. In the gel phase also, the morphology and emission properties of the system can easily be tuned based on metal coordination of the end acid groups. Polymorphism in **OPE-C_{gly}-A** is also a result of its directional hydrogen bonding, which can hold the different twisting angles of polymorphs. This is not possible in **OPE-C_{gly}-E**.

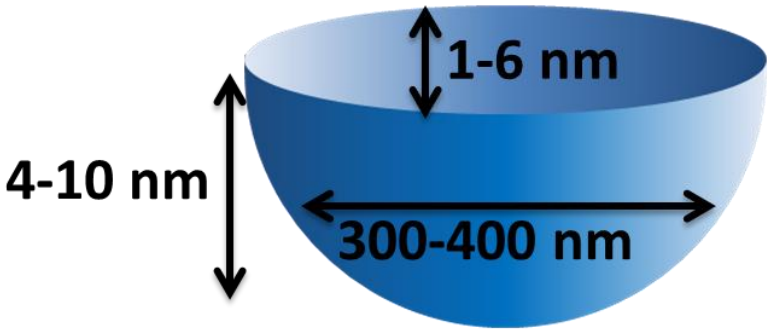

Scheme 2. (a) Schematic showing the dimensions of **OPE-C_{gly}-A-G_M** nanocontainer found from the AFM height profile analysis. Inner volume (v) of the container was calculated using the following formula, V=h*b*l Where, h (height) is the inner topographical height (10-40 nm) of the **OPE-C_{gly}-A-G_M** nanocontainer. Both l (length) and b (breadth) are considered to be same and equal to full width at half maximum (FWHM). The h, b and l values are obtained from the corresponding AFM height profiles.

2B.4. Conclusion

To summarize, this chapter discusses the design and synthesis of two novel OPE bola-amphiphiles with an aim to generate different physical states, via the tuning of non-covalent interactions. Single crystal structure elucidation of both, reveal the existence of different supramolecular interactions in them. **OPE-C_{gly}-E** exclusively shows mechanochromism whereas **OPE-C_{gly}-A** exclusively shows polymorphism and gelation ability. All these properties have been thoroughly studied to reveal that different degrees of supramolecular interactions are the guiding factors for such phenomena. This work

could pave the way for synthesizing materials with targeted properties via a control of different supramolecular interactions.

2B.5. References

1 (a) U. H. F. Bunz, *Chem. Rev.*, 2000, **100**, 1605; (b) U. H. F. Bunz, *Macromol. Rapid Commun.*, 2009, **30**, 772.

2 (a) S. Roy, A. Hazra, A. Bandyopadhyay, D. Raut, P. L. Madhuri, D. S. S. Rao, U. Ramamurty, S. K. Pati, S. K. Prasad and T. K. Maji, *J. Phys. Chem. Lett.*, 2016, **7**, 4086; (b) S-S. Jester, D. Schmitz, F. Eberhagen and Sigurd Höger, *Chem. Commun.*, 2011, 47, 8838; (c) S. Wu, M. T. González, R. Huber, S. Grunder, M. Mayor, C. Schönenberger and M. Calame, *Nat. Nanotech.*, 2008, **3**, 569.

3 (a) S. Roy, D. Samanta, P. Kumar and T. K. Maji, *Chem. Commun.*, 2018, **54**, 275; (b) A. Ajayaghosh, R. Varghese, V. K. Praveen and S. Mahesh, *Angew. Chem. Int. Ed.*, 2006, **118**, 3339.; (c) S. Mahesh, R. Thirumalai, S. Yagai, A. Kitamura and A. Ajayaghosh, *Chem. Commun.*, 2009, 5984.

4 (a) M. V. Suresh, S. J. George and T. K. Maji, *Adv. Funct. Mater.*, 2013, **23**, 5585; (b) V. M. Suresh, S. Chatterjee, R. Modak, V. Tiwari, A. Patel, T. K. Kundu and T. K. Maji, *J. Phys. Chem. C* 2014, **118**, 12241; (c) S. Roy, V. M. Suresh and T. K. Maji, *Chem. Sci.*, 2016, **7**, 2251; (d) S. Roy, M. Das, A. Bandyopadhyay, S. K. Pati, P. P. Ray and T. K. Maji, *J. Phys. Chem. C*, 2017, **121**, 23803.

5 E. L. Spitler, J. W. Colson, F. J. Uribe-Romo, A. R. Woll, M. R. Giovino, A. Saldivar, and W. R. Dichtel, *Angew. Chem. Int. Ed.*, 2012, **51**, 2623.

6 (a) C. Rest, A. Martin, V. Stepanenko, N. K. Allampally, D. Schmidt and G. Fernandez, *Chem. Commun.*, 2014, **50**, 13366; (b) M. J. Mayoral, C. Rest, J. Schellheimer, V. Stepanenko, and G. Fernandez, *Chem. Eur. J.*, 2012, **18**, 15607; (c) M. José Mayoral, C. Rest, V. Stepanenko, J. Schellheimer, R. Q. Albuquerque and G. Fernández, *J. Am. Chem. Soc.*, 2013, **135**, 2148.

7 (a) M. Kinami, B. R. Crenshaw and C. Weder, *Chem. Mater.*, 2006, **18**, 946; (b) J. N. Palasagaram and R. Ramadoss, *IEEE Sens. J.*, 2006, **6**, 1374.

8 (a) A. Gopal, M. Hifsudheen, S. Furumi, M. Takeuchi and A. Ajayaghosh, *Angew. Chem. Int. Ed.*, 2012, **51**, 10505; (b) G. Fernandez, F. Garcia, F. Aparicio, E. Matesanz and L. Sanchez, *Chem. Commun.*, 2009, 7155; (c) A. Gopal, R. Varghese and A. Ajayaghosh, *Chem. Asian J.*, 2012, **7**, 2061.

9 (a) S. Bhattacharjee and S. Bhattacharya, *Chem. Comm*., 2014, **50**, 11690; (b) V. M. Suresh, A. De and T. K. Maji, *Chem. Commun*., 2015, **51**, 14678; (c) P. Sutar and T. K. Maji. *Inorg. Chem*., 2017, **56**, 9417; (d) P. Sutar and T. K. Maji, *Chem. Commun*., 2016, **52**, 8055.

10 (a) K. Yoosaf, A. R. Ramesh, Jino George, C. H. Suresh, and K. G. Thomas, Chem. Commun., *J. Phys. Chem. C*, 2009, **113**, 11836; (b) A. R. Ramesh and K. G. Thomas, *Chem. Commun*., 2010, **46**, 3457; (c) R. Thomas, S. Varghese and G. U. Kulkarni, *J. Mater. Chem*., 2009, **19**, 4401; (d) R. Gupta, R. Thomas and G. U. Kulkarni, *J. Mater. Chem.*, 2012, **22**, 19139.

11 (a) S. A. Sharber, R. N. Baral, F. Frausto, T. E. Haas, P. Müller and S. W. Thomas III, *J. Am. Chem. Soc.*, 2017, **139**, 5164; (b) R. J. Marshall, Y. Kalinovskyy, S. L. Griffin, C. Wilson, B. A. Blight and R. S. Forgan, *J. Am. Chem. Soc.*, 2017, **139**, 6253.

12 Gaussian 09, Revision D.01, M. J. Frisch, G. W. Trucks, H. B. Schlegel, G. E. Scuseria, M. A. Robb, J. R. Cheeseman, G. Scalmani, V. Barone, B. Mennucci, G. A. Petersson, H. Nakatsuji, M. Caricato, X. Li, H. P. Hratchian, A. F. Izmaylov, J. Bloino, G. Zheng, J. L. Sonnenberg, M. Hada, M. Ehara, K. Toyota, R. Fukuda, J. Hasegawa, M. Ishida, T. Nakajima, Y. Honda, O. Kitao, H. Nakai, T. Vreven, J. A. Montgomery, Jr., J. E. Peralta, F. Ogliaro, M. Bearpark, J. J. Heyd, E. Brothers, K. N. Kudin, V. N. Staroverov, J. Kobayashi, K. Normand, A. Raghavachari, J. C. Rendell, S. S. Burant, J. Iyengar, M. Tomasi, R. Cossi, N. Rega, J. M. Millam, M. Klene, J. E. Knox, J. B. Cross, V. Bakken, C. Adamo, J. Jaramillo, R. Gomperts, R. E. Stratmann, O. Yazyev, A. J. Austin, R. Cammi, C. Pomelli, J. W. Ochterski, R. L. Martin, K. Morokuma, V. G. Zakrzewski, G. A. Voth, P. Salvador, J. J. Dannenberg, S. Dapprich, A. D. Daniels, Ö. Farkas, J. B. Foresman, J. V. Ortiz, J. Cioslowski and D. J. Fox, Gaussian, Inc., Wallingford CT, 2009.

13 (a) J.-D. Chai and M. Head-Gordon, *Phys. Chem. Chem. Phys*., 2008, **10**, 6615; (b) J.-D Chai and M. J. Head-Gordon, *Chem. Phys*., 2008, **8**, 84106.

14 S. V. a. SMART (V 5.628), XPREP, SHELXTL; Bruker AXS Inc. Madison, Wisconsin, USA, 2004.

15 G. M. Sheldrick, SADABS, Empirical Absorption Correction Program. University of Göttingen, Göttingen, 1997.

16 A. Altomare, G. Cascarano, C. Giacovazzo and A. Guagliardi, *J. Appl. Crystallogr*., 1993, **26**, 343.

17 G. M. Sheldrick, SHELXL 97, Program for the Solution of Crystal Structure, University of Göttingen, Germany, 1997.

18 L. Farrugia, *J. Appl. Crystallogr*., 1999, **32**, 837.

19 (a) G. R. Desiraju, *Acc. Chem. Res*., 1996, **29**, 441; (b) G. R. Desiraju, *Chem. Commun*., 2005, 2995.

20 G. R. Desiraju, *Cryst. Growth Des*., 2011, **11**, 896.

21 (a) M. J. Plevin, D. L. Bryce and J. Boisbouvier, *Nat. Chem*., 2010, **2**, 466; (b) M. Nishio, *CrystEngComm*., 2004, **6**, 130.

22 G. R. Desiraju, *Acc. Chem. Res*., 2002, **35**, 565.

Chapter 2C

Pure White Light Emission and Charge Transfer in Organogels of Symmetrical and Unsymmetrical π-Chromophoric *Oligo*-(*p*-phenyleneethynylene) Bola-amphiphiles

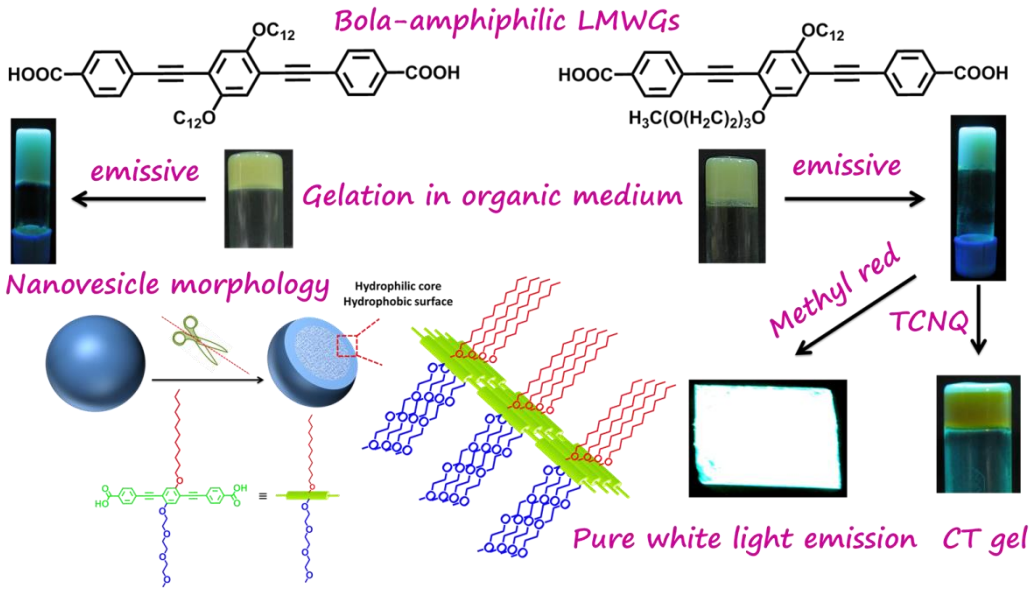

Summary

Two novel bola-amphiphilic *oligo*-(*p*-phenyleneethynylene) (OPE) dicarboxylates (**OPE-C_{12}** and **OPE-C_{mix}**) have been synthesized having non-polar and mixed-polar side chains. The aim was to induce gelation in these compounds. The presence of carboxylic acid end groups, π-rich cores and tetraethyleneglycol and dodecyl side chains in both the OPEs led to gelation in organic solvent mixtures (**OPE-C_{12}-G** and **OPE-C_{mix}-G**). Both self-assembled with a vesicular morphology. As **OPE-C_{mix}-G** contained inward projected alkyl chains, the internal polar nature of the gel scaffold was utilized to encapsulate polar dye (methyl red) and electron acceptor polar molecule (TCNQ). The dye doped gel scaffold showed a partial FRET process from donor gel to acceptor dye. The dye loading concentration was varied to realize pure white light emission with high quantum efficiency. To exhibit the solution processability of the dye doped gels, we coated the white light emitting gel on a glass substrate with no loss of quantum output. The TCNQ loaded gels further showed effective charge transfer from the donor OPE chromophore to the acceptor TCNQ. In this work, the excellent potential of OPE based soft materials in opto-electronic applications was showcased.

The work based on this chapter is published:

S. Roy, D. Samanta, P. Kumar and T. K. Maji, *Chem. Commun.*, 2018, 54, 275-278.

2C.1. Introduction

Oligo-(*p*-phenyleneethynylenes) (OPEs) are a class of π-conjugated systems where phenyl rings are connected via alkyne linkages.[1] Due to the extended π-conjugation, OPEs exhibit exceptional emission properties with a high degree of quantum efficiency.[2] The conjugated backbone also allows facile charge transport and energy migration through its molecular backbone.[3] Additionally, rotational freedom along the single bonds in the connecting unit leads to various conformers with varying emission properties.[4] We have recently prepared several novel bola-amphiphilic OPE systems with carboxylic end groups and varying alkyl chain lengths on the backbone. These showed polymorphism, mechanochromism and liquid crystallinity.[5] Furthermore, coordination directed self-assembly of these bola-amphiphilc OPE systems with metal ions, resulted in MOF nanostructures of different morphologies. These were then exploited for light harvesting, opto-electrical, bi-modal imaging and self-cleaning properties.[6] OPEs can therefore be utilized for the synthesis of several materials having properties of practical importance.

Over the last decade, there has been a wide interest in advancing the science of opto-electronics; to generate state of the art materials with improved efficiency and reduced cost.[7] Specifically, white-light emitting materials are still of immense importance due to their applications in displays and LEDs.[8] In this respect, synthesis of solution processable soft materials which can be applied over large areas without the loss of efficiency are issues that need to be addressed.[9] It has been established that the non-covalent organization of chromophores, to study the energy transfer process in different platforms like silica, clay hybrids, MOFs, gives the best tunable optical output.[10] However, the challenge remains in device fabrication, where retaining the same efficiency after solvent evaporation is a major problem. In this context, synthesizing chromophoric molecules having solvent independent high quantum efficiency and which can non-covalently encapsulate suitable chromophoric guests seem to be a reasonable approach.[11] Also, to use it in advanced opto-electronics, it must allow for an effective electron delocalization, leading to appreciable conductance. In our quest to induce these properties into soft-processable hybrids such as gels,[12] we decided to play around with the polarity of the side chains of end-capped OPE carboxylates, to induce different degrees of gelation interactions in chromophoric bola-amphiphiles. These would lead to emissive and conductive gels of high quantum efficiency which could act as light harvesting platforms for tunable emission with applications also in opto-electronics.

This chapter reports the design and synthesis of two bola-amphiphilic OPE dicarboxylates with didodecyl and triethyleneglycolmonomethylether/dodecyl (TEG) side chains (**OPE-C_{12}** and **OPE-C_{mix}**) for fabricating structures of highly processable luminescent gels (**OPE-C_{12}-G** and **OPE-C_{mix}-G**). Pure white-light emission was achieved by non-covalently encapsulating a suitable acceptor chromophoric dye, methyl red in the gel scaffold (**OPE-C_{mix}-G**). Furthermore, a charge-transfer (CT) gel, by incorporation of an electron acceptor guest TCNQ molecule in **OPE-C_{mix}**-G has also been prepared and characterized.

2C.2. Experimental Section

2C.2.1. Materials

$Pd(PPh_3)_4$, hydroquinone, methyl-4-iodobenzoate, sulforhodamine G and TCNQ were purchased from Sigma-Aldrich chemical Co. Ltd. Cuprous iodide was obtained from Loba Chemie Pvt. Ltd. N,N-dimethyl formamide (DMF) and tetrahydrofuran (THF) were obtained from Spectrochem Pvt. Ltd (Mumbai, India). THF was pre-dried using standard procedure and all other reagents, solvents were of reagent grade and used without further purification.

2C.2.2. Physical Measurements

Elemental analyses were carried out using a Thermo Scientific Flash 2000 CHN analyzer. Fourier transform infrared (FTIR) spectra were recorded by making samples with KBr pellets using Bruker FT-IR spectrometer. ^{1}H and ^{13}C NMR spectrum were recorded on a Bruker AV-400 spectrometer with chemical shifts recorded as ppm and all spectra were calibrated against TMS. Powder X-ray diffraction measurements were carried out on a Bruker D8 discover instrument using Cu-Kα radiation. UV-Vis spectra were recorded in a Perkin-Elmer lamda 900 spectrometer. Fluorescence measurements were accomplished using Perkin Elmer Ls 55 Luminescence spectrometer. The solid state fluorescence quantum yield of samples was determined by using integrating sphere in a Horiba Jobin Yvon instrument. Fluorescence lifetime measurements were recorded with a Horiba Deltaflex spectrometer. Morphology studies were performed using Lica-S440I field emission scanning electron microscopy (FESEM) by placing samples on silicon wafer under vacuum with an accelerating voltage of 10 kV. Transmission electron microscopy (TEM) studies were done on JEOL JEM-3010 with accelerating voltage of 300 kV.

2C.2.3. Synthesis of OPE-C_{12} and OPE-C_{mix}

General procedure and characterization

Chemical shifts (δ) are indicated in ppm. The following abbreviations were used to illustrate NMR signals: s = singlet, d = doublet, t = triplet, td = triplet of doublets, dd = doublet of doublets, ddd = doublet of doublets of doublets, m = multiplet. Methyl 4-ethynylbenzoate,[13] 2-(2-(2-methoxyethoxy)ethoxy)ethyl 4-methylbenzenesulfonate,[14] 4-(dodecyloxy)phenol[15] and 4,4'-((2,5-bis(dodecyloxy)-1,4-phenylene)bis(ethyne-2,1-diyl))dibenzoic acid[16] were prepared according to reported procedures. OPE-C_{12} was synthesized according to reported procedures (Scheme 2).[5,16]

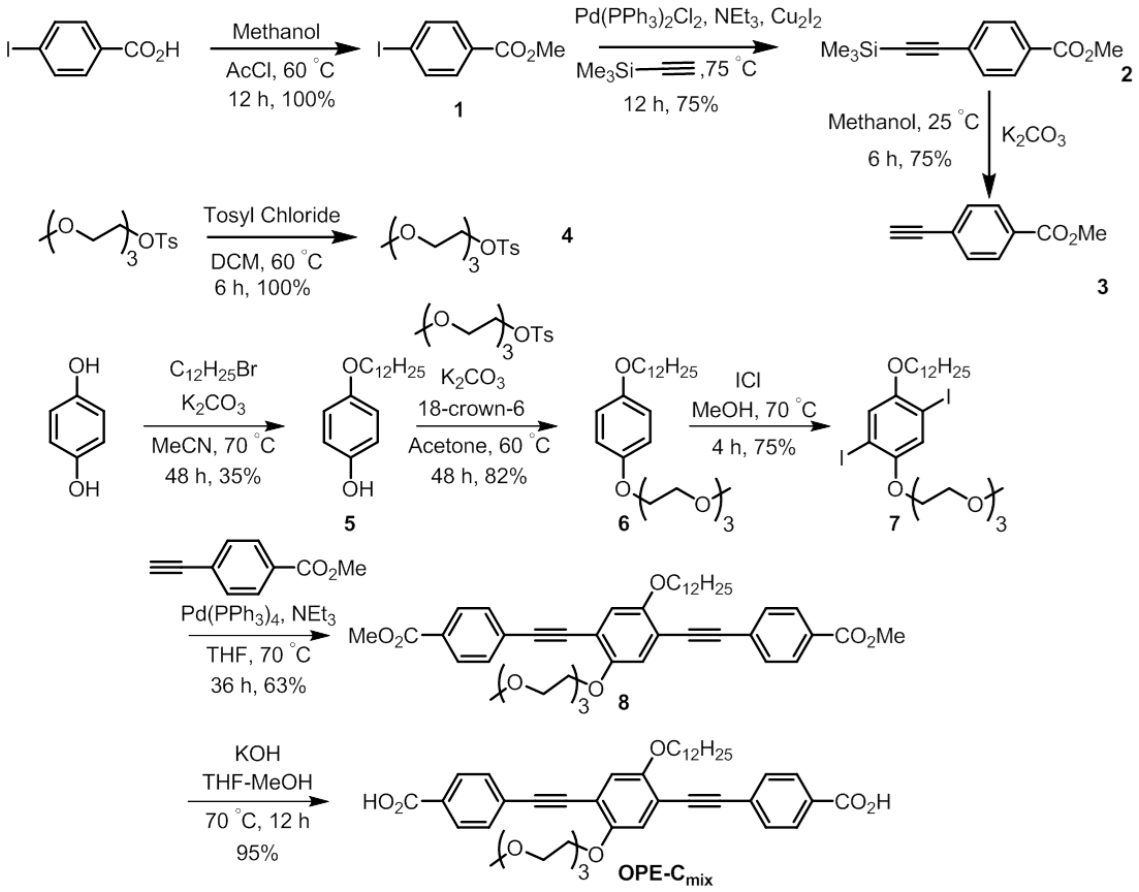

Scheme 1. Synthetic scheme for **OPE-C_{mix}**.

Synthesis of 1-(dodecyloxy)-4-(2-(2-(2-methoxyethoxy)ethoxy)ethoxy)benzene (6). Solid K_2CO_3 (4.70 g, 33.8 mmol) was added portion wise to a stirring solution of 4-(dodecyloxy)phenol (**5**) (4.70 g, 16.9 mmol), 2-(2-(2-methoxyethoxy)ethoxy)ethyl 4-methylbenzenesulfonate (**4**) (5.85 g, 16.9 mmol) and 18-crown-6 (446 mg, 1.69 mmol) in 50 mL acetone. The solution was refluxed at 60 °C for 2 days to complete the reaction.

The reaction mixture was filtered to remove excess K_2CO_3 and the filtrate was concentrated under rotary evaporator. The crude product was purified by column chromatography (silica gel, hexane/ethyl acetate = 10:1) yielding 1-(dodecyloxy)-4-(2-(2-(2-methoxyethoxy)ethoxy)ethoxy)benzene (**6**) as white solid (7.12 g, 16.8 mmol, 99% yield). ^{1}H NMR (400 MHz, $CDCl_3$) δ = 0.88 (t, *J* = 6.8 Hz, 3H), 1.27-1.37 (m, 16H), 1.49 (q, *J* = 7.2 Hz, 2H), 1.80 (q, *J* = 8.0 Hz, 2H), 3.38 (s, 3H), 3.54-3.57 (m, 2H),), 3.66-3.70 (m, 4H), 3.77-3.80 (m, 2H), 3.87 (t, *J* = 4.4 Hz, 2H), 3.92 (t, *J* = 6.4 Hz, 2H), 4.10 (t, *J* = 5.2 Hz, 2H), 7.16-7.17 (m, 2H), 7.24-7.15 (m, 2H) ppm. ^{13}C NMR (100 MHz, $CDCl_3$) δ = 14.3, 22.8, 26.2, 29.5, 29.6, 29.6, 29.8, 29.8, 29.8, 29.8, 32.1, 59.2, 68.3, 68.8, 70.1, 70.7, 70.8, 71.0, 72.1, 115.6, 115.8, 153.0, 153.7 ppm. HRMS-EI (*m/z*) for $C_{25}H_{44}O_5$ [M^+] Calcd. 424.319, found 424.318. Anal. Calcd. for $C_{25}H_{44}O_5$: C, 70.72; H, 10.44. Found: C, 70.97; H, 10.15.

Synthesis of 1-(dodecyloxy)-2,5-diiodo-4-(2-(2-(2-methoxyethoxy)ethoxy)ethoxy)benzene (7). A solution of 1-(dodecyloxy)-4-(2-(2-(2-methoxyethoxy)ethoxy)ethoxy)benzene (**7**) (6.00g, 14.1 mmol) in 30 mL methanol was added dropwise to a stirring solution of iodine monochloride (9.18 g, 56.5 mmol) in 100 mL methanol at 0 °C. The resulting reaction mixture was refluxed overnight to complete the iodination process. The reaction mixture was cooled down to 0 °C and, then, excess iodine monochloride was quenched by addition of saturated aqueous solution of sodium thiosulfate. The crude product was extracted by dichloromethane (5×50 mL), dried over $MgSO_4$ and concentrated by rotary evaporator. The crude product was chromatographed (silica gel, hexane/ethyl acetate = 15: 1) to get 1-(dodecyloxy)-2,5-diiodo-4-(2-(2-(2-methoxyethoxy)ethoxy)ethoxy)benzene (**7**) as white solid (8.79 g, 13.0 mmol, 92% yield). ^{1}H NMR (400 MHz, $CDCl_3$) δ = 0.88 (t, *J* = 6.9 Hz, 3H), 1.27-1.37 (m, 16H), 1.49 (q, *J* = 7.8 Hz, 2H), 1.80 (q, *J* = 6.4 Hz, 2H), 3.38 (s, 3H), 3.54-3.57 (m, 2H), 3.66-3.70 (m, 4H), 3.77-3.80 (m, 2H), 3.89 – 3.86 (m, 2H), 3.93 (t, *J* = 6.4 Hz, 2H), 4.12 – 4.08 (m, 2H), 7.16 (s, 1H), 7.25 (s, 1H) ppm. ^{13}C NMR (100 MHz, $CDCl_3$) δ = 14.3, 22.9, 26.2, 29.3, 29.4, 29.5, 29.7, 29.7, 29.8, 29.8, 32.1, 59.2, 69.8, 70.5, 70.6, 70.8, 71.0, 71.3, 72.2, 86.4, 86.7, 122.8, 123.9, 153.0, 153.5 ppm. HRMS-EI (*m/z*) for $C_{25}H_{42}I_2O_5$ [M^+] Calcd. 676.112, found 676.112. Anal. Calcd. for $C_{25}H_{42}I_2O_5$: C, 44.39; H, 6.26. Found: C, 44.07; H, 6.18.

Synthesis of dimethyl 4,4'-((2-(dodecyloxy)-5-(2-(2-(2-methoxyethoxy)ethoxy)ethoxy)-1,4-phenylene)bis(ethyne-2,1-diyl))dibenzoate (8). A

250 mL three-neck round-bottomed flask, charged with 1-(dodecyloxy)-2,5-diiodo-4-(2-(2-(2-methoxyethoxy)ethoxy)ethoxy)benzene (**7**) (1.00 g, 1.48 mmol), methyl 4-ethynylbenzoate (**3**) (1.18 g, 7.39 mmol), 25 mL tetrahydrofuran and 10 mL triethylamine, was degassed by freeze-pump-thaw procedure (three times). The $Pd(PPh_3)_4$ (340 mg, 296 µmol) was added to it. The resulting reaction mixture was refluxed at 70 °C for 48 h under inert atmosphere for completion of the coupling reaction. The resulting solution was concentrated and purified by column chromatography (silica gel, dichloromethane/ethyl acetate = 98:2) to obtain dimethyl 4,4'-((2-(dodecyloxy)-5-(2-(2-(2-methoxyethoxy)ethoxy)ethoxy)-1,4-phenylene)bis(ethyne-2,1-diyl))dibenzoate (**8**) (0.67 g, 904 µmol, 61% yield) as greenish-yellow solid compound. ^{1}H NMR (400 MHz, $CDCl_3$) δ = 0.87 (t, *J* = 6.9 Hz, 1H), 1.24-1.42 (m, 16H), 1.50-1.60 (m, 2H), 1.86 (q, *J* = 7.8 Hz, 2H), 3.50-3.53 (m, 2H), 3.61-3.67 (m, 4H), 3.80-3.82 (m, 2H), 3.92-3.94 (m, 8H), 4.04 (t, *J* = 6.4 Hz, 2H), 4.22 (t, *J* = 5.2 Hz, 2H), 7.02 (s, 1H), 7.06 (s, 1H), 7.59 (d, *J* = 7.7 Hz, 2H), 8.03 (d, *J* = 8.4 Hz, 2H) ppm. ^{13}C NMR (100 MHz, $CDCl_3$) δ = 14.3, 22.8, 26.3, 29.5, 29.5, 29.6, 29.8, 29.8, 29.8, 29.9, 32.1, 52.4, 52.4, 59.2, 69.8, 70.0, 70.7, 70.9, 71.3, 72.1, 89.0, 94.5, 114.2, 117.1, 117.7, 128.2, 129.7, 129.7, 129.8, 131.6, 153.6, 154.3, 166.7 ppm. HRMS-EI (*m/z*) for $C_{45}H_{56}O_9$ [M^+] Calcd. 740.392, found 740.395. Anal. Calcd. for $C_{45}H_{56}O_9$: C, 72.95; H, 7.62. Found: C, 72.89; H, 7.49.

Synthesis of 4,4'-((2-(dodecyloxy)-5-(2-(2-(2-methoxyethoxy)ethoxy)ethoxy)-1,4-phenylene)bis(ethyne-2,1-diyl))dibenzoic acid (OPE-C_{mix}). K_2CO_3 flakes (1.00 g, 7.25 mmol) was added to a solution of 4,4'-((2-(dodecyloxy)-5-(2-(2-(2-methoxyethoxy)ethoxy)ethoxy)-1,4-phenylene)bis(ethyne-2,1-diyl))dibenzoate (**8**) (500 mg, 675 µmol) in 40 mL methanol. The resulting solution was refluxed for 12 h at 70 °C to complete ester hydrolysis. The clear solution was added dropwise over 4 N aq. HCl solution (250 mL) and greenish-yellow precipitate of 4,4'-((2-(dodecyloxy)-5-(2-(2-(2-methoxyethoxy)ethoxy)ethoxy)-1,4-phenylene)bis(ethyne-2,1-diyl))dibenzoic acid (**OPE-C_{mix}**) was formed which was filtered off and washed with water (100 mL) and methanol (25 mL, caution: slightly soluble) to get pure compound (420 mg, 589 µmol, 87% yield). ^{1}H NMR (400 MHz, DMSO-d_6) δ = 0.83 (t, *J* = 6.9 Hz, 1H), 1.12-1.23 (m, 14H), 1.30-1.40 (m, 2H), 1.50 (q, *J* = 8.0 Hz, 2H), 1.50 (q, *J* = 8.0 Hz, 2H), 1.75 (q, *J* = 7.8 Hz, 2H), 3.19 (s, 3H), 3.47-3.53 (m, 6H), 3.66-3.69 (m, 2H), 3.80 (t, *J* = 4.4 Hz, 2H), 4.07 (t, *J* = 6.0 Hz, 2H), 4.20 (t, *J* = 4.4 Hz, 2H), 7.23 (s, 1H), 7.25 (s, 1H), 7.60-7.65 (m, 4H), 7.97-7.99 (m, 4H), 13.1 (br, 1H) ppm. ^{13}C NMR (100 MHz, $CDCl_3$, DMSO-d^6) δ = 13.8, 22.3,

25.7, 29.0 (2C), 29.1, 29.3, 29.3, 29.3, 29.3, 31.6, 58.6, 69.3, 69.4, 69.5, 70.2, 70.4, 70.8, 71.6, 88.3, 94.3, 113.7, 113.9, 116.7, 117.3, 127.3, 129.4, 130.3, 131.0, 153.1, 153.8, 167.5 ppm. HRMS-EI (*m/z*) for $C_{43}H_{52}O_9$ [M^+] Calcd. 712.361, found 712.360. Anal. Calcd. for $C_{43}H_{52}O_9$: C, 72.45; H, 7.35. Found: C, 72.40; H, 7.19.

Synthesis of 4,4'-(2,5-bis(dodecyloxy)-1,4-phenylene)bis(ethyne-2,1-diyl)dibenzoic acid (OPE-C_{12}). K_2CO_3 flakes (1.00 g, 7.25 mmol) was added to a solution of dimethyl 4,4'-(2,5-bis(dodecyloxy)-1,4-phenylene)bis(ethyne-2,1-diyl)dibenzoate (**6**), (Scheme 2) (500 mg, 684 μmol) in 40 mL methanol. The resulting solution was refluxed for 12 h at 70 °C to complete ester hydrolysis. The clear solution was added dropwise over 4 N aq. HCl solution (250 mL) and greenish-yellow precipitate of 4,4'-(2,5-bis(dodecyloxy)-1,4-phenylene)bis(ethyne-2,1-diyl)dibenzoic acid (**OPE-C_{12}**) was formed which was filtered off and washed with water (100 mL) and methanol (25 mL, caution: slightly soluble) to get pure compound (410 mg, 558 μmol, 82% yield). ^{1}H NMR (400 MHz, DMSO-d_6) δ = 0.87 (t, *J* = 6.9 Hz, 3H), 1.25-1.30 (m, 16H), 1.42 (q, J= 8.0 Hz, 2H), 1.75 (q, *J* = 7.8 Hz, 2H), 4.05 (t, *J* = 6.0 Hz, 2H), 7.40 (s, 1H), 7.79 (d, J= 8.0 Hz, 1H), 8.16 (d, J= 8.0 Hz, 1H), 12.8 (br, 1H) ppm. ^{13}C NMR (100 MHz, $CDCl_3$, DMSO-d^6) δ = 14.1, 22.6, 25.8, 29.2, 29.5, 29.5, 29.5, 29.5, 29.5, 29.5, 31.8, 68.0, 84.1, 95.8, 112.2, 118.2, 127.8, 129.8, 132.1, 151.2, 169.2 ppm. HRMS-EI (*m/z*) for $C_{48}H_{62}O_6$ [M^+] Calcd. 735.000, found 735.006. Anal. Calcd. for $C_{48}H_{62}O_6$: C, 78.44; H, 8.50. Found: C, 78.38; H, 7.91.

Preparation of gels of OPE-C_{12} and OPE-C_{mix}

10 mg of **OPE-C_{12}** and **OPE-C_{mix}** were dissolved in 0.25 mL of ethylacetate at 333 K. This was followed by the addition of 0.75 mL of toluene while constantly shaking the vial. The solution was allowed for stand for 1 min after which it entirely converted into a stable gel phase. The formed gels were dissolved at 333 K to form the sol state and again reverted back to the gel state thus proving their thermoreversibility. The gels could be prepared in other solvent mixtures of benzene/ ethylacetate, cyclohexane/ ethylacetate and hexane/ ethylacetate as well and is tabulated in Table 1.

Preparation of gel with methyl red (MR) dye

10 mol% of MR was dissolved in ethyl acetate along with **OPE-C_{mix}-G** at 60 ^{0}C. Toluene was added dropwise to the mixture and allowed to stand for 5 mins when an orange

colored gel formed (**MR10@ OPE-C_{mix}-G**). Mixed gels of other concentrations (1, 2 and 5) mol% were also prepared following the above procedure.

Table 1. Tabulation of the solvent ratios in which **OPE-C_{12}** and **OPE-C_{mix}** gels are prepared.

	Toluene/ EtOAc 3:1	Benzene /EtOAc 3:1	Cyclohexane /EtOAc 3:1	Hexane/ EtOAc 3:1
OPE-C_{12}	Yes	Yes	Yes	Yes
OPE-C_{mix}	Yes	Yes	Yes	Yes

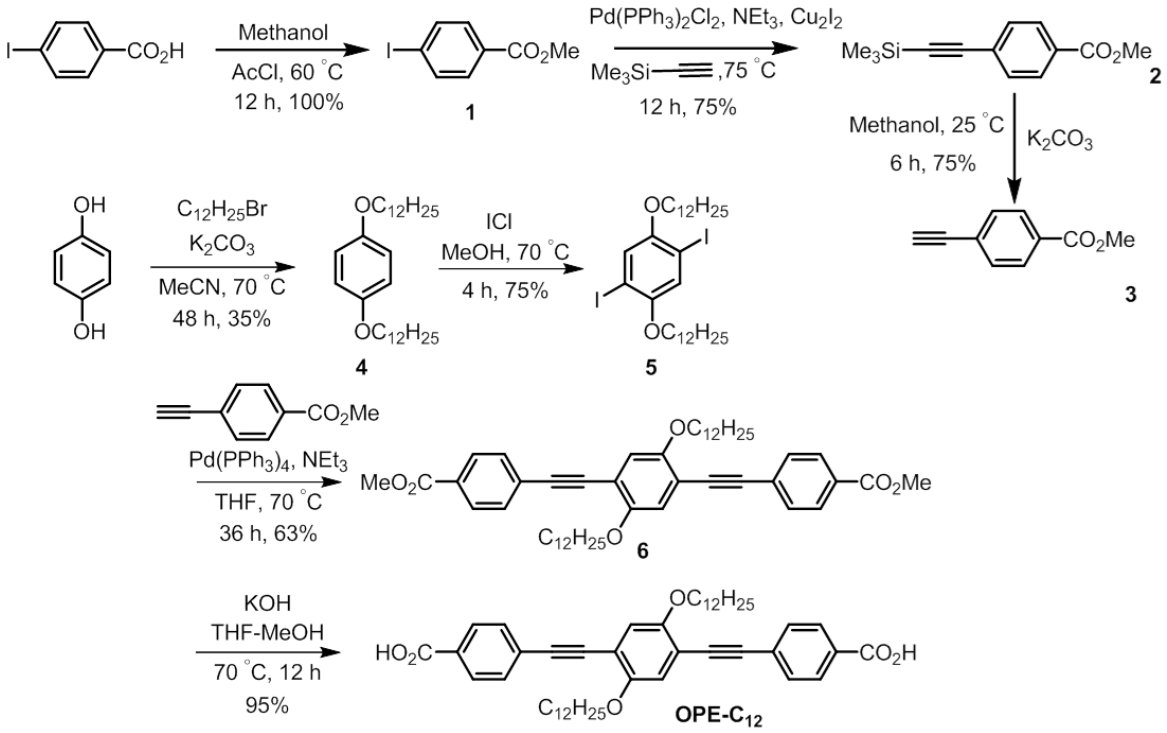

Scheme 2. Synthetic scheme of **OPE-C_{12}**.

Preparation of OPE-C_{mix} gel with TCNQ

0.50 mol% TCNQ was dissolved in ethylacetate along with **OPE-C_{mix}-G** at 60 ºC. Toluene was added dropwise to the mixture and allowed to stand for 5 mins when a dark

green colored gel formed (**$TCNQ_{0.5}$@OPE-C_{mix}-G**). **$TCNQ_{0.25}$@OPE-C_{mix}-G** was also prepared following the above procedure.

2C.3. Results and Discussion

2C.3.1. Structural Characterization

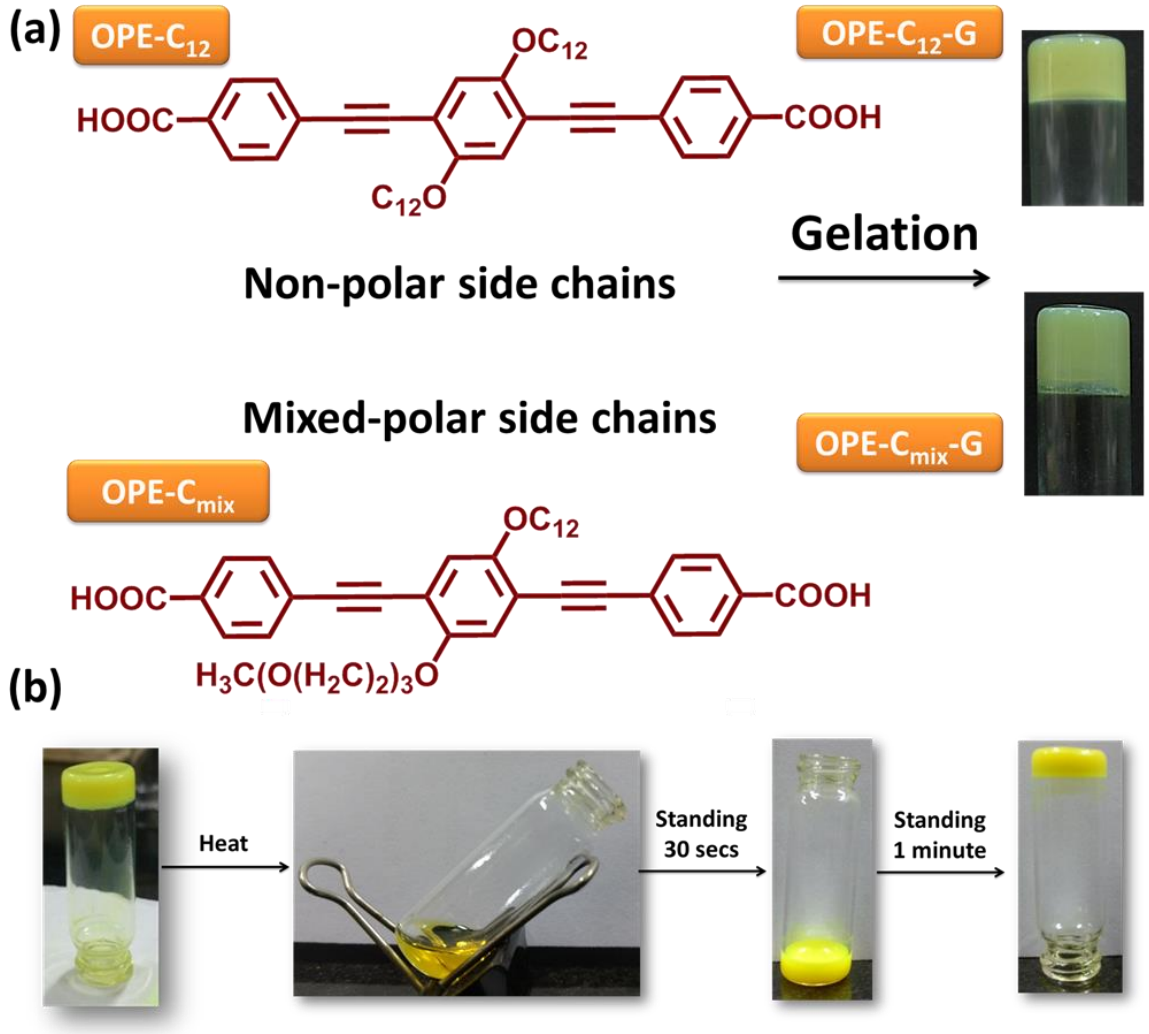

Figure 1. (a) Schematic showing the gelation of two bola-amphiphilic chromophores and (b) Images of the thermoreversibility test performed on **OPE-C_{mix}**.

The Sonogashira-Hagihara coupling scheme was employed for the synthesis of **OPE-C_{12}** and **OPE-C_{mix}**.[13] We substituted the side chains of the OPE backbone from didodecyl (**OPE-C_{12}**) on both sides to dodecyl and triethyleneglycol (**OPE-C_{mix}**) side chains on each side, keeping in mind the interesting change in physical properties this can induce (Scheme 1, 2). This resulted in two novel OPE bolamphilhiles; **OPE-C_{12}** and **OPE-C_{mix}**. Due to the presence of π-rich cores, carboxylic acid groups and/or TEG side chains in

these, we decided to check their gelation abilities in different solvents. **OPE-C_{12}** and **OPE-C_{mix}** containing two and one dodecyl alkyl chains respectively formed a gel phase in a mixture of 3:1 toluene/benzene/hexane/cyclohexane:

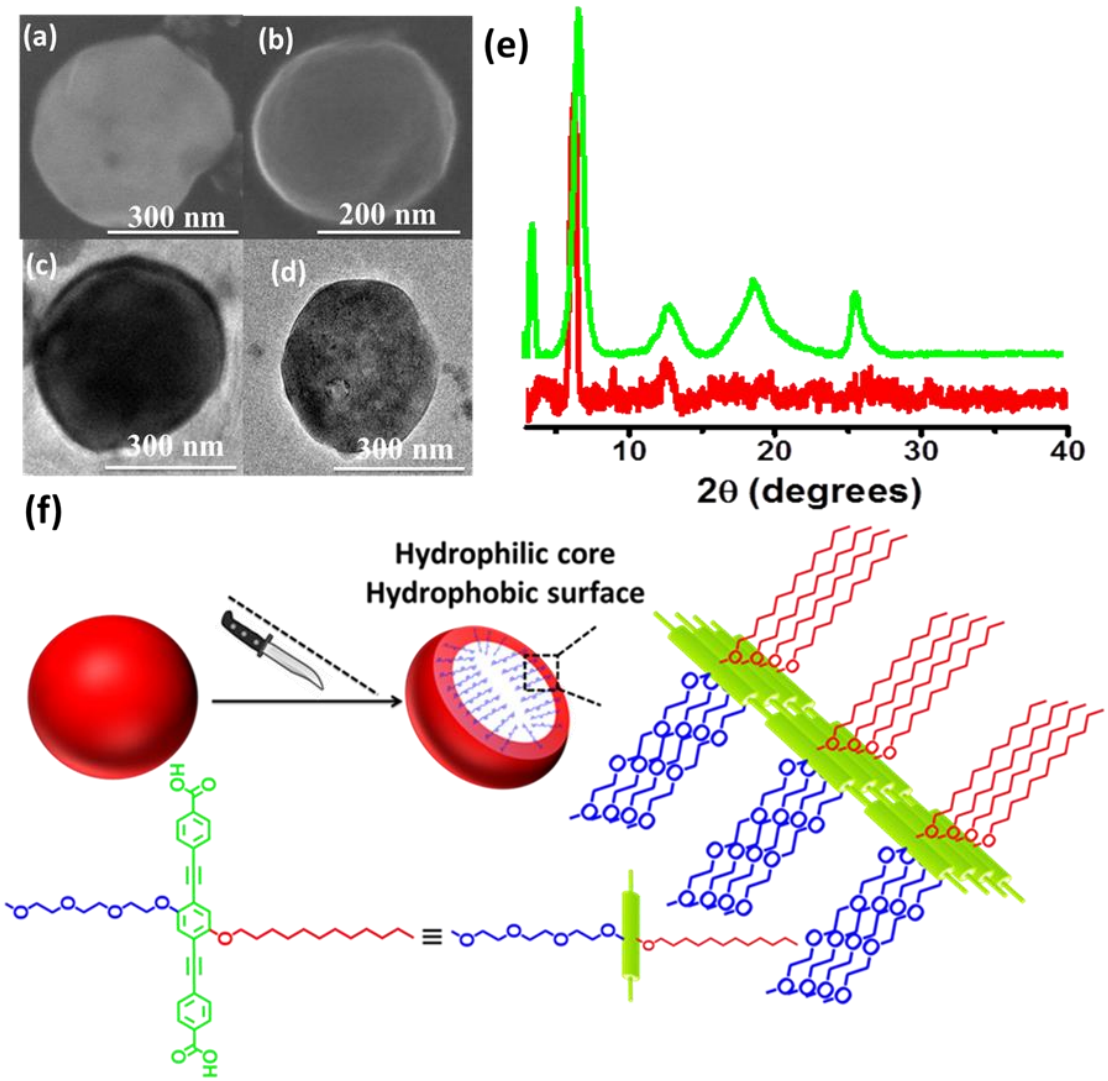

Figure 2. FESEM images of (a) **OPE-C_{12}-G** and (b) **OPE-C_{mix}-G**. PXRD of **OPE-C_{12}-G** (red) and **OPE-C_{mix}-G** (green) xerogels, TEM images of (c) **OPE-C_{12}-G** and (d) **OPE-C_{mix}-G**, (e) PXRD of **OPE-C_{12}-G** (red) and **OPE-C_{mix}-G** (green) xerogels and (f) Schematic showing the molecular packing in the vesicular form of **OPE-C_{mix}-G** having inwards projected TEG side chains and outward projected alkyl chains.

ethylacetate (Table 1). The gel formation was instant (Figure 1a). Table 1 indicates the different solvents in which **OPE-C_{12}** and **OPE-C_{mix}** transformed into the gel state. The existence of the two gel states was confirmed by the inversion test. Interestingly, the gel states were attained every time they were subjected to repeated heating and cooling cycles

(Figure 1b). This indicated the thermo-reversibility of **OPE-C_{12}-G** and **OPE-C_{mix}-G**. The gels also transformed into the sol state upon sonication and immediately formed back to the gel state when allowed to stand. This revealed their thixotropic nature. The critical gelation concentration of **OPE-C_{12}-G** and **OPE-C_{mix}-G** was 4.1 wt% and 3.6 wt%, respectively. PXRD peaks portrayed the crystalline nature of both **OPE-C_{12}-G** and **OPE-C_{mix}-G** (Figure 2e). Field emission scanning electron microscopy (FESEM) and transmission electron microscopy (TEM) provided insights into the nanomorphology of **OPE-C_{12}-G** and **OPE-C_{mix}-G** (Figure 2a-d). It was observed that both **OPE-C_{12}-G** and **OPE-C_{mix}-G** formed a vesicular morphology with a diameter of 300-350 nm. TEM images of **OPE-C_{12}-G** and **OPE-C_{mix}-G** also corroborate that both are nanovesicles, with a dark shell and bright core.[6a]

To further probe structural packing of the gels, we carried out water contact angle measurements on gel coated glass substrates. Interestingly, both the coatings showed hydrophobic contact angles of 145^0 and 130^0 for **OPE-C_{12}-G** and **OPE-C_{mix}-G** respectively (Figure 3). This was further indicative of the fact that both gels contained surface projected alkyl chains, which decrease the surface energy, leading to water repellence. This observation also pointed out that **OPE-C_{mix}-G** contains inward projected polar glycol chains (Figure 2f).

2C.3.2. Photoluminescence Studies

Due to the presence of a chromophoric bola-amphiphilic unit in all of these structures, we then decided to investigate the photoluminescence properties of **OPE-C_{12}**, **OPE-C_{mix}**, **OPE-C_{12}-G** and **OPE-C_{mix}-G**. Solution of **OPE-C_{12}** and **OPE-C_{mix}** in ethyl acetate/toluene mixture resulted in absorption peak maxima at 320 nm and 380 nm, respectively (Figure 4a,c). The emission maximum was found at 430 nm for both in the solution state (Figure 4b,d). In the solid state, **OPE-C_{12}** absorbed at 430 nm and **OPE-C_{mix}** absorbed at 400 nm (Figure 5a). Upon excitation at at 380 nm, **OPE-C_{12}** showed an emission maximum at 485 nm whereas the maximum was found at 500 nm for **OPE-C_{mix}** (Figure 5b). The gels showed the same absorption maxima as the corresponding ligands (Figure 6a), while the emission peak maxima appeared at 500 nm and 520 nm for **OPE-C_{12}-G** and **OPE-C_{mix}-G** respectively (Figure 6b). Both the corresponding gels exhibited cyan emission under UV light (Figure 6b inset).

It was also observed that there was a shoulder at 520 nm for **OPE-C_{12}-G**. This generally arises when there is a large degree of torsion in the central phenyl ring away from the plane containing the terminal phenyl rings.[17] As the peak maximum for **OPE-C_{mix}-G** was observed at 520 nm, it is indicating, that the torsion angle between its terminal and central phenyl rings is more than that of **OPE-C_{12}-G**. This may be due to the asymmetry induced

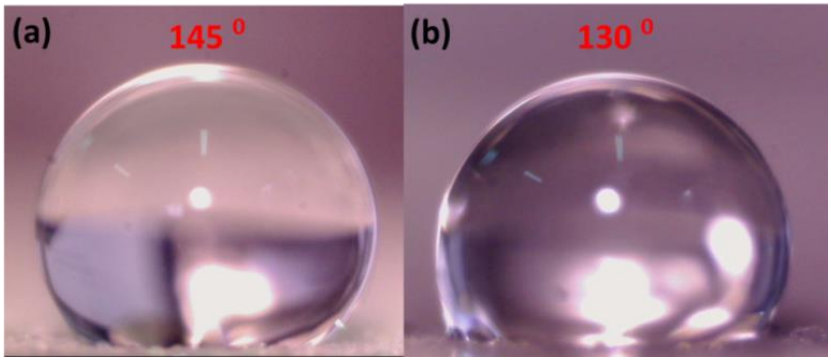

Figure 3. Contact angles of a 5µL water droplet on glass surfaces coated with (a) **OPE-C_{12}-G** and (b) **OPE-C_{mix}-G** xerogels.

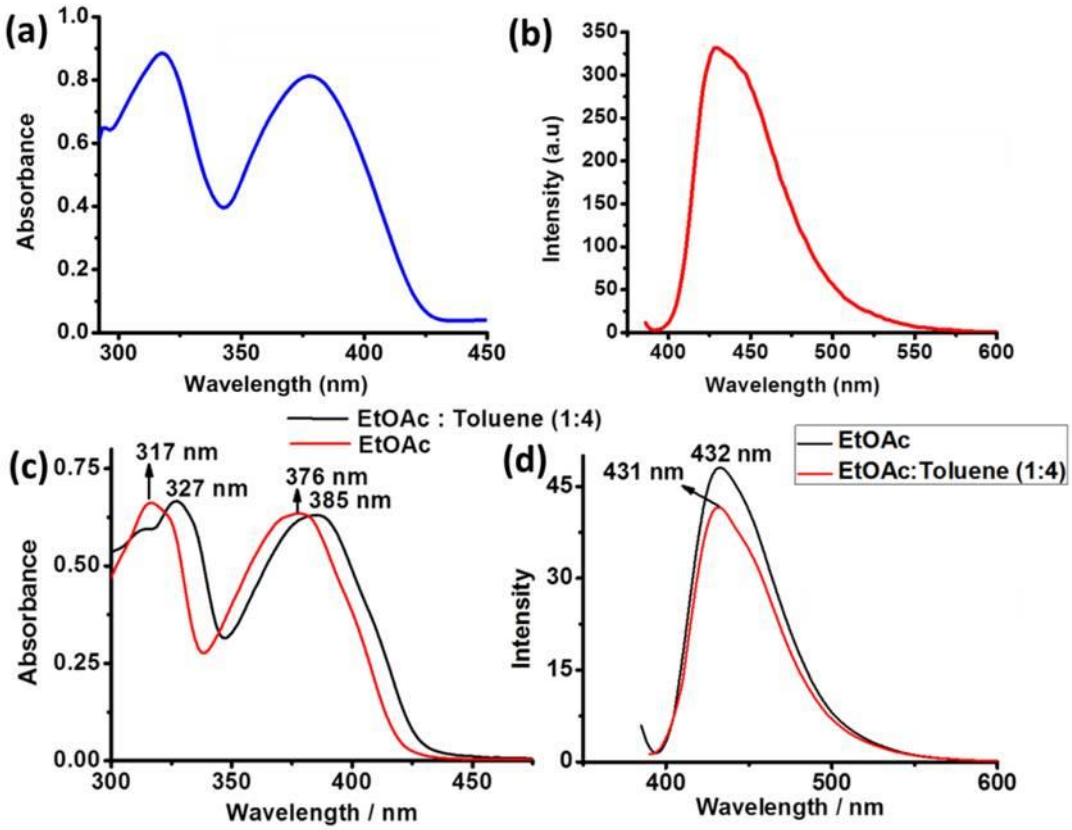

Figure 4. (a,c) UV-Vis spectra for **OPE-C_{12}** and **OPE-C_{mix}** respectively in a ethyl acetate/toluene mixture and (b,d) emisison spectra for **OPE-C_{12}** and **OPE-C_{mix}** in a ethyl acetate (black) and ethyl acetate/toluene (red) mixture.

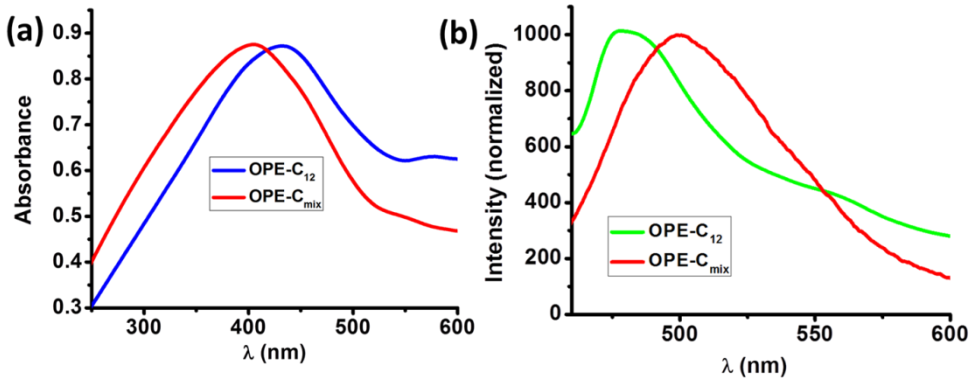

Figure 5. (a) Solid state UV spectra and of **OPE-C$_{12}$** (blue) and **OPE-C$_{mix}$** (red) and (b) Solid state emission spectra of **OPE-C$_{12}$** (green) and **OPE-C$_{mix}$** (red). (λ_{ex}=380 nm).

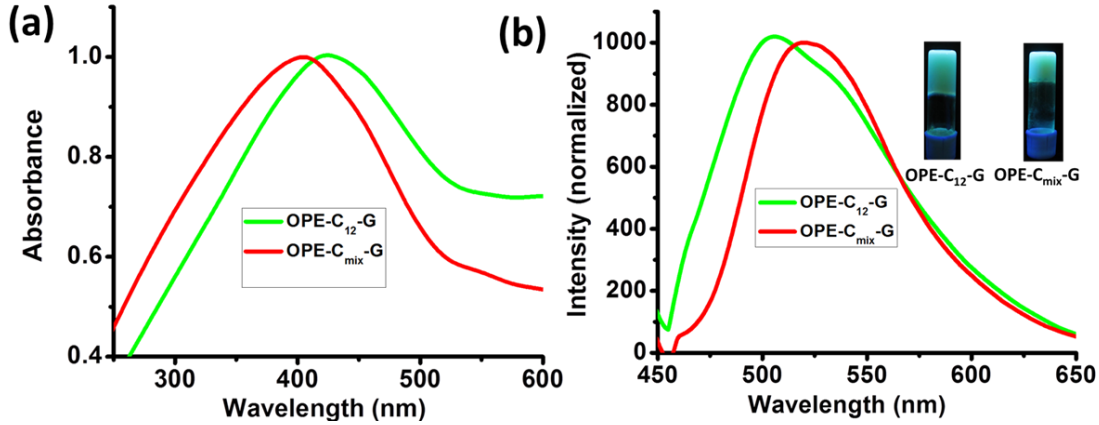

Figure 6. (a) Solid state UV spectra of **OPE-C$_{12}$-G** (green) and **OPE-C$_{mix}$-G** (red) xerogels and (b) Solid state emission spectra of **OPE-C$_{12}$-G** (green) and **OPE-C$_{mix}$-G** (red). (λ_{ex}=380 nm).

in the system due to the presence of TEG side chains. The quantum yield of the gels was also recorded to obtain a value for 32% and 40% for **OPE-C$_{12}$-G** and **OPE-C$_{mix}$-G**, respectively. These high values of quantum yields projected them as excellent materials for advanced optics.

Dichromaticity approach indicates that an overlap of cyan and orange colors could lead to white light emission. In order to control such emission overlaps, a partial overlap of donor-acceptor systems are desired. Based on the relative concentrations of both, the emission intensity could be controlled. **OPE-C$_{mix}$-G** was selected as the material of our interest due to its emission covering the cyan region. To utilize a specific dye molecule to achieve this aim, we found methyl red (MR) whose absorption overlaps partially with the emission spectrum of **OPE-C$_{mix}$-G** and also emits covering the orange region of spectrum. Figure 7a shows that the emission spectrum of 520 nm whereas the absorption

of methyl red peaks at 500 nm. This partial overlap was ideal for incorporating this dye into the gel for energy transfer applications and also to tune its emission color. Another advantage in combining **OPE-C_{mix}-G** and MR was the favorable interaction between the inward projected glycol chains with the carboxylic acid groups of MR, thus leading to proper encapsulation. The pure gel **OPE-C_{mix}-G** exhibited cyan emission (λ_{max}= 520 nm) along with an emission tail in the blue region upon excitation at 380 nm. Its CIE coordinate was found to be (0.27, 0.60) (Figure 7d). Incorporation of MR in **OPE-C_{mix}-G** was carried out in situ during gel formation. **MR@OPE-C_{mix}-G** gel formation was evidenced by a change in color from green to orange under visible light (Figure 7a, inset).

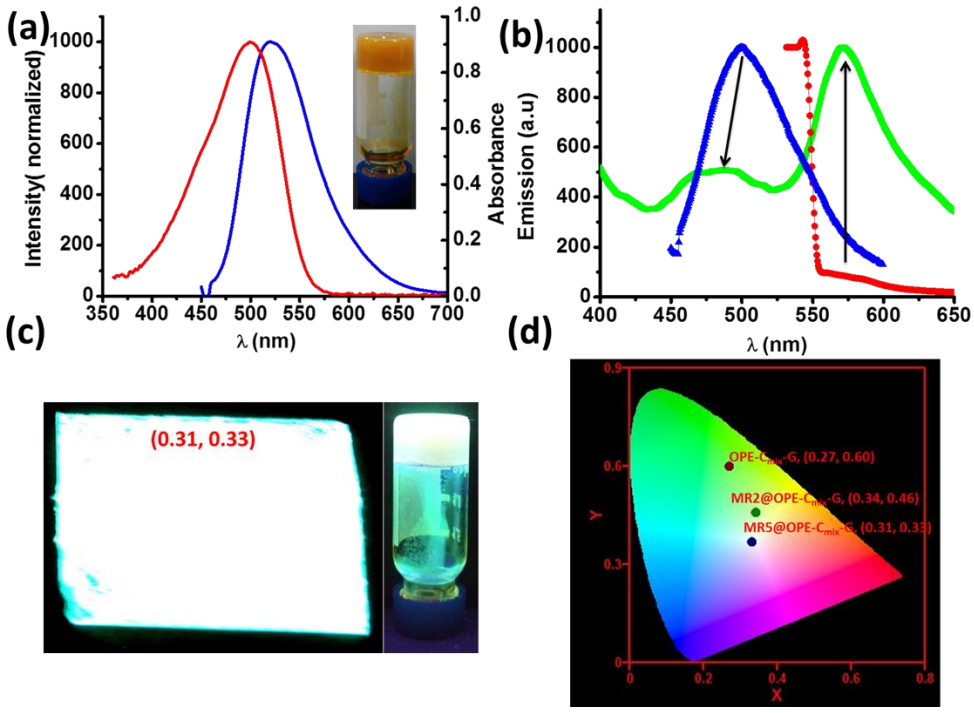

Figure 7. (a) Plot showing spectral overlap between the donor gel emission (blue) and acceptor dye absorbance (red). Inset: image of orange colored gel formation in **MR@OPE-C_{mix}** upon MR loading, (b) Emission profile upon exciting **OPE-C_{mix}-G** (blue); **MR10@OPE-C_{mix}G** (green) at 380 nm. Emission spectra of **MR10@OPE-C_{mix}-G** upon direct excitation at 500 nm (red), (c) Image under UV light of **MR5@OPE-C_{mix}-G** coated glass substrate and in an inverted glass vial and (d) CIE coordinates of different loading percentages of **MR@OPE-C_{mix}-G**.

MR@OPE-C_{mix}-G also passed the thermo-reversibility test. Steady state fluorescence studies were carried out with 10 mol% of MR in **OPE-C_{mix}-G** (**MR10@ OPE-C_{mix}-G**). Upon excitation at 380 nm, it showed two peaks at 500 nm corresponding to donor

emission and at 590 nm related to dye emission, respectively, with CIE of (0.33, 0.37) (Figure 7b,d). In **MR10@OPE-C_{mix}-G**, the MR emission intensity at 590 nm showed marked decrease upon direct excitation at MR (500 nm) as compared to the excitation at 380 nm, i.e., **OPE-C_{mix}** donor (380 nm, Figure 7b). The excitation spectra observed at 590 nm indicated peaks at 500 nm and 400 nm, respectively (Figure 8a). All these observations pointed to funneling of excitation energy from donor gel scaffold to the encapsulated dye. To further conclusively prove the light harvesting property of **MR10@OPE-C_{mix}-G**, we measured fluorescence decay profiles on **OPE-C_{mix}-G** and **MR10@OPE-C_{mix}-G**. Decay profiles monitored at 485 nm, upon excitation of **OPE-C_{mix}-G** (404 nm), revealed an excited state lifetime of 1.9 ns (Figure 9a). The same monitoring for **MR10@OPE-C_{mix}-G** showed a lifetime of 1.2 ns, indicating a decrease in the donor lifetime in the hybrid gel. Furthermore, direct excitation of MR at 485 nm, monitored at 590 nm, showed a lower lifetime of 0.9 ns, compared to indirect excitation at 404 nm, where the MR lifetime was found to be 1.7 ns (Figure 9b). All these observations clearly indicated a FRET process between **OPE-C_{mix}-G** and MR. Furthermore, to bring the CIE closer to pure white-light emission (0.33, 0.33), we decreased the concentration of MR to 5 mol%. We observed that emission bands appeared at 500 nm and 590 nm similar to **MR10@OPE-C_{mix}-G** albeit with different intensities (Figure 8b). The CIE coordinate was calculated to be (0.31, 0.33) indicating a pure white light emission (Figure 7d). The images of **MR5@OPE-C_{mix}-G** also revealed pure white light emission with high intensity (Figure 7c). Figure 8b also shows that upon increasing the loading concentration from 1 mol% to 10 mol%, the donor band at 500 nm becomes gradually broadened along with a blue-shift in the emission maxima to 450 nm. This indicates that higher loading percentages led to a combination of monomeric and aggregated OPE-based emission. The quantum yield of **MR5@OPE-Cmix-G** was found to be 35% which is comparable to the best white light emitting soft materials.[10,11] To show the processability of the gel hybrids, we coated them onto a glass plate (Figure 7c). Due to the easy solution processability and thixotropy of the gel, we could create a smooth coating on the surface of a glass plate. Upon illumination, the coated glass surface exhibited white light emission with high intensity.

2C.3.3. Charge Transfer Gels

The ease of incorporating MR further encouraged us to incorporate redox active molecules within the gel. Redox dopants such as TCNQ can induce effective charge

delocalization by forming donor-acceptor charge transfer systems with electron rich molecules.

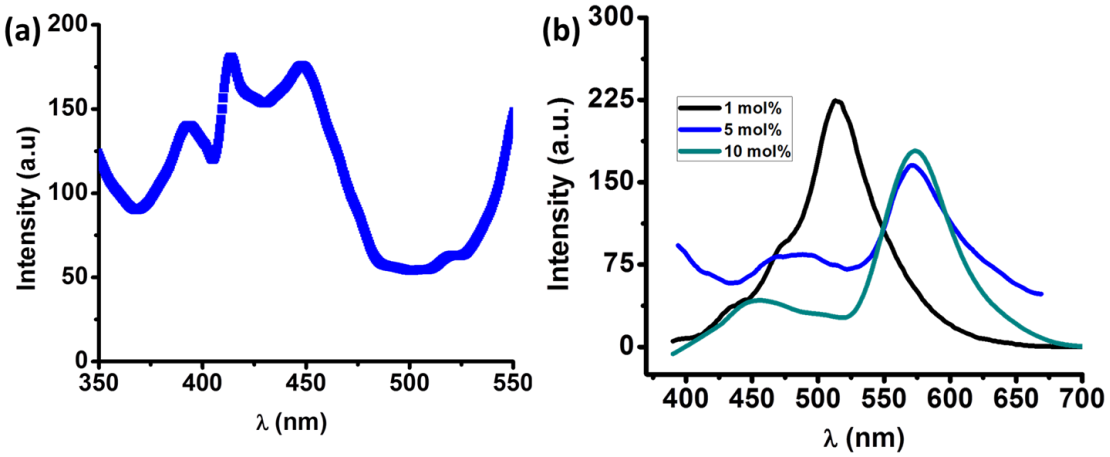

Figure 8. (a) Excitation spectra of **MR10@OPE-C$_{mix}$-G** monitored at 590 nm and (b) Emission plots (λ_{ex}= 380 nm) of pure **OPE-C$_{mix}$-G** and **MR@OPE-C$_{mix}$-G** at different loading concentrations of MR.

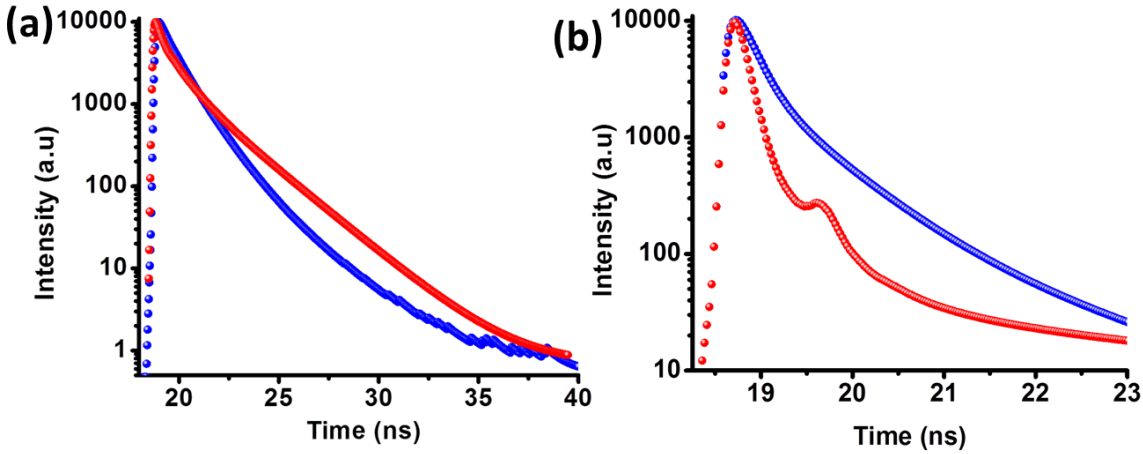

Figure 9. Lifetime decay profiles for (a) **OPE-C$_{mix}$-G** (red) and **MR10@OPE-C$_{mix}$-G** (blue) monitored at 485 nm and (b) MR (red) and **MR10@OPE-C$_{mix}$-G** (blue) monitored at 590 nm.

We envisaged that it will generate delocalized electrons via charge transfer interactions with electron rich **OPE-C$_{mix}$-G**. The in situ loading of TCNQ was performed in the same manner as the MR dye incorporation step.[13] This was accompanied by a significant quenching in emission of **OPE-C$_{mix}$-G** (Figure 10b) and indicated that a non-radiative charge transfer process was taking place within the TCNQ loaded gel scaffold. This

quenched the inherent gel emission. Buoyed by this observation we recorded the absorption spectra and steady state fluorescence measurements on **TCNQ$_{0.5}$@OPE-C$_{mix}$-G** and **TCNQ$_{0.25}$@OPE-C$_{mix}$-G**. As seen in Figure 10a, upon loading of 0.25 mol% of TCNQ, a new absorption band appeared at 500 nm when compared to the UV spectra of **OPE-C$_{mix}$-G** (Figure 10a). This band maybe ascribed to a charge transfer band arising out of an efficient charge transfer between TCNQ and **OPE-C$_{mix}$-G**. Upon increasing the doping the concentration to 0.5 mol%, The CT band intensity increased, signaling more facile charge transfer interaction in the TCNQ incorporated gel scaffold. To further confirm the CT process in **TCNQ@OPE-C$_{mix}$-G**, we investigated its photophysical properties. As expected, the emission intensity at 500 nm decreased significantly upon increased loading concentration from 0.25 mol% to 0.5 mol% (Figure 10b). This occurred because the non-radiative charge transfer process predominates in **TCNQ@OPE-C$_{mix}$-G** leading to the quenching in emission.

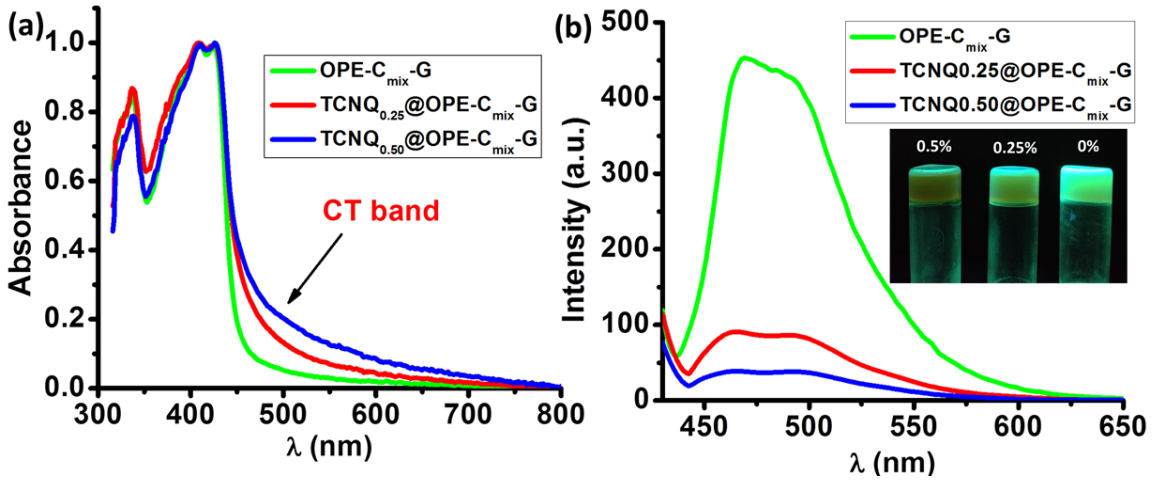

Figure 10. (a) UV spectra and (b) Emission profile of different TCNQ loaded gels showing the appearance of the CT band and quenching of emission respectively. Inset: Corresponding images under UV light.

2C.4. Conclusion

To summarize, this chapter demonstrates the synthesis of two novel π-chromophoric bola-amphiphiles via a Sonogashira-Hagihara coupling. The variance in the alkyl-TEG side chains has allowed us to tune the polarity of the systems. The ability of these systems to form gels allowed us to exploit their interesting opto-electronic properties by using them as soft-processable materials. Doping of methyl red in one of the representative gels showed interesting FRET properties. This further led to pure white light emission from the gel with a high quantum yield. Doping of redox active molecules was also performed

to realize a charge transfer gel. The work in this chapter could pave the way towards realizing the immense potential of opto-electronically active organic bola-amphiphilic OPE systems by transforming them into solution processable soft hybrids.

2C.5. References

1 U. H. F. Bunz, *Chem. Rev.*, 2000, **100**, 1605; (b) U. H. F. Bunz, *Macromol. Rapid Commun.*, 2009, **30**, 772.

2 (a) U. H. F. Bunz, K. Seehafer, M. Bender and M. Porz, *Chem. Soc. Rev.*, 2015, **44**, 4322; (b) J. R. Acharya, H. Zhang, X. Li and E. E. Nesterov, *J. Am. Chem. Soc.*, 2009, **131**, 880.

3 (a) J. Chen, M. A. Reed, A. M. Rawlett and J. M. Tour, *Science*, 1999, **286**, 1550; (b) Z. J. Donhauser, B. A. Mantooth, K. F. Kelly, L. A. Bumm, J. D. Monnell, J. J. Stapleton, D. W. Price Jr., A. M. Rawlett, D. L. Allara, J. M. Tour and P. S. Weiss, *Science* 2001, **292**, 2302.

4 (a) S. A. Sharber, R. N. Baral, F. Frausto, T. E. Haas, P. Müller and S.W. Thomas III, *J. Am. Chem. Soc.*, 2017, **139**, 5164; (b) R. Gupta, R. Thomas and G. U. Kulkarni, *J. Mater. Chem.*, 2012, **22**, 19139; (c) R. Thomas, S. Varghese and G. U. Kulkarni, *J. Mater. Chem.*, 2009, **19**, 4401.

5 S. Roy, A. Hazra, A. Bandyopadhyay, D. Raut, P. L. Madhuri, D. S. S. Rao, U. Ramamurty, S. K. Pati, S. K. Prasad and T. K. Maji, *J. Phys. Chem. Lett.*, 2016, **7**, 4086.

6 (a) M. V. Suresh, S. J. George and T. K. Maji, *Adv. Funct. Mater.*, 2013, **23**, 5585; (b) V. M. Suresh, S. Chatterjee, R. Modak, V. Tiwari, A. Patel, T. K. Kundu and T. K. Maji, *J. Phys. Chem. C*, 2014, **118**, 12241; (c) S. Roy, V. M. Suresh and T. K. Maji, *Chem. Sci*., 2016, **7**, 2251; (d) S. Roy, M. Das, A. Bandyopadhyay, S. K. Pati, P. P. Ray and T. K. Maji, *J. Phys. Chem. C*, 2017, **121**, 23803.

7 (a) J. E. Kwon and S. Y. Park, *Adv. Mater.*, 2011, **23**, 3615; (b) F. Bonaccorso, Z. Sun, T. Hasan and A. C. Ferrari, *Nat. Photonics*, 2010, **4**, 611;

8 (a) S. Roy, A. Chakraborty and T. K. Maji, *Coord. Chem. Rev.*, 2014, **273**, 139; (b) M. Shang, C. Li and J. Lin, *Chem. Soc. Rev.*, 2014, **43**, 1372; (c) K. Müller Buschbaum, F. Beuerle and C. Feldmann, *Microporous Mesoporous Mater.*, 2015, **216**, 171.

9 (a) P. Sutar, V. M. Suresh and T. K. Maji, *Chem. Commun.*, 2015, **51**, 9876 (b) P. Sutar and T. K. Maji, *Inorg. Chem.*, 2017, **56**, 9417.

10 K. V. Rao, K. K. R. Datta, M. Eswaramoorthy and S. J. George, *Chem. Eur. J.*, 2012, **18**, 2184.

11 (a) S. S. Babu, J. Aimi, H. Ozawa, N. Shirahata, A. Saeki, S. Seki, A. Ajayaghosh, H. Möhwald and T. Nakanishi, *Angew. Chem. Int. Ed.*, 2012, **51**, 3391; (b) K. V. Rao, K. K. R. Datta, M. Eswaramoorthy and S. J. George, *Adv. Mater.*, 2013, **25**, 1713.

12 (a) P. Vemula, U. Aslam, A. Mallia and G. John, *Chem. Mater.*, 2007, **19**, 138; (b) S. Bhowmik, S. Banerjee and U. Maitra, *Chem. Commun.*, 2010, **46**, 8642; (c) E. M. Surender, S. J. Bradberry, S. A. Bright, C. P. McCoy, D. C. Williams and T. Gunnlaugsson, *J. Am. Chem. Soc.*, 2017, **139**, 381; (d) A. Ajayaghosh, V. K. Praveen and C. Vijayakumar, *Chem. Soc. Rev.*, 2008, **37**, 109.

13 N. V. Harris, S. Christopher and B. Keith, *Synlett*, 1990, 577.

14 S. Chakraborty, S. G. Ramkumar and S. Ramakrishnan, *Macromolecules*, 2017, **50**, 5004.

15 P. K. Lo and H. F. Sleiman, *J. Am. Chem. Soc.*, 2009, **131**, 4182.

16 M. Sankarapillai, T. Rajasekaran, Y. Shiki, K. Akihide and A. Ayyappanpillai, *Chem. Commun.*, 2009, **40**, 5984.

17 R. J. Marshall, Y. Kalinovskyy, S. L. Griffin, C. Wilson, B. A. Blight and R. S. Forgan, *J. Am. Chem. Soc.*, 2017, **139**, 6253.

Chapter 3A

Self-cleaning MOF: Realization of Extreme Water Repellence in Coordination Driven Self-Assembled Nanostructures

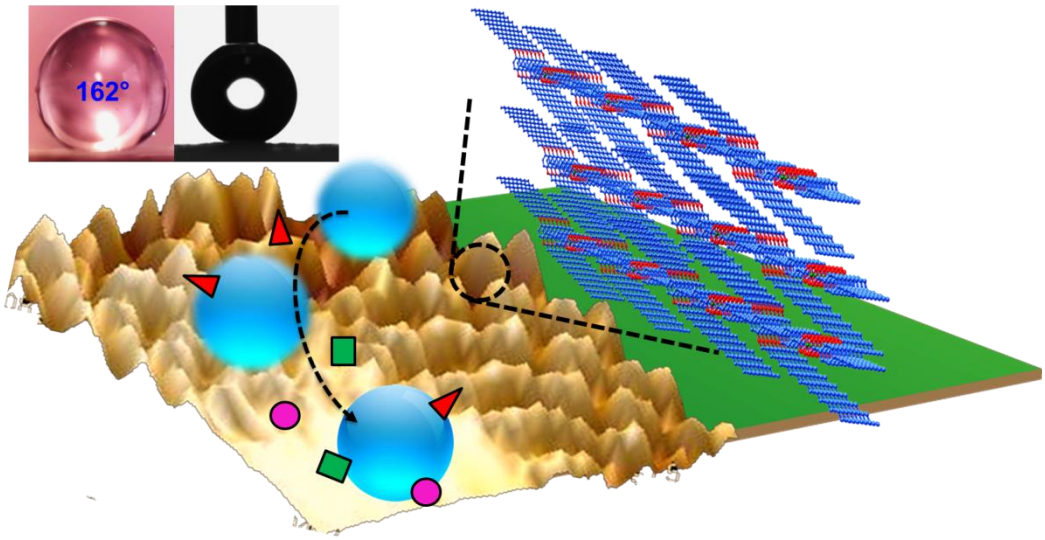

Summary

Bio-inspired self-cleaning surfaces have found industrial applications in oil-water separation, stain resistant textiles, anti-biofouling paints in ships etc. Interestingly, self-cleaning metal-organic framework (MOF) materials having high water contact angles and corrosion resistance have not been realized so far. To address this issue, we have used the fundamentals of self-assembly to expose hydrophobic alkyl chains on MOF surface. This decreases the surface free energy and hence increases hydrophobicity. Coordination directed self-assembly of dialkoxyoctadecyl-*oligo*-(*p*-phenyleneethynylene)dicarboxylate (**OPE-C_{18}**) with Zn^{II} in DMF/H_2O mixture leads to a three dimensional supramolecular porous framework $\{Zn(OPE\text{-}C_{18})\cdot 2H_2O\}_n$ (**NMOF-1**) with nanobelt morphology. Inherently superhydrophobic and self-cleaning **NMOF-1** has high thermal and chemical stability. The periodic arrangement of 1D Zn-OPE-C_{18} chains with octadecyl alkyl chains projecting outward reduces the surface free energy leading to superhydrophobicity in **NMOF-1** (contact angle; 160-162°). The hierarchical surface structure thus generated, enables **NMOF-1** to mimic the lotus leaf in its self-cleaning property with an unprecedented tilt angle of 2°. Additionally, superhydrophobicity remains intact over a wide pH range (1-9) and under high ionic concentrations. We believe that such a development in this field will herald a new class of materials capable of water repellent applications.

The work based on this chapter is published:

S. Roy, V. M. Suresh and T. K. Maji, *Chem. Sci.*, 2016, **7**, 2251-2256.

3A.1. Introduction

The progress in scientific research has witnessed the efforts of scientists to mimic the intricate and precise design of nature for fabricating novel functional materials.[1] In this context, the "Lotus Effect" has incurred immense interest for designing biomimetic self-cleaning materials.[2] It involves easy rolling of water droplets over the lotus leaf. The leaf surface shows characteristic micro and nanoscale roughness with a "re-entrant texture" which is determined to be a prerequisite for such water repellence.[3] This multiscale or hierarchical roughness reduces the surface free energy, increases the static contact angle (CA) (>150°) and reduces the tilt angle (<10°) leading to superhydrophobic surfaces with self-cleaning properties.[4] Therefore, the shape, size, rigidity and ordering with combined surface micro and nanostructure are the guiding principles for the design of artificial self-cleaning materials.[5] Towards this, carbon nanotubes (CNTs),[6] lithographic patterning,[7] aligned polymer nanofibers,[8] self-assembled monolayer (SAM) modified surfaces[9] have been successfully designed as superhydrophobic surfaces with very high CAs. In this context, superhydrophobic metal-organic frameworks (MOFs)[10] would provide the advantage of both inherent porosity and surface water repellence. This could lead to applications of this material in oil-water separation membranes, waste water treatments and fuel purification technology.[11]

Recently, MOFs have been studied for superhydrophobic applications either via post-synthetic modification (PSM) by fluoroalkyl chains or by generating external surface corrugation.[12] Kitagawa *et al.*, proposed a novel method of synthesizing superhydrophobic MOF materials by generating external surface corrugation derived from aromatic surface groups.[12b] However, it lacked the basic requirements for practical applicability i.e. solution processability and self-cleaning property. In this context, coordination driven self-assembly of rigid π-conjugated organic linker, containing long hydrophobic alkyl chains[13] would provide solution processable nanoMOF (NMOF)[14] structures. Here, the surface free energy will be dictated by the alkyl chains decorating the NMOF surface and create low adhesion of water droplet to it. We therefore conjectured that coordination driven self-assembly of *oligo*-(*p*-phenyleneethynylene) dicarboxylate with alkoxyoctadecyl (C_{18}) chains (**OPE-C_{18}**)[15] would generate a supramolecular NMOF structure which would be promising for superhydrophobic self-cleaning applications.

This chapter reports the rational design and synthesis of a self-cleaning nanoscale supramolecular 3D porous framework $\{Zn(OPE\text{-}C_{18})\cdot 2H_2O\}_n$ (**NMOF-1**) with inherent

superhydrophobicity based on the self-assembly of **OPE-C_{18}** and Zn^{II}. The micro-spaces between **NMOF-1** micro-particles are capable of creating solid-air-water composite interface to develop high moisture resistance. The nanoscale roughness is created by the presence of periodic alkyl chains to generate a hierarchical structure with pH tolerability. This design is an easy and straightforward bottom-up approach for the construction of superhydrophobic MOF nanostructures with remarkably low sliding angles and excellent self-cleaning properties extendable to large areas. To the best of our knowledge, fabrication of self-cleaning MOFs and an in-depth analysis of their characteristic surface structure are yet to be reported.

3A.2. Experimental Section

3A.2.1. Materials

$Pd(PPh_3)_4$ and $Zn(OAc)_2{\cdot}2H_2O$ were obtained from Sigma-Aldrich Chemical Co and cuprous iodide was obtained from Loba Chemie Pvt. Ltd. N,N-dimethyl formamide (DMF) and tetrahydrofuran (THF) were obtained from Spectrochem Pvt. Ltd (Mumbai, India). Tetrahydrofuran was pre-dried using standard procedure and all other reagents, solvents were of reagent grade and used without further purification.

3A.2.2. Physical Measurements

The elemental analyses were carried out using a Thermo Scientific Flash 2000 CHN analyzer. Infrared spectral studies were done by making samples with KBr pellets using Bruker FT-IR spectrometer. Thermal stability of the **NMOF-1** is analyzed using Mettler Toledo TGA 850 instrument under inert atmosphere in the temperature range of 25-850 °C at a heating rate of 3 °C /min. Powder X-ray diffraction studies were recorded on a Bruker D8 discover instrument using Cu-Kα radiation. Morphological studies have been carried out using Lica-S440I Field Emission Scanning Electron Microscope (FESEM) by placing samples on a silicon wafer under high vacuum with an accelerating voltage of 10 kV. Transmission Electron Microscopy (TEM) analysis has been performed using JEOL JEM-3010 with an accelerating voltage at 300 kV. For this analysis **NMOF-1** was dispersed in ethanol by sonication before drop casting on a carbon-coated copper grid. Energy dispersive spectroscopy (EDS) analysis was performed with an EDAX genesis instrument attached to the FESEM column. Height profiles of the nanostructures were

acquired with a JPKSPM Data Processing software. UV–Vis spectra were recorded on a Perkin Elmer Model Lambda 900 spectrophotometer. Fluorescence studies were accomplished using Perkin Elmer Ls 55 Luminescence spectrometer.

Adsorption Measurements

Porosity measurements were carried out using QUNATACHROME QUADRASORD-SI analyser at 77 K for N_2 and 195 K for CO_2. In the sample tube the adsorbent samples (~100-150 mg) were placed which had been prepared at 170 °C under a 1×10^{-1} Pa vacuum for about 12 h prior to measurement of the isotherms. Helium gas (99.999% purity) at a certain pressure was introduced in the gas chamber and allowed to diffuse into the sample chamber by opening the valve. The amount of gas adsorbed was calculated from the pressure difference (P_{cal} - P_e), where P_{cal} is the calculated pressure with no gas adsorption and P_e is the observed equilibrium pressure. All the operations were computer-controlled. Solvent vapor adsorptions were carried out at 298K using BELSORP AQUA 3 solvent vapor analyzer. A sample of about ~100 –150 mg was prepared by heating at 170 °C for about 12 h under vacuum (1×10^{-1} Pa) prior to measurement of the isotherms. The solvent molecules used to generate the vapor were degassed fully by repeated evacuation. Dead volume was measured with helium gas. The adsorbate was placed into the sample tube, then the change of the pressure was monitored and the degree of adsorption was determined by the decrease in pressure at the equilibrium state. All operations were computer controlled and automatic.

Contact Angle Measurements

Contact angles were measured using an indigenous set up coupled with a Logitech camera for capturing the images. Contact angles were also measured using dedicated contact angle analyzer, OCA30 from Data Physics instrument (GmbH, Germany). 4 µL of the sessile water droplets were employed for measuring the static contact angles. A minimum of ten measurements were made.

3A.2.3. Synthesis of 4,4'-(2,5-bis(octadecyloxy)-1,4-phenylene)bis(ethyne-2,1-diyl)dibenzoic acid (H_2OPE-C_{18}) and {Zn(OPE-C_{18})·2H_2O}$_n$ (NMOF-1).

H_2OPE-C_{18} was synthesized according to reported Sonogashira Hagihara coupling procedure as discussed previously in chapter 2A (Scheme 1).[13b] A mixture of **H_2OPE-C_{18}**

(20 mg, 0.02 mmol) and $Zn(OAc)_2 \cdot 2H_2O$ (5 mg, 0.02 mmol) in a 1:1 DMF/H_2O mixture (10 mL) was stirred for 15 minutes. Then 120 µL triethylamine was added to the above reaction mixture and immediate appearance of a white colloidal turbidity was observed. After 2 hours, the reaction was stopped and the precipitate was centrifuged and washed well with THF and water to yield **NMOF-1** as a bright green powder (Scheme 2). Elemental analysis: Calcd. for $C_{60}H_{86}O_8Zn$: C, 72.0; H, 8.7; Found: C,72.6; H, 8.5. FT-IR (cm^{-1}): 3430(s), 2913(s), 2851(s), 1690(s), 1595 (s), 1413(s), 1276(s), 1214(w), 860(w), 775(w), 550(w).

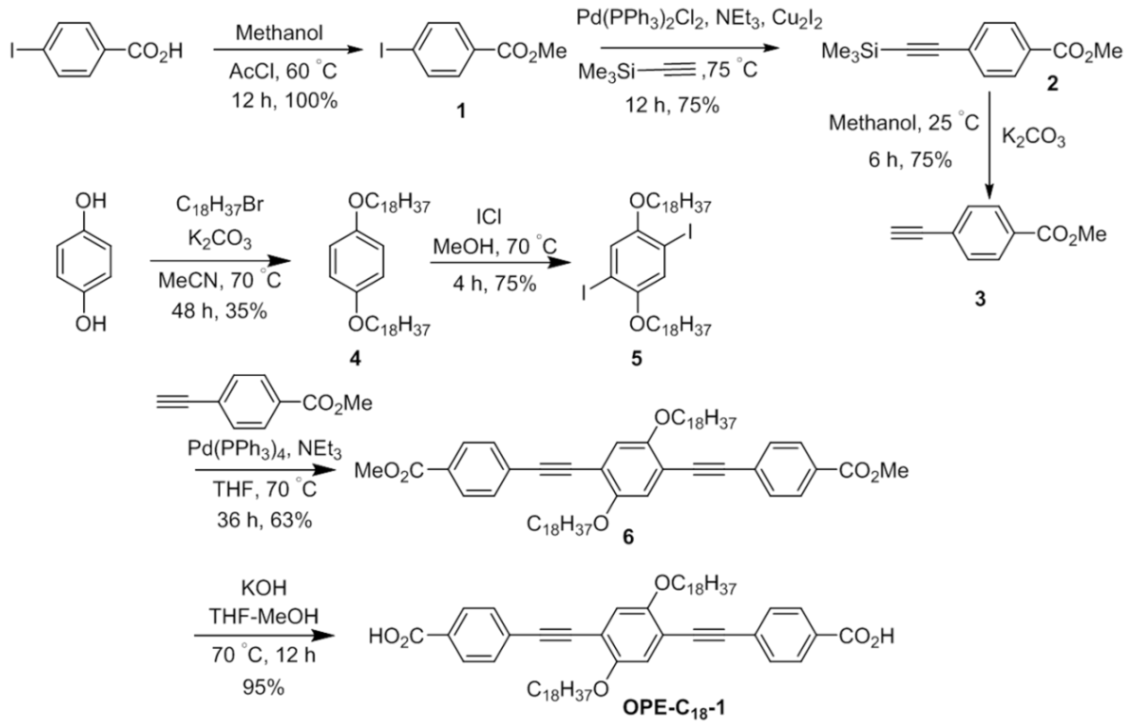

Scheme 1. Synthetic scheme for **H_2OPE-C_{18}**.

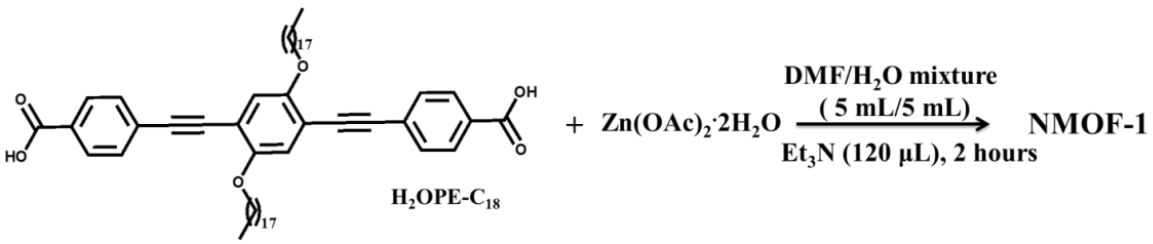

Scheme 2. Synthetic scheme for the fabrication of **NMOF-1.**

3A.3. Results and Discussion

3A.3.1. Structural Characterization

NMOF-1 has been synthesized by stirring **H_2OPE-C_{18}** and $Zn(OAc)_2 \cdot 2H_2O$ in DMF/H_2O mixed solvent system in the presence of triethylamine at room temperature (Scheme 2). Coordination of Zn^{II} to OPE-C_{18} is evidenced by the spontaneous formation of colloidal turbidity on addition of the aqueous $Zn(OAc)_2$ solution. The reaction mixture is stirred for 2 hours at room temperature and centrifuged. EDS analysis of the resulting colloid showed the presence of Zn^{II} (Figure 1a) and CHN analysis suggests a molecular formula of $\{Zn(OPE\text{-}C_{18}) \cdot 2H_2O\}_n$ (**NMOF-1**), thereby proposing 1:1 coordination of Zn^{II} ion with **OPE-C_{18}**. FT-IR spectrum of **NMOF-1** shows strong peaks at 1595 cm^{-1} and 1413 cm^{-1}, corresponding to asymmetric and symmetric stretching vibrations of carboxylate groups and the difference (Δ value) is found to be 182 cm^{-1} (Figure 1b). This suggests a bidentate coordination mode of Zn^{II} metal ion to **OPE-C_{18}** (Scheme 3). The presence of a broad peak at 3460 cm^{-1} confirms the presence of Zn^{II} bound coordinated water molecules. These results suggest a hexacoordination environment around Zn^{II} ion with four oxygens from two carboxylate groups of **OPE-C_{18}** and two coordinated water molecules. Thermogravimetry analysis further indicates its stability up to 340 °C (Figure 2). N_2 adsorption isotherm at 77 K of **NMOF-1** shows type II uptake profile (Figure 3a). However, CO_2 adsorption isotherm at 195 K showed a gradual uptake of CO_2 with increasing pressure (Figure 3b). The final amount is observed

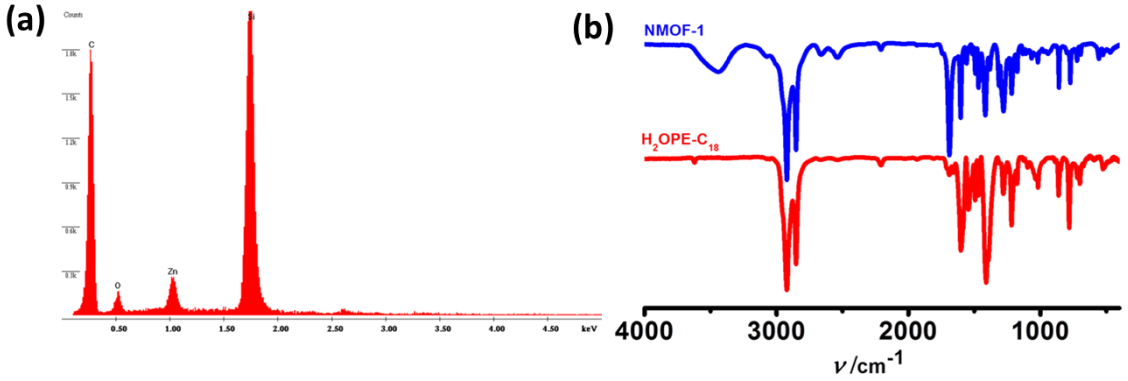

Figure 1. (a) EDS analysis showing the presence of Zn^{II} metal ion in **NMOF-1** and (b) FT-IR spectra of **H_2OPE-C_{18}** (red) and **NMOF-1** (blue).

to be 35 cc/g at p = 1 atm which corresponds to 1 molecule of CO_2 per formula unit of **NMOF-1**.The permanent porosity indicates the presence of a porous 3D structural

organization in **NMOF-1** (Scheme 3). Powder X-ray diffraction (PXRD) suggests high crystallinity of **NMOF-1** (Figure 4a). Indexing of PXRD provided insights into its packing. Modeling through the Crysfire software suggests monoclinic crystal system of **NMOF-1** with a cell volume of 2197 $Å^3$ and cell parameters of a = 29.40(5) Å, b = 4.146(7) Å and c = 22.81(5) Å.

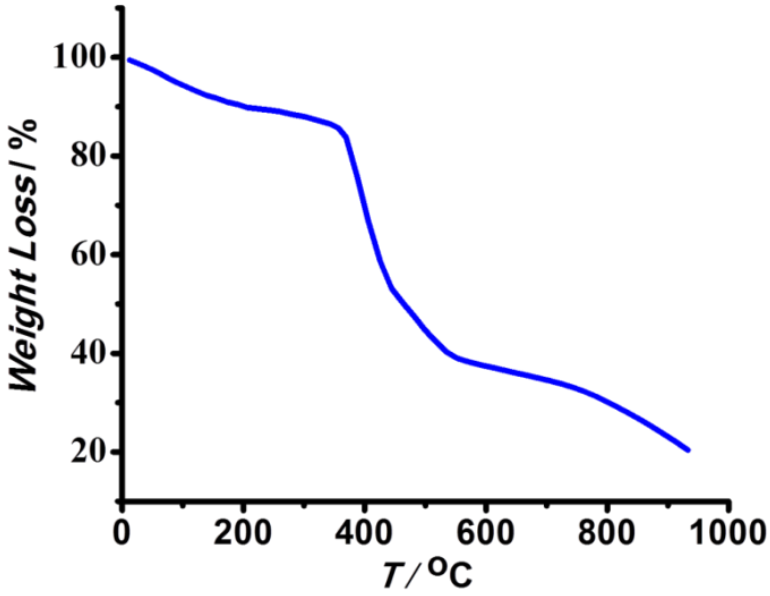

Figure 2. TGA profile of **NMOF-1** in the temperature range 25-850 °C with a heating rate of 3 °C/min.

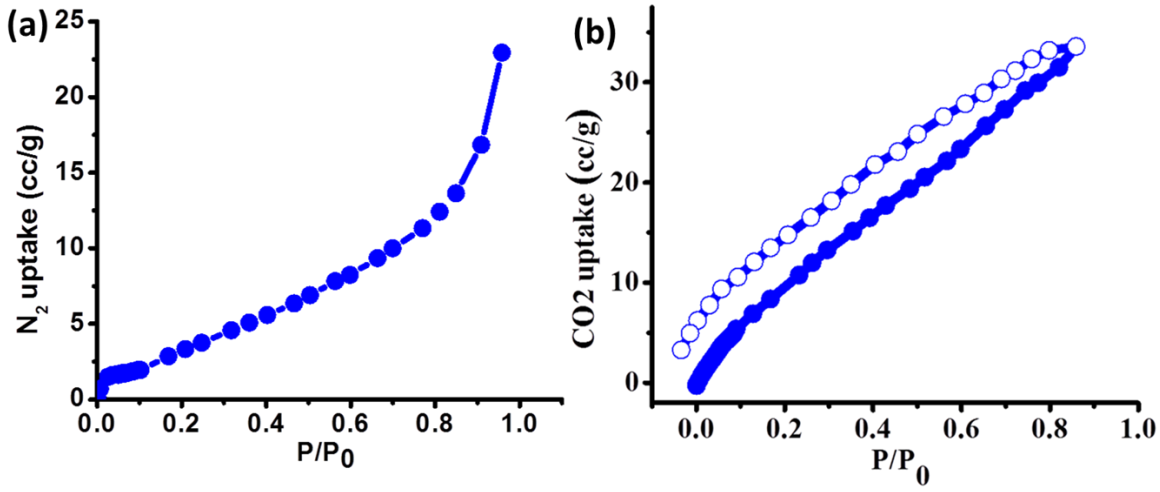

Figure 3. (a) N_2 at 77 K and (b) CO_2 at 195 K adsorption isotherms of **NMOF-1**.

A close equivalence of experimental and indexing results indicates the accuracy of calculation (Table 1). The (100) peak at 3.9° (d = 23 Å) corresponds to the repeating distance of Zn^{II} centres connected by **OPE-C_{18}** suggesting the formation of 1D coordination chain. Therefore the coordination of the terminal carboxylate groups of **OPE-C_{18}** to Zn^{II} extends **NMOF-1** in 1D (Scheme 3).

Table 1. Indexing data of **NMOF-1** using Crysfire software[16]

Cell Parameters: a = 29.40(5) Å, b = 4.146(7) Å, c = 22.81(5) Å, β = 127.83(18) °, V = 2197 Å^3.

h	***k***	***l***	D_{obs}	D_{cal}	D_{obs}-D_{cal}	Q_{obs}	Q_{cal}	$2\theta_{obs}$	$2\theta_{cal}$	***Diff***
1	0	0	23.00143	23.22249	-.22107	.00189	.00185	3.838	3.802	.037
2	0	-1	14.62921	14.69038	-.06117	.00467	.00463	6.037	6.011	.025
1	0	-2	11.01247	10.97007	.04240	.00825	.00831	8.022	8.053	-.031
3	0	-1	9.52050	9.54601	-.02551	.01103	.01097	9.282	9.257	.025
2	0	1	7.82030	7.81825	.00205	.01635	.01636	11.306	11.309	-.003
4	0	-4	5.57757	5.58686	-.00929	.03214	.03204	15.877	15.850	.027
6	0	-3	4.39640	4.38679	.00961	.04154	.04170	20.177	20.213	-.036
3	1	-1	3.80355	3.80355	.00000	.06912	.06912	23.369	23.369	.000

Diffraction peak ($60\bar{3}$) at 20.2° (d = 4.4 Å) indicates weak π-π interactions between **OPE-C_{18}** unit of 1D chains that resulted in 2D layers. Such stacking of the 2D layers is reinforced by the orientation of adjacent alkyl chains indicated by the ($10\bar{2}$) peak at 8° (d=11 Å). The long alkyl chains interact via van der Waals forces to extend the packing into a 3D supramolecular framework. This generates a supramolecular porous structure extended via lamellar packing between adjacent **OPE-C_{18}** units of two successive **NMOF-1** layers (Scheme 3). Interestingly, **NMOF-1** retained its structural integrity even at higher temperatures as evident from temperature dependant PXRD measurements

(Figure 4b). Measurements were carried out at three different temperatures; PXRD analysis at 100 °C, 200 °C and 300 °C showed that the characteristic peaks of **NMOF-1** are retained at all temperatures. This result clearly reveals exceptional thermal stability of **NMOF-1**.

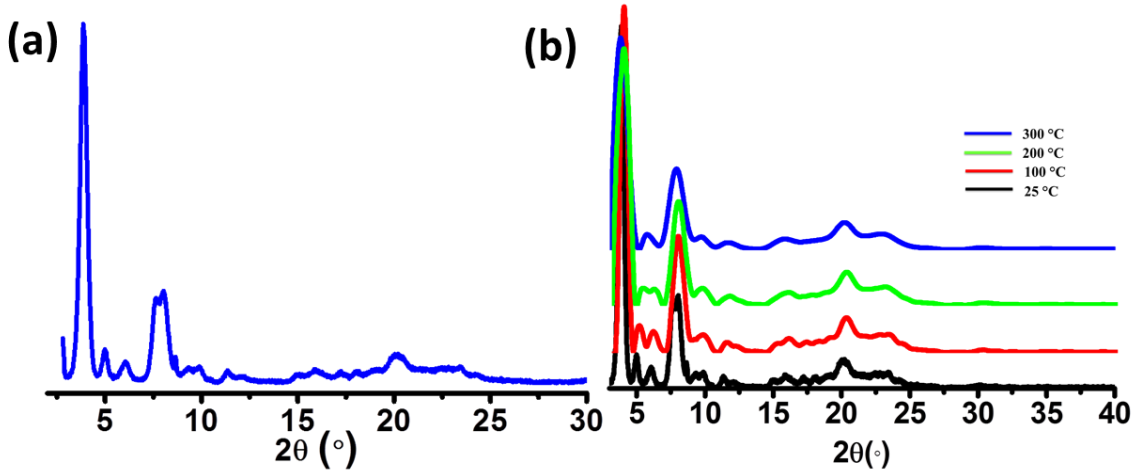

Figure 4. PXRD patterns of **NMOF-1** at (a) 25 °C and (b) Variable temperatures (25- 300 °C) showing its structural integrity at higher temperatures.

3A.3.2. Morphology Transformation

The nanomorphology of **NMOF-1** was investigated using field emission scanning electron microscopy (FESEM), transmission electron microscopy (TEM) and atomic force microscopy (AFM). FESEM, TEM and AFM revealed the presence of belt-like nanostructures of **NMOF-1** (Figure 5a, b, j, k).

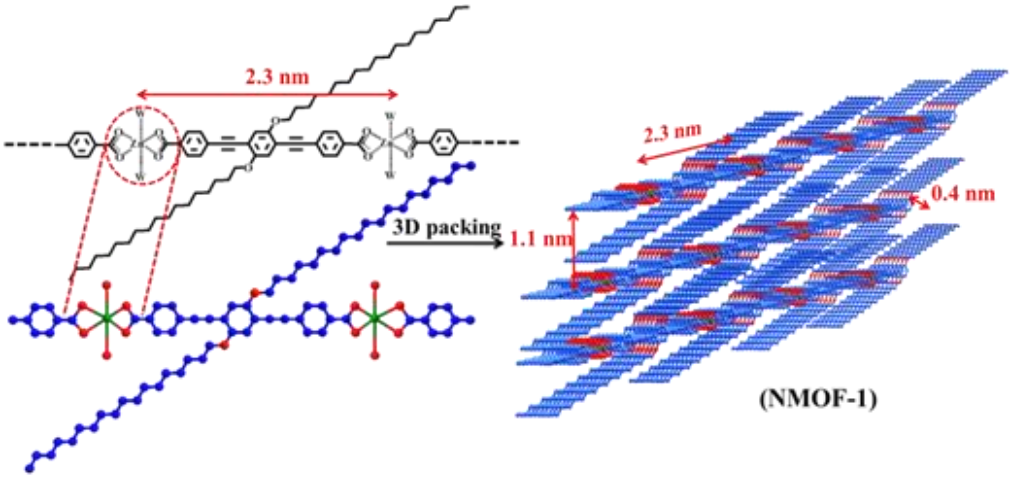

Scheme 3. Bottom-up approach for coordination driven self-assembly between Zn^{II} and **OPE-C_{18}** to form a 3D porous supramolecular structure of **NMOF-1**.

The nanobelts offered a length of 700 - 1000 nm and a width of 200 - 300 nm. The height profile analysed from AFM was found to be about 80 nm and as shown in Figure 6a,b the length of **NMOF-1** nanobelts is composed of the 1D chains of ZnOPE-C_{18}. The width of the belts is formed by the weak π-π interactions between the 1D chains forming the 2D layer of the nanobelts. Finally the height of the nanobelts is formed by the 3D packing of **NMOF-1** via the interaction of the alkyl chains. Interestingly, when the reaction time was increased to 6 hours, nanoscrolls of **NMOF-1** were observed. FESEM and TEM measurements further confirmed the formation of the nanoscrolls from the nanobelts (Figure 5c-i). Intermediate reaction times offered semi-scrolled nanostructures. The nanoscrolls showed a length of 400 - 800 nm and a width of 40 - 100 nm. AFM height profile of nanoscrolls showed a value of about 270 nm (Figure 6c,d). The increase in height for nanoscrolls is attributed to the scrolling effect. These results suggest the scrolling of belt occurs in a longitudinal direction leaving long alkyl chains at the surface of the nanobelts and nanoscrolls. As the reaction progresses, the belts start to scroll up to minimize the repulsive forces between the alkyl chains of **OPE-C_{18}** and solvents in the reaction medium (Figure 5m, Scheme 4). To study the effect of dynamicity of the alkyl chains on the surface, nanoscrolls of **NMOF-1** were allowed to stand in acetonitrile, a less polar solvent than water. After 4 days of standing in solution, partially unscrolled structures of **NMOF-1** taking the shape of nano-containers were observed on FESEM analysis (Figure 7). A decrease in the hydrophobic interactions between the alkyl chains in a less polar solvent allows the scrolls to relax and open up along the long-alkyl chain direction therefore resulting in a new morphology of **NMOF-1**.

3A.3.3. Superhydrophobicity and Surface Analysis

The presence of alkyl chains and its dynamicity along the surface and pores of the nanostructures further motivated us to study the hydrophobic properties of **NMOF-1**.To investigate the polarity of the self-assembly and supramolecular organization, we carried out water and benzene adsorption experiments at room temperature. The water adsorption isotherms of **NMOF-1** showed negligible uptake at the low pressure region with a gradual uptake at higher pressures, finally reaching to 20 mL at P/P_0 = 1.0. This suggests hydrophobic nature of the framework (Figure 8a). The hydrophobicity of the pore surface was further validated by the benzene adsorption isotherms showing an uptake of 102 cc/g (Figure 8a) which corresponds to ~1 benzene molecule per formula unit of **NMOF-1**. Therefore, its pore can be utilized for polar/ non-polar solvent separations. For surface

characterizations, the free organic linker (**H_2OPE-C_{18}**) was initially investigated for superhydrophobicity. The contact angle was determined to be 140-146° proving the hydrophobicity of **H_2OPE-C_{18}** (Figure 9).

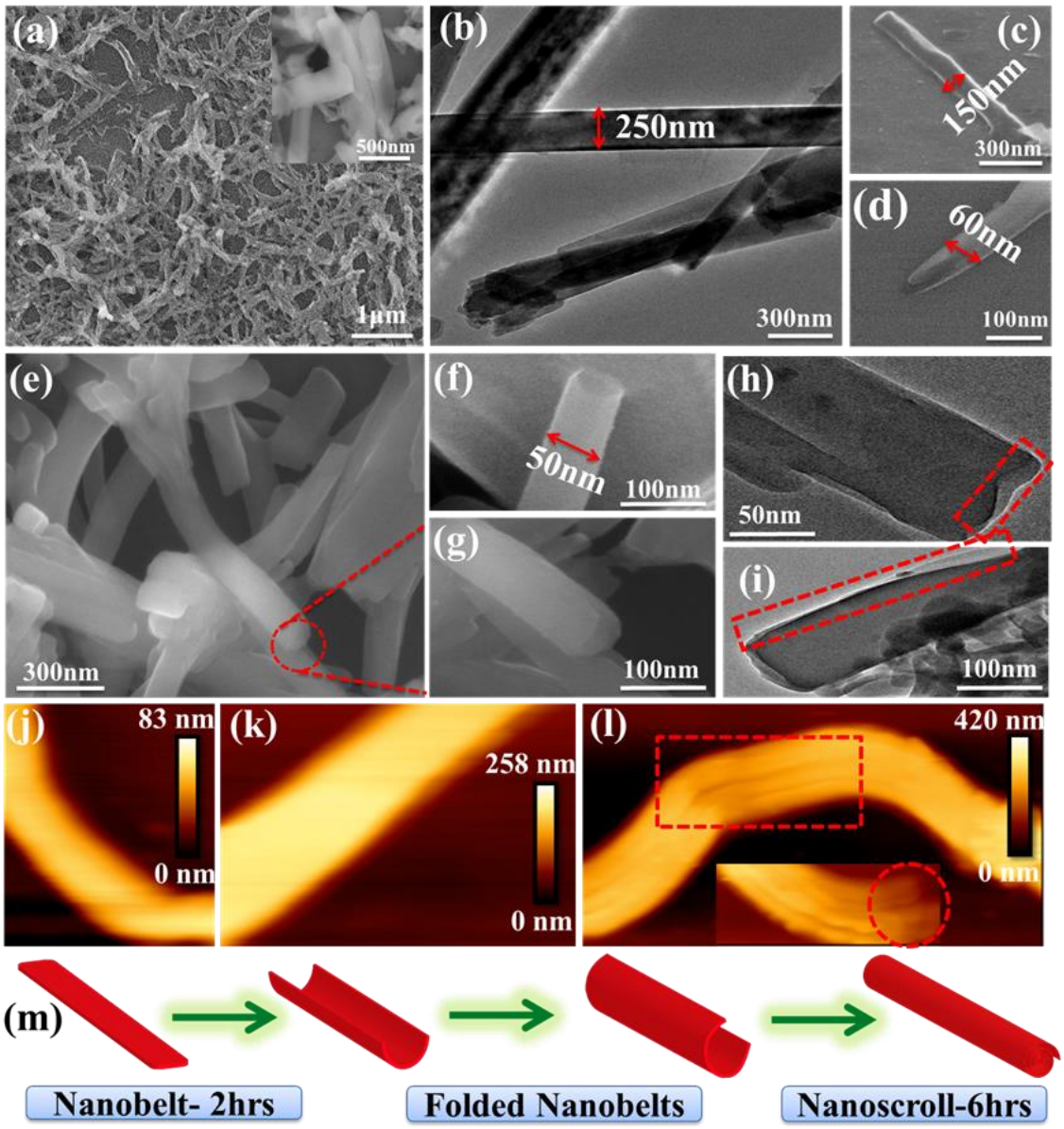

Figure 5. (a) FESEM image (Inset: nanobelts at higher magnification) and (b) TEM image of **NMOF-1** nanobelts, (c, d) FESEM images of semi-scrolled nanobelts, (e, f, g) FESEM and (h, i) TEM images of nanoscrolls at different magnifications showing the changes in cross section upon scrolling, AFM image of (j, k) Nanobelt and (l) Nanoscroll (Inset: single nanoscroll showing opening at the mouth and (m) Schematic showing the possible morphological transformation of nanobelts to nanoscrolls in **NMOF-1**.

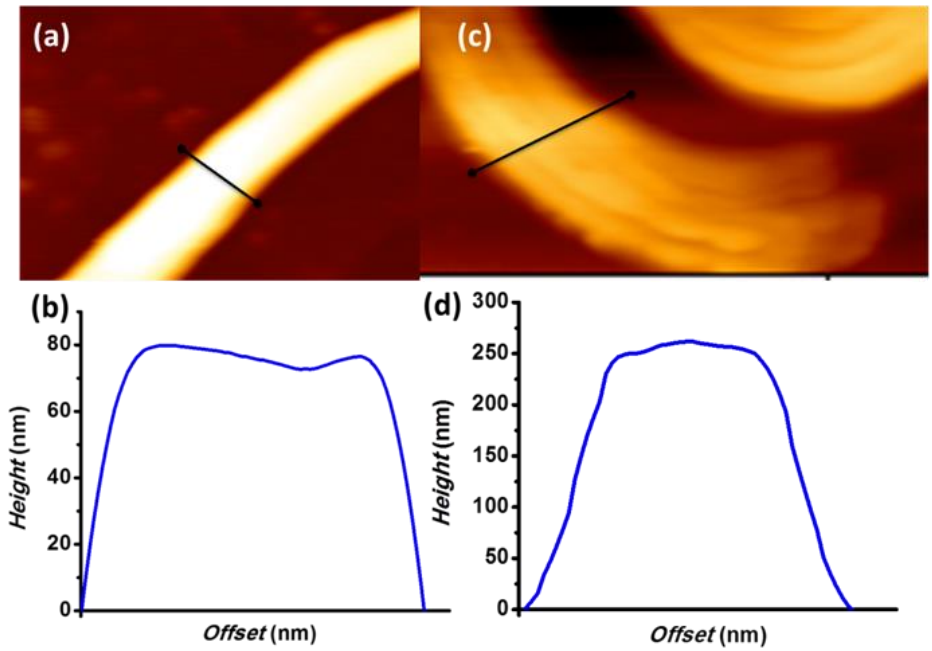

Figure 6. AFM images and the corresponding height profile of (a, b) Nanobelt and (c, d) Nanoscroll. The changes in height profile clearly imply the scrolling of nanobelt on increasing the reaction time from 2 to 6 hrs.

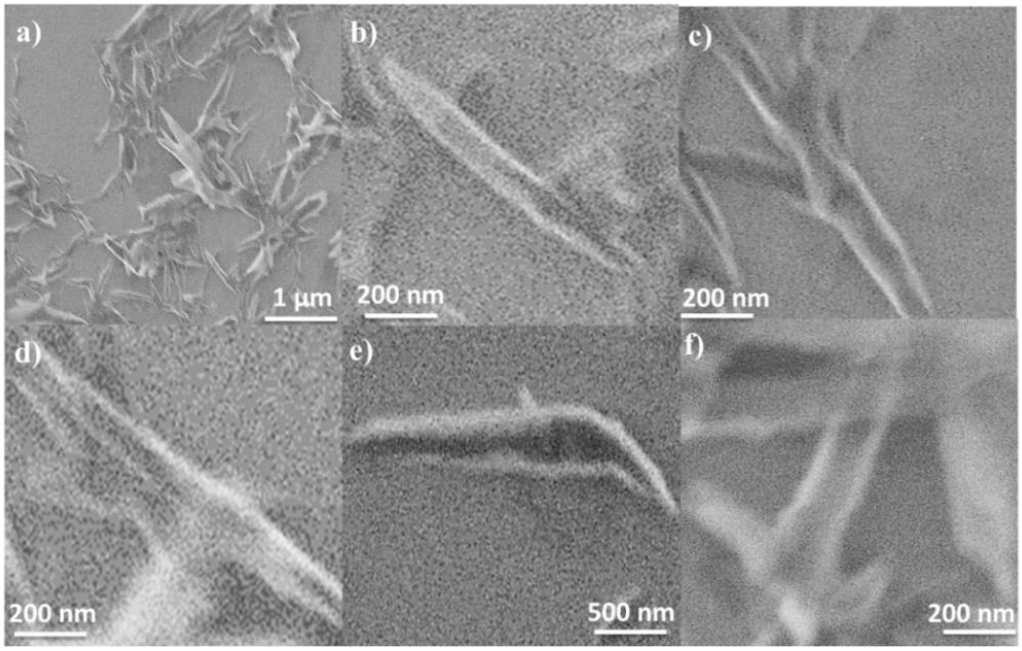

Figure 7. (a-f) FESEM images of nanoscroll after keeping in acetonitrile solution for two days showing the opening (or unfolding) of the scrolled nanostructures.

However, superhydrophobicity was not realized. Hydrophobicity of the **NMOF-1** surface was then investigated by coating its ethanolic dispersion on a glass substrate. The

nanoscale structure of **NMOF-1** makes it highly solution processable and easy to coat on glass. Water contact angles were measured on **NMOF-1** coated glass substrates and were determined to be 160- 162° in a circle fitting mode (Figure 8b).

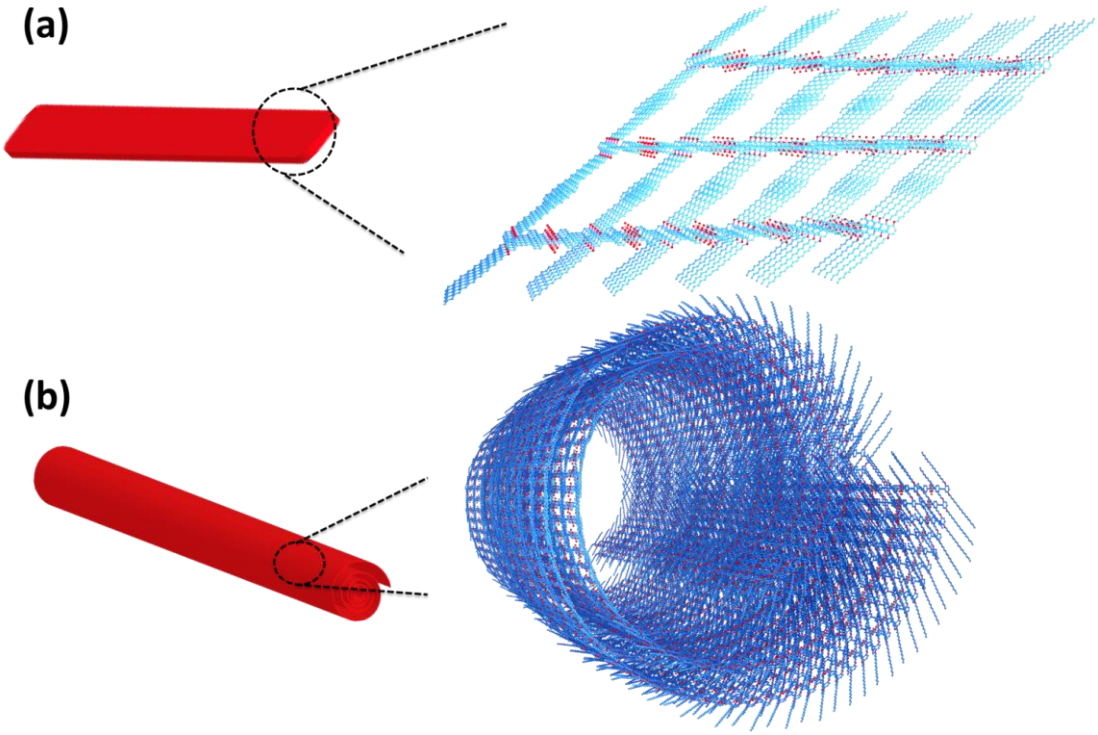

Scheme 4. Figure showing the structural correlation of **NMOF-1** (a) Nanobelts from its 3D packing and (b) Nanoscrolls from the rolling up of nanobelts.

These high contact angle values are the highest reported for MOFs without any post-synthetic modifications of the pore as well as the external surface (Table 2). Therefore, to gain insight into this superhydrophobic property of **NMOF-1**, FESEM and AFM analysis was performed. FESEM of coated **NMOF-1** shows uniform distribution of spherical particles with size in the range 10- 30 μm (Figure 10). The occurrence of such particles generates the micro-roughness with trapped air pockets in between them. This distribution is ideal for hydrophobic applications. To investigate further, non-contact mode AFM imaging of **NMOF-1** was performed. 2D AFM images authenticated the presence of spherical particles of **NMOF-1** (Figure 11a). The particles show needle like protrusions in the nanoscale regime. The 3D AFM image shows the height of the spheres in the range of 300 - 500 nm (Figure 11b). 3D AFM image of a single sphere validates the presence of spikes 50 - 100 nm wide with an inter-spacing of 10 - 50 nm having height of 200 - 300 nm (Figure 11c,d). These descriptions confirm the presence of hierarchical surface

roughness. Such periodic existence of large and small particles generates areas containing peaks and troughs throughout the surface (Figure 11b,d). This is commonly known as the "hills and valley" type surface terrain with trapped air pockets in between. The hills and valley are observed even in the nanoscale regime. The Cassie-Baxter model[17] (Figure 11f) predicts that such surface roughness will lead to a superhydrophobic structure. The uniformity in micro/sub-microscale roughness of **NMOF-1** therefore provides an ideal surface for super-hydrophobic and self-cleaning applications.

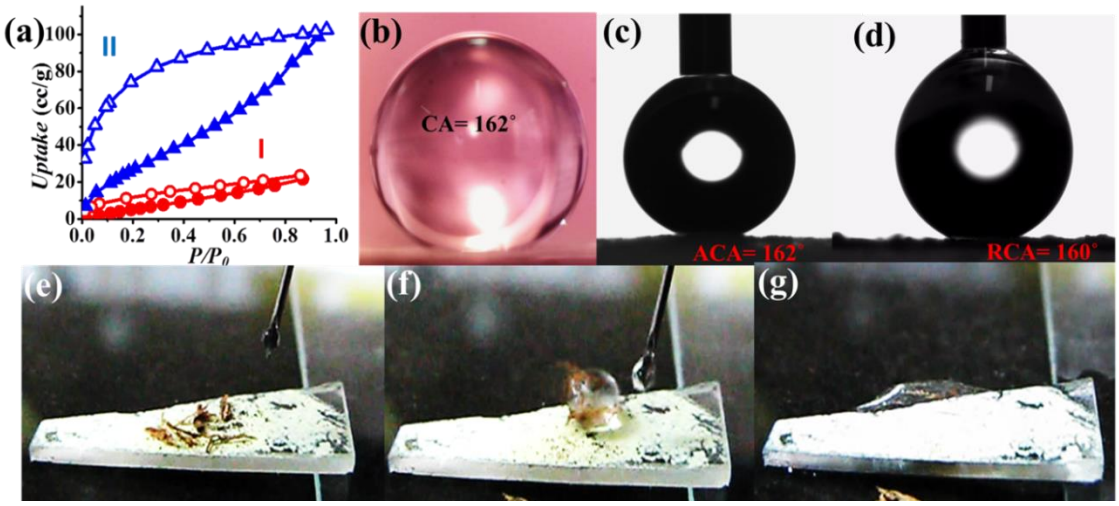

Figure 8. (a) Solvent vapor adsorption isotherms of **NMOF-1** at 298K: I: Water (red) and II: benzene (blue), P_0 is the saturated vapour pressure; 3.17 kPa (water) and 12.60 kPa (benzene) at 298K. Water contact angles of **NMOF-1** coated substrate: (b) Static contact angle, (c) Advancing contact angle and (d) Receding contact angle and (e-g) Video snapshots of self-cleaning experiment showing the removal of dirt from surface.

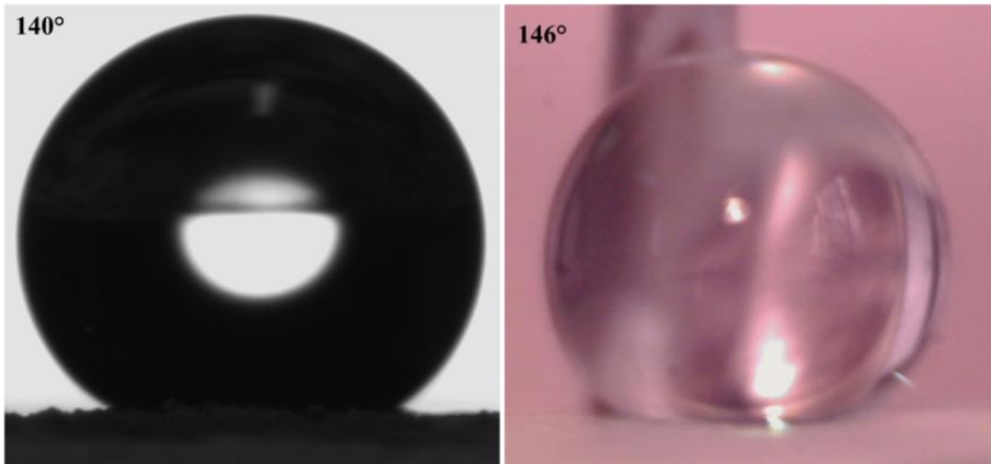

Figure 9. Water contact angles measured on **H_2OPE-C_{18}** coated glass surface.

Table 2. Reported superhydrophobic MOFs in the literature highlighting the comparison of contact angles, stability in the pH range and self-cleaning properties with the current work.

MOF	CA(°)	PSM	Self-cleaning	pH stability range	Reference
MOFF-2	151±1	No	-	-	12c
MOFF-3	135±2	No	-	-	12c
MIL-53(Al)-AM4	>150	Yes	-	-	12a
MIL-53(Al)-AM6	>150	Yes	-	-	12a
NH_2-MIL-53(Al)	151-169	Yes	-	-	12d
PESD-1	>150	No	-	-	12b
NMOF-1	160-162	No	Yes	1-9	Current Work

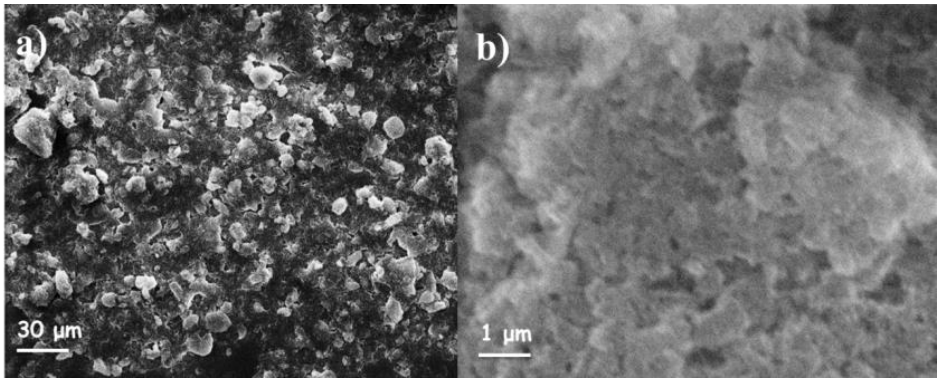

Figure 10. (a, b) FESEM images of **NMOF-1** coated on glass substrate at different magnifications.

3A.3.4. Self-Cleaning Property

The advancing and receding contact angles of **NMOF-1** were measured to be 162° and 160° respectively, leading to a very small contact angle hysteresis of 2° (Figure 8c,d).

This further prompted us to investigate its self-cleaning property. It was examined by placing dust particles on the **NMOF-1** coated glass surface. The water droplets indeed rolled off the surface carrying the dust particles along with it (Figure 8e-g). However, for any practical applications of **NMOF-1**,

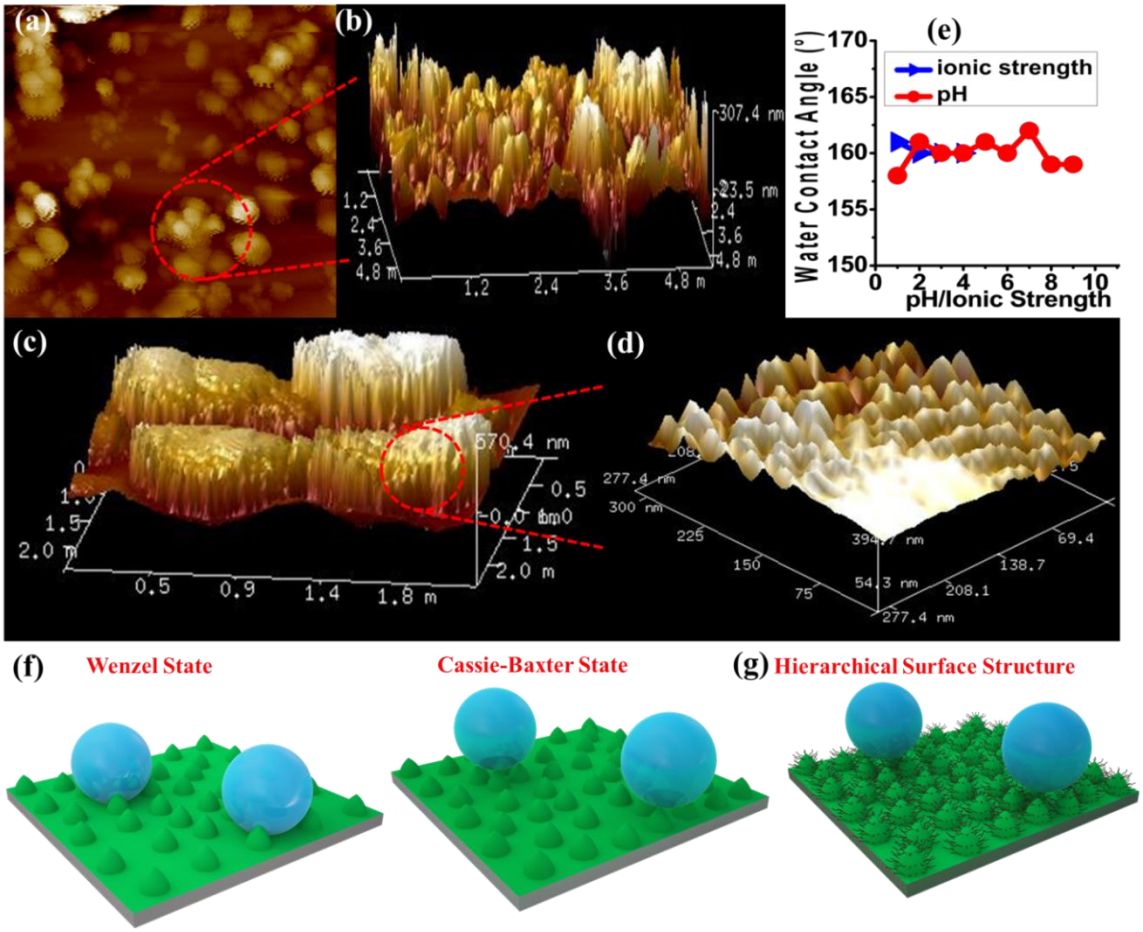

Figure 11. (a) 2D-AFM image of **NMOF-1** micro-particles on coated glass surface and (b) Corresponding 3D-AFM, (c) 3D-AFM image of four adjacent microspheres of **NMOF-1** and (d) Corresponding high magnified image showing continuous nano-roughness present on each micro-particle, (e) Plots showing changes in CA with pH/ionic strength, (f) Schematic showing the different states used to explain surface water repellence: left: Wenzel state or the wetting state. right: Cassie-Baxter state or the superhydrophobic state (A transition from the Wenzel to the Cassie-Baxter model occurs when we consider that rough textures on a surface trap air-pockets in between) and (g) Incorporation of hierarchical surface for the generation of the self-cleaning effect in **NMOF-1**.

it must be stable under a variety of extreme conditions such as high acidic and basic conditions and also solutions of high ionic strength. An experiment was designed where aqueous solutions of different pH were used to measure contact angles.

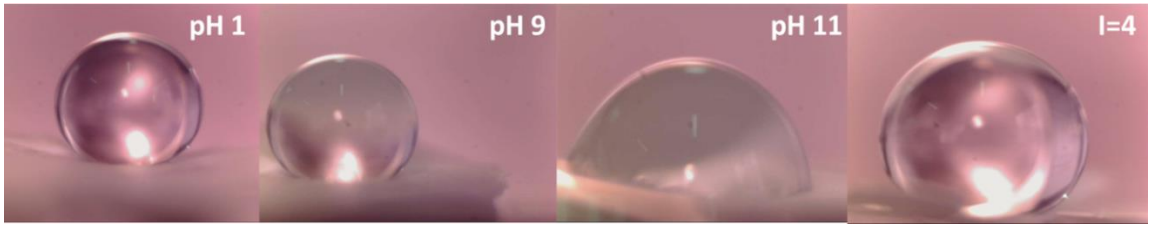

Figure 12. Water contact angles of **NMOF-1**: under acidic condition (pH of solution =1), under basic condition (pH of solution = 8), at high ionic strength (I= 4) and at pH= 11.

Interestingly, the glass surface with **NMOF-1** coating showed amazing stability with high contact angles in the entire acidic pH range (1-6) and also under mildly basic conditions (up to pH=9). The contact angle varied from its original value only slightly in the entire range (pH=1 to 9). Also under high ionic strength solutions, contact angles showed only a minimal change (I=1-4) (Figure 11e, 12). The supramolecular packing of **NMOF-1** leaves the alkyl chains of **OPE-C_{18}** both between the 2D layers as well as on the external surface (Scheme 3).

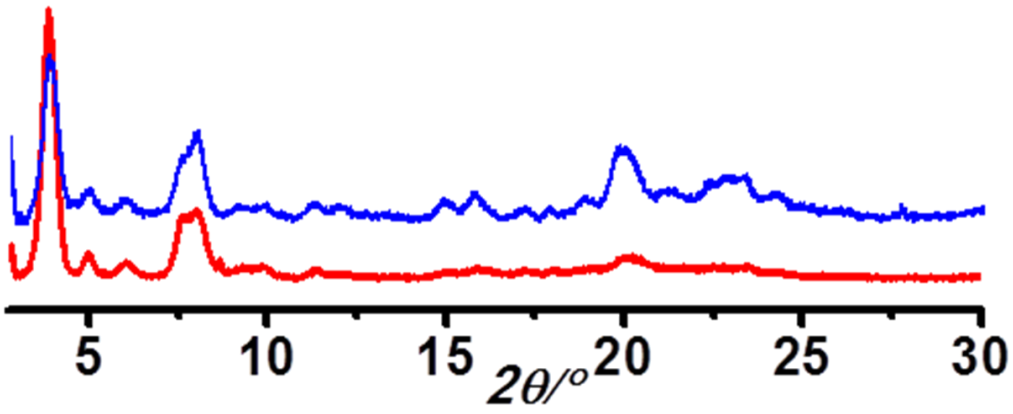

Figure 13. PXRD pattern of **NMOF-1** before (red) and after (blue) the study of self-cleaning property with water.

On coating the glass surface, spherical organizations of **NMOF-1** nanobelts were observed which creates air pockets in between two successive particles. This prevents the wetting of the surface. Also the periodic alignment of alkyl chains on the surface creates nanospaced roughness generating a hierarchical surface structure which assists easy

rolling of water droplets on it (Figure 8g). Likewise, the presence of long alkyl chains on the surface of **NMOF-1** shields the framework from decomposing under such extreme conditions rendering it as a highly stable self-cleaning material. The PXRD peaks showed good correspondence before and after the self-cleaning experiment (Figure 13) indicating the robustness of **NMOF-1** in such applications. The results were compared to other reported MOFs and have been tabulated in Table 2.

3A.4. Conclusion

In conclusion, a novel ligand design strategy has been exploited for the fabrication of an inherently superhydrophobic and self-cleaning nanoscale metal-organic framework **NMOF-1**. The control of reaction parameters has generated nanobelts and nanoscroll morphologies. The micro/nanoscale surface roughness generated was also cultivated for superhydrophobic and self-cleaning application of **NMOF-1** which is unique in MOF chemistry. Its exceptional stability under extreme acidic, basic and ionic conditions renders its applicability as a pH stable self-cleaning and luminescent material. The shape-shifting porous hybrids can also be utilized for a host of dimension dependent applications like optical waveguiding, charge transport etc. Exploitation of supramolecular organization and nanomorphology of MOFs for large area coating and its in-depth surface analysis is done for the first time in this chapter. This could potentially open up new avenues in the design of superhydrophobic self-cleaning MOF materials without tedious post-synthetic modifications and usher in a new class of materials meeting industrial needs.

3A.5. References

1 (a) W. J. P. Barnes, *Science,* 2007, **318**, 203; (b) W.-J. Chung, J.-W. Oh, K. Kwak, B. Y. Lee, J. Meyer, E. Wang, A. Hexemer and S.-W. Lee, *Nature,* 2011, **478**, 364; (c) P. H. J. Kouwer, M. Koepf, A. A. Le Sage, M. V. Jaspers, A. M. van Buul, Z. H. Eksteen-Akeroyd, T. Woltinge, E. Schwartz, H. J. Kitto, R. Hoogenboom, S. J. Picken, R. J. M. Nolte, E. Mendes and A. E. Rowan, *Nature,* 2013, **493**, 651; (d) K. Schacht, T. Jüngst, M. Schweinlin, A. Ewald, J. Groll and T. Scheibel, *Angew. Chem., Int. Ed.,* 2015, **54**, 2816; (e) L. Wen, Y. Tian and L. Jiang, *Angew. Chem., Int. Ed.*, 2015, **54**, 3387; (f) P. K. Vemula and G. John, *Acc Chem Res.*, 2008, **41**, 769.

2 (a) R. Blossey, *Nat. Mater*., 2003, **2**, 301; (b) S. Srinivasan, V. K. Praveen, R. Philip and A. Ajayaghosh, *Angew. Chem., Int. Ed*., 2008, **47**, 5750; (c) K. M. Wisdom, J. A. Watson, X. Qu, F. Liu, G. S. Watson and C.-H. Chen, *Proc. Natl. Acad. Sci. U. S. A.*, 2013, **110**, 7992; (d) J. Zhang, A. Wang and S. Seeger, *Adv. Funct. Mater*., 2014, **24**, 1074.

3 (a) X.-M. Li, D. Reinhoudt and M. Crego-Calama, *Chem. Soc. Rev.*, 2007, **36**, 1350; (b) K. Liu, X. Yao and L. Jiang, *Chem. Soc. Rev*., 2010, **39**, 3240; (c) P. Roach, N. J. Shirtcliffe and M. I. Newton, *Soft Matter*, 2008, **4**, 224; (d) T. Sun, L. Feng, X. Gao and L. Jiang, *Acc. Chem. Res*., 2005, **38**, 644; (e) B. Xin and J. Hao, *Chem. Soc. Rev*., 2010, **39**, 769.

4 (a) C. Neinhuis and W. Barthlott, *Ann Botany*, 1997, **79**, 667; (b) R. Makiura, S. Motoyama, Y. Umemura, H. Yamanaka, O. Sakata and H. Kitagawa, *Nat. Mater*., 2010, **9**, 565; (c) A. Tuteja, W. Choi, G. H. McKinley, R. E. Cohen and M. F. Rubner, *MRS Bulletin*, 2008, **33**,752.

5 (a) A. Tuteja, W. Choi, M. Ma, J. M. Mabry, S. A. Mazzella, G. C. Rutledge, G. H. McKinley and R. E. Cohen, *Science*, 2007, **318**, 1618; (b) B. P. Dyett, A. H. Wu and R. N. Lamb, *ACS Appl. Mater. Interfaces.*, 2014, **6**, 18380; (c) T. L. Liu and C.-J. C. Kim, *Science*, 2014, **346**, 1096; (d) T. Verho, C. Bower, P. Andrew, S. Franssila, O. Ikkala and R. H. A. Ras, *Adv. Mater*., 2011, **23**, 673.

6 (a) X. Dong, J. Chen, Y. Ma, J. Wang, M. B. Chan-Park, X. Liu, L. Wang, W. Huang and P. Chen, *Chem. Commun*., 2012, **48**, 10660; (b) Y. C. Jung and B. Bhushan, *ACS Nano*, 2009, **3**, 4155.

7 (a) J. Feng, M. T. Tuominen and J. P. Rothstein, *Adv. Funct. Mater*., 2011, **21**, 3715; (b) Y. Lai, C. Lin, H. Wang, J. Huang, H. Zhuang and L. Sun, *Electrochem. Commun*., 2008, **10**, 387; (c) S. P. R. Kobaku, A. K. Kota, D. H. Lee, J. M. Mabry and A. Tuteja, *Angew. Chem., Int. Ed.*, 2012, **51**, 10109; (d) F. L. Geyer, E. Ueda, U. Liebel, N. Grau and P. A. Levkin, *Angew. Chem., Int. Ed*., 2011, **50**, 8424.

8 (a) N.-R. Chiou, C. Lu, J. Guan, L. J. A. Lee and J. Epstein, *Nat. Nanotech*., 2007, **2**, 354; (b) L. Feng, S. Li, H. Li, J. Zhai, Y. Song, L. Jiang and D. Zhu, *Angew. Chem., Int. Ed*., 2002, **41**, 1221; (c) D. Zahner, J. Abagat, F. Svec, J. M. J Fréchet and P. A. Levkin, *Adv. Mater*., 2011, **23**, 3030.

9 (a) N. Belman, K. Jin, Y. Golan, J. N. Israelachvili and N. S. Pesika, *Langmuir*, 2012, **28**, 14609; (b) J. Genzer and K. Efimenko, *Science*, 2000, **290**, 2130.

10 (a) S. Kitagawa, R. Kitaura and S.-i. Noro, *Angew. Chem., Int. Ed.*, 2004, **43**, 2334; (b) T. K. Maji, R. Matsuda and S. Kitagawa, *Nat. Mater*., 2007, **6**, 142; (c) H. Li, M. Eddaoudi, M. O'Keeffe and O. M. Yaghi, *Nature*, 1999, **402**, 276; (d) Z. R. Herm, B. M. Wiers, J. A. Mason, J. M. van Baten, M. R. Hudson, P. Zajdel, C. M. Brown, N. Masciocchi, R. Krishna and J. R. Long, *Science*, 2013, **340**, 960; (e) S. M. Cohen, *Chem. Sci*., 2010, **1**, 32; (f) S. Roy, A. Chakraborty and T. K. Maji, *Coord. Chem. Rev*., 2014, **273-274**, 139; (g) R. Haldar, R. Matsuda, S. Kitagawa, S. J. George and T. K. Maji, *Angew. Chem., Int. Ed.*, 2014, **53**, 11772; (h) Z. Zhang, H. T. H. Nguyen, S. A. Miller and S. M. Cohen, *Angew. Chem., Int. Ed.*, 2015, **54**, 6152; (i) R. A. Fischer, *Angew. Chem., Int. Ed.*, 2014, **53**, 5716; (j) J. Heine and K. Müller-Buschbaum, *Chem. Soc. Rev.*, 2013, **42**, 9232; (k) Y. K. Seo, J. W. Yoon, J. S. Lee, Y. K. Hwang, C. H. Jun, J. S. Chang, S. Wuttke, P. Bazin, A. Vimont, M. Daturi, S. Bourrelly, P. L. Llewellyn, P. Horcajada, C. Serre and G. Férey, *Adv. Mater*., 2012, **24**, 806; (l) Y. He, B. Li, M. O'Keeffe and B. Chen, *Chem. Soc. Rev*. 2014, **43**, 5618; (m) G. K.H. Shimizu, J. M. Taylor and S. Kim, *Science*, 2013, **341**, 354.

11 (a) A. K. Kota, G. Kwon, W. Choi, J.M Mabry and A. Tuteja, *Nat. Commun*., 2012, **3**, 1025; (b) K. He, H. Duan, G. Y. Chen, X. Liu, W. Yang and D. Wang, *ACS Nano*., 2015, **9**, 9188; (c) L. Ren, Y. Ahn and B. E. Logan, *Environ. Sci. Technol*., 2014, **48**, 4199; (d) I. M. Atadashi, M. K. Aroua and A. A. Aziz, *Renew Energy*., 2011, **36**, 437.

12 (a) J. G. Nguyen and S. M. Cohen, *J. Am. Chem. Soc*., 2010, **132**, 4560; (b) K. P. Rao, M. Higuchi, K. Sumida, S. Furukawa, J. Duan and S. Kitagawa, *Angew. Chem., Int. Ed.*, 2014, **53**, 8225; (c) T.-H. Chen, I. Popov, O. Zenasni, O. Daugulis and O. S. Miljanic, *Chem. Commun*., 2013, **49**, 6846; (d) C. Serre, *Angew. Chem., Int. Ed.*, 2012, **51**, 6048; (e) T. T. Y. Tan, M. R. Reithofer, E. Y. Chen, A. G. Menon, T. S. A. Hor, J. Xu and J. M. Chin, *J. Am. Chem. Soc.*, 2013, **135**, 16272; (f) B. Liu, M. Ma, D. Zacher, A. Bétard, K. Yusenko, N. M- Nolte, C. Wöll and R. A. Fischer, *J. Am. Chem. Soc*., 2011, **133**, 1734; (g) C. Yang, U. Kaipa, Q. Z. Mather, X. Wang, V. Nesterov, A. F. Venero and M. A. Omary, *J. Am. Chem. Soc*., 2011, **133**, 18094; (h) A. Bétard, S. Wannapaiboon and R. A. Fischer, *Chem. Commun*., 2012, **48**, 10493.

13 (a) V. M. Suresh, S. Chatterjee, R. Modak, V. Tiwari, A. B. Patel, T. K. Kundu and T. K. Maji, *J. Phys. Chem. C*, 2014, **118**, 12241; (b) V. M. Suresh, S. J. George and T. K. Maji, *Adv. Funct. Mater*., 2013, **23**, 5585.

14 (a) L. He, Y. Liu, J. Liu, Y. Xiong, J. Zheng, Y. Liu and Z. Tang, *Angew Chem., Int. Ed.*, 2013, **52**, 3741; (b) Y. Liu and Z. Tang, *Adv. Mater.*, 2013, **25**, 5819; (c) X. Liu, L. He, J. Zheng, J. Guo, F. Bi, X. Ma, K. Zhao, Y. Liu, R. Song and Z. Tang, *Adv. Mater.*, 2015, **27**, 3273; (d) Y. Li, J. Tang, L. He, Y. Liu, Y. Liu, C. Chen and Z. Tang, *Adv. Mater.*, 2015, **27**, 4075; (e) M. Zhao, K. Deng, L. He, Y. Liu, G. Li, H. Zhao and Z. Tang, *J. Am. Chem. Soc.*, 2014, **136**, 1738.

15 (a) T. A. Makal, X. Wang and H.-C. Zhou, *Cryst. Growth. Des*., 2013, **13**, 4760; (b) U. H. F. Bunz, *Chem. Rev*., 2000, **100**, 1605.

16 (a) D. Louer, M. Louer, *J. Appl. Cryst.*, 1972, **5**, 271; (b) A. Boultif, D. Louer, *J. Appl. Cryst.*, 1991, **24**, 987.

17 (a) A. B. D. Cassie and S. Baxter, *Trans. Faraday Soc.,* 1944, **40**, 546; (b) R. N. Wenzel, *Ind. Eng. Chem.*, 1936, **28**, 988.

Chapter 3B

Colossal Increase in Electric Current and High Rectification Ratio in a Photo-conducting, Self-cleaning and Luminescent Schottky Barrier NMOF Diode

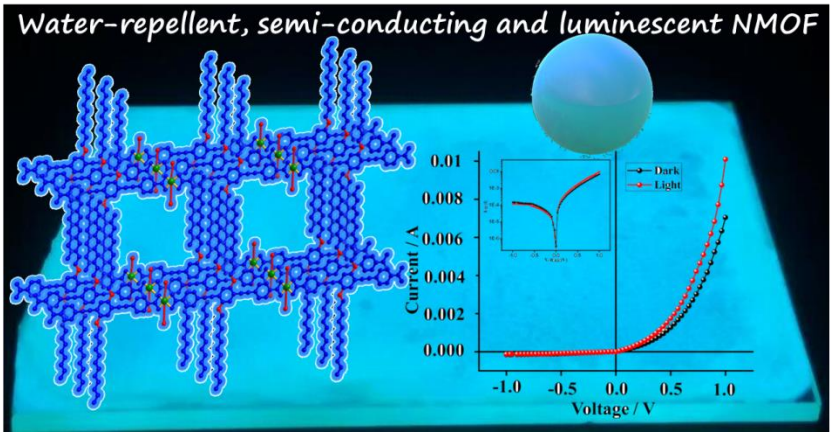

Summary

Metal-organic frameworks (MOFs) are mostly electrically insulating systems. Only recently, there have been reports of MOFs showing high conductivity. However, a large void still remains in the fabrication of photo-conducting MOFs which can function under extreme conditions for advanced opto-electronic applications. This issue was addressed by self-assembling an electrically active and luminescent bola-amphiphilic organic linker, dialkoxydodecyl-*oligo*-(*p*-phenyleneethynylene)dicarboxylate (**OPE-C_{12}**) with Zn^{II} which led to a self-cleaning and semi-conducting nanoscale MOF $\{Zn(OPE\text{-}C_{12})\cdot 2H_2O\}_n$ (**NMOF-1**). The fabricated device using **NMOF-1**, showed Schottky barrier behavior along with a 1000 and 1400 fold increase in current at +0.2 V in the absence and presence of light, respectively. A high rectification ratio of 47 and 83 was also observed under dark and photo-irradiated condition. Along with high thermal stability, moisture resistance and luminescence, **NMOF-1** can be used in advanced opto-electronics probably even under water, being the first porous MOF material showing such properties.

The work based on this chapter is published:

S. Roy, M. Das, A. Bandyopadhyay, P. P. Ray, S. K. Pati and T. K. Maji, *J. Phys. Chem. C*, 2017, **123**, 23803−23810.

3B.1. Introduction

The application spectrum of porous materials such as metal-organic frameworks (MOFs), covalent-organic frameworks (COFs) and conjugated microporous polymers (CMPs) have recently widened from gas storage/ separation, luminescence and drug delivery[1] to photo-catalysis,[2] electro-catalysis[3] and electronic devices.[4] Specifically, the opto-electronic applications of MOFs and CMPs have the potential to impact the energy landscape of porous materials by generating more advanced solar cells, and electrodes for photocatalysis.[5] Electro-active porous materials also have the potential to impact fuel cell technology by acting as catalysts for oxygen reduction reaction (ORR) and oxygen evolution reaction (OER).[3a,6] Additionally, a high photocurrent can lead to increased efficiency in these systems and hence is highly desired. Although most MOF structures are intrinsically insulating, electrically conducting MOFs have recently been advanced to a great degree by seminal research efforts from the groups of Dincă and Allendorf.[7] High electrical conductivity in MOFs was reported mainly by utilizing redox active organic linkers or by immobilizing electron acceptor molecules into the porous framework to generate facile electron transfer in the extended structure.[8] Jiang *et al*. have further delved into the photo-conducting properties of COFs which have potential in solar cell applications.[9] However, the main lacunae still remains in creating nanostructured MOF materials which provide uniformity in device fabrication via easy solution processability thereby negating problems of discontinuity and junction potentials related to electron flow. Conversely, creating new NMOFs[10] and simultaneously achieving high electrical conduction still remains largely unexplored. To tackle this problem, we have devised a new concept of using highly π-conjugated and optically active bola-amphiphilic organic linkers, and self-assembling them with metal ions in polar solvents to generate nanostructures of MOF. In this context, rigid, rod-like *oligo*-(*p*-phenyleneethynylenes) (OPEs)[11] with alkyl side chains would be ideal systems where the extended π-conjugation generates luminescence and high charge carrier mobility. Furthermore, excellent light absorption would generate a high concentration of charge carriers and self-assembly with metal ions would also increase the diffusion length of charge carriers before recombination leading to high values of photocurrent.[12] OPEs with long alkyl chains could also result in water repellent properties which can pave the way towards devices functioning under extreme conditions.[13] All of these characteristics could lead to solution processable, luminescent, water-repellent and semi-conducting NMOFs which may find

potential applications in field effect transistors (FETs), light-emitting diodes (LEDs), photovoltaic cells (PCs), and Schottky barrier diodes.

This chapter reports the coordination directed self-assembly of dialkoxydodecyl-*oligo*-(*p*-phenyleneethynylene)dicarboxylate (**OPE-C_{12}**) with Zn^{II} to form $\{Zn(OPE\text{-}C_{12})\cdot 2H_2O\}_n$ (**NMOF-1**) having a 3D luminescent supramolecular porous structure. **NMOF-1** showed high water contact angles and self-cleaning behavior. It further showed an appreciable conductance profile with high values of electro-current. Device fabricated from it also showed a Schottky barrier diode (SBD) like behavior having a gigantic increase in current at a low turn-on voltage of +0.2 V and high rectification ratio compared to the best materials.[14] The excellent optical activity of **NMOF-1** also led to high photo-currents with a marked increase in conductivity, carrier mobility and a decrease in barrier height and series resistance upon irradiating the device with light. Theoretical calculations unravel the n-type semi-conducting behaviour of **NMOF-1** and throw light upon the mechanism of conduction which is mainly via the 1D chains of **NMOF-1**.

3B.2. Experimental Section

3B.2.1. Materials

$Pd(PPh_3)_4$ and $Zn(OAc)_2\cdot 2H_2O$ were obtained from Sigma-Aldrich Chemical Co and cuprous iodide was acquired from LobaChemie Pvt. Ltd. N,N-dimethyl formamide (DMF) and tetrahydrofuran (THF) were obtained from Spectrochem Pvt. Ltd (Mumbai, India). Tetrahydrofuran was pre-dried using standard procedure and all other reagents, solvents were of reagent grade and used without further purification.

3B.2.2. Physical Measurements

The elemental analyses were carried out using a Thermo Scientific Flash 2000 CHN analyzer. Infrared spectral studies were performed by making samples with KBr pellets using Bruker FT-IR spectrometer. Raman spectroscopic studies were recorded using a custom built Raman spectrometer with 1800 lines/mm grating. Typically, 632.8 nm HeNe gas lasers were used for the experiments, with a power of about 8mW at the sample. Powder X-ray diffraction studies were recorded on a Bruker D8 discover instrument using Cu-Kα radiation. Thermal stability of the **NMOF-1** was analyzed using Mettler Toledo

TGA 850 instrument under inert atmosphere in the temperature range of 25-850 °C at a heating rate of 3 °C /min. UV–Vis spectra were recorded on a Perkin Elmer Model Lambda 900 spectrophotometer. Fluorescence studies were accomplished using Perkin Elmer Ls 55 Luminescence spectrometer. Morphological studies have been carried out using Lica-S440I Field Emission Scanning Electron Microscope (FESEM) by placing samples on a silicon wafer under high vacuum with an accelerating voltage of 100 kV. Transmission Electron Microscopy (TEM) analysis has been performed using JEOL JEM-3010 with an accelerating voltage at 300 kV. For this analysis **NMOF-1** was dispersed in ethanol by sonication before drop casting on a carbon coated copper grid. Energy dispersive spectroscopy (EDS) analysis was performed with an EDAX genesis instrument attached to the FESEM column. AFM data were collected using a Perkin Elmer Model. Height profiles of the nanostructures were acquired with a Nanoscope Analysis Data Processing software. The surface chemical composition is probed by XPS in an Omicron spectrometer using Mg Kα radiation ($h\gamma = 1486.6$ eV) and a high resolution 7-Channeltron hemispherical analyzer. Electrochemical performance of **NMOF-1** was measured by using a glassy carbon electrode (GCE) voltammetry. They were performed using an Autolab PGSTAT12 potentiostat/galvanostat in a conventional three-electrode cell.

Adsorption Measurements

Porosity measurements were carried out using QUNATACHROME QUADRASORD-SI analyser at 77 K for N_2 and 195 K for CO_2. In the sample tube the adsorbent samples (~100-150 mg) were placed which had been prepared at 170 °C under a 1×10^{-1} Pa vacuum for about 12 h prior to measurement of the isotherms. Helium gas (99.999% purity) at a certain pressure was introduced in the gas chamber and allowed to diffuse into the sample chamber by opening the valve. The amount of gas adsorbed was calculated from the pressure difference (P_{cal} - P_e), where P_{cal} is the calculated pressure with no gas adsorption and P_e is the observed equilibrium pressure. All the operations were computer-controlled. Benzene and water vapor adsorptions were carried out at 298K using BELSORP AQUA 3 solvent vapor analyzer. A sample of about ~100– 150 mg was prepared by heating at 170 °C for about 12 h under vacuum (1×10^{-1} Pa) prior to measurement of the isotherms. The solvent molecules used to generate the vapor were degassed fully by repeated evacuation. Dead volume was measured with helium gas. The

adsorbate was placed into the sample tube, then the change of the pressure was monitored and the degree of adsorption was determined by the decrease in pressure at the equilibrium state. All operations were computer controlled and automatic.

Contact Angle Measurements

Contact angles were measured using an indigenous set up coupled with a Logitech camera for capturing the images. Contact angles were also measured using dedicated contact angle analyzer, OCA30 from Data Physics instrument (GmbH, Germany). 4 μL of the sessile water droplets were employed for measuring the static contact angles. A minimum of ten measurements were made.

Conductivity Measurements of NMOF-1 and H_2OPE-C_{12}

To measure the conductivity of the materials, a thin film of the material was then prepared on the glass substrate by spin coating technique at 1200 rpm for 2 minutes and subsequently dried. Two ohmic parallel electrodes were taken from the film. The dimensions of the electrodes were of 9 mm × 1 mm with a gap of 1 mm between two electrodes. For conductivity measurement, a two-probe contact method was adopted to obtain a current voltage (I-V) characteristics graph, where the electrodes were connected with a Keithley 2400 source meter. The process was performed under room temperature and in open atmosphere. The conductivity was measured with the help of the slope of linear fitted I-V curve, by using equation:

$$\sigma = \left(\frac{\Delta I}{\Delta V}\right)\left(\frac{l}{A}\right)$$

Where, σ is the conductivity, I the current, V the applied voltage, l is the distance between electrodes, A is the cross sectional area of sample.

Fabrication of ITO/ NMOF-1 /Al and ITO/H_2OPE-C_{12}/Al Schottky diode

The Schottky barrier diode (SBD) was fabricated in ITO/**NMOF-1**/Al and ITO/**H_2OPE-C_{12}**/Al configuration. Indium tin oxide (ITO) coated glass substrates was cleaned with soap solution, acetone, ethanol and distilled water sequentially in an ultrasonic bath. The material was dispersed in ethanol medium and ultrasonicated well to form a stable dispersion. A thin film of the material was then prepared on the ITO coated glass by spin coating technique at 1200 rpm for 2 minutes and subsequently dried. Aluminum was

chosen as the rectifier metal contact and deposited on the films by thermal evaporation technique to construct metal-semiconductor junction. The effective diode area was maintained at 7.065 x 10^{-6} m^2 by shadow mask.

Device Characterization

The current flowing across a Schottky diode can be expressed by the ideal diode equation from thermionic emission theory[15]:

$$I = I_0 \left[exp\left(\frac{qV}{nkT}\right) - 1 \right] \quad (1)$$

where I_0 is the reverse saturation current, V is the applied bias, q is the electronic charge, n is the ideality factor, *k* the Boltzman constant and T the absolute temperature. The ideality factor is taken into account for non-ideal behaviour of diode. For ideal diodes n=1. The reverse saturation current can be represented by[15]:

$$I_0 = AA^* T^2 \, exp\left(\frac{-q\phi_b}{kT}\right) \quad (2)$$

Where, A, A^* and ϕ_b are effective diode area, Richardson constant and Schottky barrier height respectively. Effective diode area was maintained at 7.065 x 10^{-6} m^2 and Richardson constant which has theoretical value of 32 $Acm^{-2}K^{-2}$.[16] According to the Cheung-Cheung method, ideality factor, series resistance, barrier height of the Schottky diode can be calculated by the following equations[15]:

$$\frac{dV}{dln(I)} = \frac{nkT}{q} + IR_s \quad (3)$$

$$H(I) = V - \left(\frac{nkT}{q}\right) ln\left(\frac{I}{AA^* T^2}\right) \quad (4)$$

And

$$H(I) = IR_S + n\phi_b \quad (5)$$

Where, R_S is the series resistance of the diode. The dV/dln(I) vs I and H(I) vs I graphs are portrayed in the Figure 19. The diode parameters are listed in Table 2.

Standard SCLC theory was employed to determine the different charge transport parameters. Carrier mobility is a very important parameter to analyze device

performance. Effective carrier mobility was estimated from SCLC region of I vs V^2 graph (Figure 21) by Mott-Gurney equation [17]:

$$\boldsymbol{I = \frac{9\mu_{eff}\ \varepsilon_0\varepsilon_r A}{8}\left(\frac{V^2}{d^3}\right)} \qquad \textbf{(6)}$$

Where $\varepsilon_0$is the dielectric permittivity of vacuum, ε_r the dielectric constant of the material (ε_r= 11.7 was taken), μ_{eff} the effective electron mobility and d the thickness of the film (about ~1 μm for our device). Transit time (τ) and diffusion length (L_D) of the charge carriers are few more key parameters to analyze charge transport across the junction. For this purpose τ was evaluated from equation (7), by using the slope of SCLC region (reg 2) in logarithmic representation of forward I-V curve, shown in Figure 17.[17a] Diffusion length of the charge carriers were further extracted from the following equation (8):[17a]

$$\boldsymbol{\tau = \frac{9\varepsilon_0\varepsilon_r A}{8d}\left(\frac{V}{I}\right)} \qquad \textbf{(7)}$$

$$\boldsymbol{L_D = \sqrt{2D\tau}} \qquad \textbf{(8)}$$

Where, D is the diffusion coefficient and can be calculated from Einstein-Smoluchowskiequation[17a]:

$$\boldsymbol{\mu_{eff} = \frac{qD}{kT}} \qquad \textbf{(9)}$$

K is the Boltzman constant and T is temperature in Kelvin. The carrier concentration (N) near the junction of the devices was estimated by[17a]:

$$\mathbf{N = \frac{\sigma}{q\mu}} \qquad \textbf{(10)}$$

3B.2.3. Computational Details

We have used density functional theory (DFT) method as implemented in the SIESTA package for all the calculations.[18] Generalized gradient approximation (GGA) in the Perdew–Burke–Ernzerhof (PBE) form[19] has been considered to take the exchange–correlation into account. We have used double-zeta-polarized (DZP) numerical atomic-orbital basis sets for all the atoms. Norm-conserving pseudo-potentials[20] in the fully nonlocal Kleinman–Bylander form have been used for all the atoms.[21]To account for the non-covalent interactions, we have used PBE along with DFT-D2.[22] We have used 400

Ry mesh cut-off value. A vacuum of 20 Å has been used in all the three directions to avoid any spurious interactions in the system.

3B.2.4. Synthesis of 4,4'-(2,5-bis(dodecyloxy)-1,4-phenylene)bis(ethyne-2,1-diyl)dibenzoic acid (H_2OPE-C_{12}) and {Zn(OPE-C_{12})·2H_2O}$_n$ (NMOF-1).

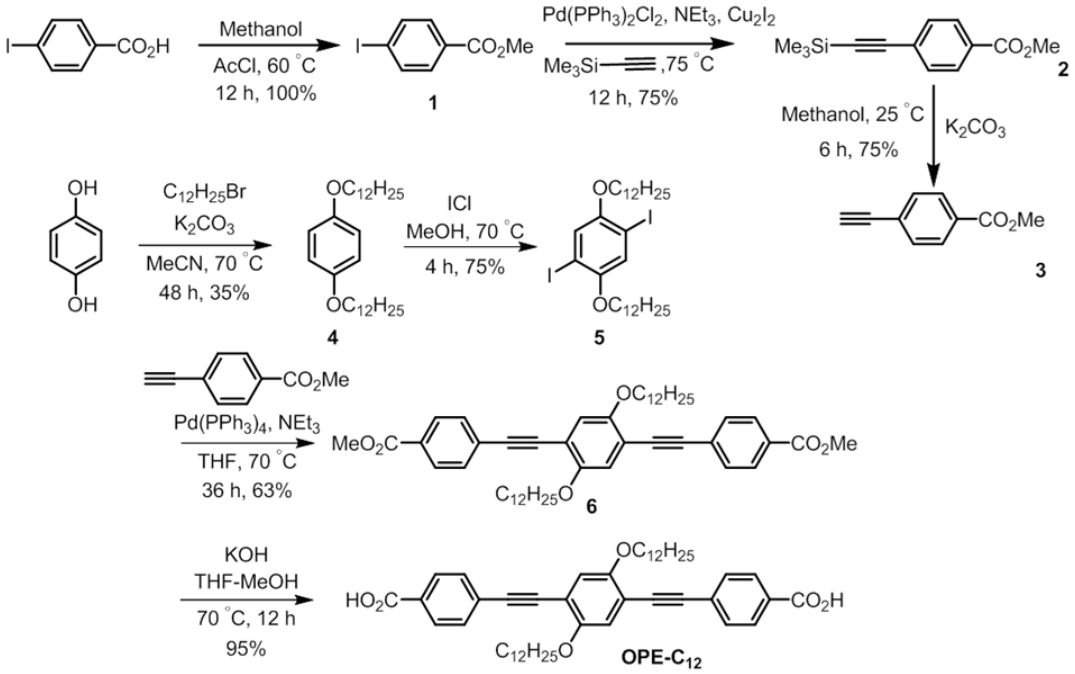

Scheme 1. Synthetic scheme for **H_2OPE-C_{12}**.

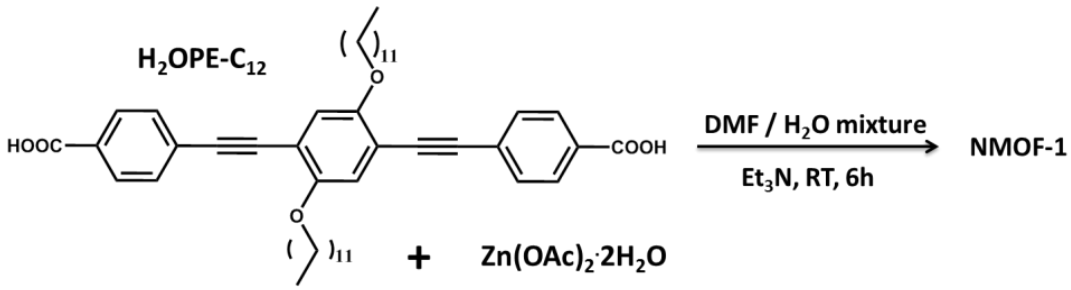

Scheme 2. Synthetic scheme for the synthesis of **NMOF-1.**

H_2OPE-C_{12} was synthesized according to reported Sonogashira Hagihara coupling procedure as discussed in Chapter 2C.[12c] A mixture of **H_2OPE-C_{12}** (30 mg, 0.035 mmol) and Zn(OAc)$_2$·2H_2O (11mg, 0.07 mmol) in a 1:1 DMF/H_2O mixture (10 mL) was stirred for 15 minutes. Then 100 µL triethylamine was added to the above reaction mixture and immediate appearance of a white colloidal turbidity was observed. After 6 hours, the reaction was stopped and the precipitate was centrifuged and washed well with THF and

water to yield **NMOF-1** as a bright green powder. Elemental analysis: Calcd. for $C_{48}H_{64}O_8Zn$: C, 71.4; H, 7.9; Found: C,69.1; H, 7.7. FT-IR (cm^{-1}): 3460(s), 2917(s), 2834(s), 1695(s), 1598 (s), 1400(s), 1215(s), 1014(w), 748(w), 504(w)

3B.3. Results and Discussion

3B.3.1. Structural Characterization

H_2OPE-C_{12} was synthesized with alkoxy-dodecyl functionalization of side chains and carboxylic acid end groups following reported Sonogashira-Hagihara coupling procedures[12c] (Scheme 1). **NMOF-1** was then synthesized by stirring **H_2OPE-C_{12}** and $Zn(OAc)_2{\cdot}2H_2O$ in DMF-H_2O-triethylamine mixed solvent system at room temperature for six hours (Scheme 2). Colloidal turbidity appeared spontaneously upon the addition of metal solution to the ligand solution. This was an indication of coordination of Zn^{II} to **H_2OPE-C_{12}**. EDS and XPS analysis (Figure 1, 2) confirmed the presence of Zn, C and O. XPS showed the presence of C1s, O1s and Zn2p peaks. CHN analysis afforded the molecular formula of $\{Zn(OPE\text{-}C_{12}){\cdot}2H_2O\}_n$ (**NMOF-1**). IR and Raman spectral analysis indicated the presence of water and carboxylate C-O stretching frequencies in **NMOF-1** (Figure 3, 4). Furthermore, the difference between the asymmetric (1598 cm^{-1}) and symmetric (1400 cm^{-1}) carboxylic acid stretching modes of ~198 cm^{-1} showed the bi-dentate coordination of the carboxylates to Zn^{II}. Therefore, we predict that four carboxylate oxygen, and two water oxygen atoms make up the hexa-coordination environment around Zn^{II} in **NMOF-1**. TG analysis revealed that **NMOF-1** is stable upto 320 ºC.

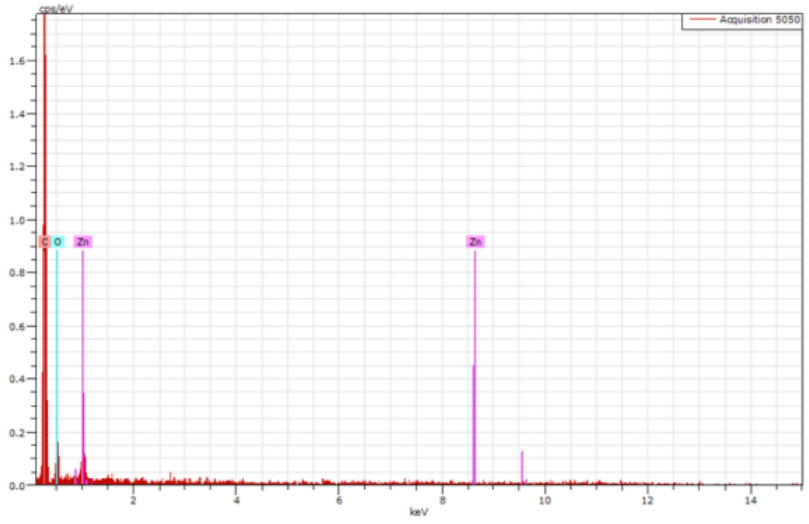

Figure 1. EDS analysis indicating the presence of Zn^{II} metal ion in **NMOF-1**.

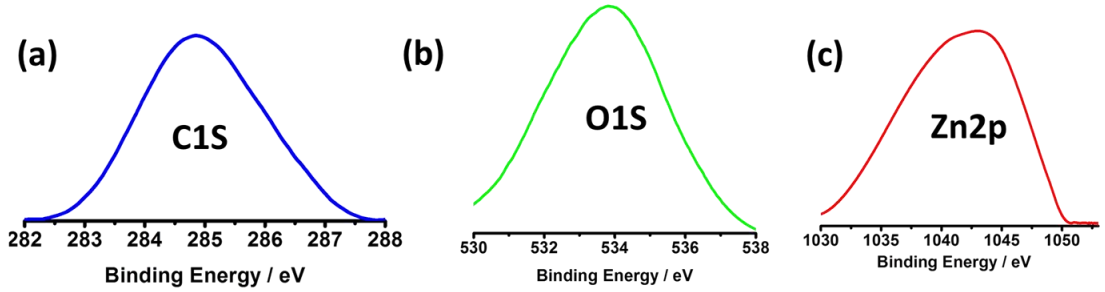

Figure 2. XPS transitions for (a) C1s (blue), (b) O1s (green) and (c) Zn2p (red) in **NMOF-1**.

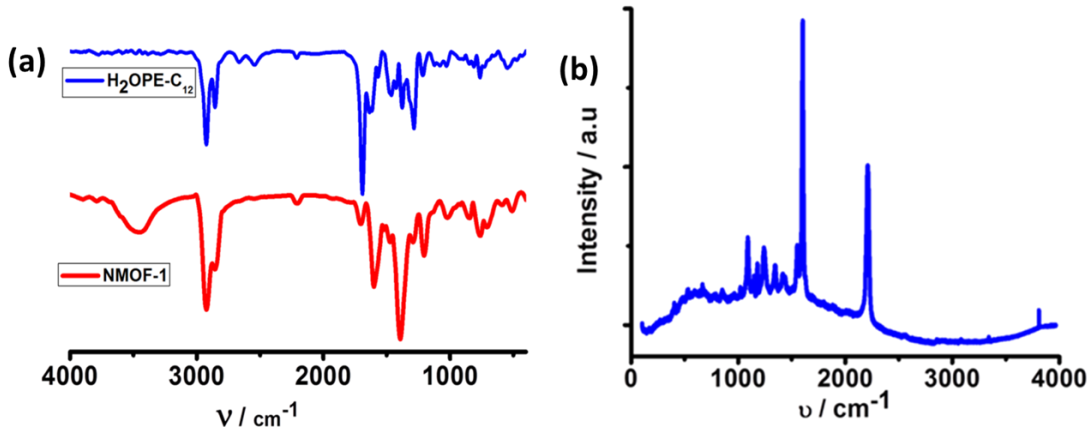

Figure 3. (a) FT-IR spectra of **H_2OPE-C_{12}** (blue) and **NMOF-1** (red) and (b) Raman spectrum of **NMOF-1**.

A weight loss of 4.0% upto 150 ºC indicated the loss of two coordinated water molecules (Figure 4). N_2 adsorption isotherm at 77 K showed surface adsorption as indicated by the type II profile (Figure 5a). However, CO_2 adsorption isotherm at 195 K showed a type I adsorption profile with an uptake of 46 cc/g at P/P_0= 1 corresponding to 1 molecule of CO_2 per formula unit of **NMOF-1**, indicative of its microporous nature (Figure 5b). The crystallinity of **NMOF-1** was validated by powder X-ray diffraction (PXRD) measurement (Figure 5c). Modeling and indexing of the PXRD peaks were done using the Crysfire software (Table 1). It suggested an orthorhombic crystal system of **NMOF-1** with cell parameters of a =10.4 Å, b = 15.2 Å and c = 20.0 Å, α = β = γ = 90° and cell volume of 3168 $Å^3$. The accuracy of the calculation was validated via a good correspondence between the theoretical and experimental data as indicated in Table 1. The (001) peak at 4.4° with d-spacing of 20.2 Å corresponded to the repeating distance of

OPE-C_{12} coordinated to the Zn^{II} centres. This also indicated that the ID coordination chain is extended along the *c*-axis via Zn^{II} coordination. The peak at 20.7^0 (220), corresponding to the π-π distance (4.2 Å) in between the adjacent phenyl rings of **OPE-C_{12}**, extend the packing in 2D. The 7.3° peak shows a *d*-spacing of 12.1Å. This peak is attributed to interdigitation of alkyl chains. We therefore hypothesize that this interdigitation between dodecyl alkyl chains of adjacent 2D layers extends the packing into 3D to lead to a porous supramolecular 3D framework of **NMOF-1** (Scheme 3).

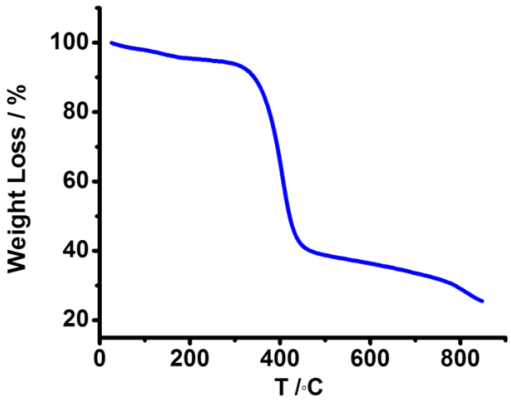

Figure 4. TGA profile of **NMOF-1** in the temperature range 25-850 °C with a heating rate of 3 °C/ min.

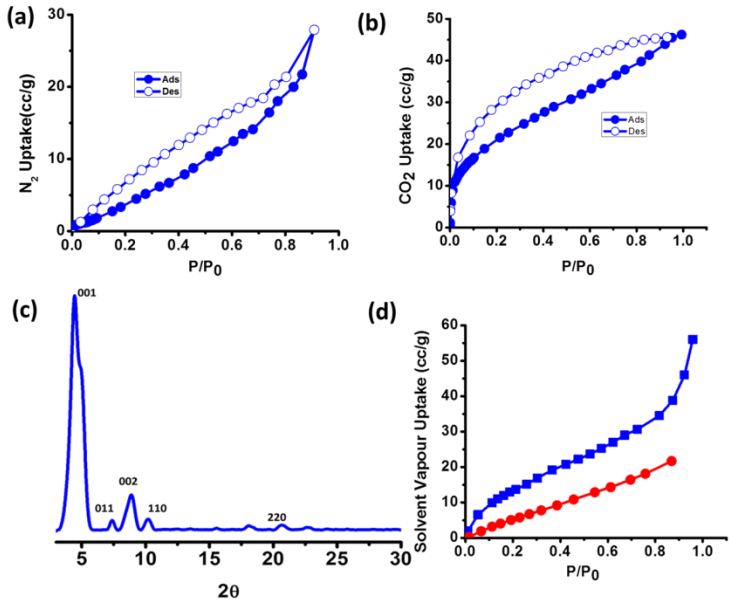

Figure 5. (a) N_2 at 77 K and (b) CO_2 adsorption isotherms at 195 K of **NMOF-1**. Filled circles indicate adsorption points and empty circles indicate desorption points, (c) PXRD pattern and (d) Water (red) and benzene (blue) vapour adsorption isotherms at 298 K of **NMOF-1**.

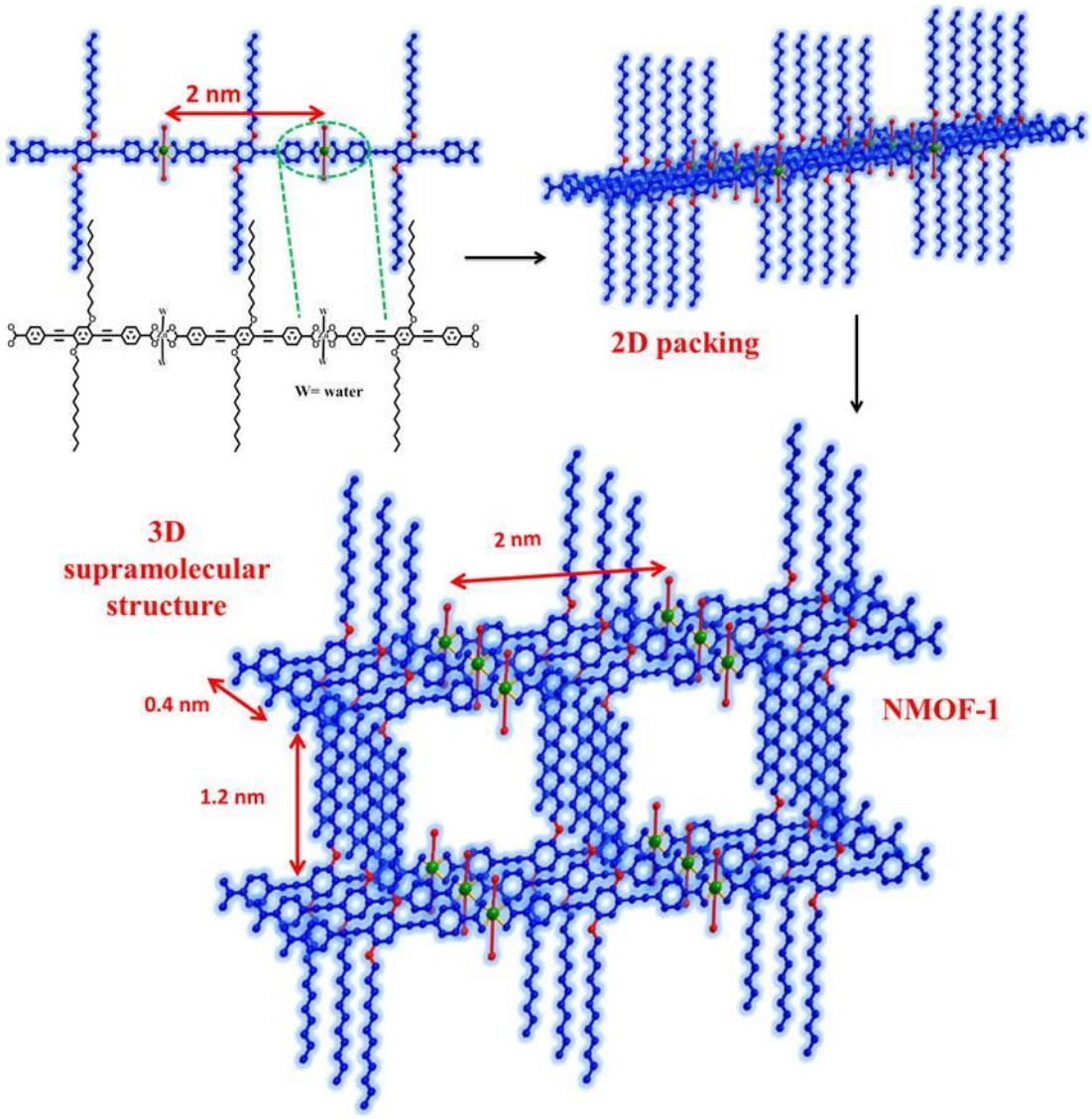

Scheme 3. (a) Schematic showing the coordination directed self-assembly of **OPE-C_{12}** with Zn^{II} leading to the formation of supramolecular porous structure in **NMOF-1** and (b) Scheme showing the different packing interactions leading to the 3D porous hydrophobic structure of **NMOF-1**.

The nanoscale architecture of **NMOF-1** was further investigated by field emission scanning electron microscopy (FESEM), transmission electron microscopy (TEM) and atomic force microscopy (AFM). FESEM revealed the presence of nanosheets of **NMOF-1**. The sheets have a dimension of 300- 600 nm length and 300- 500 nm width (Figure 6a-c). TEM images further confirm the existence of square shaped nanosheets of **NMOF-1** (Figure 6d). High resolution TEM (HRTEM) images reveal a high degree of structural ordering of metal-coordinated **OPE-C_{12}** units forming the extended porous 3D

supramolecular structure. This was visualized from the regularly spaced dark line-like regions with an interspacing distance of 1– 1.5 nm (Figure 6e,f) and this value corresponded well with *d*-spacing of 1.2 nm between π-stacked chains obtained from the powder pattern. The electron diffraction pattern suggested the highly crystalline nature of the framework and careful analysis revealed the presence of the (001), (011) and (220) planes in **NMOF-1**(Figure 7). The presence of π-π stacking corresponding to the d-spacing of 0.42 nm found in the PXRD pattern ((220) peak) was seen. Two perpendicularly displaced spots having a distance of 1.1 nm and 2.1 nm can be correlated to the (011) and (001) peaks found in PXRD. These correspond to the 1D chain repeating unit and interdigitation present in **NMOF-1** and give an idea of how the **NMOF-1** unit cell is oriented.

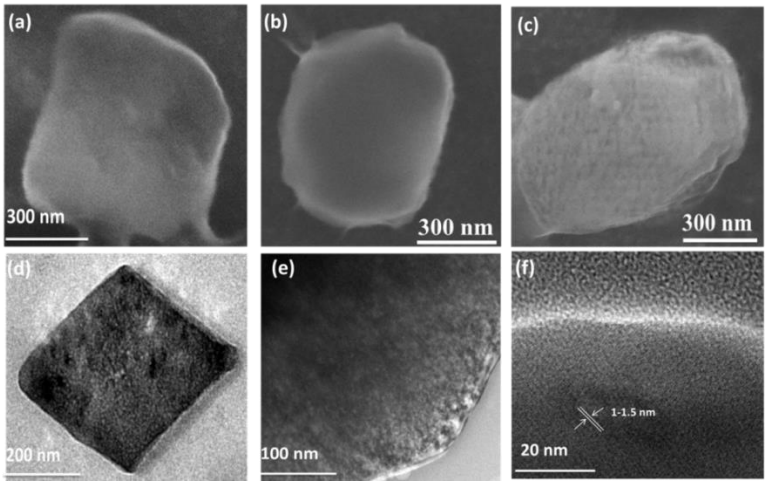

Figure 6. (a-c) FESEM and (d) TEM images of a single nanosheet of **NMOF-1**, (e, f) HRTEM images of **NMOF-1** portraying a high degree of structural ordering.

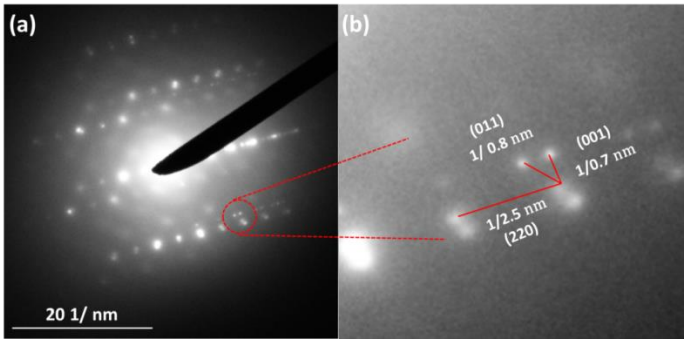

Figure 7. (a) Electron diffraction (ED) pattern of **NMOF-1** showing its high crystallinity and (b) Zoomed image of the ED pattern showing the indexingof the planes contained in **NMOF-1**.

Table 1. Indexing data of **NMOF-1** using Crysfire software using the TP program[23]

Crystal system: orthorhombic

Cell Parameters: a = 10.4259(4) Å b = 15.1889(8) Å c = 20.0086(7) Å α= β = γ = 90 °, V = 3168. 51 Å^3

h	*k*	*l*	d_{obs}	d_{cal}	d_{obs}-d_{cal}	Q_{obs}	Q_{cal}	$2\theta_{obs}$	$2\theta_{cal}$	*Diff*
0	0	1	20.18318	20.00857	-0.0382	.002455	.002498	4.3745	4.4127	-0.0382
0	1	1	12.09796	12.09796	0.0000	.006832	.006832	7.3012	7.3012	0.000
0	0	2	9.99350	10.00428	-0.01078	.010013	.009991	8.8415	8.8319	0.0096
1	1	0	8.66789	8.59572	0.07217	.013310	.013534	10.1970	10.2828	-0.0858
0	2	2	4.29343	4.29786	-0.00443	.054249	.054137	20.6712	20.6497	0.0215

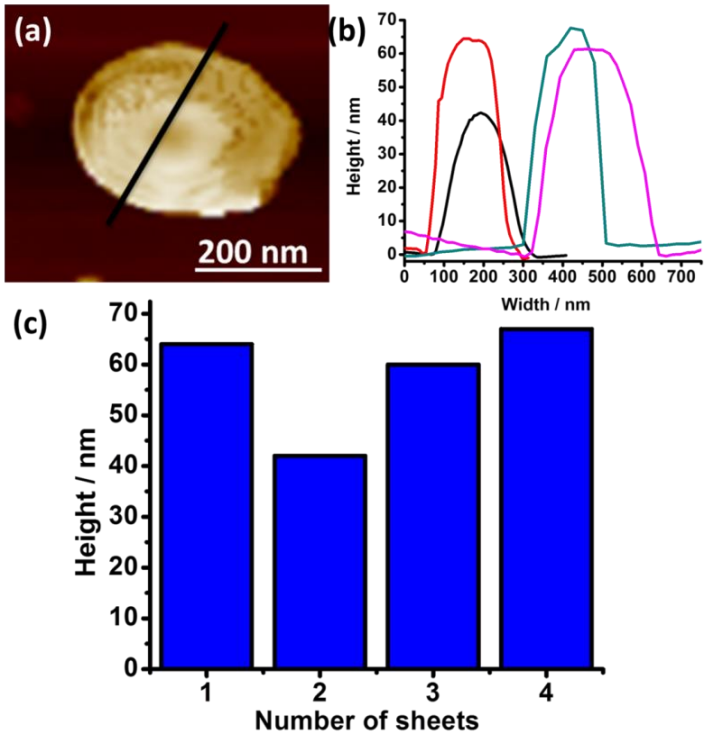

Figure 8. (a) AFM image of a single nanosheet and (b) Plot showing the height of the nanosheets of **NMOF-1**.

AFM images corroborated the presence of nanosheets of **NMOF-1**. Furthermore, height profile analysis revealed a height of 40-70 nm for the nanostructures which suggests approximately 90-160 π-stacked **OPE-C_{12}** 1D chains are present (Figure 8).

3B.3.2. Superhydrophobicity and Self-Cleaning in NMOF-1

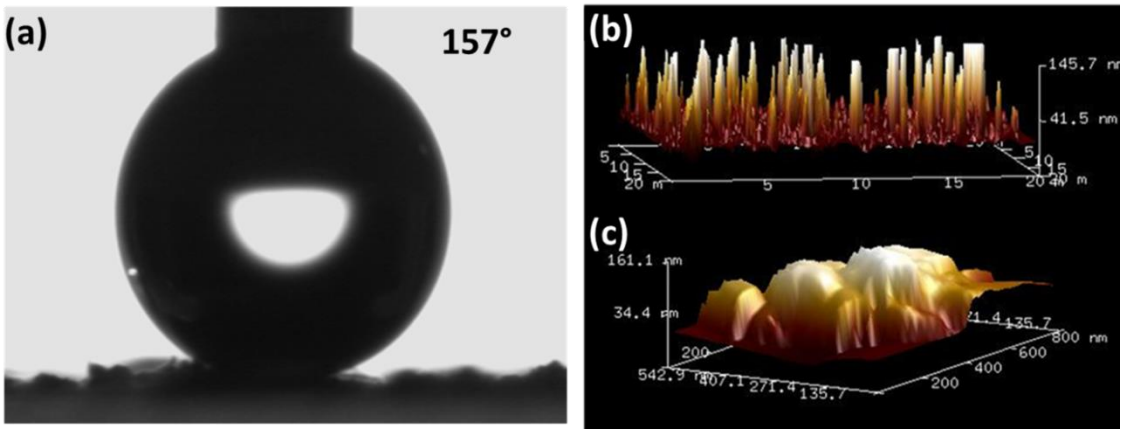

Figure 9. (a) Water contact angles on **NMOF-1** coated on a glass substrate. 3D-AFM image of (b) Micrometer and (c) Nanometer range coverage of **NMOF-1** surface showing the roughness leading to a "hills and valley" type morphology required for the self-cleaning property.

It has been previously reported by our group, that the presence of long alkyl chains at the periphery of OPE based nanoscale MOF structures assists in not only generating a superhydrophobic surface, but can also lead to self-cleaning ability.[13] From our structural prediction of **NMOF-1**, it is clear that dodecyl chains will form a hydrophobic pore and also surface projection of these dodecyl alkyl chains will induce hydrophobicity of the surface. We therefore performed adsorption experiments with benzene and water to elucidate the nature of the pore surface. As expected, **NMOF-1** showed high quantity of adsorption of benzene solvent vapor (60 ml) whereas there was minimal uptake of water vapor. This portrayed a highly hydrophobic nature of **NMOF-1** pores (Figure 5d). The easy solution processability of **NMOF-1** further allowed us to apply it on large areas of a glass substrate by simple drop-casting. It led to a thin film of **NMOF-1** on it. Water contact angles were measured on this coated glass substrate by putting water droplets of 4μL volume. **NMOF-1** coated samples on a glass substrate showed water contact angles of 153-157º which proved its superhydrophobic nature (Figure 9a). The contact angle hysteresis was also calculated to be ~5° which ascertained that **NMOF-1** might act as a self-cleaning material. Buoyed by these observations, we went on to check for its self-

cleaning property. Water droplets smoothly rolled on the surface of the **NMOF-1** coated glass slide without any noticeable change in its contact angle. The sliding angle was 5-6º which further affirmed the self-cleaning nature of the material. To investigate the reason behind the self-cleaning behavior, we imaged the coated surface with AFM.

3D AFM micrographs reveal a rough surface at the microscale showing the "hills and valley" type morphology required for the superhydrophobicity (Figure 9b). Further probing at the nanoregime showed that the same surface morphology remained intact leading to a hierarchical surface structure (Figure 9c). This allows the easy rolling of water droplets on the surface of the superhydrophobic structure thus mimicking the lotus leaf effect.

3B.3.3. Opto-electronic Properties of NMOF-1

NMOF-1 showed a highly stable dispersion in THF and allowed uniform coating on a large area of glass substrate (Figure 10a). **NMOF-1** in THF showed emission maxima at 460 nm (λ_{ex}=390 nm) (Figure 10b,c) while in the solid state it showed UV peak maximum at 375 nm and exhibited cyan fluorescence with a maximum at 475 nm upon excitation at 380 nm (Figure 11). To further investigate the redox property, we carried out cyclic voltammetric experiments of **NMOF-1** on glassy carbon electrodes in anhydrous acetonitrile with TBAP as the supporting electrolyte. Well defined oxidation and reduction peaks were observed at 0.13 V and -0.15 V respectively with respect to Ag/Ag^+ non-aqueous electrode (Figure 12). From this profile, the electrochemical band gap was calculated to be 2.18 eV.

As the cyclic voltammogram was obtained under non-aqueous conditions, Ag/Ag^+ reference electrode was used and hence conversion into RHE voltages was required to carry out the band gap calculations. The following standard equation was used for the conversion:

$$E_{RHE}=E_{Ag/Ag+} + E + 0.059*pH\ldots\ldots..(1)$$ where

E_{RHE}= the corresponding potential for RHE

$E_{Ag/Ag+}$= the standard electrode potential for the Ag/Ag^+ couple

and E= the observed potential using the Ag/Ag^+ couple

Using this equation the onset oxidation and reduction potentials were found to be 1.342 and 0.842 V respectively.

$$E_{oxRHE} = 0.799 + 0.13 + 0.413 = 1.342V$$

$$E_{redRHE} = 0.799 - 0.37 + 0.413 = 0.842V$$

Hereon, the following formula was utilized to determine the experimental electrochemical HOMO and LUMO levels in terms of eV unit:

$$E\ (HOMO) = -e\ [E_{ox}^{onset} + 4.4] \ldots..(2)$$

$$E\ (LUMO) = -e\ [E_{red}^{onset} + 4.4] \ldots. (3)$$

And the HOMO and LUMO levels were found to be -5.33 and -3.15 eV respectively having a band gap of 2.18 eV.

$$E\ (HOMO) = -e\ [1.342 - 0.41 + 4.4] = -5.33\ eV$$

$$E\ (LUMO) = -e\ [-0.842 - 0.41 + 4.4] = -3.148\ eV$$

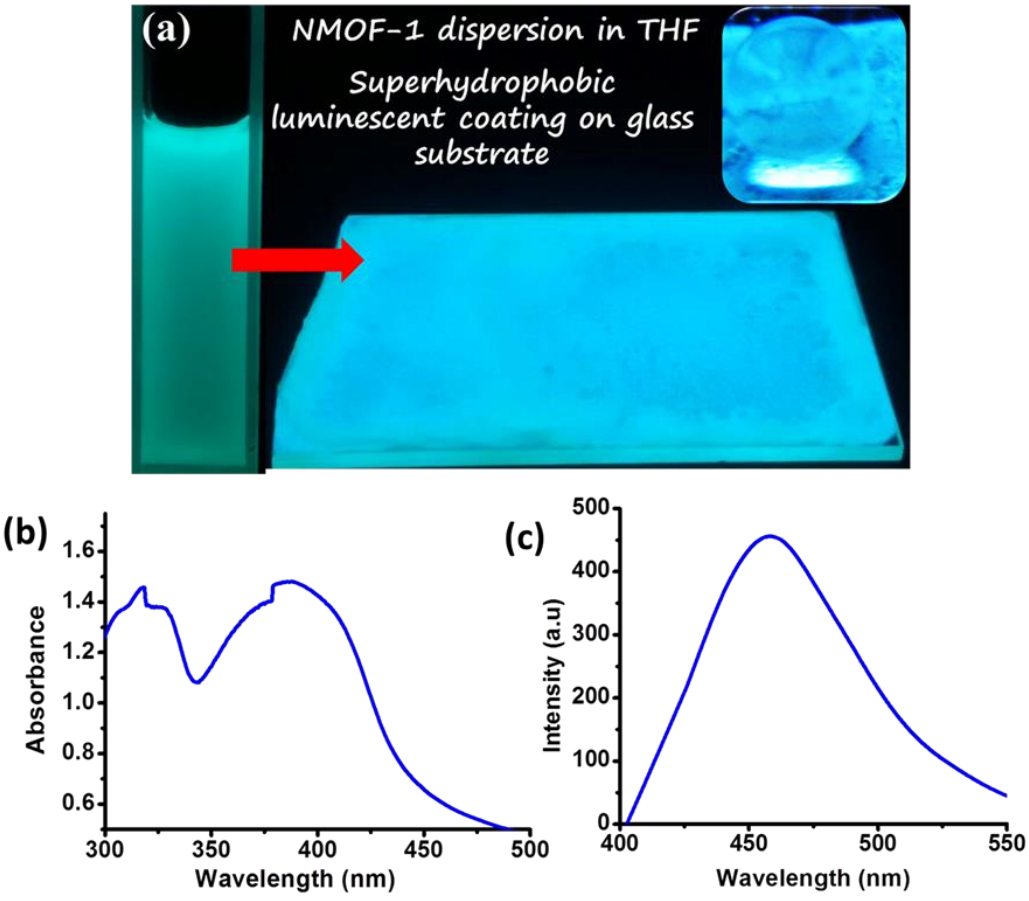

Figure 10. (a) Images of bright emission under UV light of **NMOF-1** in THF and on a glass substrate. Inset: image of a water droplet on the **NMOF-1** coated glass substrate under UV light. (b) UV and (c) PL for **NMOF-1** dispersed in THF.

This electrochemical observation further prompted us to move forward towards probing the inherent conductivity of **NMOF-1** and also to fabricate device structures due to its easy solution processability.

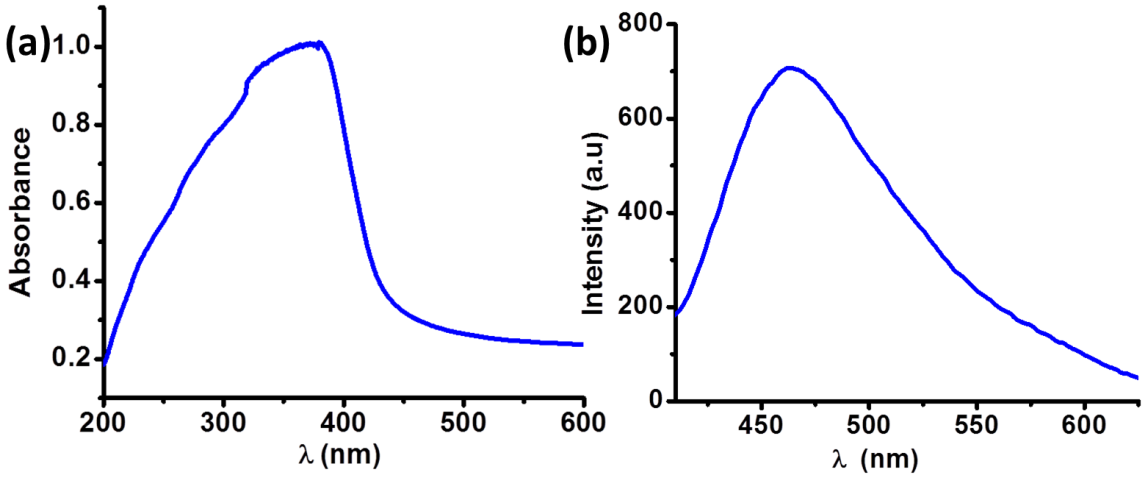

Figure 11. Solid state (a) UV and (b) PL profile for **NMOF-1**.

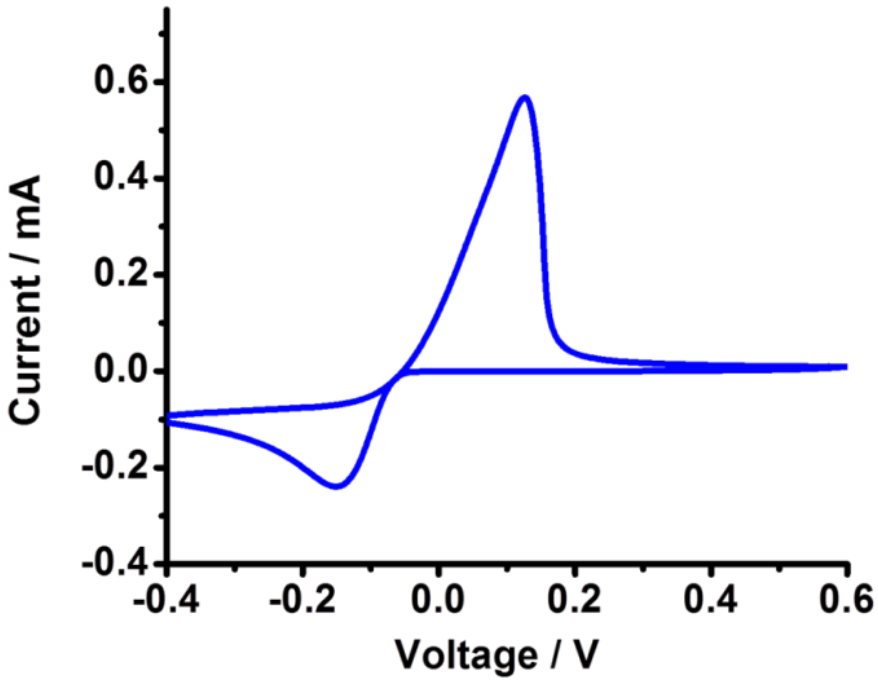

Figure 12. Voltammogram of **NMOF-1** on a glassy carbon electrode in anhydrous acetonitrile solution containing TBAP as a supporting electrolyte at a scan rate of 50 mV/sec.

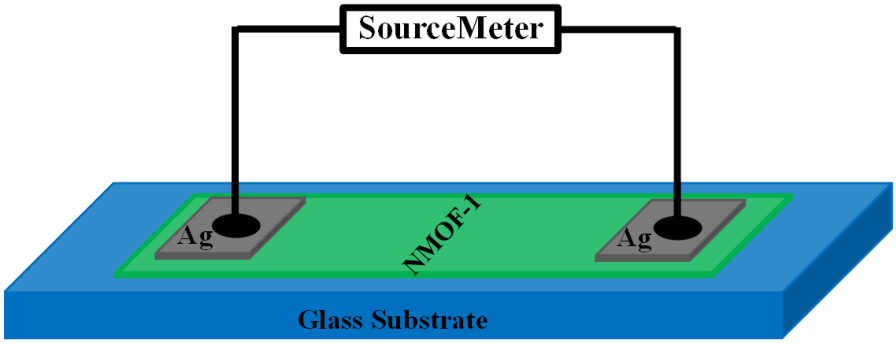

Scheme 4. Method used to measure **NMOF-1** conductance.

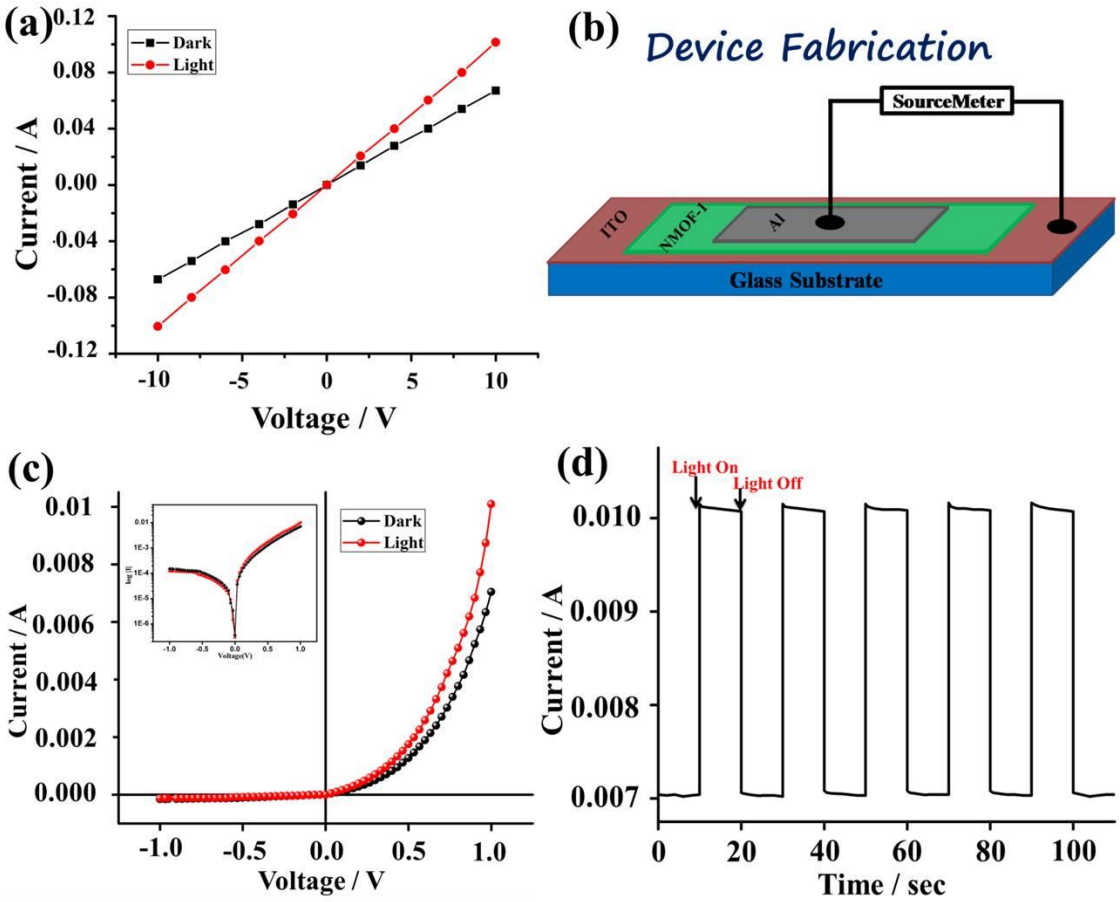

Figure 13. (a) Current vs voltage graph for conductivity measurement of **NMOF-1** with ohmic contact in planar electrode structure, (b) Schematic showing the device structure of **NMOF-1**, (c) Current-voltage (I-V) characteristics of the ITO/**NMOF-1**/Al Schottky diode and (d) Transient photocurrent response of the ITO/**NMOF-1**/Al Schottky diode.

We measured the conductivity of the material on a thin film of **NMOF-1** (Scheme 4). Current-voltage (I-V) measurements of **NMOF-1** were recorded with a Keithley 2400 sourcemeter under dark and light condition. The measured conductivity of the material was 9.6×10^{-6} S/ cm (Figure 13a), typical of a semi-conductor. However, with photo-

irradiation, the conductivity of **NMOF-1** increased to 1.4×10^{-5} S/ cm which was a marked improvement from the non-irradiated conditions. We envisaged that the conduction might arise due to either "through bond": i.e. along the 1D chain or "through space" i.e. along the π-stacks. This prompted us to theoretically model the structure and calculate the origins and characteristics of the conductivity. We performed a set of density functional theory calculations to validate and explain the experimental results. We considered two different packings: one consisting of three **OPE-C_{12}** molecules connected by two Zn^{II} atoms forming the 1D chain and the other along the π-π stacked direction (Figure 14). We then optimized the structures and found that in the molecules along the coordination chain, the Zn-Zn distance is 23.5 Å, which compares well with the experimental result, whereas, in the stacked molecules the interlayer distance is 3.4 Å (as we do not consider the extended 3D system

theoretically). This distance, the stacking pattern and a stack formation energy value of 0.71 eV in the optimized geometry suggested a strong π-π interaction in the structure. HOMO and LUMO orbital pictures simulated from the above modeling for the 1D chain suggested that the HOMO level originates from the unhybridized p_z orbitals involved in electron delocalization and the LUMO level lies along the 1D chain involving the phenyl rings and the empty Zn^{II} 4s orbitals. This proposed a "through bond" charge transfer in **NMOF-1** (Figure 15, 16).

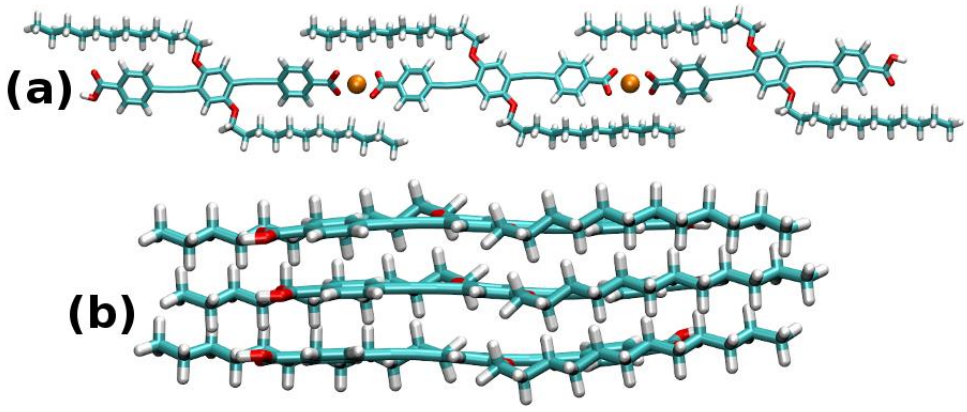

Figure 14. (a) Three molecules along a 1D chain (formed by **OPE-C_{12}**-Zn-**OPE-C_{12}** bonds) and (b) Along the π-π stacked direction, cyan, red, silver and orange colours denote C, O, H and Zn atoms, respectively.

3B.3.4. Device Fabrication Using NMOF-1

We then envisioned that the nanoscale architecture would allow us efficiently coat it on conductive electrodes for device fabrication. This, and the previous conductivity profile

of **NMOF-1** led to our great interest in application of this material in Schottky barrier diode (SBD). So, to verify if the **NMOF-1** shows Schottky behavior, multiple devices were fabricated in ITO/**NMOF-1**/Al sandwich structure and current-voltage (I-V) measurements were performed in the bias range -1 V to +1V (Figure 13b,c).

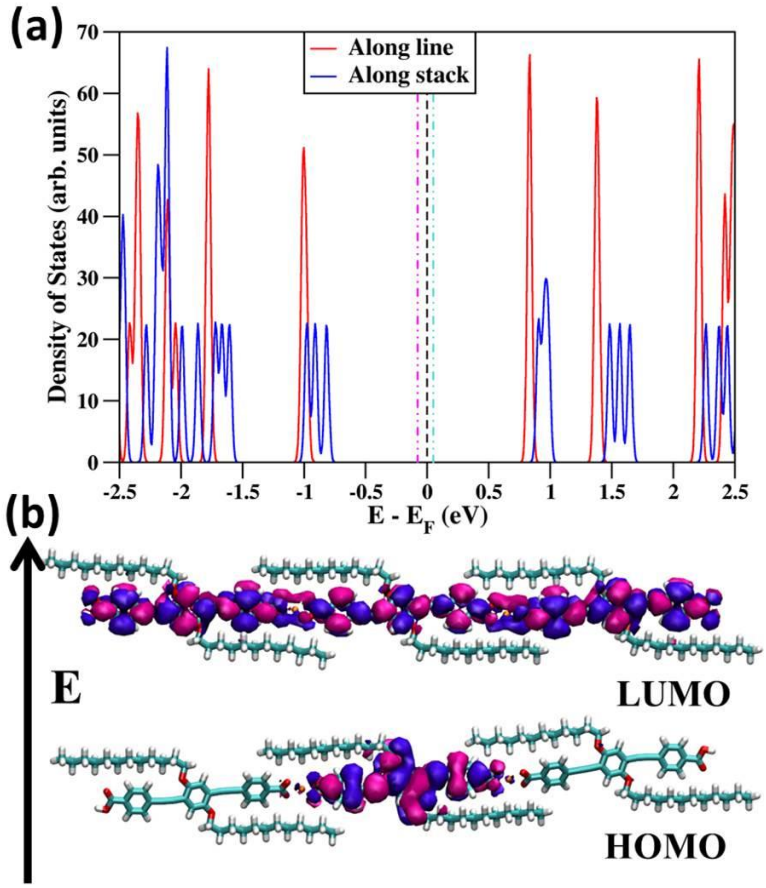

Figure 15. (a) Density of states calculations of the packing along the 1D chain (red) and along the π-π stack (blue) (b) HOMO (lower) and LUMO (upper) plots of **NMOF-1**.

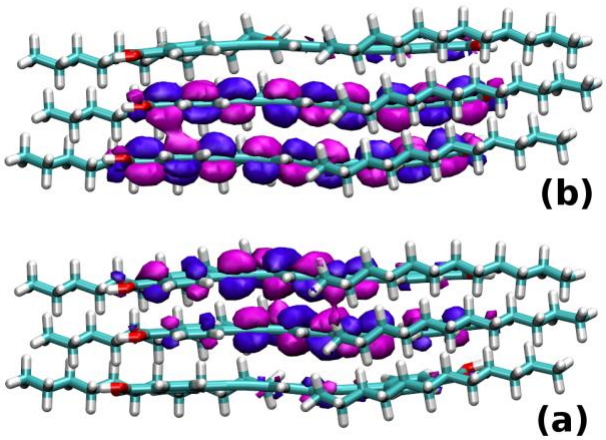

Figure 16. (a) HOMO and LUMO plots along the π-stacking direction.

With the ITO/**NMOF-1** Ohmic contact, the representative I-V characteristics of the Al/**NMOF-1** is displayed in Figure 13c. Evidently, the Al/**NMOF-1** interface exhibited rectifying nature which is the signature of a Schottky barrier diode. The I-V characteristic of the SBD was also measured under photo irradiation condition, under AM 1.5 radiation. Rectification ratio (I_{on}/I_{off}) of the SBD at ±1V was obtained as 47 at dark and 83 under photo condition. To the best of our knowledge, this is the first such study in a framework material with permanent porosity showing such high rectification ratios at just ±1V. The characteristics curve under light showed larger current which illustrated the photoresponse of the device. For investigating the photoresponse, we measured the transient photocurrent of the device under AM 1.5 radiation at bias voltage of 1V (Figure 13d). The photosensitivity was found to be 1.43. Transient photocurrents were extremely rapid, steady, prompt and reproducible during several switched on–off cycles of the visible light irradiation for the device. Often grain boundaries create deep traps to slow down the electron transport.[24] The rectangular response indicated that no grain boundaries exist in the direction of electron diffusion. This finding also suggested that the excited electrons move efficiently in the external circuit.[24]

Table 2. Schottky Diode parameters.

Sample	Cond^{n}.	On/off	Photosensityvity	I.F.	R_S (Ω)	R_s(H) (Ω)	φ_b(eV)
NMOF-1	Dark	47	1.43	1.82	270	330	0.35
	Light	83		1.78	245	235	0.33

The current voltage characteristic of the NMOF based Schottky diode was further analyzed by thermionic emission theory and Cheung's method was employed to extract important diode parameters.[25] The values of ideality factors (n) of **NMOF-1** were estimated to be 1.82 and 1.78 under dark and light, respectively. It deviated from ideal behaviour and this difference is due to the presence of inhomogenities of Schottky barrier height and existence of interface states, and series resistance.[25] But importantly, the value of ideality factor approached unity under light. Also, series resistance (R_s) of the fabricated devices reduced when the device was subjected to illumination (Table 2). Barrier heights of the Schottky diodes were 0.35 eV and 0.33 eV for Al/**NMOF-1** under dark and photo condition respectively (Table 2). These values suggested that illuminated

condition has led to a slightly lower turn on voltage. Here again, we want to emphasize that the series resistance of this device (R_s = 270 Ω) was significantly lower than those of schottky devices based on other coordination polymers (R_s=413kΩ),[14a] (Rs=797Ω).[14b] Also, the obtained barrier height was relatively lower compared to other coordination polymer based SBD reported earlier.[14a,b] This can be beneficial for devices that require a lower turn on voltage. So, it can be said that our device parameters are excellent in context of MOF based SBD. For a better insight into the charge transport phenomena, we investigated the I-V curves in details. The characteristic I-V curves under both conditions in the logarithmic scale revealed that it can be differentiated in three slopes (Figure 17).

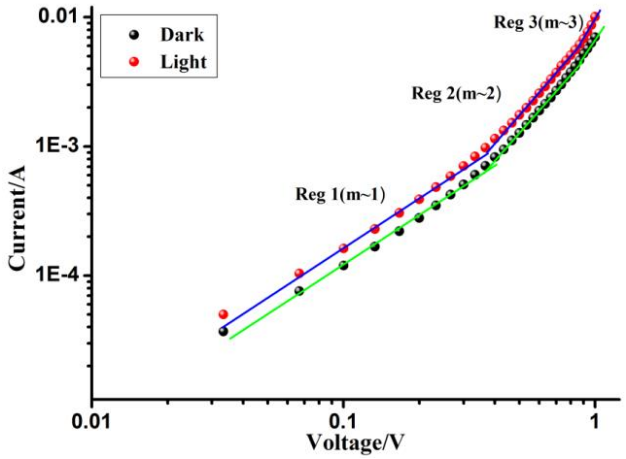

Figure 17. Current-voltage (I-V) characteristics of the ITO/ **NMOF-1**/Al Schottky diode under forward bias (in logarithmic scale).

The three regions have slopes of nearly 1, 2 and 3 respectively. In first region, when the slope is ~1, current follows the relation I α *V,* which refers to the Ohmic regime. In the second region, the slope is about 2, where current is proportional to V^2 (Figure 17-19). This is the very characteristic a of trap free space charge limited current(SCLC) regime.[26] If the injected carriers are more than the background carriers, the injected carriers spread and create a space charge field. The currents are controlled by this field and are known as SCLC.[26b,c] Beyond this region, the current follows the relation Iα V^m, where m~3. The SCLC theory which has recently drawn popular attention was adopted here to estimate the mobility of materials.[26b,c] Following this model the mobility has been estimated estimated as 0.069 $cm^2V^{-1}s^{-1}$ from Mott-Gurney law.[15, 26a,b] Estimated values of effective carrier mobility, transit time, carrier concentration and diffusion length demonstrate that the charge transport properties of the material improved after light soaking (Table 3).

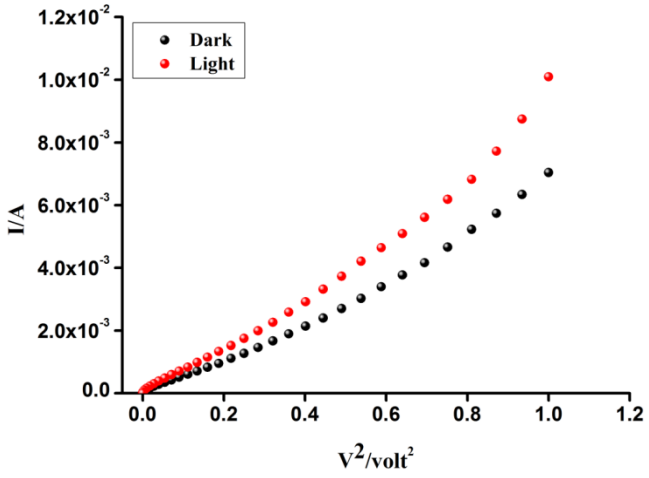

Figure 18. I vs V^2 graph for the Al/**NMOF-1**/ITO Schottky diode under dark and light condition.

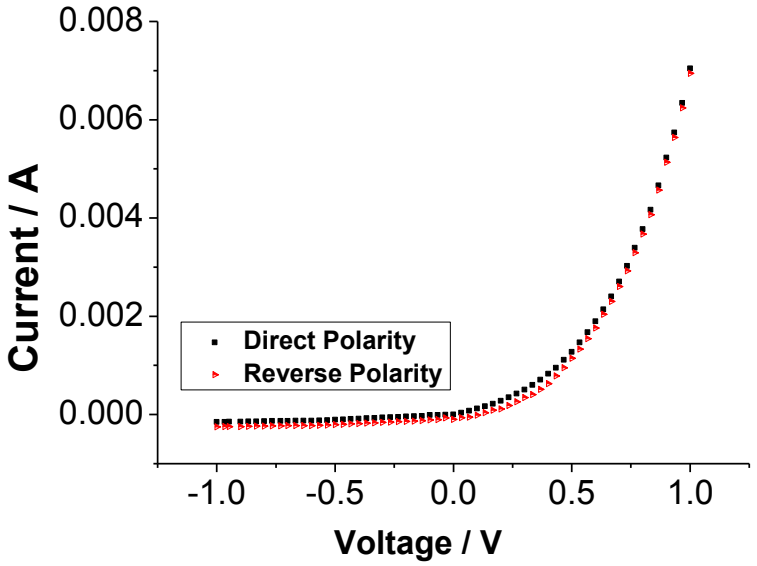

Figure 19. I vs V graph for the Al/**NMOF-1**/ITO Schottky diode in direct and reverse polarity.

The mobility implied higher transport rate under irradiation, while number of charge carriers also increased under light. Notably, the obtained values of mobility for the **NMOF-1** was higher than or comparable to those found for MOF and other organic semiconductors.[14a,b,27,28]

Not only that, the diffusion length of the charge carriers was found to be 198 nm in **NMOF-1**, which is almost 167% larger compared to the 74 nm reported for Cd(II)-MOF

based SBD.[14b] The increased diffusion length under illumination revealed that the charge carriers got to travel more length before being recombined which led to the eventual increase in current displayed by the device under light.

Table 3. Tabulation of charge transport data for **NMOF-1** device.

Sample	Cond^{n}	μ_{eff}*10^{-6} (m^2 V^{-1} s^{-1})	τ (μS)	$\mu_{eff}\tau$* 10^{-12} (cm^2 V^{-1})	N_D(*10^{21}) (m^{-3})	L_D (nm)
NMOF-1	Dark	6.9	0.11	75	87	198
	Light	10.1	0.08	81	90	206

The diode parameters of the **NMOF-1** SBD indicates it's superior performance compared to other MOF based SBDs, while it also demonstrates much enhanced charge transfer kinetics compared to some of the reported MOFs. So, this self-cleaning and luminescent material can pave the way for a very promising future in device application.

As a control experiment, we measured the conductivity of **H_2OPE-C_{12}**. The obtained values of conductivity are 7.7 × 10^{-6} S/ cm and 8.3 × 10^{-6} S/ cm under dark and light respectively, which was slightly lower than **NMOF-1** along with negligible photoconduction (Figure 20). This comparative value arose because **H_2OPE-C_{12}** is hydrogen bonded via terminal carboxylate groups leading to a 1D chain of periodically repetitive OPEs.[11c] We also fabricated the device with the ligand in Al/**H_2OPE-C_{12}**/ITO sandwich configuration and measured the I-V characteristics under both dark and light condition (Figure 21). However, there was a stark contrast in the device performances of both materials. While **NMOF-1** based device showed good rectification and photosensitivity, the performance of **H_2OPE-C_{12}** based device was minimal. The ligand based device showed very poor Schottky nature, with rectification ratio of 1.77 and 1.78 under dark and light condition respectively, which was far less than **NMOF-1**. Also, the photosensitivity of the device was 1.07, which was again rather low compared to **NMOF-1**. This indicated that the regular periodicity obtained via coordination of Zn^{II} with **OPE-C_{12}** creates a facile pathway for electron flow across the 1D chain leading to improved device performance. To understand the Schottky diode formation and transport behavior in the 3D network, we calculated the density of states (DOS) of the previously described model system. To know the effect of each type of bonding direction, we plotted in Figure 15a the DOS of the molecules along the two packing directions.

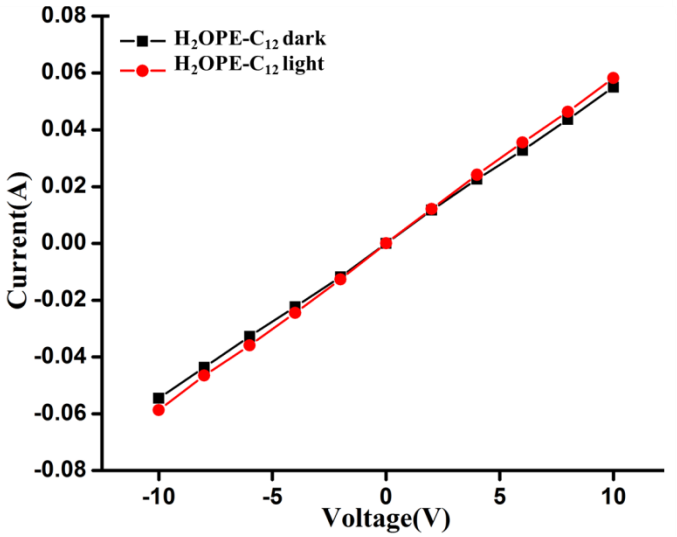

Figure 20. Current vs voltage graph for conductivity measurement of **H_2OPE-C_{12}**.

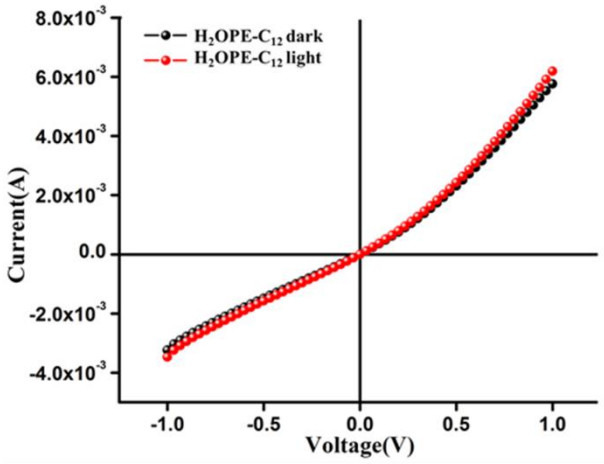

Figure 21. Current-voltage (I-V) characteristics of the ITO/**H_2OPE-C_{12}**/Al Schottky diode.

The overall system was a semiconductor with a HOMO-LUMO gap of 1.63 eV. Now, when we considered the stacks and the chains separately, the Fermi energy of these systems was at -3.46 and -3.34 eV, respectively. These can form Schottky diode with Al (Work function = -4.08 eV) only if they are n-type semiconductor. The DOS plot (Figure 15a) suggested that along the chain, the charge carriers of the molecules are of n-type and along the stack, the charge transport is not quite effective. Therefore, it was clear that the diode formation and hence the transport along the 1D chain was more effective.

Additionally, the HOMO to Fermi energy value was 0.98 eV and Fermi level to LUMO energy difference was 0.90 eV in the 1D chain. This suggested a very low value of activation energy barrier which further pointed to the feasibility of facile electron transfer leading to a high value of electrical conductivity. To investigate the origin of photo-conductivity of **NMOF-1**, we carried out theoretical calculations using our modeled structure and studied the effect of electromagnetic radiations on the HOMO-LUMO gap of **NMOF-1** (Figure 22). It was seen that the HOMO-LUMO gap decreased progressively upon increasing the voltage upto a certain extent. This leads to transfer of more number of charge carriers in the conduction band and hence more electrical conduction leading to the high photo-conductivity in **NMOF-1**. This rectification behavior along with high photoconductivity for **NMOF-1** betters other porous MOF materials reported so far (Table 4).

Table 4. Device performance comparison among **NMOF-1** and other best-known MOF and organic materials.

MOF[ref]	Nano structure	Superhydrophobicity	Rectification Ratio	Photo conductivity	Barrier height	Series resistance	Mobility ($cm^2 V^{-1} s^{-1}$)	Diffusion length(nm)
$TCNQ@Cu_3(BTC)_2$[7a]	No	No	-	No	-	-	-	
$Ni_3(HITP)_2$[7f]	No	No	-	No	-	-	-	
$Cd_2(TTFTB)$[7c]	No	No	-	No	-	-	-	
MOF BDC[27]	-	No	-	-	-	-	0.001	
$Mn_2(DSBDC)$[7b]	-	No	-	-	-	-	0.01	
ANPPIT[14c]	-	No	4.7 (at ±2V)	-	-	-	-	
Cd(II)-MOF[14a]	-	No	100(at ±10V)	-	0.41 eV	413 kΩ	-	
Cd(II)-MOF[14b]	-	No	46 at ±5V	Yes	0.37 eV	797 Ω	0.00011	74
NMOF-1	Yes	Yes	47(at ±1V)	Yes	0.35 eV	270 Ω	0.069	198

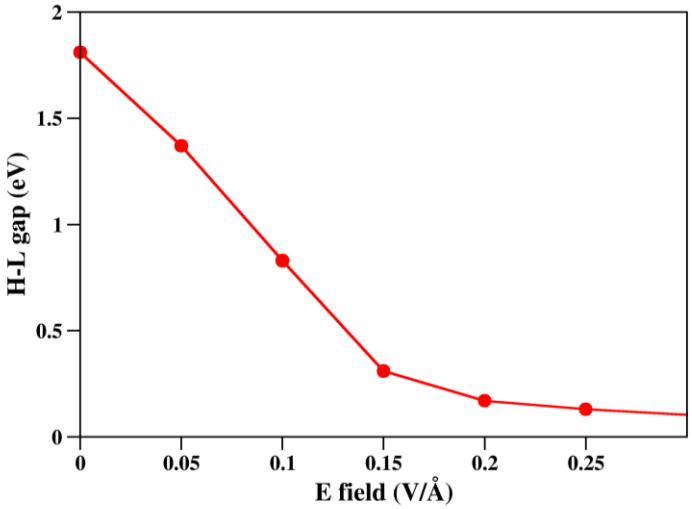

Figure 22. Change of molecular orbital energies with varying the externally applied electric fields for **NMOF-1**.

3B.4. Conclusion

To summarize, the work in this chapter employed a bola-amphiphilic ligand to construct a nanoscale metal-organic framework (**NMOF-1**) which showed excellent water repellence and electrical conductivity. The nanoscale architecture allowed easy solution processability for coating on glass substrates. This feature was exploited for realizing high water contact angles and self-cleaning applications. Furthermore, this has also allowed us to fabricate a uniform thin film Schottky barrier diode from this structure. The use of OPE based ligands has led to high values of electrical current and excellent photo-response in **NMOF-1**. The colossal current increase at very low turn on voltages also points to practical applications of **NMOF-1**. Combination of luminescence, superhydrophobicity/ self-cleaning, photo-electronic property and promising charge transport property projects **NMOF-1** as a highly moisture resistant MOF Schottky barrier device. The design principle can also be followed to generate future devices which can function efficiently, probably even under water. Such behavior is rare in MOF systems and can advance the field of porous opto-electronic materials.

3B.5. References

1 (a) J-R. Li, R. J. Kuppler and H.-C. Zhou, *Chem. Soc. Rev.*, 2009, **38**, 1477; (b) T. Faust, *Nat. Chem.*, 2015, **7,** 270; (c) J. Heine and K. Müller-Buschbaum, *Chem. Soc. Rev.*, 2013, **42**, 9232; (d) S. Roy, A. Chakraborty and T. K. Maji, *Coord. Chem.*

Rev. 2014, **273-274**, 139; (e) K. Müller-Buschbaum, F. Beuerle and C. Feldmann, *Microporous Mesoporous Mater*., 2015, **216**, 171.

2 (a) A. Dhakshinamoorthy, A. M. Asiri and H. Garcia, *Angew. Chem. Int. Ed.* 2016, **55**, 5414; (b) S. Wang and X. Wang, *Small*, 2015, **11**, 3097.

3 (a) E. M. Miner, T. Fukushima, D. Sheberla, L. Sun, Y. Surendranath and M. Dincă, *Nat. Commun.*, 2016, **7**, 10942; (b) N. Kornienko, Y. Zhao, C. S. Kley, C. Zhu, D. Kim, S. Lin, C. J. Chang, O. M. Yaghi and P. Yang, *J. Am. Chem. Soc.*, 2015, **137**, 14129.

4 (a) V. Stavil, A. A. Talin and M. D. Allendorf, *Chem. Soc. Rev.*, 2014, **43**, 5994; (b) M. G. Campbell, S. F. Liu, T. M. Swager and M. Dincă, *J. Am. Chem. Soc.*, 2015, **137**, 13780; (c) S. Rana, R. Rajendra, B. Dhara, P. K. Jha and N. Ballav, *Adv. Mater. Interfaces*, 2016, **3**, 1500738.

5 (a) C. Gu, N. Huang, Y. Chen, L. Qin, H. Xu, S. Zhang, F. Li, Y. Ma and D. Jiang, *Angew. Chem. Int. Ed.*, 2015, **54**, 13594; (b) V. Nevruzoglu, S. Demir, G. Karaca, M. Tomakin, N. Bilgin and F. Yilmaz, *J. Mater. Chem. A*, 2016, **4**, 7930; (c) S. Goswami, L. Ma, A. B. F. Martinson, M. R. Wasielewski, O. K. Farha and J. T. Hupp, *ACS Appl. Mater. Interfaces*, 2016, **8**, 30863.

6 (a) X. Wang, J. Zhou, H. Fu, W. Li, X. Fan, G. Xin, J. Zheng and X. Li, *J. Mater. Chem. A*, 2014, **2**, 14064; (b) L. Zhang, X. Wang, R. Wang and M. Hong, *Chem. Mater.*, 2015, **27**, 7610; (c) K. Yuan, X. Zhuang, H. Fu, G. Brunklaus, M. Forster, Y. Chen, X. Feng and U. Scherf, *Angew. Chem. Int. Ed.*, 2016, **55**, 6858.

7 (a) A. A. Talin, A. Centrone, A. C. Ford, M. E. Foster, V. Stavila, P. Haney, R. A. Kinney, V. Szalai, F. ElGabaly, H. P. Yoon, F. Léonard and M. D. Allendorf,. *Science*, 2014, **343**, 66; (b) L. Sun, M. G. Campbell and M. Dincă, *Angew. Chem. Int. Ed.* 2016, **55**, 3566; (c) L. Sun, S. S. Park, D. Sheberla and M. Dincă, *J. Am. Chem. Soc.*, 2016, **138**, 14772; (d) M. D. Allendorf, M. E. Foster, F. Léonard, V. Stavila, P. L. Feng, F. P. Doty, K. Leong, E. Y. Ma, S. R. Johnston and A. A. Talin, *J. Phys. Chem. Lett.*, 2015, **6**, 1182; (e) M. G. Campbell, D. Sheberla, S. Liu, T. M. Swager and M. Dincă, *Angew. Chem. Int. Ed.*, 2015, **54**, 4349; (f) D. Sheberla, L. Sun, M. A. Blood-Forsythe, S. Er, Wade, R. Casey, C. K. Brozek, A. Aspuru-Guzik and M. Dincă, *J. Am. Chem. Soc*., 2014, **136**, 8859.

8 B. Dhara, S. S. Nagarkar, J. Kumar, V. Kumar, P. K. Jha, S. K. Ghosh, S. Nair and N. Ballav, *J. Phys. Chem. Lett*., 2016, **7**, 2945.

9 (a) X. Feng, L. Liu, Y. Honsho, A. Saeki, S. Seki, S. Irle, Y. Dong, A. Nagai and D. Jiang, *Angew. Chem. Int. Ed.*, 2012, **51**, 2618; (b) L. Chen, K. Furukawa, J. Gao, A. Nagai, T. Nakamura, Y. Dong and D. Jiang, *J. Am. Chem. Soc.*, 2014, **136**, 9806; (c) X. Feng, L. Chen, Y. Honsho, O. Saengsawang, L. Liu, L. Wang, A. Saeki, S. Irle, S. Seki, Y. Dong and D. Jiang, *Adv. Mater.*, 2012, **24**, 3026.

10 (a) A. Carné-Sánchez, I. Imaz, M. Cano-Sarabia and D. Maspoch, *Nat. Chem.*, 2013, **5**, 203; (b) L. He, Y. Liu, J. Liu, Y. Xiong, J. Zheng, Y. Liu and Z. Tang, *Angew Chem., Int. Ed.*, 2013, **52**, 3741; (c) Y. Liu and Z. Tang, *Adv. Mater.* 2013, **25**, 5819.

11 (a) U. H. F. Bunz, *Chem. Rev.*, 2000, **100**, 1605; (b) U. H. F. Bunz, *Macromol. Rapid Commun.*, 2009, **30**, 772; (c) S. Roy, A. Hazra, A. Bandyopadhyay, D. Raut, P. L. Madhuri, D. S. S. Rao, U. Ramamurty, S. K. Pati, S. K. Prasad and T. K. Maji, *J. Phys. Chem. Lett.*, 2016, **7**, 4086.

12 (a) Z. J. Donhauser, B. A. Mantooth, K. F. Kelly, L. A. Bumm, J. D. Monnell, J. J. Stapleton, D. W. Price Jr., A. M. Rawlett, D. L. Allara, J. M. Tour and P. S. Weiss, *Science,* 2001, **292**, 2302.; (b) J. Chen, M. A. Reed, A. M. Rawlett and J. M. Tour, *Science,* 1999, **286**, 1550; (c) V. M. Suresh, S. J. George and T. K. Maji, *Adv. Funct. Mater.*, 2013, **23**, 5585.

13 S. Roy, V. M. Suresh and T. K. Maji, *Chem. Sci.*, 2016, **7**, 2251.

14 (a) B. Bhattacharya, A. Layek, M. M. Alam, D. K. Maity, S. Chakrabarti, P. P. Ray and D. Ghoshal, *Chem. Commun.*, 2014, **50**, 7858; (b) S. Halder, A. Dey, A. Bhattacharjee, J. Ortega-Castro, A. Frontera, P. P. Ray and P. A. Roy, *Dalton Trans.*, 2017, **46**, 11239; (c) S. Dalapati, R. Saha, S. Jana, A. K. Patra, A. Bhaumik, S. Kumar and N. A. Guchhait, *Angew. Chem. Int. Ed.*, 2012, **51**, 12534.

15 S. K. Cheung and N. W. Cheung, *Appl. Phys. Lett.*, 1986, **49**, 85.

16 R. Yatskiv, J. Grym, K. Zdansky and K. Piksova, *Carbon*, 2012, **50**, 3928.

17 (a) M. Das, J. Datta, A. Dey, R. Jana, A. Layek, S. Middya and P. P. Ray, *RSC Adv.*, 2015, **5**, 101582; (b) M. Das, S. Middya, J. Datta, A. Dey, R. Jana, A. Layek and P. P. Ray, *J. Electron. Mater.*, 2016,**45**, 4293

18 J. M. Soler, E. Artacho, J. D. Gale, A. García, J. Junquera and P. D. O. Sánchez-Portal, *J. Phys.: Condens. Matter.*, 2002, **14**, 2745.

19 K. Burke, J. P. Perdew and M. Ernzerhof *Int. J. Quantum Chem.*, 1997, **61**, 287.

20 N. Troullier and J. L. Martins, *Phys. Rev. B: Condens. Mater.*, 1991, **43**, 1993.

21 L. Kleinman, and D. Bylander, *Phys. Rev. Lett.*, 1982, **48**, 1425.

22 S. Grimme, *J. Comp. Chem.*, 2006, **27**, 1787.

23 (a) D. Louer and M. Louer, *J. Appl. Cryst.*,1972, **5**, 271; (b) A. Boultif and D. Louer, *J. Appl. Cryst.*, 1991, **24**, 987.

24 M. Sookhakian, Y. M. Amin, R. Zakaria, W. J. Basirun, M. R. Mahmoudian, B. Nasiri-Tabrizi, S. Baradaran and M. Azarang, *J. Alloys Compd.*, 2015, **632**, 201.

25 M. Das, J. Datta, A. Dey, R. Jana, A. Layek, S. Middya and P. P. Ray, *RSC Adv.*, 2015, **5**, 101582.

26 (a) P. W. M. M. Blom, J. M. de Jong and M. G. van Munster, *Phys. Rev. B*, 1997**,** **55**, R656; (b) M. Das, J. Datta, R. Jana, S. Sil, S. Halder and P. P. Ray, *New J. Chem.*, 2017, **41**, 5476; (c) A. Jain, P. Kumar, S. C. Jain, V. Kumar, R. Kaur and R. M. Mehra, *J. Appl. Phys.*, 2007**,** **102**, 94505.

27 T. Musho and N. Wu, *Phys. Chem. Chem. Phys.*, 2015**,** **17**, 26160.

28 F. C. Krebs and M. Jørgensen, *Macromolecules*, 2003**,** **36**, 4374.

Chapter 4A

Solvent Modulated Emission Properties in a Superhydrophobic *Oligo*-(*p*-phenyleneethynylene) based 3D Porous Supramolecular Framework

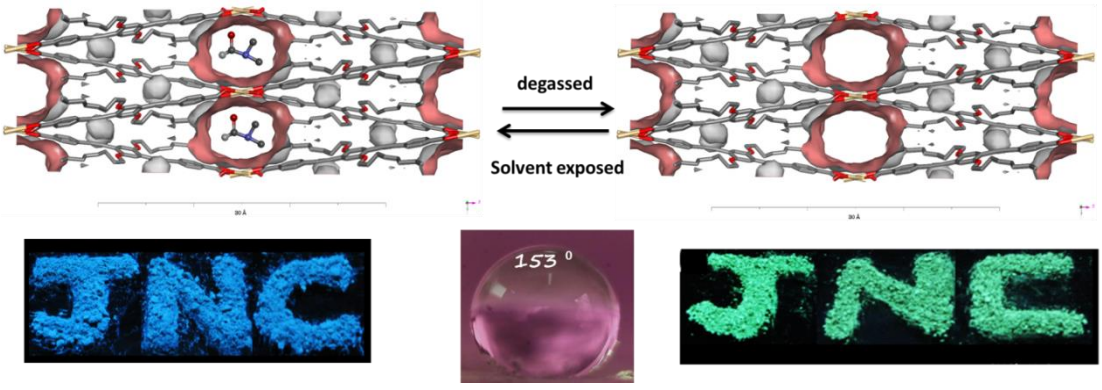

Summary

A chromophoric *oligo*-(*p*-phenyleneethynylene) (OPE) bola-amphiphile with dioxyoctyl side chains (H_2OPE-C_8) has been self-assembled with Cd^{II} to form a 1D coordination polymer $\{Cd(OPE\text{-}C_8)(DMF)_2(H_2O)\}_n$ (**1**) which is further interdigitated to form a 2D network. Such 2D networks are further interwoven to form a 3D supramolecular framework with surface projected alkyl chains. The de-solvated framework showed permanent porosity as realized from the CO_2 adsorption profile. **1** showed high water contact angles, portraying its superhydrophobic nature. **1** also showed a linker based cyan luminescence. Solvent removal led to a bathochromic shift in emission into the green region. Re-solvation with DMF brought back the original cyan emission whereas for THF, ethanol and methanol, it persisted at an intermediate state. DFT calculations unraveled that upon solvent removal, the rotational freedom attained around the single bonds connecting the alkyne units, led to twisting of OPE phenyl rings, and generated the red shift in emission.

The work based on this chapter is communicated:

S. Roy, V. M. Suresh, A. Hazra, A. Bandyopadhyay, S. K. Pati, S. Laha and T. K. Maji, *Manuscript submitted.*

4A.1. Introduction

Luminescent materials have found widespread applications in sensors, LEDs, bio-imaging, light harvesting etc.[1] Porous luminescent metal-organic frameworks (MOFs) cover all these applicative areas, with a host of other advantages.[2] In general, emission in MOFs can be realized from the lanthanide metal ions, π-chromophoric linkers, ligand-to -metal charge transfer (LMCT) or metal-to-ligand charge transfer (MLCT).[3] Furthermore, permanent porosity of MOFs allows for the encapsulation of a variety of guest molecules and this allows further modulation of the emission properties.[4] This can arise due to either (a) inherent emission of the guest, (b) exciplex formation, (c) CT complex formation or (d) structural changes induced due to guest removal/encapsulation.[5] Structural modification occurs, when the MOF structure distorts upon de-solvation, leading to a different emission from that had initially originated from the assynthesized structure. Further, reversible tuning of this emission can occur when the solvent molecules recoordinate to the unsaturated metal center (UMS) or occupy the pores of the MOFs. This versatility in tuning the emission color, offers excellent sensing applications of these systems via vapochromism. The emission of MOFs have also been successfully utilized in sensing of metal cations and anions.[6] Furthermore, light harvesting using luminescent MOFs, has also been achieved via encapsulation of emissive dyes in its pores.[7] They have also been scaled down to the nanoscale to fabricate thin-film devices for opto-electronics.[8]

Several π-conjugated systems have been exploited to generate MOFs with excellent luminescent properties.[2c,3b] *Oligo-p*-phenyleneethynylenes (OPEs) are one such class of molecules which lead to highly luminescent MOF structures. OPEs are chromophoric systems, whose structure is built up with aryl units connected via ethyne linkages.[9] This creates structural rigidity and extensive π- conjugation, leading to its excellent luminescence and intrinsic conductivity. Simultaneous existence of both properties is indispensable, for organic light emitting transistors (OLET) and device applications.[10] Additionally, the ease of functionalization of OPE side chains with long alkyl groups would decrease the surface energy, leading to internal porous and external surface water repellent properties in the MOF structures. We have recently showed that linking bola-amphiphilic *oligo-p*-phenyleneethynylene (OPE) ligands with long alkyl chains to metal ions, generated luminescent, semi-conducting and superhydrophobic nanoscale MOFs.[11] The nanoscale architecture, also generated through this approach, allowed coating over

large areas for self-cleaning, device fabrication and bio-imaging applications .[11,12] Interestingly, hydrophobicity in MOFs is also of paramount importance for flue gas separation, via negating a competitive interaction of moisture with CO_2.[13] Simultaneously superhydrophobic and luminescent structures are also important to further the field of device applications where moisture resistance could lead to better and long-lived device performance. However, structure property correlation is important in the design of such materials for these improved and advanced applications.

This chapter demonstrates the self-assembly of a dioxyoctyl functionalized OPE dicarboxylate (**H_2OPE-C_8**) with Cd^{II} that resulted in a 3D supramolecular porous framework $\{Cd(OPE\text{-}C_8)(DMF)_2(H_2O)\}_n$ (**1**) in a DMF/ethanol mixture. Photoluminescence measurements indicated a linker based cyan emission of **1**. Degassed **1** (**1a**) showed a bathochromic shift in emission to the green region. Such a change in emission is supported by DFT calculations. Interestingly, the emission of **1** could be tuned based on reintroduction of different solvent vapors. **1** therefore falls in an elite class of porous coordination polymers with superhydrophobicity and guest modulated emission property.

4A.2. Experimental Section

4A.2.1. Materials

$Pd(PPh_3)_4$ and $Cd(NO_3)_2{\cdot}4H_2O$ were obtained from Sigma-Aldrich Chemical Co and cuprous iodide was acquired from LobaChemie Pvt. Ltd. N,N-dimethyl formamide (DMF) and tetrahydrofuran (THF) were obtained from Spectrochem Pvt. Ltd (Mumbai, India). Tetrahydrofuran was pre-dried using standard procedure and all other reagents, solvents were of reagent grade and used without further purification.

4A.2.2. Physical Measurements

The elemental analyses were carried out using a Thermo Scientific Flash 2000 CHN analyzer. Infrared spectral study was performed by making samples with KBr pellets using Bruker FT-IR spectrometer. ^1H spectrum was recorded on a Bruker AV-400 spectrometer with chemical shifts recorded as ppm and all spectra were calibrated against TMS. Powder X-ray diffraction studies were recorded on a Bruker D8 discover instrument using Cu-Kα radiation. Thermal stability of **1** was analyzed using Mettler Toledo TGA 850 instrument under inert atmosphere in the temperature range of 25-800

°C at a heating rate of 3 °C /min. UV–Vis spectra were recorded on a Perkin Elmer Model Lambda 900 spectrophotometer. Fluorescence studies were accomplished using Perkin Elmer Ls 55 Luminescence spectrometer. Fluorescence lifetime measurements were recorded with a Horiba Deltaflex spectrometer.

Adsorption Measurements

Porosity measurements were carried out using QUNATACHROME QUADRASORD-SI analyser at 77 K for N_2 and 195 K for CO_2. In the sample tube the adsorbent samples (~100-150 mg) were placed which had been prepared at 170 °C under a 1×10^{-1} Pa vacuum for about 12 h prior to measurement of the isotherms. Helium gas (99.999% purity) at a certain pressure was introduced in the gas chamber and allowed to diffuse into the sample chamber by opening the valve. The amount of gas adsorbed was calculated from the pressure difference (P_{cal} - P_e), where P_{cal} is the calculated pressure with no gas adsorption and P_e is the observed equilibrium pressure. All the operations were computer-controlled and automatic. Water, methanol and THF vapor adsorptions were carried out at 298 K using BELSORP AQUA 3 solvent vapor analyzer. A sample of about ~100 –150 mg was prepared by heating at 170 °C for about 12 h under vacuum (1×10^{-1} Pa) prior to measurement of the isotherms. The solvent molecules used to generate the vapor were degassed fully by repeated evacuation. Dead volume was measured with helium gas. The adsorbate was placed into the sample tube, then the change of the pressure was monitored and the degree of adsorption was determined by the decrease in pressure at the equilibrium state. All operations were computer controlled and automatic.

Contact Angle Measurements

Contact angles were measured using an indigenous set up coupled with a Logitech camera for capturing the images. Contact angles were also measured using dedicated contact angle analyzer, OCA30 from Data Physics instrument (GmbH, Germany). 4 µL of the sessile water droplets were employed for measuring the static contact angles. A minimum of ten measurements were made.

4A.2.3. Computational Details

All the optical and electronic properties have been calculated using Gaussian 09 DFT software.[14] We have used the hybrid HSE06 functional[15] combined with 6-31+G(d) basis

set for C, H and O and LANL2DZ pseudopotential based approach for Cd atoms for all the calculations.

4A.2.4. Single Crystal X-ray Diffraction (SCXRD)

Suitable single crystal of **1** was mounted on a thin glass fiber with commercially available super glue. X-ray single-crystal structural data were collected on a Bruker Smart-CCD diffractometer equipped with a normal focus and a 2.4 kW sealed tube X-ray source with graphite monochromated Mo-Kα radiation (λ = 0.71073 Å) operating at 50 kV and 30 mA. The program SAINT[16] was used for the integration of diffraction profiles, and absorption correction was made with the SADABS[17] program. All the structures were solved by SHELXT[16] and refined by the full-matrix least-squares method using SHELXL-2017.[18] All the hydrogen atoms were fixed by HFIX and placed in ideal positions. The potential solvent accessible area or void space was calculated using the PLATON[19] multipurpose crystallographic software. All crystallographic and structure refinement data are summarized in Table 1. Selected bond lengths and angles for **1** are given in Table 2. All calculations were carried out using SHELXL-2017,[18] and WinGX system, Ver 1.80.05.[20]

4A.2.5. Synthesis of 4,4'-(2,5-bis(octyloxy)-1,4-phenylene)bis(ethyne-2,1-diyl)dibenzoic acid (H_2OPE-C_8) and 1

Synthesis of 4,4'-(2,5-bis(octyloxy)-1,4-phenylene)bis(ethyne-2,1-diyl)dibenzoic acid (**H_2OPE-C_8)** was carried out following reported procedures.[12] K_2CO_3 flakes (1.00 g, 7.25 mmol) was added to a solution of **6** (500 mg, 808 μmol) in 40 mL methanol. The resulting solution was refluxed for 12 h at 70 °C to complete ester hydrolysis. The clear solution was added dropwise over 4 N aq. HCl solution (250 mL) and green precipitate of 4,4'-(2,5-bis(octyloxy)-1,4-phenylene)bis(ethyne-2,1-diyl)dibenzoic acid (**H_2OPE-C_8**) was formed which was filtered off and washed with water (100 mL) and methanol (25 mL, caution: slightly soluble) to get pure compound (430 mg, 690 μmol, 85% yield). ^{1}H NMR (400 MHz, $CDCl_3$) δ = 0.87 (t, *J* = 6.9 Hz, 3H), 1.28-1.30 (m, 8H), 1.42 (q, *J* = 7.1 Hz, 2H), 1.75 (q, *J* = 7.9 Hz, 2H), 4.05 (t, *J* = 5.2 Hz 2H), 7.79 (d, *J* = 6.8 Hz, 1H), 8.16 (d, *J* = 6.8 Hz, 1H) ppm HRMS-EI (*m/z*) for $C_{40}H_{46}O_6$ [M+] Calcd. 622.716, found 622.719. Anal. Calcd. for $C_{40}H_{46}O_6$: C, 77.14; H, 7.45. Found: C, 76.98; H, 7.34.

Synthesis of $\{Cd(OPE\text{-}C_8)(DMF)_2(H_2O)\}_n$ **(1)**

An ethanolic solution (1 mL) of $Cd(NO_3)_2 \cdot 4H_2O$ (0.25 mmol) was layered on a buffer layer (0.75 mL) of DMF/ethanol which was previously layered onto an DMF solution of **H_2OPE-C_8** (0.75 mmol), in a crystal tube. After 5 days, green colored block-shaped crystals appeared in the middle of the tube and were separated and washed with ethanol. The bulk amount of the sample was prepared by the direct mixing of the respective reagents in DMF/ethanol solution under stirring for 24 h, and the phase purity was checked with the PXRD and elemental analysis. Yield: 64%, Elemental analysis: Calcd. for $C_{46}H_{46}CdN_2O_9$: C, 56.42; H, 4.73; N, 2.86. Found: C, 56.14; H, 3.91; N, 2.48. IR (KBr, cm^{-1}): ν(H_2O) 3440; ν(ArC-H) 2960, ν(C-O) 2162, 2098; ν(ArC=C) 1400. (Figure 5)

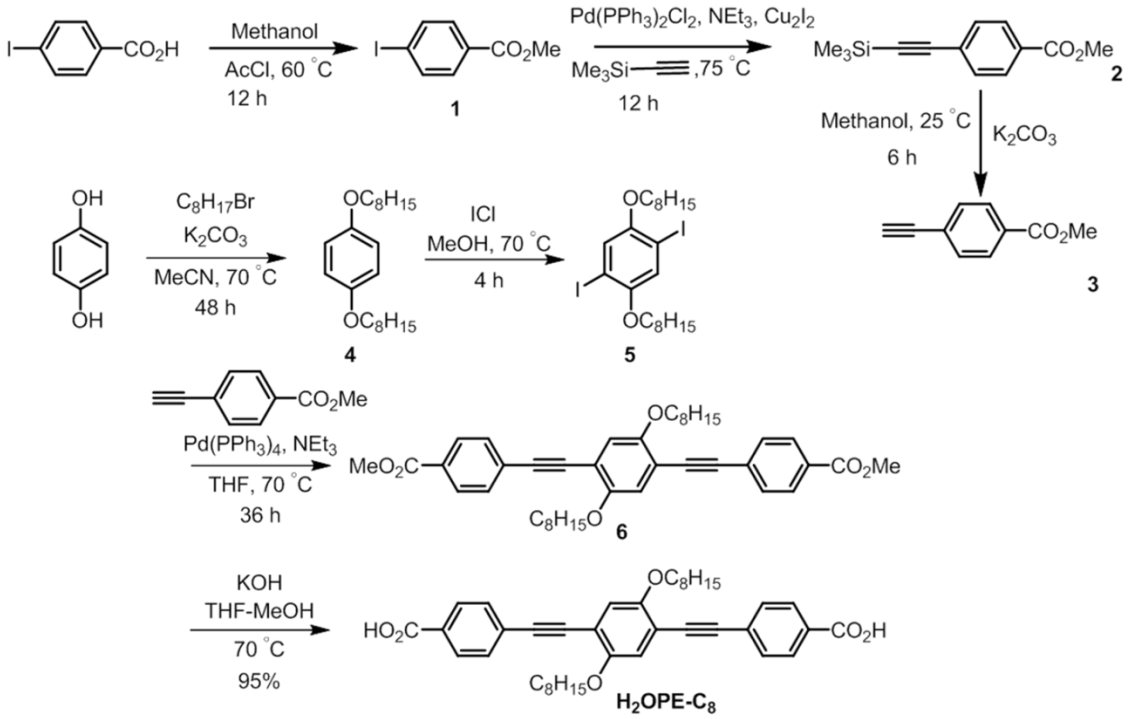

Scheme 1. Synthetic scheme for **H_2OPE-C_8**.

4A.3. Results and Discussion

4A.3.1. Structural Characterization

H_2OPE-C_8 was synthesized according to reported Sonogashira-Hagihara coupling procedures.[12] Green, block-shaped crystals of **1** were isolated in a crystal tube following procedures described above. Single crystal X-ray crystallographic structure determination revealed that **1** crystallized in the orthorhombic crystal system having a space group *P*bnb

(Table 1). The Cd^{II} centre here is hepta-coordinated with four coordination sites made up by carboxylates oxygen of two adjacent OPE carboxylates (Figure 1a). Two oxygens from two dimethylformamide molecules make up the fifth and sixth coordination sites. The seventh

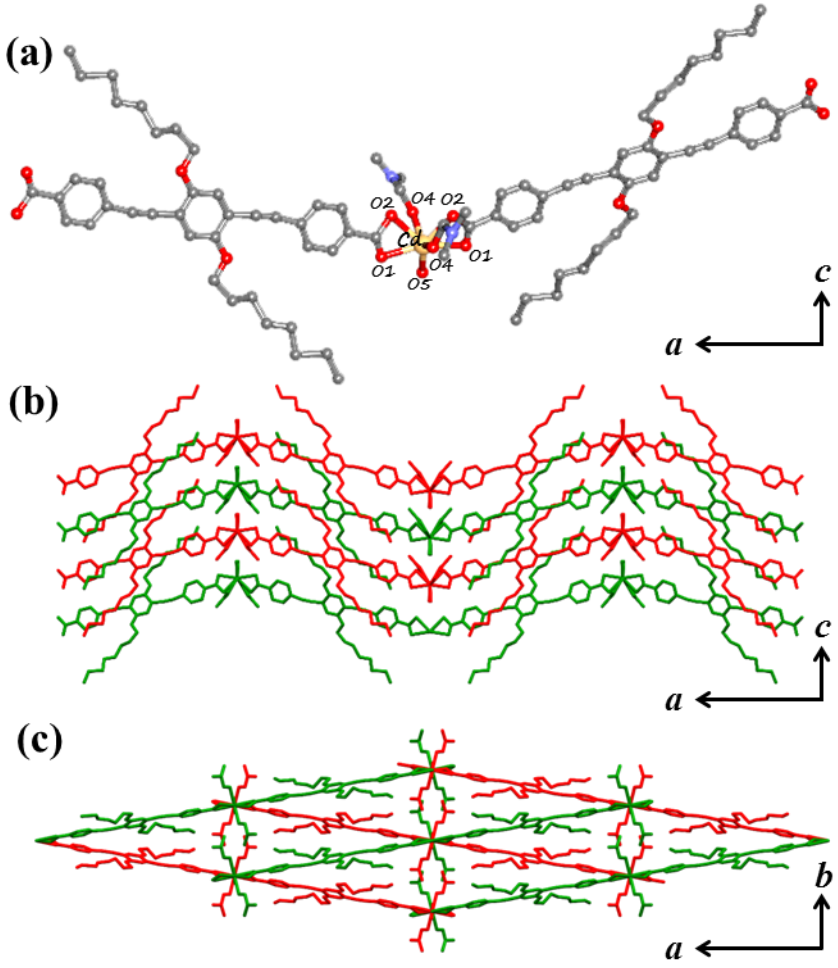

Figure 1. Structural representation of **1**: (a) View of the asymmetric unit and the 1D coordination chain, (b) View of the 2D sheet formed via interdigitation of alkyl chains of zig-zag 1D chain and (c) View of the 3D structure formed via interweaving of the 2D sheets.

coordination site is filled by a water molecule. The three phenyl rings constituting the OPE backbone lie in the same plane and there exists minimal twisting of the OPE core (Figure 1a) The 1D chain of **1** is generated by the coordination of terminal carboxylates of adjacent **OPE-C_8** to Cd^{II} which extends in a zig-zig fashion (Figure 1a). Two such 1D chains pass each other in a criss-cross fashion meeting at the respective Cd^{II} centers (Figure 2, highlighted in red and green). Each individual 1D chain is further packed into itself via interdigitation of alkyl chains to form unique 2D sheets in the *ac* plane (Figure

1b, 3). These 2D sheets (red and green) are further interpenetrated oblique to the *ab* plane, via C−H···π interactions (*d* = 3.517 Å) between C1 hydrogen and terminal phenyl ring of the adjacent ring and C−H···O interactions (D−A distance;

Table 1. Crystallographic data and structure refinement parameters for **1**.

	1
empirical formula	$C_{46}H_{60}CdN_2O_9$
M	897.36
crystal system	orthorhombic
space group	*P*ccn
a (Å)	47.191(5)
b (Å)	8.5100 (15)
c (Å)	11.670 (3)
α (deg)	90.000
β (deg)	90.000
γ (deg)	90.000
V (Å^3)	4686.6 (15)
Z	4
T (K)	100 K
λ (Mo $K_α$)	0.71073
D_c (g/cm^3)	1.269
μ (mm^{-1})	0.519
$θ_{min}/θ_{max}$	2.7/ 25.0
total data	46878
unique reflection	4087
R_{int}	0.142
data [I>2σ(I)]	1507
R[a]	0.0965
R_w[b]	0.2084
GOF	1.03
Δρ min/max [e Å^{-3}]	-0.42, 0.84

[a]$R=\sum||F_o|-|F_c||/\sum|F_o|$. [b]$R_w=[\sum\{w(F_o^2-F_c^2)^2\}/\sum\{w(F_o^2)^2\}]^{1/2}$

Table 2. Selected Bond Distances [Å] and Angles [°] for **1**.

Cd1-O1	2.381(7)	O1-Cd1-O2A	51.2(4)
Cd1-O2A	2.423(15)	O1-Cd1-O4	92.4(4)
Cd1-O4	2.351(16)	O1-Cd1-O5	79.5(4)
Cd1-O5	2.200(14)	O1-Cd1-C1	26.0(4)
Cd1-O2	2.414(16)	O1-Cd1-O4A	84.4(4)
Cd1-O4A	2.291(18)	O1-Cd1-O1_a	161.4(4)
Cd1-O1_a	2.381(7)	O2A_a -Cd1-C1	121.2(5)
Cd1-O2A_a	2.423(15)	O4_a-Cd1-C1	86.9(5)
Cd1-O4_a	2.351(16)	O5_a-Cd1-C1	106.5(5)
Cd1-O5_a	2.200(14)	C1-Cd1-C1_a	146.7(5)
Cd1-O2_a	2.414(16)	O2_a-Cd1-C1	115.7(5)
Cd1-O4A_a	2.291(18)	O4A_a -Cd1-C1	99.7(5)

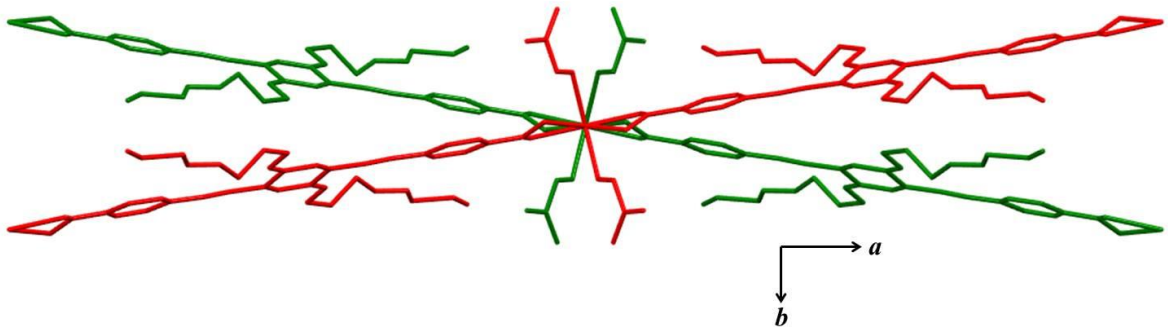

Figure 2. View of the criss-cross arrangement of two individual 1D chains contained in the *ab* plane.

3.021 Å, ∠D−H···A; 158.84^0) between the same C1 hydrogen and the oxy-octyl oxygen (Figure 4). This leads to generation of a 3D supramolecular architecture of **1.** When viewed along the *c*-axis, inward projecting oxy-oxtyl chains and coordinated DMF molecules are found in the pore (Figure 1c). This arrangement also leads to the oxy-octyl chains projecting outwards towards the surface, which might lead to possible superhydrophobicity of the surface as well as the pores (Figure 1c).

IR spectrum of **1** revealed the presence of water molecules (Figure 5). Thermogravimetric analysis of single crystals of asssynthezied compound **1** revealed the coordinated water and DMF molecules are released at about 160 °C after which, the desolvated framework (**1a**) is stable upto 350 °C, without any further weight loss (Figure 6). Powder X-ray diffraction (PXRD) of **1** revealed a good coherence with the simulated pattern from the SCXRD, suggesting phase purity of the compound (Figure 7).

Interestingly, there was a noticeable change in the structure of **1** upon desolvation, observed via the loss of numerous Braggs' reflections and also shift of the low angle peak at higher angles. This suggests an expected structural reorganization (Figure 7).

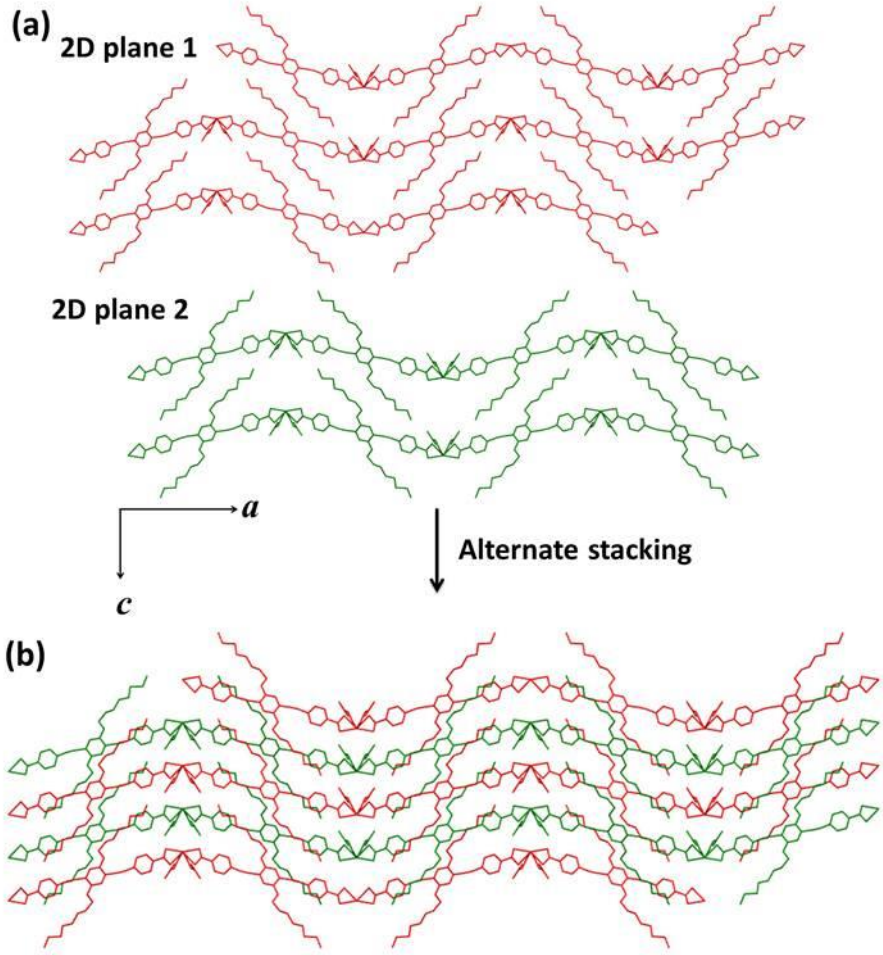

Figure 3. (a) View of two individual 2D sheets formed by the interdigitatiom of 1D chains marked as red and green respectively and (b) their alternate arrangement in the *ac* plane.

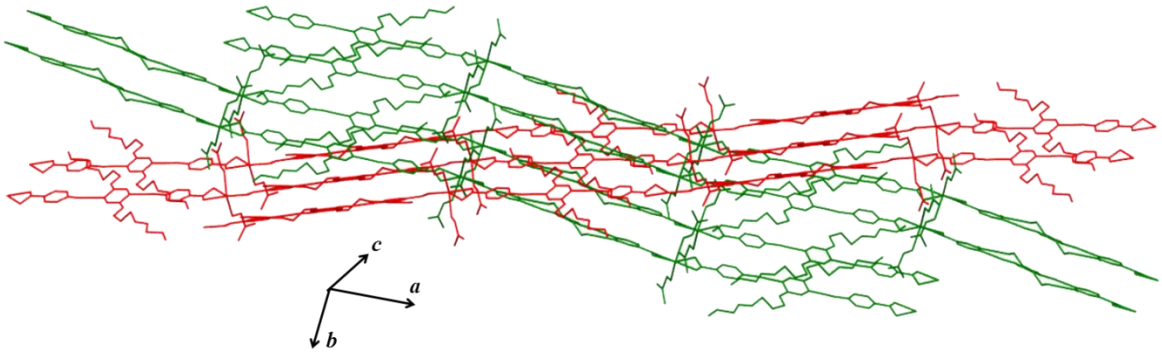

Figure 4. View of the 3D framework showing the interpenetration of individual 2D planes when viewed at an angle from the *c*-axis.

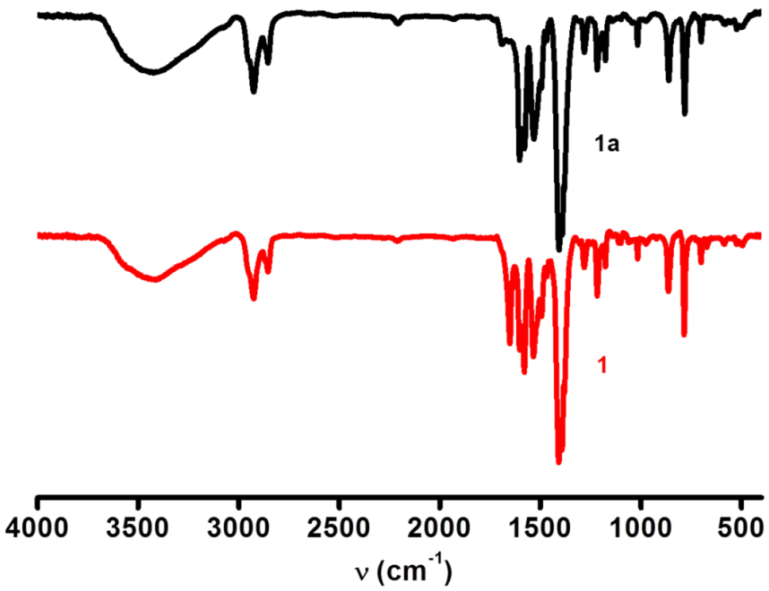

Figure 5. IR spectrum for **1** (red) and **1a** (black).

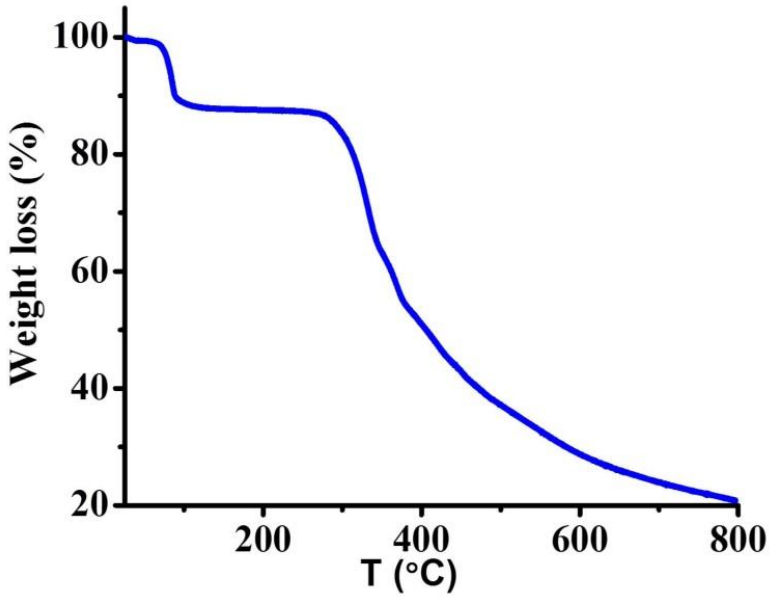

Figure 6. Thermogravimetric analysis of **1** under N_2 atmosphere.

PXRD also reveals that the structure comes back to the assynthesized one (**1**) upon exposure to DMF vapors proving the reversibility of structural transformation (Figure 8). Adsorption experiments on **1**, degassed at 160 °C under vacuum were carried out to investigate its porosity. The N_2 adsorption curve at 77 K revealed a minimal uptake of 30 mL with a type II profile (Figure 9a). However, the CO_2 adsorption profile at 195 K revealed a type I profile with a final uptake of 40 mL indicating the microporosity in **1** (Figure 9b). Langmuir surface area calculated from CO_2 adsorption profile was calculated to be 135 m^2/g.

4A.3.2. Water Contact Angle Measurements on 1 and 1a

As discussed before, SCXRD revealed surface projected periodic octyl chains (Figure 10b). This interested us in probing its pore hydrophobicity and surface contact angles, as long alkyl chains are reported to decrease the surface free energy and hence increase hydrophobicity.[11a] Water adsorption measurements on **1a** showed a final value of 25 cc/g, with negligible uptake at low pressure.

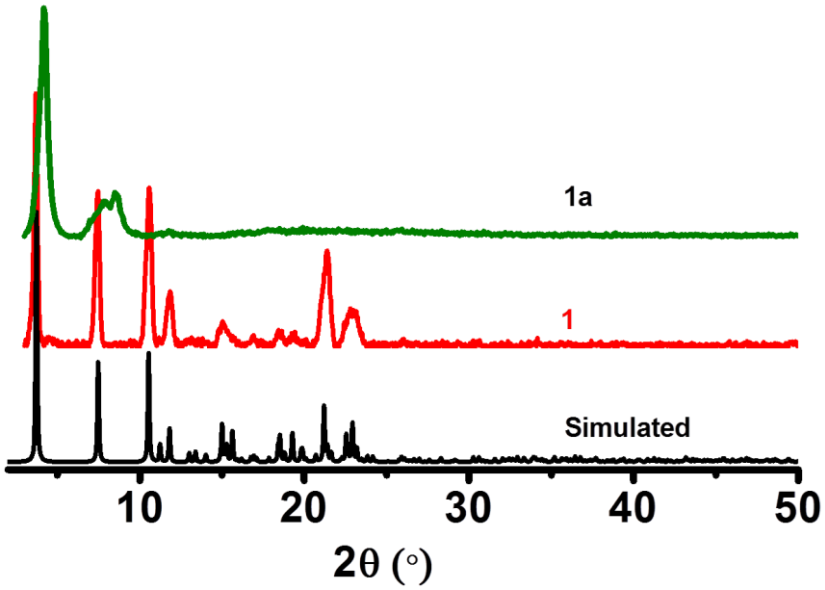

Figure 7. PXRD reflections for simulated (black)**, 1** (red) and **1a** (green).

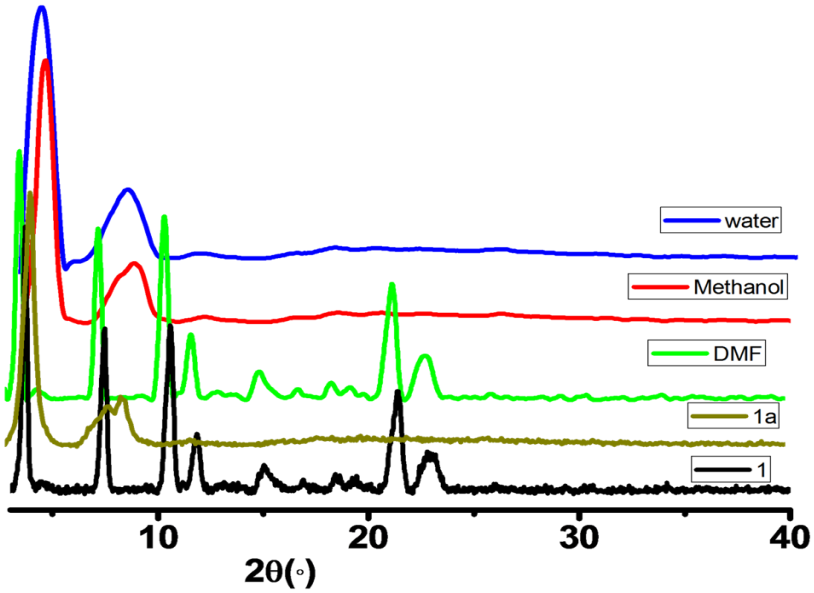

Figure 8. PXRD patterns for **1** (black)**, 1a** (olive), DMF@**1a** (green), methanol@**1a** (red) and water@**1a** (blue).

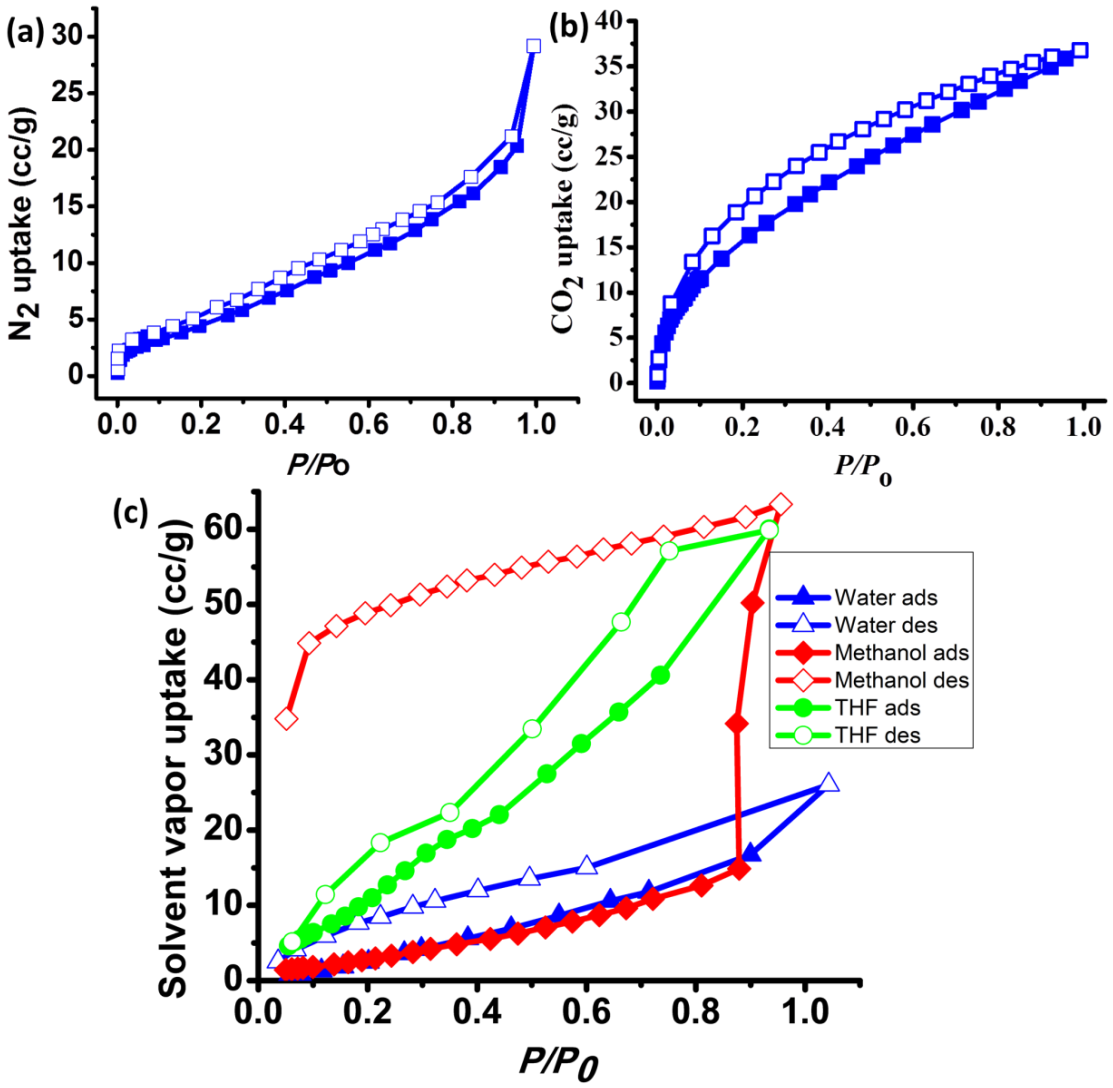

Figure 9. (a) N_2 adsorption isotherm at 77 K, (b) CO_2 adsorption at 195 K (filled and unfilled squares represent adsorption and desorption respectively) and (c) Solvent vapor adsorption plots at 293 K for **1**.

Hence, the pore surface has less affinity towards water (Figure 9c). For contact angle measurements, we drop casted an ethanolic solution of **1** on a glass plate and put 5 µL volume water droplets on the coated surface. The contact angle measured at different positions of the coated surface varied between 153-157°, proving that the surface was indeed superhydrophobic (Figure 10a). Interestingly, **1a** also revealed contact angle values similar to **1**. This indicated that the surface projected alkyl chains contribute directly to the surface hydrophobicity, and no other structural factor influences the contact angle.

4A.3.3. Photophysical Investigation on 1 and 1a

We have then performed detailed photophysical investigation of **1** and **1a. 1** absorbed at 400 nm in the solid state and emitted at 488 nm, showing a strong cyan luminescence (Figure 11a,b).

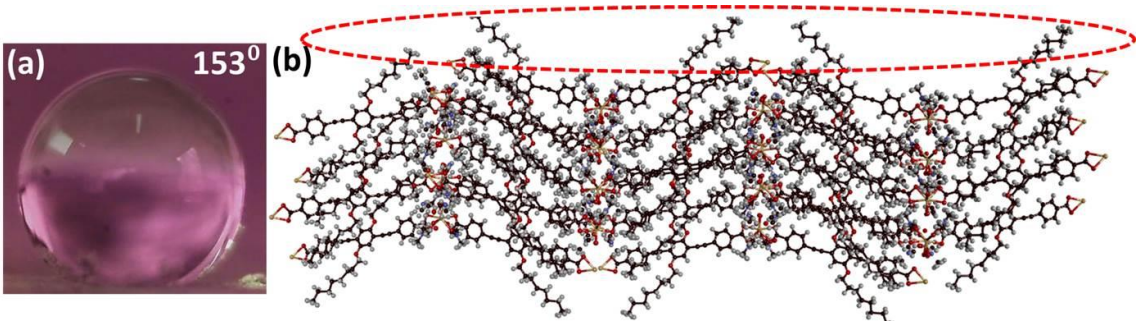

Figure 10. (a) Water contact angle of **1** coated glass substrate and (b) Packing diagram of **1**, viewed along the *b* axis showing surface projected alkyl chains.

H_2OPE-C_{12} also showed the same emission maximum upon the same excitation (Figure 11c). This proved that the emission of **1** was ligand centred. We calculated the HOMO-LUMO (H-L) levels of the fragmented asymmetric unit of the compound by HSE06. It was clearly seen that the both the HOMO and LUMO of **1** was populated by the orbitals of π-chromophoric OPE, further confirming our conjecture that the emission originates from the ligand (Figure 12). **1** and **1a** also showed an absorption maximum centered around 400 nm (Figure 13). However when the emission spectrum of **1a** was recorded at the same excitation wavelength, there was a red shift of the emission wavelength to 525 nm (Figure 14a). It is known that OPE systems show a change in emission color based on the degree of twisting of the central phenyl ring i.e. ligand conformation.[21] Previous reports suggest that there occurs a large bathochromic shift, when the central phenyl ring is twisted out of plane of the terminal phenyl rings.[22] Excimer formation also leads to a bathochromic shift in emission. So rule out one possibility over the other, we carried out lifetime measurements on **1** and **1a**. Lifetimes of both **1** and **1a** monitored at 488 nm and excited at 405 nm revealed a minimal change. **1** had an excited state lifetime of 1.6 ns whereas **1a** revealed a lifetime of 1.8 ns (Figure 15). Additionally, there was a minimal change of 2 nm in the UV spectrum of **1** and **1a** suggesting no ground state interaction (Figure 13). These ruled out any possibilities of excimer formation. Thus, the bathochromic shift in **1a** may be due to the twisting of OPE chains. To gain more insight

into this phenomenon, theoretical modelling was carried out. The central benzene ring of **1**, was rotated by 20°, to check the effect of the molecular plane rotation on the emission

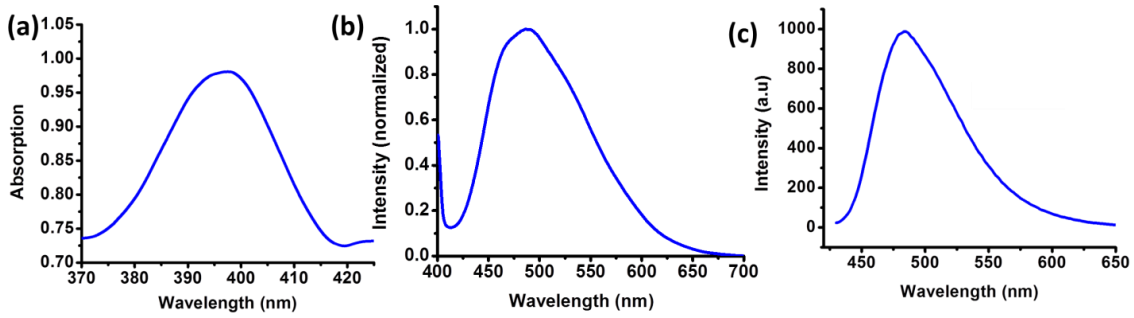

Figure 11. (a) UV and (b) PL of **1**, (c) PL of **H_2OPE-C_8** in the solid state.

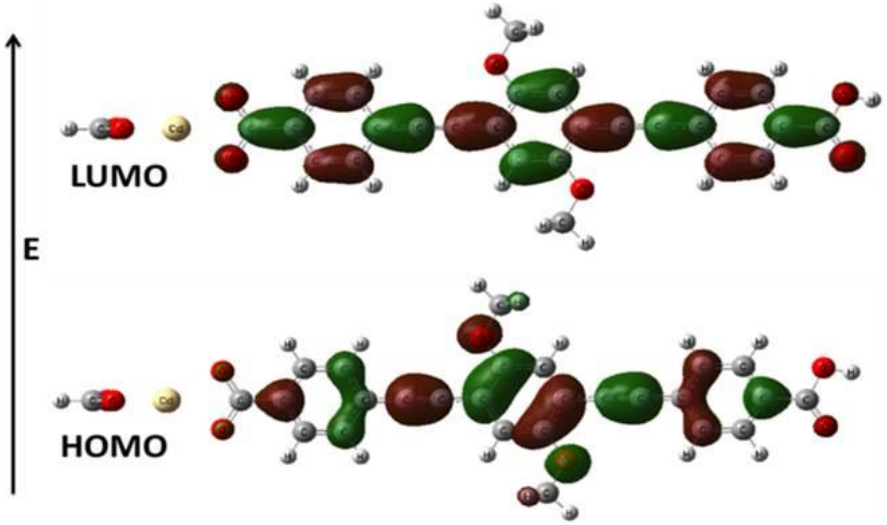

Figure 12. HOMO (lower) and LUMO (upper) plot for **1**.

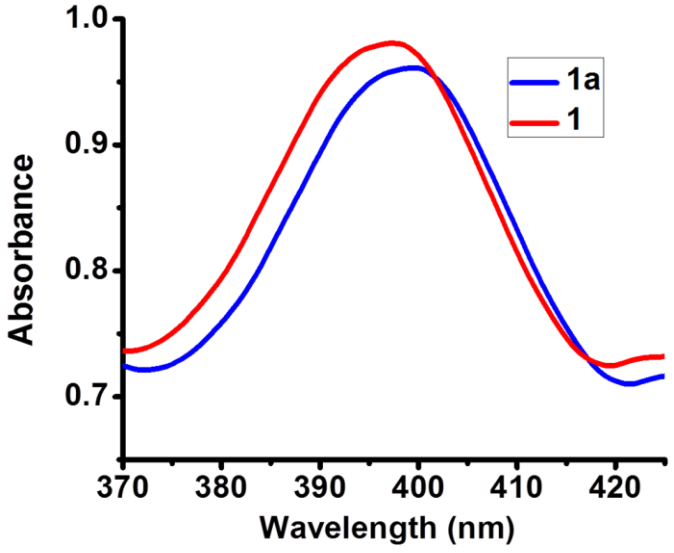

Figure 13. Solid state UV spectra for **1** (red) and **1a** (blue).

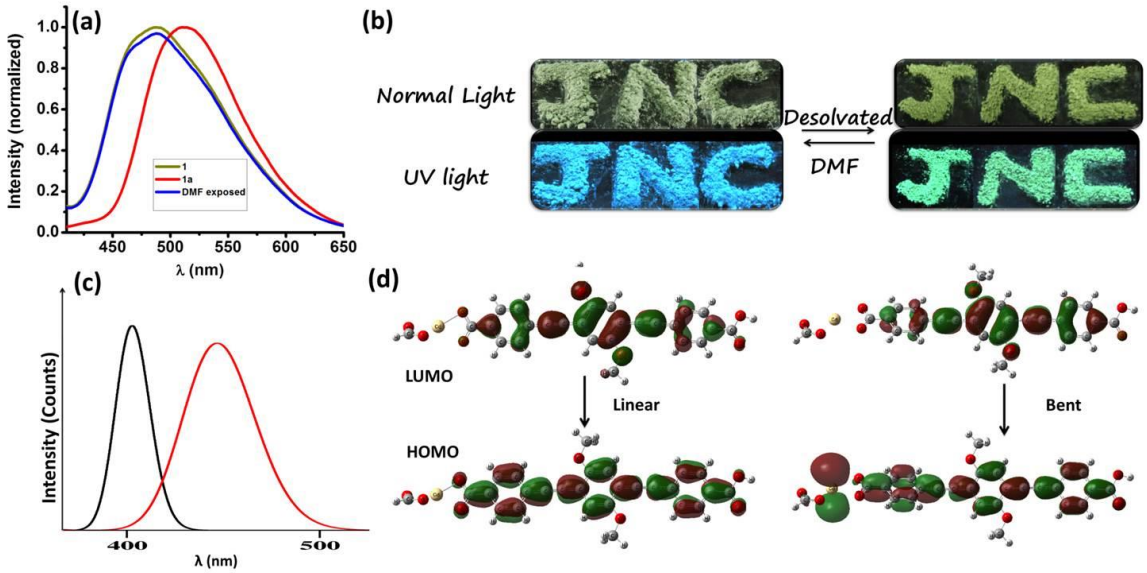

Figure 14. (a) Experimental and (c) Theoretical PL plots for **1**, **1a** and DMF exposed **1a**, Images of (b) **1** and **1a** under normal and UV light, (d) HOMO (lower) and LUMO (upper) plot for linear (left) and bent (right) structures of **1**.

spectra of the system. It was found that the emission spectra of the rotated system was red shifted by 44.8 nm with peaks at 447.6 nm for the twisted system and 402.8 nm for the linear system (Figure 14c). To find the reason, we further plotted the wavefunctions corresponding to these transitions, and saw that in the rotated system, the nature of the orbital overlap changes, leading to a red shift of the spectra. In both the cases, the transitions were of π-π in nature, but for the linear case, the transition occurred from an upper energy level (where the corresponding molecular orbital has 9 nodes) to the lower energy level (where the molecular orbital has 8 nodes). In case of the twisted molecule, the transition occurred from an energy level with the molecular orbital having 9 nodes to a lower energy level where the molecular orbital also had 9 nodes. This leads to a lower energy gap or higher wavelength transition for the twisted system (Figure 14d). Visual observations under normal and UV lights for **1** and **1a** also corroborated the red shift in emission (Figure 14b). Upon resolvation with DMF, the emission of **1** came back again to the original emission peak position of 488 nm (Figure 16b). Visual observation also corroborated the above wavelength shift (Figure 16a). It can be clearly seen in the figure, that **1** emits cyan fluorescence whereas **1a** emits strong green emission. However, upon exposure to water, the emission maxima did not shift back to the original one, neither was there a change in the green emission color (Figure 16a). To test whether other organic

solvent vapors can indeed be re-introduced using **1a**, we exposed it to chloroform, THF, acetonitrile, acetone, ethanol and methanol.

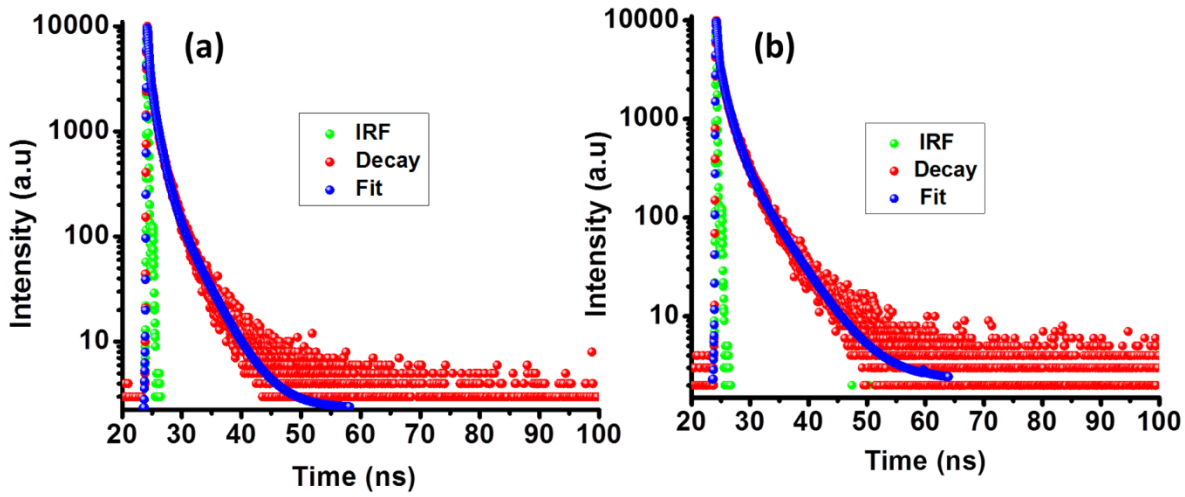

Figure 15. Fluorescence decay profiles upon excitation at 405 nm for (a) **1** and (b) **1a** monitored at 488 nm and 525 nm respectively.

Interestingly, the emission color reversed back to the cyan color, only for DMF and acetonitrile. Figure 16a summarizes the emission wavelengths observed upon exposure to the above mentioned solvent vapors. It was also clear that ethanol, methanol, acetone and THF only brought back the emission wavelength to an intermediate value between the assynthesized and degassed samples. Visual observation also suggests the appearance of an intermediate emission color. It may be concluded that incorporation of these solvents into the pore induces twisting of phenyl rings of OPE chains, only up to a certain degree, after which it gets fixed. This in turn shifts the emission color only up to an intermediate state. This is further proved by observing PXRD patterns of all the solvent re-exposed structures of **1a**. The PXRD pattern of DMF@**1a**, matches almost exactly with **1** revealing the reversibility in the structure. corresponding PL profile showing the associated changes in emission. Expectedly water@**1a**, matched closely with **1a** indicating that the degassed structure remains almost intact after water exposure. Methanol@**1a** PXRD pattern revealed no correspondence with the pattern of either **1** or **1a** revealing an intermediacy (Figure 8). This further proves different levels of structural reorganization upon solvent re-exposure. To conclusively prove the solvent tuned emission behavior of **1**, we then carried out solvent vapor adsorption isotherms on **1a**. The adsorption profiles of water, methanol and THF vapors were analyzed (Figure 9c).

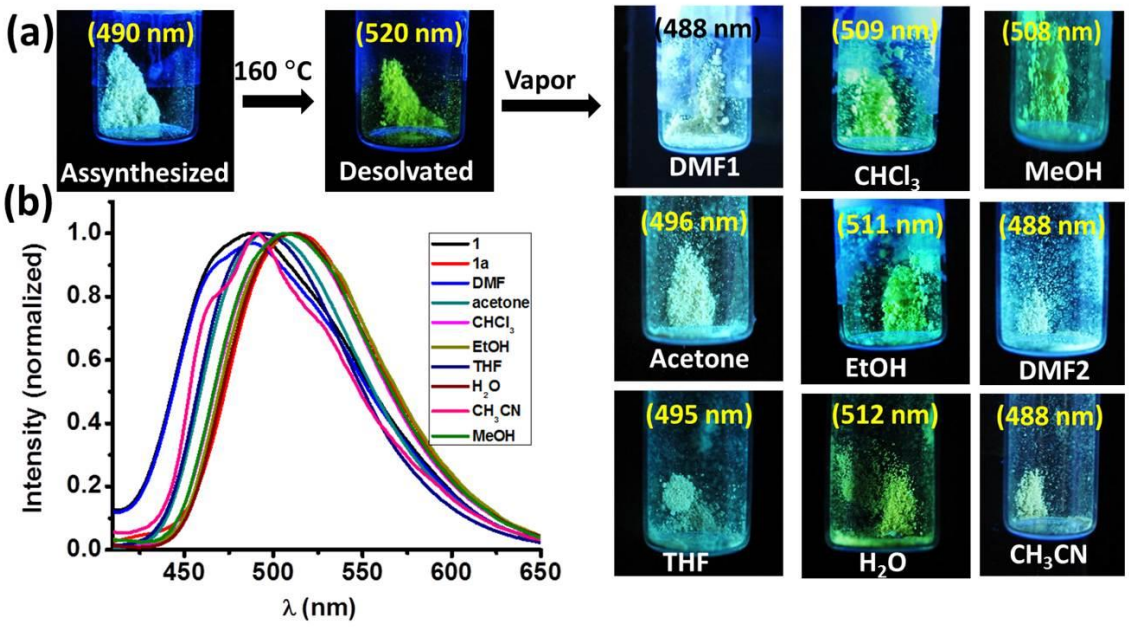

Figure 16. (a) Images showing the emission color changes and the corresponding wavelengths of emission when **1a** was exposed to different solvent vapors and (b) The corresponding PL profile showing the associated changes in emission.

The uptake profile for methanol initially showed minimal uptake at lower pressures. However it portrayed a gated behavior at higher pressures, leading to a final uptake of 64 ml/g. This corresponded to 1.6 molecules per formula unit of **1a**. The adsorption profile of THF showed a gradual uptake of 60 mL, corresponding to 0.75 molecules per formula unit of **1a**. It was discussed in earlier sections that water showed a minimal uptake at low pressure. Based on these results, it can be inferred that at ambient conditions, the diffusion of solvent molecules affects the degree of rotation of OPE chains, leading to the variable emission seen in **1**.

4A.4. Conclusion

In summary, this chapter described the synthesis and structural characterization of a luminescent, semi-conducting and superhydrophobic 3D supramolecular porous framework (**1**). The study revealed that superhydrophobicity arose due to surface projected alkyl chains which are known to decrease surface energy. Additionally we realized that **1** shows solvent modulated emission behavior based on de-solvation and re-solvation. Solvent vapor adsorption studies and theoretical calculations provide explanations for such behavior. As this work coherently relates all the properties with a

structural basis, we believe that this could act as a guiding principle for the design of porous materials showing water-repellent and tunable emission behavior.

4A.5. References

1 (a) S. V. Eliseeva and J-C. G. Bünzli, *Chem. Soc. Rev.*, 2010, **39**, 189; (b) A. W. Freeman, S. C. Koene, P. R. L. Malenfant, M. E. Thompson and J. M. J. Fréchet, *J. Am. Chem. Soc*., 2000, **122**, 12385.

2 (a) K. Müller-Buschbaum, F. Beuerle and C. Feldmann, *Microporous Mesoporous Mater*., 2015, **216**, 171; (b) Y. Cui, Y. Yue, G. Qian and B. Chen, *Chem. Rev*., 2012, **112**, 1126; (c) M. D. Allendorf, C. A. Bauer, R. K. Bhakta and R. J. T. Houk, *Chem. Soc. Rev*., 2009, **38**, 1330; (d) G. Maurin, C. Serre, A. Cooper and G. Férey, Chem. Soc. Rev. 2017, **46**, 3104.

3 (a) S. Roy, A. Chakraborty and T. K. Maji, *Coord. Chem. Rev*., 2014, **273-274**, 139; (b) Y. Cui, B. Chen, and G. Qian, *Coord. Chem. Rev*., 2014, **273-274**, 76.

4 M. C. So, G. P. Wiederrecht, J. E. Mondloch, J. T. Hupp and O. K. Farha, *Chem. Commun*., 2015, **51**, 3501.

5 (a) Y. Wu, G-P. Yang, Y. Zhao, W-P. Wu, B. Liu and Y-Y. Wang, *Dalton Trans*., 2015, **44**, 3271; (b) T. H. Noh, H. Lee, J. Jang and O-S. Jung, *Angew. Chem. Int. Ed*., 2015, **127**, 9416; (c) K. C. Stylianou, R. Heck, S. Y. Chong, J. Bacsa, J. T. A. Jones, Y. Z. Khimyak, D. Bradshaw and M. Rosseinsky, *J. Am. Chem. Soc*., 2010, **132**, 4119; (d) K-L. Zhang, H-Y. Gao, Z-C. Pan, W. Liang and G-W. Diao, *Polyhedron*., 2007, **26**, 5177; (e) M. Frisch and C. L. Cahill, *Dalton Trans*., 2005, 1518.

6 (a) B. Chen, Y. Yang, F. Zapata, G. Lin, G. Qian and E. B. Lobkovsky, *Adv. Mater*., 2007, **19**, 1693; (b) Y. K. Park, S. B. Choi, H. Kim, K. Kim, B-H. Won, K. Choi, J-S. Choi, W-S. Ahn, N. Won, S. Kim, D. H. Jung, S-H. Choi, G-H. Kim, S. S. Cha, Y. S. Jhon J. K. Yang and J. Kim, *Angew. Chem. Int. Ed*., 2007, **46**, 8230; (c) K-L. Wong, G-L. Law, Y-Y. Yang and W-T. Wong, *Adv. Mater*., 2006, **18**, 1051 (d) H. Liu, H. Wang, T. Chu, M. Yu and Y. Yang, *J. Mater. Chem. C*, 2014, **2**, 8683.

7 (a) X. Zhang, M. A. Ballem, M. Ahrén, A. Suska, P. Bergman and K. Uvdal, *J. Am. Chem. Soc*., 2010, **132**, 10391; (b) X. Zhang, Z-K. Chen and K. P. Loh, *J. Am. Chem. Soc*., 2009, **131**, 7210; (c) X. Zhang, W. Wang, Z. Hu, G. Wang and K. Uvdal, *Coord. Chem. Rev*., 2015, **284**, 206.

8 (a) F. Zhang, Y. Wang, T. Chu, Z. Wang and Y. Yang, *Analyst.*, 2016, **141**, 4502; (b) A. H. Assen O. Yassine, O. Shekhah, M. Eddaoudi and K. N. Salama, *ACS Sens.*, 2017, **2**, 1294.

9 (a) U. H. F. Bunz, *Chem. Rev.*, 2000, **100**, 1605; (b) U. H. F. Bunz, *Macromol. Rapid Commun.*, 2009, **30**, 772; (c) U. H. F. Bunz, K. Seehafer, M. Bender and M. Porz, *Chem. Soc. Rev.*, 2015, **44**, 4322.

10 (a) J. R. Acharya, H. Zhang, X. Li and E. E. Nesterov, *J. Am. Chem. Soc.*, 2009, **131**, 880; (b) S. Roy, A. Hazra, A. Bandyopadhyay, D. Raut. P. L. Madhuri, D. S. Shankar Rao, U. Ramamurty, S. K. Pati, S. K. Prasad and T. K. Maji, *J. Phys. Chem. Lett.*, 2016, **7**, 4086; (c) S. Roy, D. Samanta, P. Kumar and T. K. Maji, *Chem. Commun.*, 2018, **54**, 275.

11 (a) S. Roy, V. M. Suresh and T. K. Maji, *Chem. Sci.*, 2016, **7**, 2251; (b) S. Roy, M. Das, A. Bandyopadhyay, S. K. Pati, P. P. Ray and T. K. Maji, *J. Phys. Chem. C*, 2017, **121**, 23803.

12 V. M. Suresh, S. Chatterjee, R. Modak, V. Tiwari, A. Patel, T. K. Kundu and T. K. Maji, *J. Phys. Chem. C*, 2014, **118**, 12241.

13 N. T. T. Nguyen, H. Furukawa, F. Gandara, H. T. Nguyen, K. E. Cordova and O. M. Yaghi, *Angew. Chem. Int. Ed.*, 2014, **126**, 10821.

14 M. J. Frisch, G. W. Trucks, H. B. Schlegel, G. E. Scuseria, M. A. Robb, J. R. Cheeseman, G. Scalmani, V. Barone, B. Mennucci and G. A. Petersson, Gaussian 09, Revision A.02; Gaussian, Inc.: Wallingford, CT, 2009.

15 (a) J. Heyd, G. Scuseria and M. Ernzerhof, *J. Chem. Phys.*, 2003, **118**, 8207; (b) J. Heyd, J. E. Peralta, G. E. Scuseria and R. L. Martin, *J. Chem. Phys.*, 2005, **123**,174101; (c) J. Heyd, G. E. Scuseria and M. Ernzerhof, *J. Chem. Phys.*, 2006, **124**, 219906.

16 S. V. a. SMART (V 5.628), SAINT (V 6.45a), XPREP, SHELXTL; Bruker AXS Inc. Madison, Wisconsin, USA, 2004.

17 G. M. Sheldrick, SADABS, Empirical Absorption Correction Program. University of Göttingen, Göttingen, 1997.

18 G. M. Sheldrick, SHELXL 97, Program for the Solution of Crystal Structure, University of Göttingen, Germany, 1997.

19 A. Spek, *J. Appl. Crystallogr.*, 2003, **36**, 7.

20 L. Farrugia, *J. Appl. Crystallogr.*, 1999, **32**, 837.

21 S. A. Sharber, R. N. Baral, F. Frausto, T. E. Haas, P. Müller and S. W. Thomas III, *J. Am. Chem. Soc*., 2017, **139**, 5164.

22 R. J. Marshall, Y. Kalinovskyy, S. L. Griffin, C. Wilson, B. A. Blight and R. S. Forgan, *J. Am. Chem. Soc*., 2017, **139**, 6253.

Chapter 4B

Moisture Resistant, Luminescent and Electrically Conducting Metal-organic Framework

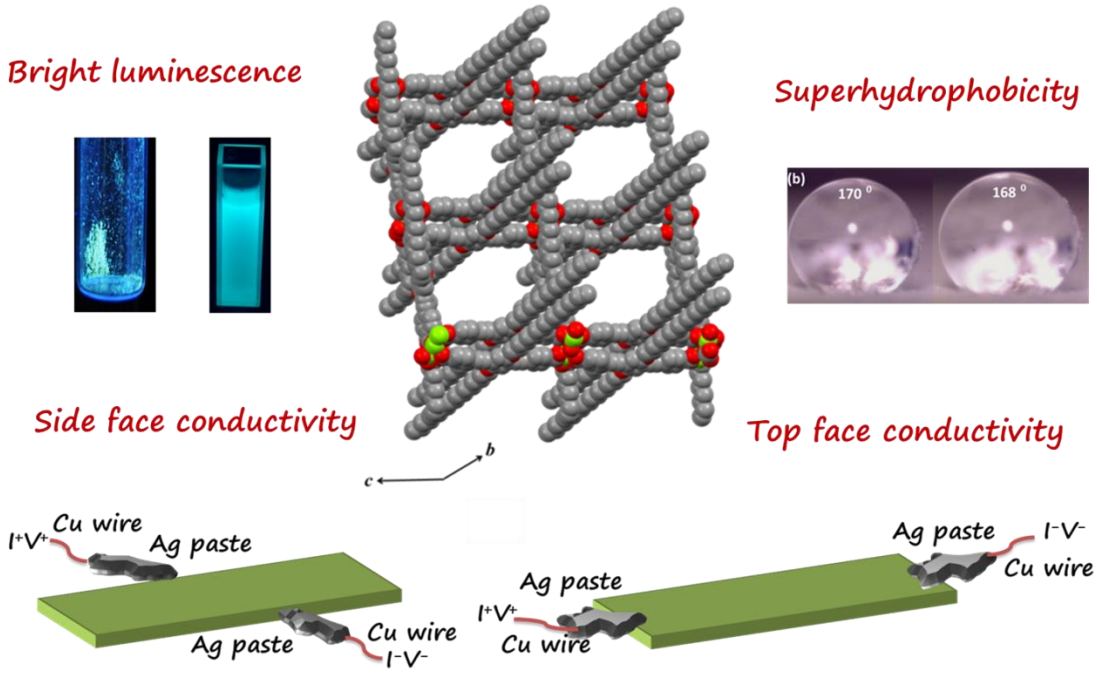

Summary

Moisture resistant, luminescent and electrically conducting MOF materials have gained recent interest due to their impact on the energy landscape. Research in this field is still at the nascent state and demands a deeper understanding of design principles for advancement of this field. In this chapter, a MOF using a bola-amphiphilic π-conjugated organic linker and Mg^{II} metal ion was synthesized. The MOF has been characterized via single crystal X-ray diffraction to reveal a 2D porous structure having a molecular formula $\{[Mg_3(OPE\text{-}C_{18})_3(H_2O)_2]\cdot 2DMF\}_n$ (**1**), with surface projected alkyl chains, leading to superhydrophobicity. **1** shows a linker based cyan emission with high quantum yield. Thin film and single crystal two probe conductivity measurements on different faces reveal the semi-conducting property of **1**. Simultaneously, luminescent and electrically conducting MOFs are rare and to the best of our knowledge, **1** is only the third permanently porous MOF structure, showing moisture resistant opto-electronic characteristics.

The work based on this chapter is communicated:

S. Roy, S. Bhattacharyya, A. Bandyopadhyay, S. K. Pati, and T. K. Maji, *Manuscript submitted.*

4B.1. Introduction

Metal-organic frameworks (MOFs) are a crystalline class of hybrid porous polymers constructed via periodic linkages between metal nodes and organic/organometallic linkers.[1] Research in the field of MOFs has revolutionized gas storage and separation, catalysis and membrane based separation of gases and liquids.[2] MOFs have shown other promising applications as well, such as drug delivery, proton conduction, sensing and nanoscale morphology tunability.[3] The recent function of MOFs that is being explored is their electrical properties.[4] The reason being that structural tunability of MOFs allows band gap control and high surface area, essential for a well-functioning electrical device. A vast choice of organic linkers with a known band structure can help create a family of MOFs having different band gaps suited to different electrical functions.[5] The metal ion in MOFs also plays a significant role in controlling the coordination environment and providing the conducting pathway through its unfilled orbitals.[4a] Electrical conductance in MOFs can occur in three charge transport pathways: 1) "through space" (π-stacking), 2) "through bond" (via covalent bonds) and 3) charge hopping, directed by the Marcus theory. All three mechanisms can be utilized to generate electrically conducting MOFs. Electrically conducting MOFs therefore have the potential to substantially imapct the energy landscape by introducing a new class of materials suitable for electrical device fabrication in Schottky barrier diodes (SBDs),[6] field effect transistors (FETs),[7] and light emitting diodes (LEDs).[8] Coupled with water-repellence, MOFs also have the potential to be used as underwater semi-conductor devices. Structural tunability of MOFs can also induce moisture resistance via use of water repellent organic linkers for its construction.[9]

Use of bola-amphiphilic ligands with an end-capping polar coordinating groups with an inner non-polar π-rich groups could serve the purpose of both "through space" and "through bond" charge transport mechanisms via its stacking interactions of the phenyl rings and assembling with metal ions through end groups, respectively. *Oligo-p*-(phenyleneethynylenes) (OPEs) are one such class of π-conjugated ligands whose synthetic tunability allows incorporation of water-repellent functional groups in the side chains and coordinating functional groups along with charge transport properties for MOF construction.[10] We have recently reported one such work in which the use of water repellent and electrically conducting organic linker for nanoscale MOF (NMOF) construction has led to a photo-conducting and moisture resistance Schottky Barrier

NMOF diode.[6a] Therefore, this work along with another previous report, gives the idea of using bola-amphiphilic, π-conjugated organic linkers generates high charge carrier mobility and also mimics the lotus leaf surface, thereby assisting in water repellence.[10] Taking a cue from these works, we decided to translate the same properties into bulk MOFs. Till date, only a handful of reports give an organizational understanding of surface water repellence and conducting pathways in MOFs and this would provide the advantage of a structural understanding of both the properties.[11]

This chapter describes the synthesis of a bola-amphiphilic oxy-octadecyl functionalized *oligo*-(*p*-phenyleneethynylene) ligand (**H_2OPE-C_{18}**) for the construction of bulk MOF structures and crystallized it with $Mg(NO_3)_2$ to get the single crystal structure $\{[Mg_3(OPE\text{-}C_{18})_3(H_2O)_2]\cdot 2DMF\}_n$ (**1**) having a 3D structure. **1** showed superhydrophobic property with an ultra-high contact angle of 168°. It also showed cyan luminescence with a high quantum yield. Electrical conductivity measurements on different faces of the single crystal and thin films showed conductivity in the semi-conducting regime. **1** is therefore a member of a small group of MOF structures showing appreciable conductivity and is also the third report of a water repellent and semi-conducting MOF structure.

4B.2. Experimental Section

4B.2.1. Materials

$Pd(PPh_3)_4$ and $Mg(NO_3)_2\cdot 6H_2O$ were obtained from Sigma-Aldrich Chemical Co and cuprous iodide was acquired from LobaChemie Pvt. Ltd. N,N-dimethyl formamide (DMF) and tetrahydrofuran (THF) were obtained from Spectrochem Pvt. Ltd (Mumbai, India). Tetrahydrofuran was pre-dried using standard procedure and all other reagents, solvents were of reagent grade and used without further purification.

4B.2.2. Physical Measurements

The elemental analyses were carried out using a Thermo Scientific Flash 2000 CHN analyzer. Infrared spectral studies were performed by making samples with KBr pellets using Bruker FT-IR spectrometer. Powder X-ray diffraction studies were recorded on a Bruker D8 discover instrument using Cu-Kα radiation. Thermal stability was analyzed using Mettler Toledo TGA 800 instrument under inert atmosphere in the temperature range of 25-850 °C at a heating rate of 3 °C /min. UV–Vis spectra were recorded on a

Perkin Elmer Model Lambda 900 spectrophotometer. Fluorescence studies were accomplished using Perkin Elmer Ls 55 Luminescence spectrometer. Fluorescence lifetime measurements were recorded with a Horiba Deltaflex spectrometer. Electrochemical performance of **1** was measured by using a glassy carbon electrode (GCE) voltammetry. They were performed using an Autolab PGSTAT12 potentiostat/galvanostat in a conventional three-electrode cell.

Adsorption Measurements

Porosity measurements of **1** were carried out using QUNATACHROME QUADRASORD-SI analyser at 77 K for N_2 and 195 K for CO_2. In the sample tube the adsorbent samples (~100-150 mg) were placed which had been prepared at 170 °C under a 1×10^{-1} Pa vacuum for about 12 h prior to measurement of the isotherms. Helium gas (99.999% purity) at a certain pressure was introduced in the gas chamber and allowed to diffuse into the sample chamber by opening the valve. The amount of gas adsorbed was calculated from the pressure difference (P_{cal} - P_e), where $P_{cal}$is the calculated pressure with no gas adsorption and P_e is the observed equilibrium pressure. All the operations were computer-controlled. Benzene and water vapor adsorptions were carried out at 298K using BELSORP AQUA 3 solvent vapor analyzer. A sample of about ~100 –150 mg was prepared by heating at 170 °C for about 12 h under vacuum (1×10^{-1} Pa) prior to measurement of the isotherms. The solvent molecules used to generate the vapor were degassed fully by repeated evacuation. Dead volume was measured with helium gas. The adsorbate was placed into the sample tube, then the change of the pressure was monitored and the degree of adsorption was determined by the decrease in pressure at the equilibrium state. All operations were computer controlled and automatic.

Conductivity Measurements

Conductivity measurement on a thin film of the material was performed on a glass substrate by spin coating technique at 1200 rpm for 2 minutes and subsequently dried. Two ohmic parallel electrodes were taken from the film. The dimensions of the electrodes were of 9 mm × 1 mm with a gapping of 1 mm between two electrodes. For conductivity measurement, a two-probe contact method was adopted to obtain a current voltage (I-V) characteristics graph, where the electrodes were connected with a Keithley 2450 source meter. The process was performed under room temperature and in an open atmosphere.

The conductivity was measured with the help of the slope of linear fitted I-V curve, by using equation:

$$\sigma = \left(\frac{\Delta I}{\Delta V}\right)\left(\frac{l}{A}\right)$$

Where, σ is the conductivity, I is the current, V is the applied voltage, l is the distance between electrodes, A is the cross sectional area of sample.

The same equation was used to measure conductivities on single crystals of **1**. Silver Paste contacts were made on different faces of single crystals of **1**. Copper wires were attached to the silver paste contacts and I-V profiles were measured using a Keithley 2450 sourcemeter under open atmosphere.

Contact Angle Measurements

Contact angles were measured using an indigenous set up coupled with a Logitech camera for capturing the images. Contact angles were also measured using dedicated contact angle analyzer, OCA30 from Data Physics instrument (GmbH, Germany). 4 μL of the sessile water droplets were employed for measuring the static contact angles. A minimum of ten measurements were made.

4B.2.3. Computational Details

Density functional theory calculations have been performed to obtain the electronic and optical properties of the system using the SIESTA package.[12] We have considered Generalized gradient approximation (GGA) in the Perdew–Burke–Ernzerhof (PBE)[13] form for accounting the exchange-correlation function. Double ζ polarized (DZP) numerical atomic-orbital basis sets all the atoms. A sufficient mesh cutoff value of 400 has been used in calculations. We have used a vacuum of 20 Å around the molecule in all directions to avoid unwanted interactions. Systems are considered to be optimized if the magnitude of the forces acting on each atoms is less than 0.04 eV/Å. We have used HSE06 functional[14] to calculate the accurate HOMO-LUMO gap of the system as implemented in Gaussian09 package.[15]

4B.2.4. Single Crystal X-ray Diffraction (SCXRD)

Suitable single crystal of **1** was mounted on a thin glass fiber with commercially available super glue. X-ray single-crystal structural data were collected on a Bruker Smart-CCD diffractometer equipped with a normal focus and a 2.4 kW sealed tube X-ray source with

graphite monochromated Mo-Kα radiation (λ = 0.71073 Å) operating at 50 kV and 30 mA. The program SAINT[16] was used for the integration of diffraction profiles, and absorption correction was made with the SADABS[17] program. All the structures were solved by SHELXT[16] and refined by the full-matrix least-squares method using SHELXL-2017.[18] All the hydrogen atoms were fixed by HFIX and placed in ideal positions. The potential solvent accessible area or void space was calculated using the PLATON[19] multipurpose crystallographic software. All crystallographic and structure refinement data are summarized in Table 1. Selected bond lengths and angles for **1** are given in Table 2 (Supporting Information). All calculations were carried out using SHELXL-2017,[18] and WinGX system, Ver 1.80.05.[20]

4B.2.5. Synthesis of 4,4'-(2,5-bis(octadecyloxy)-1,4-phenylene)bis(ethyne-2,1-diyl)dibenzoic acid (H_2OPE-C_{18}) and 1

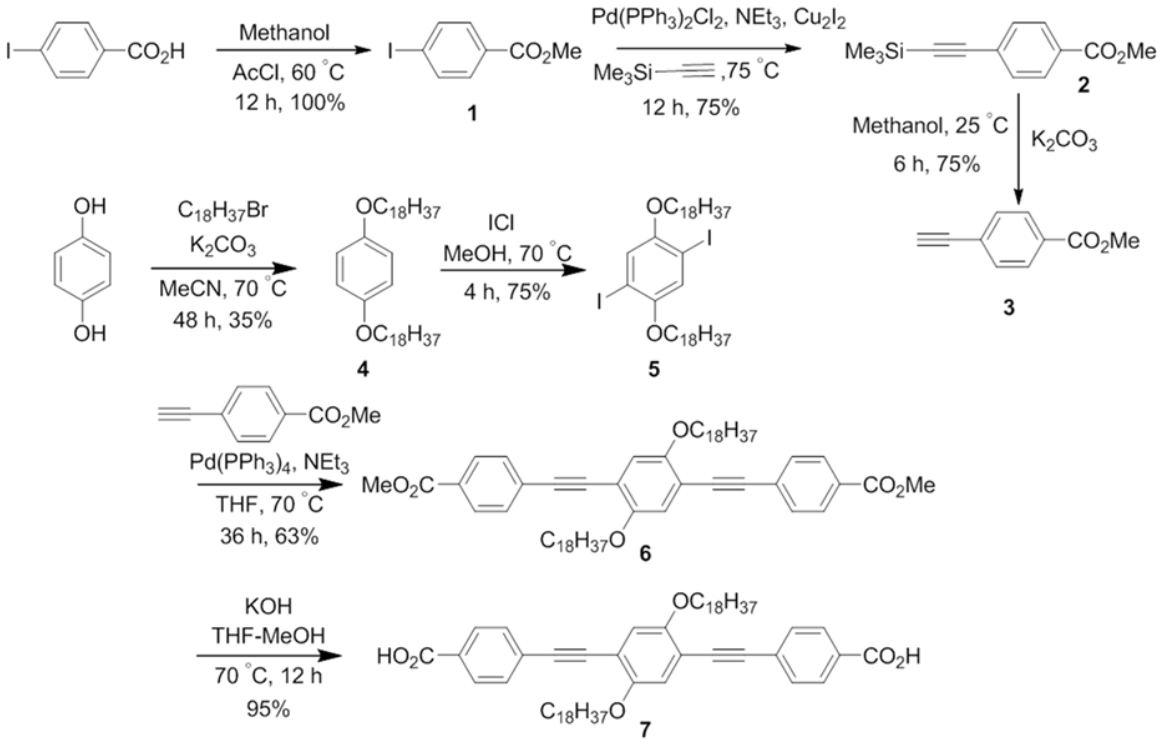

Scheme 1. Synthetic scheme for **H_2OPE-C_{18}**.

Synthesis of **H_2OPE-C_{18}** was carried out following reported procedures and is discussed in details in Chapter 2A (Scheme 1).[9]

Synthesis of $\{[Mg_3(OPE\text{-}C_{18})_3(H_2O)_2]\cdot 2DMF\}_n$ (1)

An ethanolic solution (1 mL) of $Mg(NO_3)_2{\cdot}6H_2O$ (0.25 mmol) was layered on a buffer layer (0.75 mL) of DMF/ethanol which was previously layered onto a DMF solution of **$H_2OPE\text{-}C_{18}$** (0.75 mmol), in a crystal tube. After 10 days, green colored block-shaped crystals appeared in the middle of the tube and were separated and washed with ethanol. The bulk amount of the sample was prepared by the direct mixing of the respective reagents in DMF/ethanol solution under stirring for 24 h, and the phase purity was checked with the PXRD and elemental analysis. Yield: 56%, Elemental analysis: Calcd. for $C_{186}H_{268}Mg_3N_2O_{22}$: C, 75.55; H, 9.14; N, 0.95. Found: C, 75.67; H, 8.81; N, 0.91. IR (KBr, cm^{-1}): ν(H_2O) 3370; ν(ArC-H) 2950, ν(C-O) 1600; ν(ArC=C) 1420 (Figure 5).

4B.3. Results and Discussion

4B.3.1. Structural Characterization

$H_2OPE\text{-}C_{18}$ was synthesized according to reported Sonogashira-Hagihara coupling procedures (Scheme 1). Block shaped green crystals of **1** were obtained after 10 days by layering an ethanolic solution of $Mg(NO_3)_2$ onto a buffer layer on a DMF solution of $H_2OPE\text{-}C_{18}$ in a 1:1 molar ratio. Single crystal X-ray diffraction (SCXRD) analysis revealed that **1** crystallizes in the triclinic crystal system with a $P\bar{1}$ space group (Table 1). The structure of **1** can be visualized as an extension of a Mg_3-core secondary building unit (SBU) via OPE dicarboxylate linkages in two crystallographic axes having the formula $Mg_3(O_2C)_6(OH_2)_2$ (Figure 1). There are two crystallographically independent Mg^{II} atoms, Mg1 and Mg2 in the structure. Each Mg1 is penta-coordinated and connected to four carboxylate oxygen atoms (O1, O4, O7 and O8) from three different OPE-C_{18}. The fifth position is occupied by the water molecule (O10). Each Mg2 is hexa-coordinated and connected to six carboxylate oxygen atoms (O2, O3, O7 and its symmetry related counterparts). One OPE-C_{18} $(OPE\text{-}C_{18})_1$ dicarboxylate connects four Mg^{II} centres by syn-syn bridging (O1, O2, and O3, O4) and acts as a tetradentate ligand whereas the other OPE-C_{18} $(OPE\text{-}C_{18})_2$ binds to four Mg^{II} centres by μ-oxo bridging (μ_2-O1) as well as cis-chelating (O7, O8) (Figure 1). Two symmetry related $(OPE\text{-}C_{18})_1$ binds the $Mg_3(O_2C)_6(OH_2)_2$ (SBU) along the *c*-axis forming the 1D double column like structure (Figure 2). Such 1D double columns are further connected by $(OPE\text{-}C_{18})_2$ to form a 2D grid-like porous structure in the *bc* plane (Figure 2, 3). There are very weak

C−H···π interactions between the alkyl chains and π-cores of adjacent OPEs building the column. This further reinforces the 1D packing in **1**. Another interesting feature of the structure of **1** is that there are long oxyoctadecyl chains decorated towards the periphery of the porous structure (Figure 4c). The Mg-O bond distances are in between 1.857(15)-2.259(17) Å (Table 2), which comfortably falls within the expected Mg-O bond distances with no anomaly.

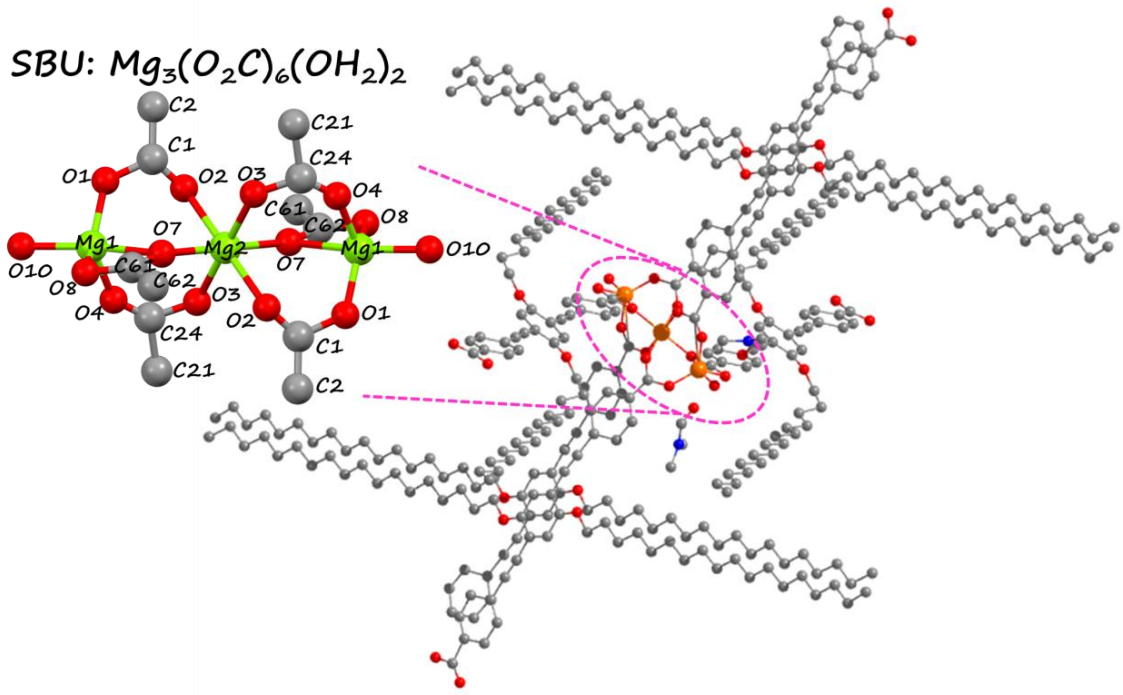

Figure 1. Single crystal structure of **1**: Asymmetric unit showing the coordination of OPE dicarboxylates around the Mg centres. Inset: representation of the $Mg_3(O_2C)_6(OH_2)_2$ SBU showing the coordination environment around Mg centres.

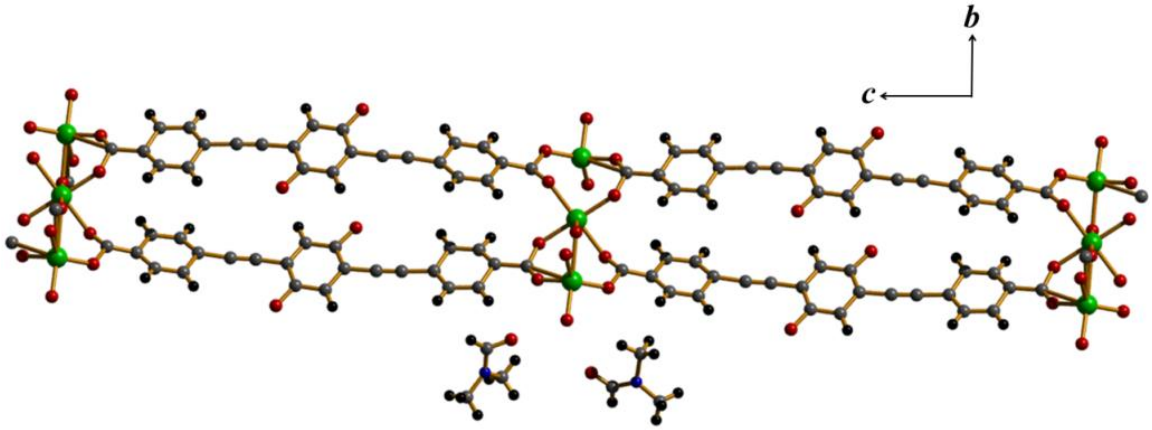

Figure 2. Structural figure of **1** showing the formation of 1D double column via OPE dicarboxylate coordination to Mg^{II} centres.

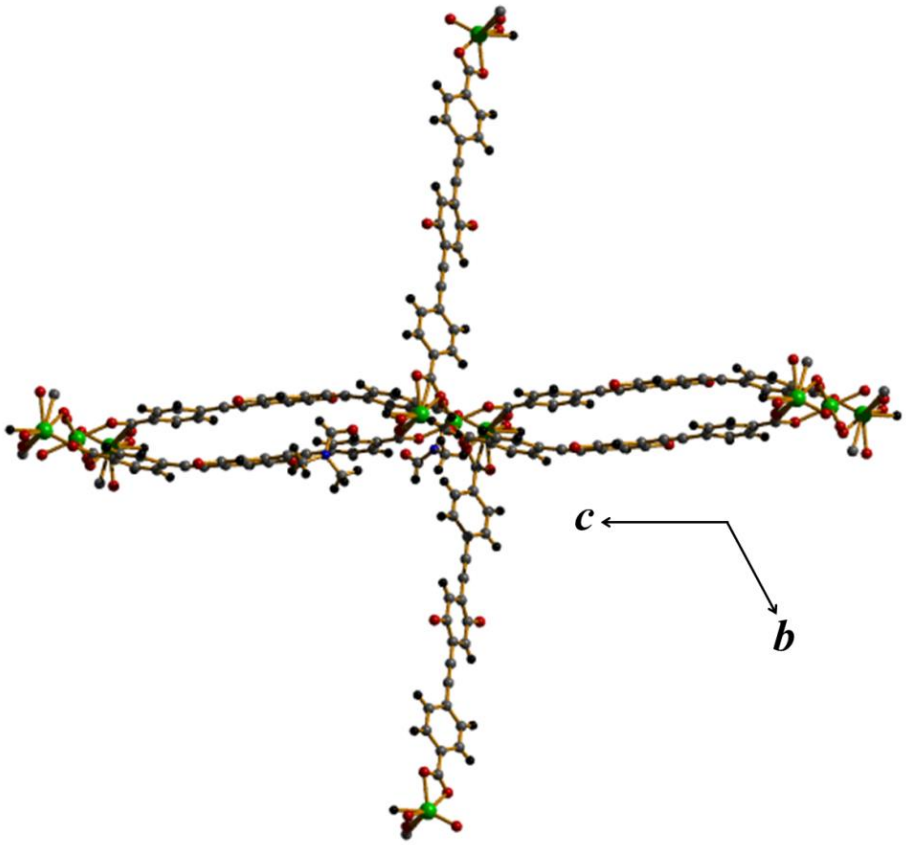

Figure 3. Structural figure of **1** showing the coordination of OPEs perpendicular direction, leading to the 2D grid formation.

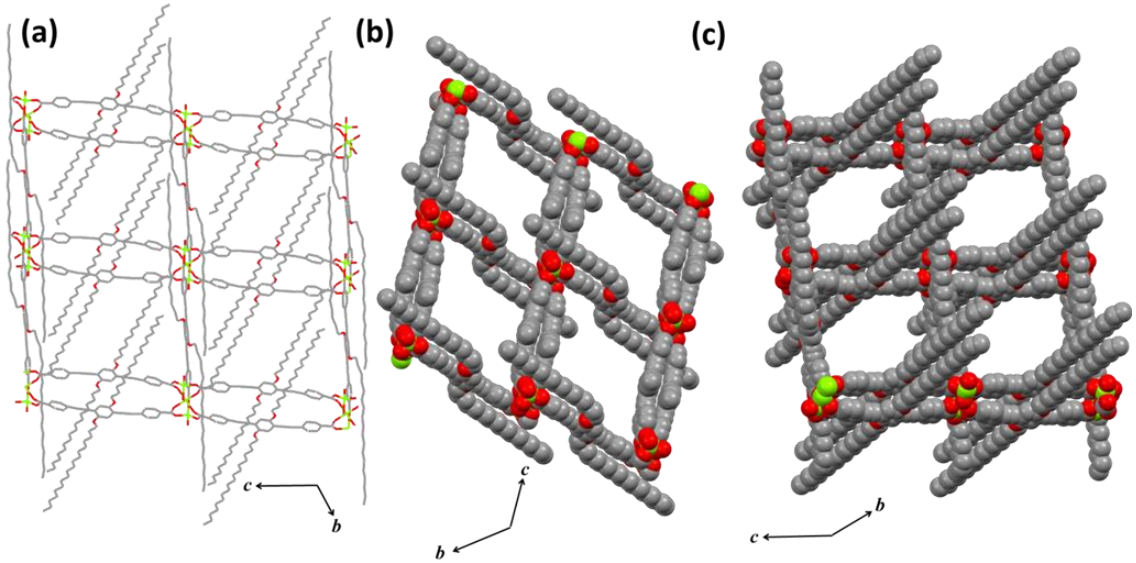

Figure 4. Single crystals of **1**: (a) view showing the 2D grid formation (b) spacefill model view of the pores formed in the 2D grid (c) spacefill model showing the surface projected alkyl chains in the 2D grid. (Solvent molecules have been omitted for clarity).

Table 1. Crystallographic data and structure refinement parameters for **1**.

	1
empirical formula	$C_{186}H_{268}Mg_3N_2O_{22}$
M	4689. 29
crystal system	$P\bar{1}$
space group	triclinic
a (Å)	12.922 (5)
b (Å)	16.274 (6)
c (Å)	23.651 (9)
α (deg)	104.790 (16)
β (deg)	94.937 (18)
γ (deg)	100.106 (17)
V (Å^3)	4689.0 (3)
Z	1
T (K)	100 K
λ (Cu K$_α$)	1.5406
D$_c$ (g/cm^3)	1.047
μ (mm^{-1})	0.613
$\theta_{min}/\theta_{max}$	2.9/ 47.2
total data	64117
unique reflection	8480
R_{int}	0.196
data [I>2σ(I)]	2738
R^a	0.2015
$R_w{}^b$	0.5995
GOF	1.26
Δρ min/max [e Å^{-3}]	-0.28, 0.62

$^aR=\sum||F_o|-|F_c||/\sum|F_o|$. $^bR_w=[\sum\{w(F_o^2-F_c^2)^2\}/\sum\{w(F_o^2)^2\}]^{1/2}$

Table 2. Selected Bond Distances [Å] and Angles [°] for **1**.

Mg1-O1	1.857(15)	O1-Mg1-O7	93.0(6)
Mg1-O7	2.259(17)	O1-Mg1-O8	123.9(7)
Mg1-O8	2.132(19)	O1-Mg1-O10	97.1(7)
Mg1-O10	1.968(19)	O1-Mg1-O4_b	121.8(8)
Mg1-O4_b	1.875(15)	O7-Mg1-O8	61.4(7)
Mg2-O2	2.168(16)	O7-Mg1-O10	161.4(7)
Mg2-O7	2.093(15)	O2–Mg2-O7	83.4(5)
Mg1-O3_b	2.072(14)	O2-Mg2-3_b	93.6(6)
Mg1-O3_c	2.072(14)	O2-Mg2-3_c	86.4(6)
Mg1-O2_d	2.168(16)	O2-Mg2-O2_d	180.00
Mg1-O7_d	2.093(15)	O2-Mg2-O7_d	96.6(5)

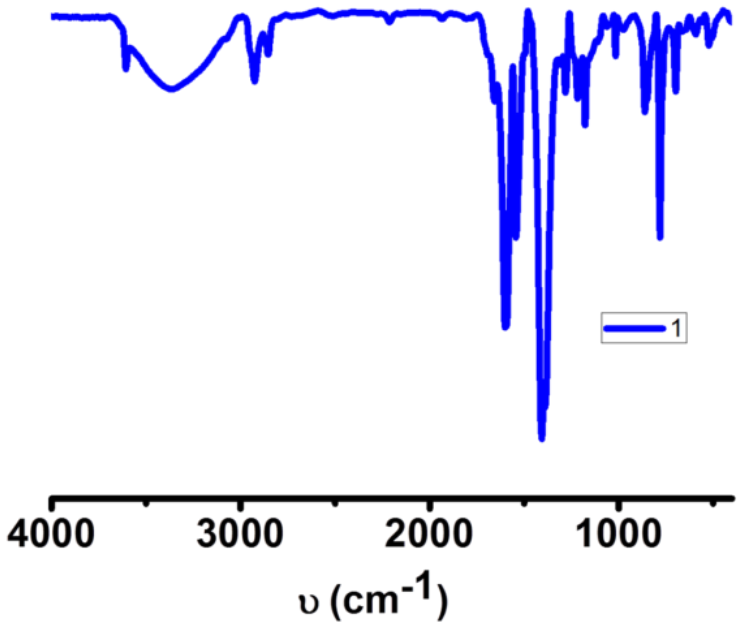

Figure 5. IR spectrum for **1**.

Presence of water molecules in **1** was further confirmed from the infrared (IR) spectrum (Figure 5). TGA analysis of the assynthesized **1** shows a weight loss of 3% between 160-180 °C following which the structure was stable upto 300 °C (Figure 6). The mass loss of 3% corresponds to the loss of guest DMF molecules. Porosity measurements were carried out after degassing **1** at 180 °C overnight. **1** was non-porous towards N_2 as deduced from the Type II isotherm at 77K (Figure 7). However, it showed a gradual uptake of 50 cc/g

CO_2 at 195K upto a pressure of 1 bar (Figure 8a). The long alkyl chains are protruded into the pore that might have resulted in the low diffusion barrier and porosity in the framework. PXRD analysis indicated a high degree of crystallinity in **1** which was maintained in the degassed sample as well (Figure 9, 10). The high degree of crystallinity, porosity, conjugation and long alkyl chains present in the structure further motivated us to investigate its luminescent, charge transport and water repellent properties.

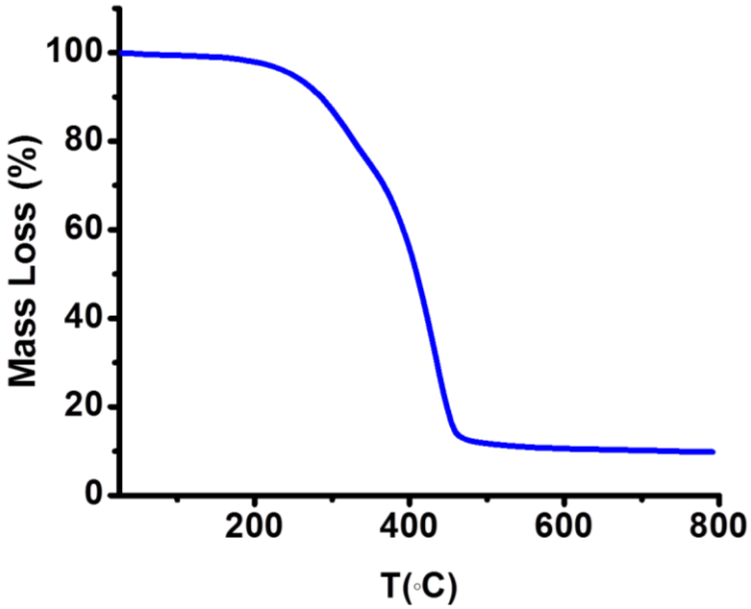

Figure 6. Thermogravimetric analysis of **1** under N_2 atmosphere.

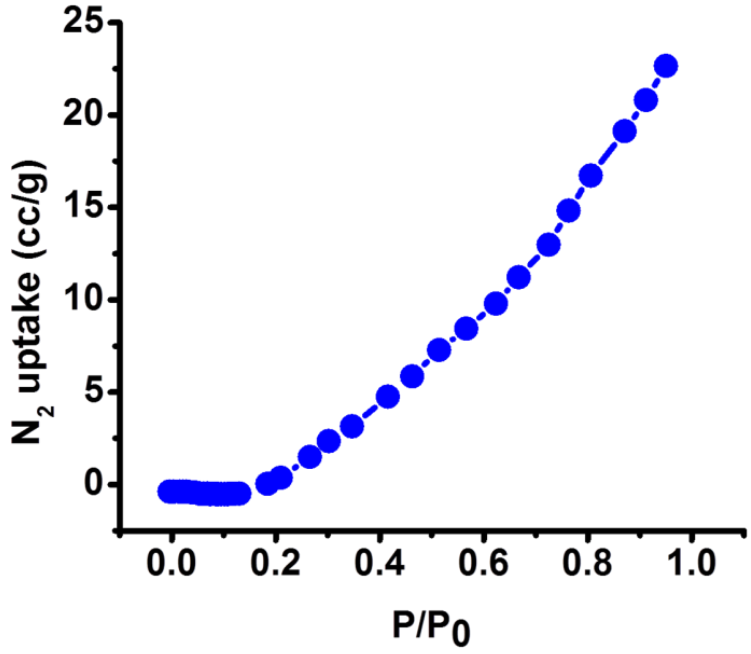

Figure 7. N_2 adsorption isotherm at 77 K for **1**.

4B.3.2. Superhydrophobicity in 1

It has been well studied that surface projected alkyl and fluoroalkyl chains increase the surface roughness, decrease the surface energy and thereby induce superhydrophobicity in a structure. As our ligand also contained long alkyl chains, we decided to check for its water repellence property first. Water contact angles measured on a glass substrate coated with **H_2OPE-C_{18}** showed a contact angle of 140-145° as was previously reported by us (Figure 8b).[9] This showed its hydrophobic nature. Since it was observed that **1** contained such surface periodic alkyl chain distribution, and as ligand property gets translated into the MOF structure,[9] we coated it on a glass substrate and proceeded to measure water contact angles. For the experiment, a 4 µL volume of water droplet was placed on different positions and images were recorded to measure the contact angle. The coated surface showed contact angles of 169±1° (Figure 8c). This proved the superhydrophobicty of the structure. Interestingly, this proves that rigidity and periodicity of surface projected alkyl chains are the necessary criteria for inducing water repellence in a structure. As **H_2OPE-C_{18}** lacks periodicity due to the absence of a rigid framework structure, it did not portray superhydrophobicity.

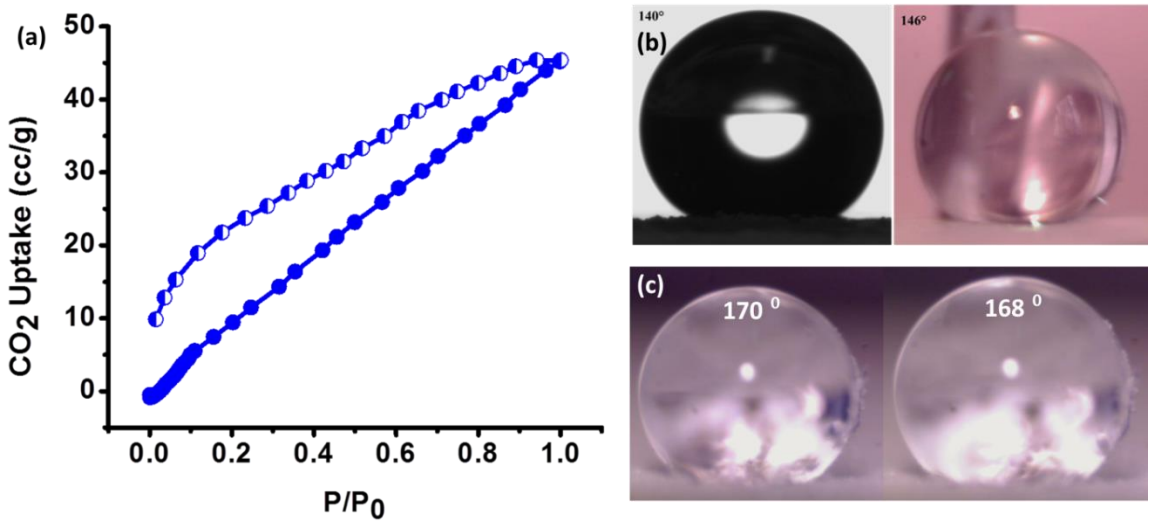

Figure 8. (a) CO_2 adsorption isotherm at 195 K for **1**. (b) Images of two 4 µL water droplets situated at different positions of **1** coated glass substrate.

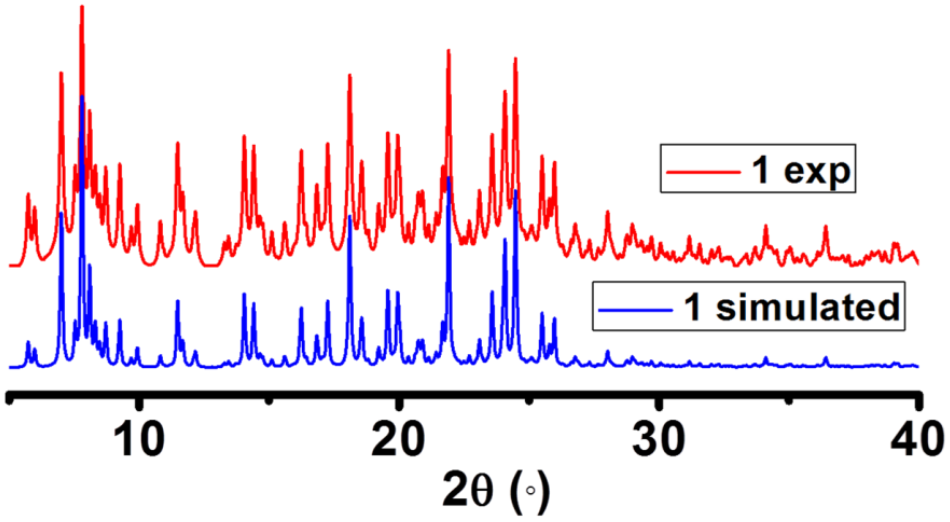

Figure 9. PXRD reflections for simulated (red) and **1.**

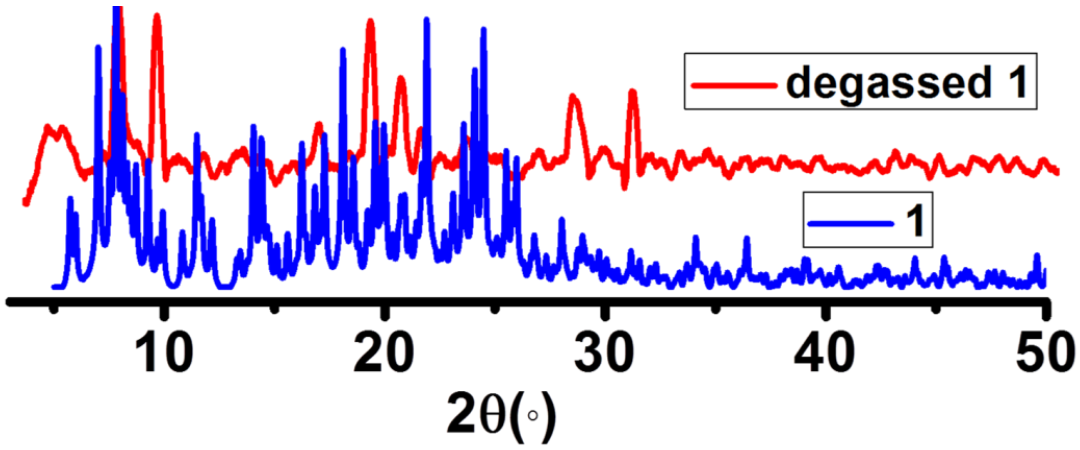

Figure 10. PXRD reflections for degassed **1** (red) and **1** (blue)**.**

4B.3.3. Opto-electronic Properties of 1

The elongated conjugation present in the structure then made us delve into the investigation of the opto-electronic properties of **1**. When dispersed in THF, it showed characteristic two absorption bands at 320 nm and 380 nm, respectively (Figure 11a). Upon excitation at 380 nm, the THF dispersion of **1** gave an emission maximum at 450 nm (Figure 11b). Images of the dispersed state under UV light also showed a bright cyan emission (Figure 11b inset). In the solid state, **1** absorbed at 400 nm and emitted at 485 nm upon excitation at 400 nm (Figure 11c, d). Images under UV of **1** also revealed bright greenish emission (Figure 11d inset). This emission is linker based as **H_2OPE-C_{18}** also absorbs and emits in the same region (Figure 12). The measured quantum yield gave a value of 22%. This revealed the excellent optical output of **1**.

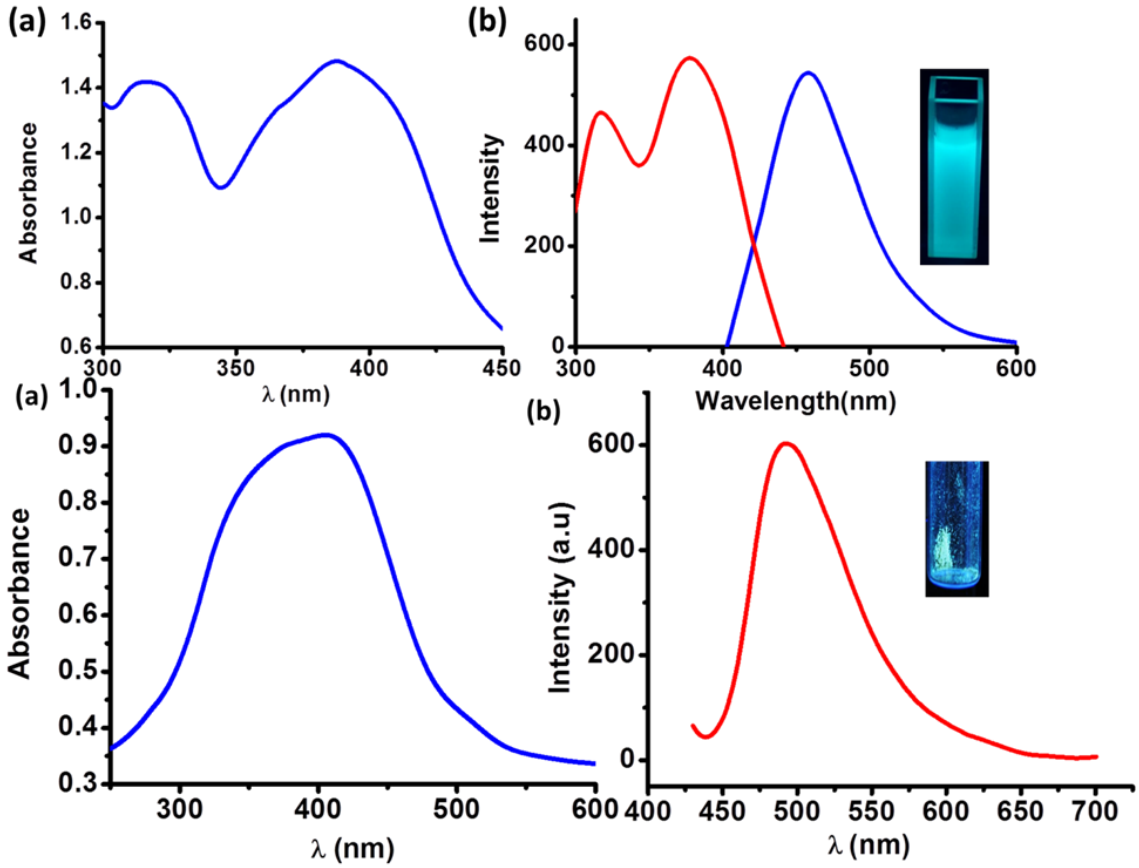

Figure 11. (a) UV and (b) PL plots of **1** in THF dispersed state. Inset: Image of **1** dispersed in THF under UV. Solid state (c) UV and (d) PL of **1**. Inset: Image of **1** in the solid state under UV.

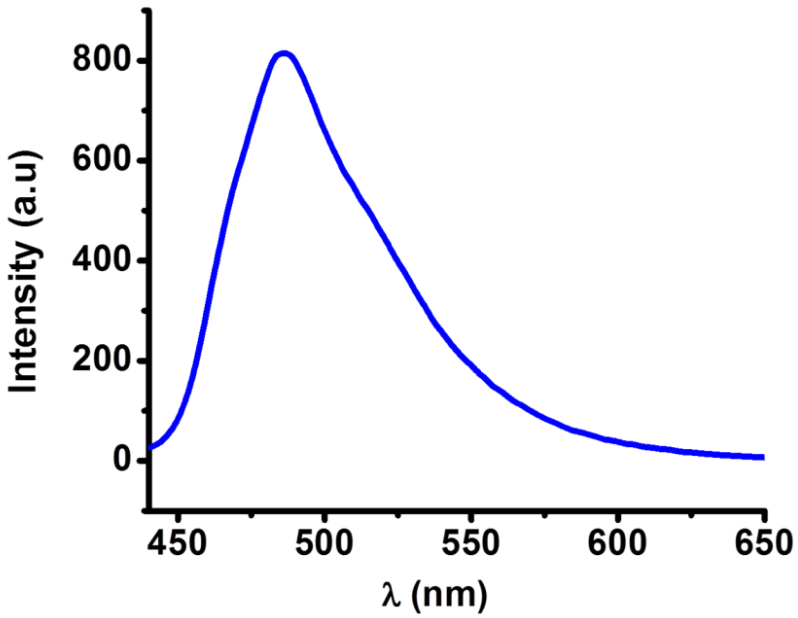

Figure 12. Solid state PL of **H_2OPE-C_{18}** excited at 420 nm.

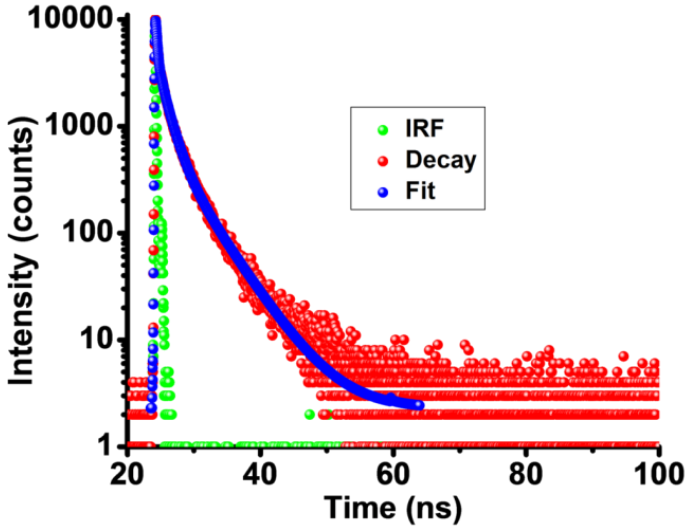

Figure 13. Fluorescence decay profiles of **1** monitored at 485 nm upon excitation at 405 nm.

Fluorescence decay profiles, monitored at 485 nm, upon excitation of **1** at 404 nm, revealed an excited state lifetime of 1.1 ns (Figure 13). To find out the electrochemical band gap, we further carried out cyclic voltammetric measurements on **1** a on a glassy carbon electrode in anhydrous acetonitrile with TBAP as the supporting electrolyte (Figure 14).Well defined oxidation and reduction peaks were obtained from which the band gap was calculated to be 2.55 eV.

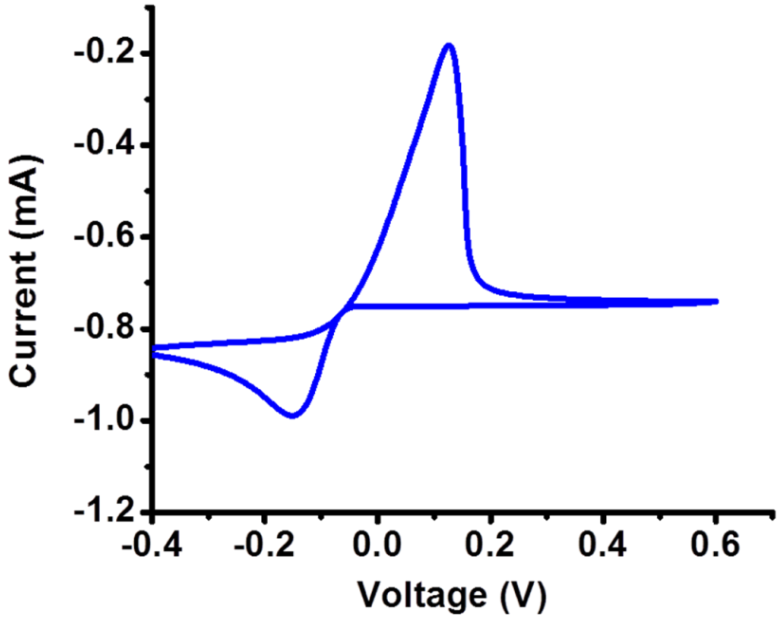

Figure 14. Voltammogram of **1** on a glassy carbon electrode in anhydrous acetonitrile solution containing TBAP as a supporting electrolyte at a scan rate of 50 mV/sec.

Details of electrochemical band gap calculation

As the cyclic voltammogram was obtained under non-aqueous conditions, Ag/Ag^+ reference electrode was used and hence conversion into RHE voltages was required to carry out the band gap calculations. The following standard equation was used for the conversion:

$$E_{RHE} = E_{Ag/Ag+} + E + 0.059*pH\ldots\ldots..(1) \text{ where}$$

E_{RHE} = the corresponding potential for RHE

$E_{Ag/Ag+}$ = the standard electrode potential for the Ag/Ag^+ couple

and E= the observed potential using the Ag/Ag^+ couple

Using this equation the onset oxidation and reduction potentials were found to be 1.342 and 0.842 V, respectively.

$$E_{oxRHE} = 0.799 + 0.200 + 0.413 = 1.412 \text{ V}$$

$$E_{redRHE} = 0.799 - 0.071 + 0.413 = 1.141 \text{ V}$$

Herein, the following formula was utilized to determine the experimental electrochemical HOMO and LUMO levels in terms of eV unit:

$$E\ (HOMO) = -e\ [E_{ox}^{onset} + 4.4]\ldots..(2)$$

$$E\ (LUMO) = -e\ [E_{red}^{onset} + 4.4]\ldots. (3)$$

And the HOMO and LUMO levels were found to be -5.402 and -2.849 eV, respectively having a band gap of 2.55 eV.

$$E\ (HOMO) = -e\ [1.412 - 0.41 + 4.4] = -5.402 \text{ eV}$$

$$E\ (LUMO) = -e\ [-1.141 - 0.41 + 4.4] = -2.849 \text{ eV}$$

We then went on to investigate the electrical conduction property of **1**. As we were able to grow its, single crystals as well as create thin films, we decided to experiment on both the forms. Electrical measurements on different faces of the single crystals were carried out using wire-paste approach while aluminium contacts were used in the thin film approach. A two-probe method was employed to carry out all the measurements in an open atmosphere under ambient conditions. For the single crystal measurements, silver paste was applied to opposite sides of side face and broad face of the single crystals via a bonding machine (Figure 15a, c). Further, copper wires were attached to the contacts and I-V characteristics were measured using a Keithley 2450 sourcemeter. The obtained conductivities for the side face of the block shaped crystal was 3.77×10^{-10} $S.cm^{-1}$ while

that of the long face of the crystal was measured to be 1.19×10^{-9} S.cm^{-1} (Figure 15b, d). These values point to an almost isotropic conductivity in different faces of single crystals of **1**. Going back to the structural description, we see that **1** packs in almost similarly in perpendicular directions via OPE dicarboxylate connections to the Mg SBU nodes. The pathway of charge transport therefore occurs via the 2D grid like conjugated OPE backbone. This results in comparable conductivities obtained from perpendicular faces of block shaped single crystals of **1**. Hence, it is apparent that the mode of charge transport is "through bond" rather than a "through space" route. To further confirm this hypothesis, we carried out DFT calculations on **1**.

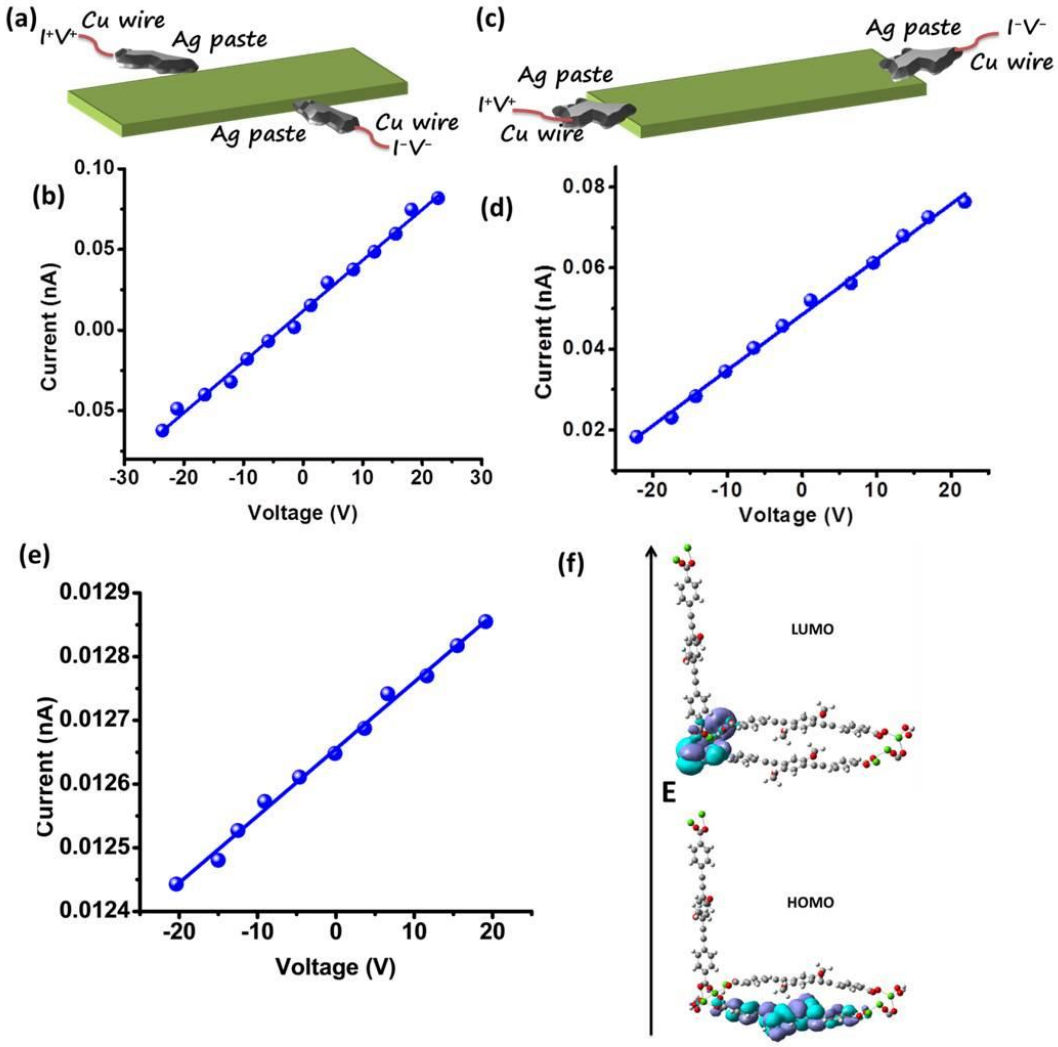

Figure 15. Schematic showing the experimental setup used for measurement of I-V characteristics of (a) side face, (c) broad face of **1** single crystals of **1**. I-V plots for (b) side face, (d) broad face of **1** single crystals, (e) thin film of **1** and (f) HOMO (lower) and LUMO (upper) plot for **1** shown using a fragmented unit for pictorial clarity.

The HOMO-LUMO gap for the **1** was found to be 2.23 eV which matches closely to the experimental band gap (Figure 15f). Furthermore, HOMO wavefunctions reside on the OPE molecules of the 1D column whereas the LUMO mainly resides on the Mg *p*-orbitals and surrounding chelating atoms of the SBU (Figure 15f). This further proves our conjecture that a charge transport occurs via the conjugated bonds and metal atom present throughout the structure. The thin film conductivity of **1** was measured to be 8.82×10^{-10} $S.cm^{-1}$ (Figure 15e). This is an intermediate value of that obtained from both faces of the single crystal. The reason can be attributed to the isotropic distribution of OPE backbones obtained upon thin film formation which gives a transitional value of conductivity for **1**.

4B.4. Conclusion

To summarize, a Mg^{II} based MOF with organic π-conjugated linker (**H_2OPE-C_{18}**) having oxy-octadecyl side chains has been crystallized and structurally well characterized. The permanently porous structure obtained shows a 2D grid like extension with surface projected alkyl chains. This further led to superhydrophobicity of the surface of **1**. Due to the use of the conjugated linker, inherernt luminescence in **1** with a high quantum output was also realized. The extended conjugation present in the system also generated facile charge transport in **1**. Electrical measurements on different faces of the single crystals and thin films of **1** revealed its semi-conducting property. This chapter thus reports the fabrication of a material that has moisture resistant opto-electronic properties and could have promise in device applications.

4B.5. References

1 (a) S. Kitagawa, R. Kitaura and S.-i. Noro, *Angew. Chem. Int. Ed.*, 2004, **43**, 2334; (b) T. K. Maji, R. Matsuda and S. Kitagawa, *Nat. Mater.*, 2007, **6**, 142; (c) H. Li, M. Eddaoudi, M. O'Keeffe and O. M. Yaghi, *Nature.*, 1999, **402**, 276-279; (d) S. Roy, A. Chakraborty and T. K. Maji, *Coord. Chem. Rev.*, 2014, **273-274**, 139; (e) Y. He, B. Li, M. O'Keeffe and B. Chen, *Chem. Soc. Rev.*, 2014, **43**, 5618.

2 (a) K. Müller-Buschbaum, F. Beuerle and C. Feldmann, *Microporous Mesoporous Mater.*, 2015, **216**, 171; (b) H-C. Zhou and S. Kitagawa, *Chem. Soc. Rev.*, 2014, **43**, 5415; (c) R. Adams, C. Carsons, J. Ward, R. Tannenbaum and W. Koros, *Microporous Mesoporous Mater.*, 2010, **131**, 13.

3 (a) J. Heine and K. Müller-Buschbaum, *Chem. Soc. Rev.*, 2013, **42**, 9232; (b) P. Horcajada, T. Chalati, C. Serre, B. Gillet, C. Sebrie, T. Baati, J. F. Eubank, D. Heurtaux, P. Clayette, C. Kreuz, J-S. Chang, Y. K. Hwang, V. Marsaud, P-N. Bories, L. Cynober, S. Gil, G. Férey, P. Couvreur and R. Gref, *Nat. Mater*., 2010, **9**, 172; (c) G. K. H. Shimizu, J. M. Taylor and S. Kim, *Science*., 2013, **341**, 354; (d) A. Carné-Sánchez, I. Imaz, M. Cano-Sarabia and D. Maspoch, *Nat. Chem*., 2013, **5**, 203.

4 (a) L. Sun, S. S. Park, D. Sheberla and M. Dincă, *J. Am. Chem. Soc*., 2016, **138**, 14772. (b) M. G. Campbell, S. F. Liu, T. M. Swager and M. Dincă, *J. Am. Chem. Soc*., 2015, **137**, 13780; (c) S. Rana, R. Rajendra, B. Dhara, P. K. Jha and N. Ballav, *Adv. Mater. Interfaces.*, 2016, **3**, 1500738.

5 (a) L. Sun, M. G. Campbell and M. Dincă, *Angew. Chem. Int. Ed.*, 2016, **55**, 3566; (b) D. Sheberla, L. Sun, M. A. Blood-Forsythe, S. Er, Wade, R. Casey, C. K. Brozek, A. Aspuru-Guzik and M. Dincă, *J. Am. Chem. Soc*., 2014, **136**, 8859; (c) V. Stavil, A. A. Talin and M. D. Allendorf, *Chem. Soc. Rev*., 2014, **43**, 5994; (d) A. A. Talin, A. Centrone, A. C. Ford, M. E. Foster, V. Stavila, P. Haney, R. A. Kinney, V. Szalai, F. ElGabaly, H. P. Yoon, F. Léonard and M. D. Allendorf,. *Science.*, 2014, **343**, 66.

6 (a) S. Roy, M. Das, A. Bandyopadhyay, S. K. Pati, P. P. Ray and T. K. Maji, *J. Phys. Chem. C*, 2017, **121**, 23803; (b) B. Bhattacharya, A. Layek, Md. M. Alam, D. K. Maity, S. Chakrabarti, P. P. Ray and D. Ghoshal, *Chem. Commun*., 2014, **50**, 7858.

7 (a) G. Wu, J. Huang, Y. Zang, J. He and G. Xu, *J. Am. Chem. Soc.*, 2017, **139**, 1360; (b) S. G. Surya, S. S. Nagarkar, S. K. Ghosh, P. Sonard and V. R. Rao, *Sens. Actuator B-Chem.*, 2016, **223**, 114.

8 (a) Y. Cui, Y. Yue, G. Qian and B. Chen, *Chem. Rev*., 2012, **112**, 1126; (b) J. Rocha, L. D. Carlos, F. A. A. Paz and D. Ananias, *Chem. Soc. Rev*., 2011, **40**, 926.

9 S. Roy, V. M. Suresh and T. K. Maji, *Chem. Sci*., 2016, **7**, 2251.

10 (a) V. M. Suresh, S. J. George and T. K. Maji, *Adv. Funct. Mater*., 2013, **23**, 5585; (b) V. M, Suresh, S. Chatterjee, R. Modak, V. Tiwari, A. Patel, T. K. Kundu and T. K. Maji, *J. Phys. Chem. C*, 2014, **118**, 12241.

11 (a) J. G. Nguyen and S. M. Cohen, *J. Am. Chem. Soc*., 2010, **132**, 4560; (b) K. P. Rao, M. Higuchi, K. Sumida, S. Furukawa, J. Duan and S. Kitagawa, *Angew. Chem. Int. Ed.*, 2014, **53**, 8225; (c) T. -H. Chen, I. Popov, O. Zenasni, O. Daugulis and O. S. Miljanic, *Chem. Commun*. 2013, **49**, 6846; (d) C. Serre, *Angew. Chem., Int. Ed.*

2012, **51**, 6048; (e) T. T. Y. Tan, M. R. Reithofer, E. Y. Chen, A. G. Menon, T. S. A. Hor, J. Xu and J. M. Chin, *J. Am. Chem. Soc.* 2013, **135**, 16272.

12 M. S. José, A. Emilio, D. G. Julian, G. Alberto, J. Javier, O. Pablo and S. -P. Daniel, *J. Phys.: Condens. Matter.*, 2002, **14**, 2745.

13 J. Heyd, G. Scuseria and M. Ernzerhof, *J. Chem. Phys*., 2003, **118**, 8207.

14 J. Heyd, J. E. Peralta, G. E. Scuseria and R. L. Martin, *J. Chem. Phys*., 2005, **123**, 174101.

15 J. Heyd, G. E. Scuseria, M. Ernzerhof, *J. Chem. Phys*., 2006, **124**, 219906.

16 S. V. a. SMART (V 5.628), SAINT (V 6.45a), XPREP, SHELXTL; Bruker AXS Inc. Madison, Wisconsin, USA, 2004.

17 G. M. Sheldrick, SADABS, Empirical Absorption Correction Program. University of Göttingen, Göttingen, 1997.

18 G. M. Sheldrick, SHELXL 97, Program for the Solution of Crystal Structure, University of Göttingen, Germany, 1997.

19 A. Spek, *J. Appl. Crystallogr*., 2003, **36**, 7.

20 L. Farrugia, *J. Appl. Crystallogr*., 1999, **32**, 837.

Chapter 5

Summary of the Thesis and Future Outlook

Summary of the Thesis and Future Outlook

The thesis work encompasses the synthesis and property study of *oligo*-(*p*-phenyleneethynylene) (OPE) based organic and inorganic/organic hybrid supramolecular assemblies. Before starting the investigations into the OPEs, five new OPE dicarboxylates and one new OPE ester were designed and synthesized with specific functions in mind. Literature procedures were then followed to generate supramolecular π-systems, organo and metallogels, NMOFs and bulk MOFs. All the new OPE derived systems were structurally well characterized and utilized for further applications. OPE based π-systems were first shown to have simultaneous liquid crystalline, mechanochromic and polymorphic behavior. The occurrence of such properties was well correlated with single crystal structural analysis, DFT calculations and nanoindentaion experiments. The role of end groups and side chains in generating such properties was then investigated. It showed how carboxylate functionalities lead to denser structural packing over ester groups, which show a less dense packing. Carboxylates also control polymorphism, nanomorphology tuning and gel formation in these bola-amphiphilic systems whereas less dense packing due to ester substitution leads to mechanochromic behavior. It was then shown that gels derived from polar OPEs can lead to guest dependent pure white light emission with a high quantum output and also charge transfer hybrids.

In another approach towards inducing unexplored properties in OPE derived materials, it was shown how to fabricate OPE based NMOF structures which show extreme water repellence. This approach led to self-cleaning porous materials unprecedented in the field. The idea of generating self-cleaning materials was further put forward to another NMOF material which showed device based simultaneous water repellence, Schottky diode like behavior and photo-conduction. This could potentially open up an avenue for utilizing porous materials as underwater opto-electronic devices.

OPE derived bulk MOF materials were also investigated keeping in mind that they could generate interesting structure property correlations. Two such bulk MOFs were synthesized from two different OPE dicarboxylates and their structures were well investigated. It was seen from this analysis that OPE emission can be tuned via twisting of OPE based linkers guided by guest molecules within the MOF. In another probe, it was found that OPE chains are directly involved in charge transport leading to conducting properties. The chain transport overrules the possibility of a through space charge transport.

The overall findings from this thesis go a long way to address the following main problems:

1) How to design and investigate the multi-functionality in phase changeable supramolecular π-systems.
2) How to design, synthesize and characterize morphology tunable self-cleaning MOF nanostructures and utilize their vast potential in opto-electronic device fabrications.
3) Can we really have a structural picture of MOFs which have corrosion-resistant opto-electrical properties?

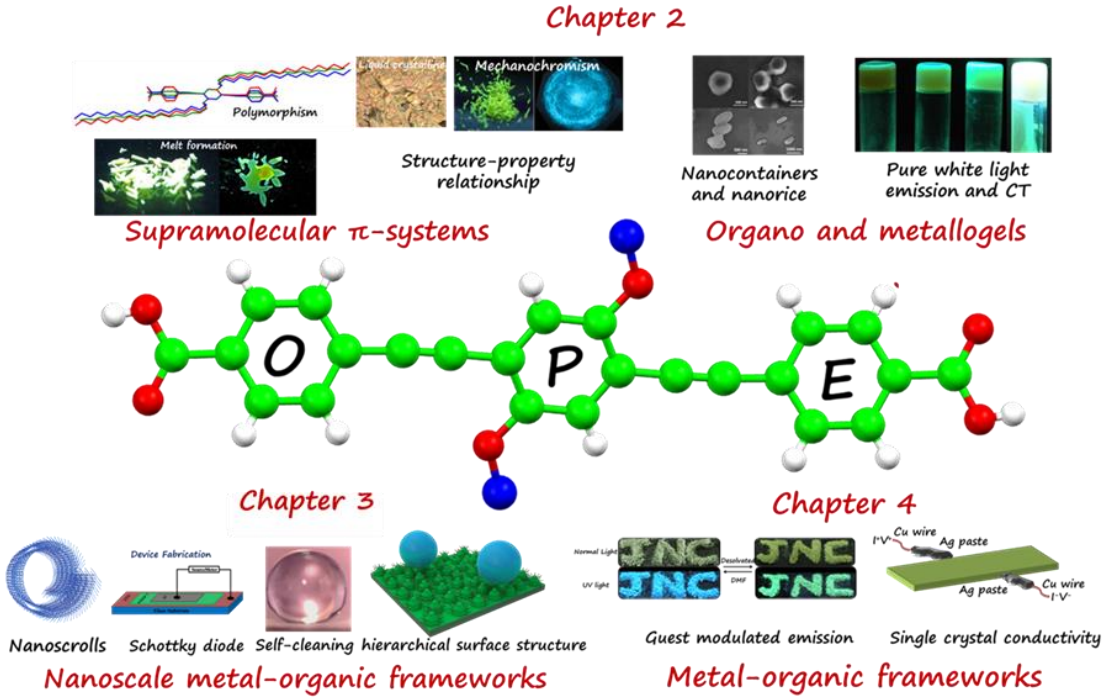

Scheme 1. Schematic summarizing the overall work of the thesis.

The choice of OPEs as a tool to construct all the above mentioned materials has generated high-performing and multi-functional supramolecular assemblies. Since the work has now been standardized into set protocols for synthesis and characterization, more such systems can be designed using OPEs and structurally similar molecules. This could open up new and interesting applications of the above mentioned materials. Furthermore, the ease of structural modifications present in OPE synthesis and the understanding of mesophasic behavior in them, begs the design of OPEs based materials which could lead to liquid crystalline porous systems. This has never been realized before and could open a world of opportunities in the advancement of technology.

It was seen in the thesis work that OPEs are also redox active in nature. Coupled with the ease of synthetic tunability, OPE structures could be generated whose redox potentials fall within the region of industrially important electro-chemical energy applications such as oxygen reduction, oxygen evolution and hydrogen evolution. The solution processability achieved in this thesis for OPE derived materials, would allow facile coating on electrodes, an essential part of any electro-chemical studies. The porosity of the OPE based MOFs and NMOFs could be further utilized for 1) encapsulation of redox active electro-catalytic guests for the above application and 2) facile diffusion of reducible substrate molecules such as oxygen and water, leading to enhancement of catalytic activity.

Another application that has not been explored in the thesis work but could be an offshoot of the good absorption property of OPEs over a wide range would be photocatalytic applications to generate clean fuels such as hydrogen. Here, the synthetic tunability of OPE systems could be used to tune the band gap into the visible region. This could lead to visible light driven hydrogen production in OPE derived materials such as supramoelcular π-systems, gels and nanoscale porous structures. Additionally band gap tuning could also lead to potential applications of OPE derived materials in photocatalytic CO_2 reduction as well.

BIOGRAPHY

Syamantak Roy obtained his B.Sc. degree from St. Xavier's College, Kolkata, University of Calcutta, in 2009. He obtained his master's degree from the Department of Chemistry, Jadavpur University, Kolkata, in 2011. Presently, he is pursuing his Ph.D. under the supervision of Prof. Tapas K. Maji at the Jawaharlal Nehru Centre for Advanced Scientific Research (JNCASR), Bangalore, India. His research work focuses on synthesis and study of multi-functional organic and inorganic/organic hybrid assemblies derived from *oligo*-(*p*-phenyleneethynylenes) (OPEs) and their various applications. He secured an All-India Rank of 86 in the CSIR-UGC NET exam (2012) and 402 in the GATE exam (2011). He has been the recipient the Best Poster Award at the 12th International Conference on Chemistry of Materials, Kovalam, Kerala, 2016 and In-house Symposium 2016, JNCASR. He also received an International Travel Support (2017), Jawaharlal Nehru Centre for Advanced Scientific Research (JNCASR), Government of India, to attend the International Symposium on Macrocyclic and Supramolecular Chemistry in Cambridge, United Kingdom, 2017 and International Travel Support (2016), Science and Research Board, Department of Science and Technology (DST), Government of India, to attend the 5th International Conference on metal-organic frameworks and open framework compounds, Long Beach, California, USA.

List of Patents and Publications

1 **S. Roy**, V. M. Suresh and T. K. Maji, Self-cleaning MOF: Realization of Extreme Water Repellence in Coordination Driven Self-Assembled Nanostructures. *Chem. Sci.*, 2016, **7**, 2251-2256.

2 **S. Roy**, A. Hazra, A. Bandyopadhyay, D. Raut, P. Lakshmi Madhuri, D. Shankar Rao, U. Ramamurty, S. K. Pati, S. K. Prasad and T. K. Maji, Reversible Polymorphism, Liquid Crystallinity, and Stimuli-Responsive Luminescence in a Bola-amphiphilic π-System: Structure-Property Correlations Through Nanoindentation and DFT Calculations. *J. Phys. Chem. Lett.*, 2016, **7**, 4086-4092.

3 **S. Roy**, D. Samanta, P. Kumar and T. K. Maji, Pure White Light Emission and Charge Transfer in Organogels of Symmetrical and Unsymmetrical π-chromophoric *Oligo-p*-(phenyleneethynylene) Bola-amphiphiles *Chem. Comm.*, 2018, **54**, 275-278.

4 **S. Roy**, A. Chakraborty and T. K. Maji, Lanthanide-Organic Frameworks for Gas Storage and as Magneto-Luminescent Materials. *Coord. Chem. Rev.*, 2014, **273**, 139-164.

5 **S. Roy**, M. Das, A. Bandyopadhyay, P. P. Ray, and T. K. Maji, Colossal Increase in Electric Current and High Rectification Ratio in a Photo-conducting, Self-cleaning and Luminescent Schottky Barrier NMOF Diode. *J. Phys. Chem. C*, 2017, **121**, 23803-23810.

6 **S. Roy**, A. Bandyopadhyay, M. Das, P. P. Ray, S. K. Pati and T. K. Maji, Redox-active and Semi-conducting Donor-Acceptor Conjugated Microporous Polymers as Metal-free ORR Catalysts. *J. Mat. Chem. A*, 2018, **6**, 5587-5591.

7 A. Chakraborty, **S. Roy**, M. Eswaramoorthy, and T. K. Maji Flexible MOF-Aminoclay Nanocomposites Showing Tunable Stepwise/Gated Sorption for C_2H_2, CO_2 and Separation for CO_2/N_2 and CO_2/CH_4. *J. Mat. Chem. A*, 2017, **5**, 8423-8430.

8 A. Singh, **S. Roy**, C. Das, D. Samanta and T. K. Maji, Metallophthallocyanine based Redox Active Metal-Organic Conjugated Microporous Polymers for OER Catalysis. *Chem. Comm.* Just Accepted. DOI: 10.1039/C8CC01291A (2018).

9 V. M. Suresh, S. Bonakala, **S. Roy**, S. Balasubramanian and T. K. Maji, Synthesis, Characterization, and Modeling of a Functional Conjugated Microporous Polymer: CO_2 Storage and Light Harvesting *J. Phys. Chem. C*, 2014, **118**, 24369-24376.

10 F. Ahmed, **S. Roy**, K. Naskar, C. Sinha, S. M. Alam, S. Kundu, J. J. Vittal and M. H. Mir, Halogen···Halogen Interactions in the Supramolecular Assembly of 2D Coordination Polymers and the CO_2 Sorption Behavior, *Cryst. Growth Des.*, 2016, **16**, 5514–5519.

11 S. Mohapatra, **S. Roy**, D. Ghoshal and T. K. Maji, Two 3D Supramolecular Frameworks Assembled from the Dinuclear Building Block: A Crystallographic Evidence of Carboxylate(O)···π Interaction, *J. Chem. Sci.*, 2014, **126**, 1153–1161.

12 V. M. Suresh, A. Bandyopadhyay, **S. Roy**, S. K. Pati and T. K. Maji, Highly Luminescent Microporous Organic Polymer with Lewis acidic 'Boron' Sites on the Pore Surface: Ratiometric Sensing and Capture of F- Ion, *Chem. Eur. J.*, 2015, **21**, 10799-10804.

13 M. Maiti, D. Sadhukhan, S. Thakurta, **S. Roy**, G. Pilet, R. J Butcher, A. Nonat, L. J Charbonnière and S. Mitra, Series of Dicyanamide-Interlaced Assembly of Zinc-Schiff-Base complexes: Crystal Structure and Photophysical and Thermal Studies, *Inorg. Chem.*, 2012, **51**, 12176–12187.

14 **S. Roy**, V. M. Suresh, A. Hazra, A. Bandyopadhyay, S. K. Pati, S. Laha and T. K. Maji, Solvent Modulated Emission Properties in a Superhydrophobic *Oligo*-(*p*-phenyleneethynylene) based 3D Porous Supramolecular Framework. Manuscript submitted.

15 **S. Roy**, D. Samanta, S. Bhattacharyya, P. Kumar, A. Hazra and T. K. Maji, Tunable Physical States of a Bola-amphiphilic π-system Assisted by Functional Group Design. Manuscript submitted.

16 D. Samanta, P. Verma, **S. Roy** and T. K. Maji, Nanovesicular MOF with Omniphilic Porosity: Bimodal Functionality for White-Light Emission and Photocatalysis by Dye Encapsulation. Manuscript Submitted.

17 **S. Roy**, S. Bhattacharyya, A. Bandyopadhyay, S. K. Pati, and T. K. Maji, Moisture Resistant, Luminescent and Electrically Conducting Metal-organic Framework. Manuscript submitted.

Patents

1 Self-cleaning nanoscale metal-organic frameworks (NMOFs) and process of preparation thereof (Indian Patent Application Number: 201641040976, Year: 2016)

S. Roy, V. M. Suresh and T. K. Maji.

2 Conjugated Microporous Polymer (Indian Patent Application Number: 201741040351, Year: 2017)

S. Roy and T. K. Maji